ADVANCES IN MATERIALS TOWARD ANTI-CORROSION AND ANTI-BIOFOULINGS

EDITED BY: Binbin Zhang, Qixin Zhou, Lingwei Ma, Dake Xu and Xiaoqiang Fan

PUBLISHED IN: Frontiers in Materials

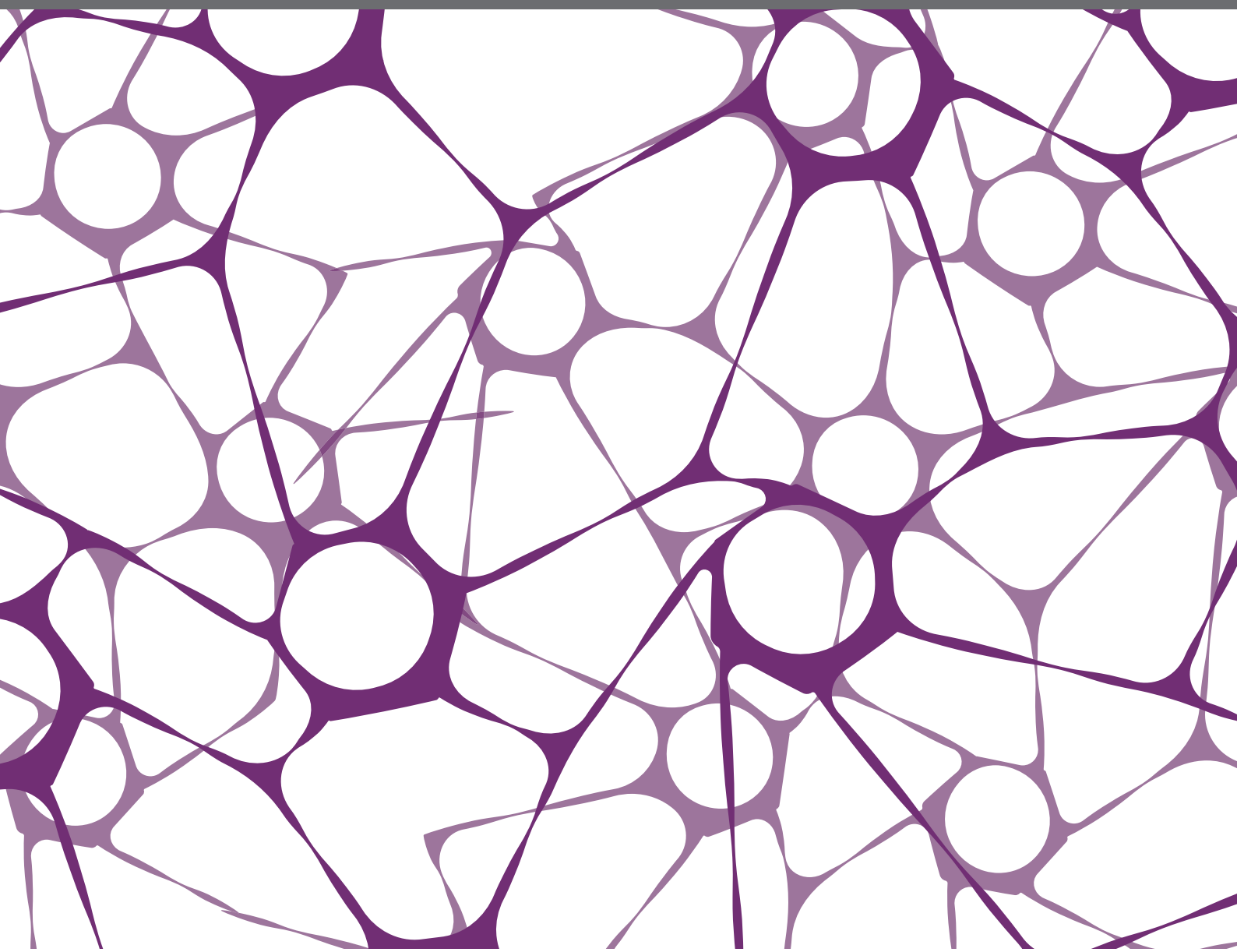

frontiers Research Topics

ISSN 1664-8714
ISBN 978-2-88976-713-7
DOI 10.3389/978-2-88976-713-7

About Frontiers

Frontiers is more than just an open-access publisher of scholarly articles: it is a pioneering approach to the world of academia, radically improving the way scholarly research is managed. The grand vision of Frontiers is a world where all people have an equal opportunity to seek, share and generate knowledge. Frontiers provides immediate and permanent online open access to all its publications, but this alone is not enough to realize our grand goals.

Frontiers Journal Series

The Frontiers Journal Series is a multi-tier and interdisciplinary set of open-access, online journals, promising a paradigm shift from the current review, selection and dissemination processes in academic publishing. All Frontiers journals are driven by researchers for researchers; therefore, they constitute a service to the scholarly community. At the same time, the Frontiers Journal Series operates on a revolutionary invention, the tiered publishing system, initially addressing specific communities of scholars, and gradually climbing up to broader public understanding, thus serving the interests of the lay society, too.

Dedication to Quality

Each Frontiers article is a landmark of the highest quality, thanks to genuinely collaborative interactions between authors and review editors, who include some of the world's best academicians. Research must be certified by peers before entering a stream of knowledge that may eventually reach the public - and shape society; therefore, Frontiers only applies the most rigorous and unbiased reviews.
Frontiers revolutionizes research publishing by freely delivering the most outstanding research, evaluated with no bias from both the academic and social point of view. By applying the most advanced information technologies, Frontiers is catapulting scholarly publishing into a new generation.

What are Frontiers Research Topics?

Frontiers Research Topics are very popular trademarks of the Frontiers Journals Series: they are collections of at least ten articles, all centered on a particular subject. With their unique mix of varied contributions from Original Research to Review Articles, Frontiers Research Topics unify the most influential researchers, the latest key findings and historical advances in a hot research area! Find out more on how to host your own Frontiers Research Topic or contribute to one as an author by contacting the Frontiers Editorial Office: frontiersin.org/about/contact

ADVANCES IN MATERIALS TOWARD ANTI-CORROSION AND ANTI-BIOFOULINGS

Topic Editors:
Binbin Zhang, Institute of Oceanology, Chinese Academy of Sciences (CAS), China
Qixin Zhou, University of Akron, United States
Lingwei Ma, University of Science and Technology Beijing, China
Dake Xu, Northeastern University, China
Xiaoqiang Fan, Southwest Jiaotong University, China

Citation: Zhang, B., Zhou, Q., Ma, L., Xu, D., Fan, X., eds. (2022). Advances in Materials Toward Anti-Corrosion and Anti-Biofoulings.
Lausanne: Frontiers Media SA. doi: 10.3389/978-2-88976-713-7

Table of Contents

frontiers | Frontiers in Materials

EDITORIAL
published: 08 July 2022
doi: 10.3389/fmats.2022.968100

Editorial: Advances in Materials Toward Anti-Corrosion and Anti-Biofoulings

Binbin Zhang[1], Qixin Zhou[2], Lingwei Ma[3], Xiaoqiang Fan[4] and Dake Xu[5]*

[1]CAS Key Laboratory of Marine Environmental Corrosion and Bio-fouling, Institute of Oceanology, Chinese Academy of Sciences, Qingdao, China, [2]Department of Chemical, Biomolecular, and Corrosion Engineering, the University of Akron, Akron, OH, United States, [3]National Materials Corrosion and Protection Data Center, University of Science and Technology Beijing, Beijing, China, [4]Key Laboratory of Advanced Technologies of Materials (Ministry of Education), School of Materials Science and Engineering, Southwest Jiaotong University, Chengdu, China, [5]Shenyang National Laboratory for Materials Science, Northeastern University, Shenyang, China

Keywords: corrosion, biofouling, microbiologically influenced corrosion (MIC), inhibitors, surface and coating

Editorial on the Research Topic

Advances in Materials Toward Anti-Corrosion and Anti-Biofoulings

Corrosion and biofoulings are intractable problems triggered by complex chemical/electrochemical/hybrid interactions between materials and surrounding environments (Hou et al., 2017; Zhang and Xu, 2021), threatening a variety of fields such as marine engineering facilities, port wharfs, offshore platforms, coastal structures, chemical industries, and military equipment. In the past decades, great efforts have been devoted to design novel materials for enhancement of anti-corrosion and anti-biofouling performance, including corrosion inhibitors (Jain et al., 2020; Bhardwaj et al., 2021), organic/inorganic/nano-composite/waterborne protective coatings (Hosseinpour et al., 2021; Lazorenko et al., 2021), surface/coatings construction with special wettability (Zhang et al., 2021; Zhang et al., 2022) *etc*. This Research Topic collected 11 original research papers from 65 contributors of the relevant fields, presenting latest advances of corrosion/biofouling mechanism and novel anti-corrosion and anti-biofouling materials including crevice corrosion, microbiologically influenced corrosion (MIC), hydrogen permeation, corrosion inhibitors, organic anti-corrosion coatings, superhydrophobic coating, pH-responsive coating, and waterborne epoxy coating.

For advances of corrosion and biofouling mechanisms, Wang et al. investigated crevice corrosion behaviors of a typical pearlitic high-speed rail steel U75V based on a visualized *In situ* monitoring system, providing important information regarding the effect of pearlitic microstructure refinement on crevice corrosion. Li et al. used carbon source starvation to vary the sulfate-reducing bacterium (SRB)-elevated MIC severity for investigating subsequent MIC impacts on deterioration of the mechanical properties of X80 carbon steel. Zhang et al. investigated and estimated the hydrogen permeation behavior (hydrogen permeation efficiency and hydrogen embrittlement) of carbon steel during corrosion in highly pressed saturated bentonite by electrochemical and extrapolation analyses. Yu et al. investigated the corrosion behavior of Ti6Al4V alloy in the Presence of HCl through surface analysis and electrochemical measurements, presenting novel and useful information of the temperature-dependence corrosion mechanism for Ti corrosion-related failures.

For advances of anti-corrosion and anti-biofouling materials, Cao et al. experimentally and theoretically studied the effective inhibition properties of imidazo (Hou et al., 2017; Zhang and Xu, 2021) pyrimidine derivatives (namely, 2,4-diphenylbenzo (Jain et al., 2020; Lazorenko et al., 2021)imidazo (Hou et al., 2017; Zhang and Xu, 2021)pyrimidine and 2-(4-octylphenyl)-4-phenylbenzo (Jain et al., 2020; Lazorenko et al., 2021)imidazo (Hou et al., 2017; Zhang and Xu, 2021)pyrimidine) as corrosion inhibitors

OPEN ACCESS

Edited and reviewed by:
Guang-Ling Song,
Xiamen University, China

****Correspondence:***
Binbin Zhang
zhangbinbin11@mails.ucas.ac.cn

Specialty section:
This article was submitted to Environmental Degradation of Materials, a section of the journal Frontiers in Materials

Received: *13 June 2022*
Accepted: *17 June 2022*
Published: *08 July 2022*

Citation:
Zhang B, Zhou Q, Ma L, Fan X and Xu D (2022) Editorial: Advances in Materials Toward Anti-Corrosion and Anti-Biofoulings. Front. Mater. 9:968100. doi: 10.3389/fmats.2022.968100

against mild steel corrosion in HCl solution. Guo et al. studied the corrosion inhibition effect of 3-amino-5-mercapto-1,2,4-triazole (AMT) inhibitor on AA2024 aluminium alloy in 3.5 wt% NaCl solution, indicating that the efficient adsorption of corrosion inhibitor molecules significantly enhanced the anti-corrosion performance. Guo et al. prepared a graphene modified epoxy surface tolerant coating on rusty carbon steel substrate, then studied its corrosion resistant performance and phytic acid-rust conversion mechanism. Minhas et al. developed a novel active protective surface based on epoxy coating and underlying lithium carbonate (Li_2CO_3)-treated anodized aluminum alloy 2024-T3. Zhang et al. fabricated an eco-friendly and mechanical robust superhydrophobic coating with low adhesion force, superior corrosion resistance and easy adaptability based on fluorine-free chemical reagents. Furthermore, the deliquescence behaviors of NaCl salt particles and the instantaneous self-coalescence phenomenon were recorded under high atmospheric humidity, demonstrating a promising marine atmospheric anti-corrosion utilizations. Hao et al. reported the design and fabrication of pH-controlled releasing behaviors of polydopamine/tannic acid-allicin@chitosan (PDA/TA-ALL@CS) multilayer coatings to realize antibacterial and antifouling effects in marine environments. Zhou et al. developed a simple and effective method to prepare graphene oxide (GO) hybridized waterborne epoxy (GOWE) coating to simultaneously improve anti-corrosion and anti-bacterial functions, which provides new insight into the multifunctional marine applications of polymer composite coatings based on 2D nano-materials.

Although some significant progress has been achieved in this Research Topic, many challenges remain for improving the long-term durability, environmental sustainability, easy applicability *etc*. As guest editors, we hope the 11 original research papers collected in this Research Topic can provide the readers with some new insights and perspectives for the design and development of advanced anti-corrosion and anti-biofouling materials.

AUTHOR CONTRIBUTIONS

All authors listed have made a substantial, direct and intellectual contribution to the work, and approved it for publication.

FUNDING

The authors acknowledge the financial supports from the Project of Innovation Development Joint Funds supported by the Shandong Provincial Natural Science Foundation (No. ZR2021LFG004); and the Youth Innovation Promotion Association Chinese Academy of Sciences (No. 2021207).

ACKNOWLEDGMENTS

As guest editors, we would like to express our gratitude to all the contributing authors and reviewers who have supported this Research Topic and the entire staff of the Frontiers in Materials Editorial Office for this precious and valuable collaboration.

REFERENCES

Bhardwaj, N., Sharma, P., and Kumar, V. (2021). Phytochemicals as Steel Corrosion Inhibitor: an Insight into Mechanism. *Corros. Rev.* 39, 27–41. doi:10.1515/corrrev-2020-0046

Hosseinpour, A., Rezaei Abadchi, M., Mirzaee, M., Ahmadi Tabar, F., and Ramezanzadeh, B. (2021). Recent Advances and Future Perspectives for Carbon Nanostructures Reinforced Organic Coating for Anti-corrosion Application. *Surfaces Interfaces* 23, 100994. doi:10.1016/j.surfin.2021.100994

Hou, B., Li, X., Ma, X., Du, C., Zhang, D., Zheng, M., et al. (2017). The Cost of Corrosion in China. *npj Mater. Degrad.* 1, 4. doi:10.1038/s41529-017-0005-2

Jain, P., Patidar, B., and Bhawsar, J. (2020). Potential of Nanoparticles as a Corrosion Inhibitor: A Review. *J. Bio. Tribo. Corros.* 6, 43. doi:10.1007/s40735-020-00335-0

Lazorenko, G., Kasprzhitskii, A., and Nazdracheva, T. (2021). Anti-corrosion Coatings for Protection of Steel Railway Structures Exposed to Atmospheric Environments: A Review. *Constr. Build. Mater.* 288, 123115. doi:10.1016/j.conbuildmat.2021.123115

Zhang, B., and Xu, W. (2021). Superhydrophobic, Superamphiphobic and SLIPS Materials as Anti-corrosion and Anti-biofouling Barriers. *New J. Chem.* 45, 15170–15179. doi:10.1039/D1NJ03158A

Zhang, B., Xu, W., Xia, D.-H., Fan, X., Duan, J., and Lu, Y. (2021). Comparison Study of Self-Cleaning, Anti-icing, and Durable Corrosion Resistance of Superhydrophobic and Lubricant-Infused Ultraslippery Surfaces. *Langmuir* 37, 11061–11071. doi:10.1021/acs.langmuir.1c01684

Zhang, B., Xu, W., Zhu, Q., Guan, F., and Zhang, Y. (2022). Nepenthes Pitcher-Inspired Lubricant-Infused Slippery Surface with Superior Anti-corrosion Durability, Hot Water Repellency and Scratch Resistance. *J. Industrial Eng. Chem.* 107, 259–267. doi:10.1016/j.jiec.2021.11.052

Conflict of Interest: The authors declare that the research was conducted in the absence of any commercial or financial relationships that could be construed as a potential conflict of interest.

Publisher's Note: All claims expressed in this article are solely those of the authors and do not necessarily represent those of their affiliated organizations, or those of the publisher, the editors and the reviewers. Any product that may be evaluated in this article, or claim that may be made by its manufacturer, is not guaranteed or endorsed by the publisher.

frontiers in Materials

ORIGINAL RESEARCH
published: 12 November 2021
doi: 10.3389/fmats.2021.767776

Corrosion Performance and Rust Conversion Mechanism of Graphene Modified Epoxy Surface Tolerant Coating

Xiaoping Guo[1,2], Hao Xu[2], Jibin Pu[2], Chao Yao[1], Jing Yang[3] and Shuan Liu[2]**

[1]School of Petrochemical Engineering, Changzhou University, Changzhou, China, [2]Key Laboratory of Marine Materials and Related Technologies, Zhejiang Key Laboratory of Marine Materials and Protective Technologies, Ningbo Institute of Materials Technology and Engineering, Chinese Academy of Sciences, Ningbo, China, [3]Hubei Huaqiang Technology Co., Ltd., Yichang, China

A graphene modified epoxy surface tolerant coating was prepared, and the corrosion performance and rust conversion mechanism of the prepared composite coating on rusty carbon steel substrate was investigated. Scanning electron microscope (SEM), X-ray powder diffractometer (XRD), and infrared (IR) spectrum were used to confirmed the iron rust conversion performance by the reaction of phytic acid and rust. electrochemical impedance spectroscopy (EIS), polarization curve, and salt spray test were used to evaluate the corrosion resistance of low surface treatment coatings. Results indicated most of the rust were dissolved and transformed with the reaction of phytic acid and rust on the rusty carbon steel; graphene could effectively improve the compactness and protective performance of the epoxy surface tolerant coating.

Keywords: corrosion, surface tolerant coating, graphene, rusty, EIS

OPEN ACCESS

Edited by:
Binbin Zhang,
Institute of Oceanology (CAS), China

Reviewed by:
Yong Zou,
Shandong University, China
Da-Hai Xia,
Tianjin University, China
Tengfei Xiang,
Anhui University of Technology, China

****Correspondence:***
Chao Yao
yaochao@cczu.edu.cn
Shuan Liu
liushuan@nimte.ac.cn

Specialty section:
This article was submitted to Environmental Degradation of Materials, a section of the journal Frontiers in Materials

Received: *31 August 2021*
Accepted: *11 October 2021*
Published: *12 November 2021*

Citation:
Guo X, Xu H, Pu J, Yao C, Yang J and Liu S (2021) Corrosion Performance and Rust Conversion Mechanism of Graphene Modified Epoxy Surface Tolerant Coating. Front. Mater. 8:767776. doi: 10.3389/fmats.2021.767776

INTRODUCTION

Heavy anticorrosive coating technology is the most economical and popular protection technology to slow down the corrosion rate of marine steel structures (Arukalam et al., 2018; Zhu et al., 2020). However, in order to ensure the anticorrosive quality of the coating, the steel substrate needs to be sandblasted or shot blasted before construction, and in most cases, the surface cleanliness after treatment is required to meet the surface treatment level Sa2.5 specified in ISO 8501-1988. Sandblasting not only brings a lot of dust and noise pollution but also increases the construction cost. Due to the influence of construction conditions, coating conditions, and the changeable coastal weather, the marine steel structure cannot be coated immediately after sandblasting or can only be coated with rust (Lei et al., 2021; Oliveira et al., 2021). In particular, some dead corners of complex steel structures cannot be treated by traditional sand blasting; besides, in the actual outdoor coating construction, it is impossible to completely and thoroughly sandblast steel. Even after sandblasting, the steel surface still has various degrees of rust and is often in a high degree of moisture. Therefore, it is particularly important to develop a simple and efficient anticorrosion coating with low surface treatment for long-term anticorrosion of equipment in the marine environment (Liao and Lee, 2016; Feng and Yuan, 2020).

Low surface treatment coating is also called surface tolerance coating, which is an anticorrosive coating that can be applied on the corroded surface of steel with simple surface treatment or without treatment. Low surface treatment coating has excellent adhesion, wettability, permeability, and rust

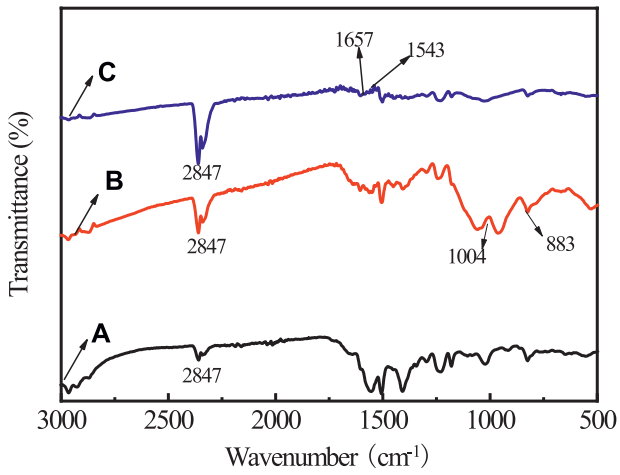

FIGURE 1 | The IR spectra for rusty carbon steel **(A)**, PA dropped on rusty carbon steel **(B)**, and PA/G/EP coating coated on rusty carbon steel **(C)**.

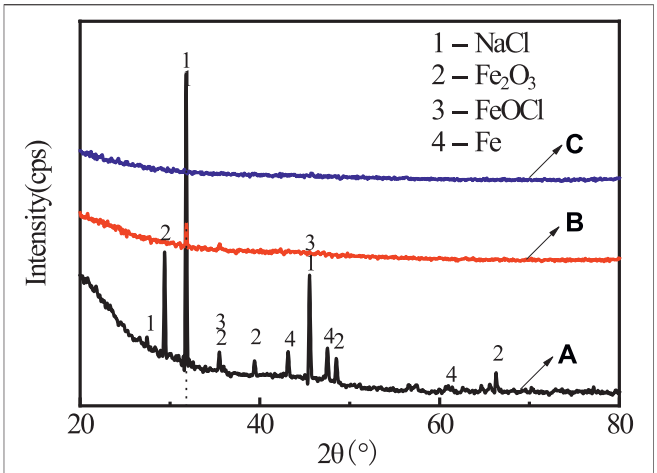

FIGURE 2 | The XRD spectra for rusty carbon steel **(A)**, 5 wt% PA solution dropped on rusty carbon steel **(B)**, and PA/G coating coated on rusty carbon steel **(C)**.

conversion. Good wetting and permeability are the basis of low surface treatment coatings (Figueroa et al., 2020; Marano et al., 2020). On the one hand, the low surface treatment coatings contain active antirust pigments or rust conversion agents, which can transform active corrosion products, generate stable iron chelate, and become a part of the complete paint film as a way of inert fillers. On the other hand, adding chelating agent and corrosion inhibitor to rust primer can improve the passivation performance of metal substrate (Jiang et al., 2020; Chang et al., 2021).

Phytic acid (PA) molecule has six phosphate groups which can combine with metal cations; it is an environmentally friendly rust inhibitor. Graphene (G) is the thinnest two-dimensional (2D) carbon material; its own unique nanostructure endows its perfect impermeability to any atoms and molecules under ambient conditions, and so G could be used as an excellent functional filler in anticorrosion coatings (Gu et al., 2015; Bai et al., 2021; Mu et al., 2021). In our previous research, we have confirmed that the original iron ions absorbed on rusty carbon steel surfaces could be transformed by PA, and a dense film was formed with the reaction of PA and rust (Xu et al., 2021). In this research, we prepared a G modified epoxy surface tolerant coating using PA as a rust conversion agent and G as a functional filler. The corrosion performance of as-prepared surface tolerant coating on rusty steel was studied by means of electrochemical measurements in 3.5 wt % NaCl solution. The results of this paper may provide an insight on providing a simple and efficient protection technology for corroded metals in the marine environment.

EXPERIMENTAL

Materials

All reagents including PA solution (PA content: 70 wt%) were purchased from Sigma-Aldrich and Aladdin and used without further purification unless otherwise noted. Epoxy resin (EP), C_{12-14} alkyl glycidyl ether (AGE), and polyamide curing agent were purchased from Hubei Greenhome Materials Technology, Inc. G powder (5–10 layers, 10–200 μm diameter, 5–15 nm thickness, 99.5 wt% purity) was purchased from Ningbo Morsh Technology. Co., Ltd. Carbon steel (1 cm × 1 cm × 1 cm) was purchased from Yuxin Technology Co., Ltd. The polyo-phenylenediamine was prepared and used as G dispersant (Cui et al., 2019).

The rusty carbon samples were prepared by dropping 3.5 wt% NaCl solution onto the clean sample and allowing it to react for 30 days at ambient temperature. Some loose corrosion products were formed on the surface of carbon steel (namely, rusty carbon steel).

Preparation of Graphene Modified Epoxy Surface Tolerant Coating

Firstly, 0.5 g G power was ultrasonically dispersed by 0.01 g polyo-phenylenediamine in 20 ml xylene solvent, and the mixture was stirred for 30 min, then 0.12 g PA, 20 ml AGE, and 30 g EP were added to the above mixture and ground until paint fineness reached 50 μm. Finally, 20 g polyamide curing agent was added, and the mixture was stirred for 30 min. The prepared composite coating (PA/G/EP) was applied to the rusty carbon steel cured at room temperature for 48 h; the coating thickness was 60 ± 2 μm. In the same way, a pure epoxy coating (EP) and PA with EP (PA/EP) were prepared and coated on rusty carbon steel at the same thickness.

Material Characterization

The rust and the PA chelate were analyzed by Intelligent Fourier Infrared Spectrometer (NICOLET 6700 FTIR) and X-ray powder diffractometer (Bruker-AXS D8 XRD). The cross-section surfaces of EP, PA/EP, and PA/G/EP were observed by scanning electron microscope (FEG 250 SEM). To prepare the cross-section surfaces, firstly, the coating was cured at 80°C for 24 h, and

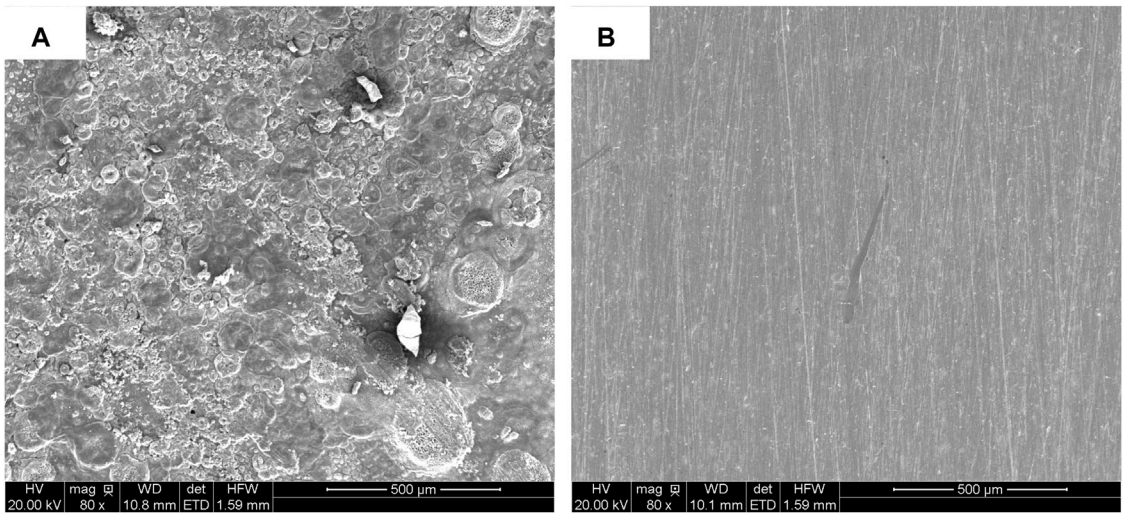

FIGURE 3 | SEM images of rusty carbon steel **(A)** and rusty carbon steel reacted with 5 wt %PA solution for 24 h **(B)**.

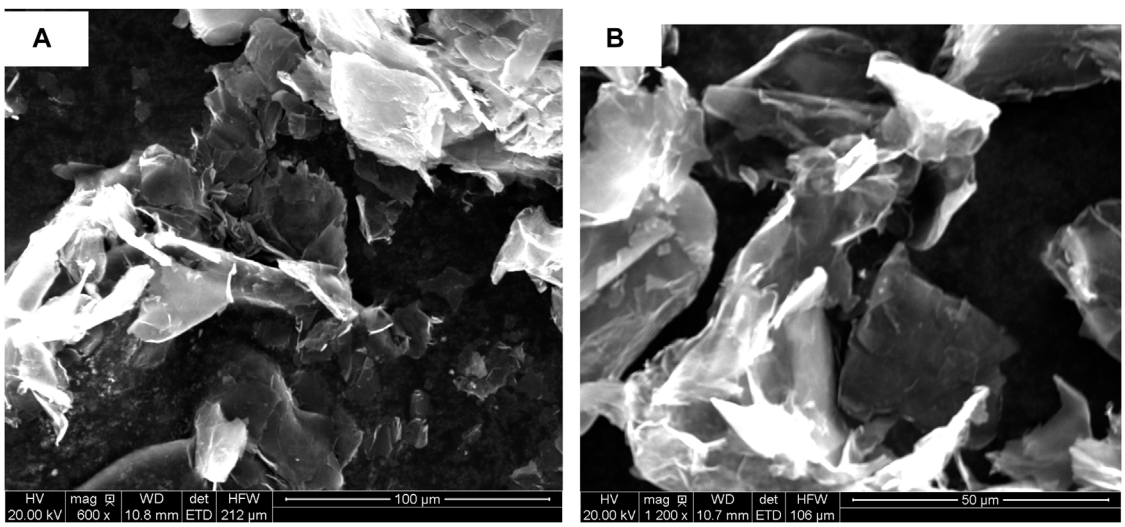

FIGURE 4 | SEM images of dispersed G in xylene solvent at low magnification **(A)** and high magnification **(B)**.

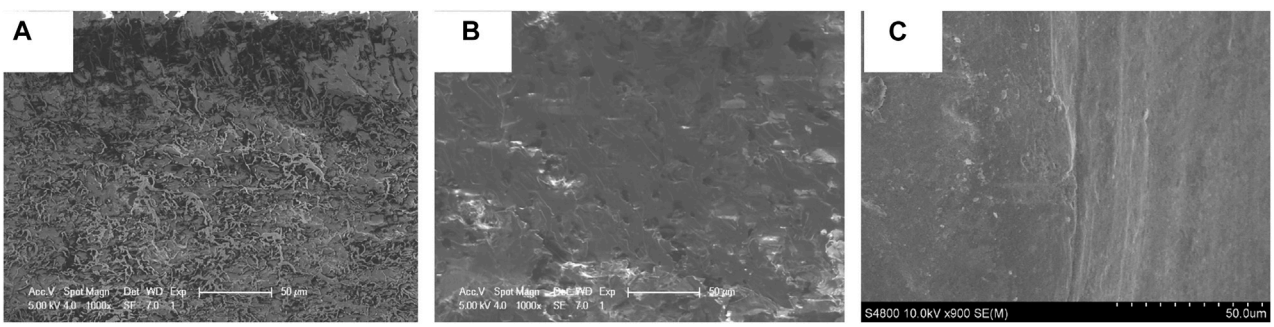

FIGURE 5 | The SEM cross-section images of prepared coatings, **(A)** pure EP, **(B)** PA/EP, and **(C)** PA/G/EP.

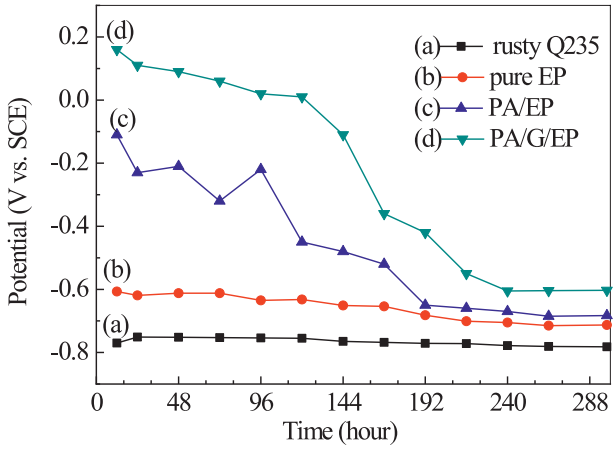

FIGURE 6 | The open circuit potential curves of rusty carbon steel **(A)**, EP **(B)**, PA/EP **(C)**, and PA/G/EP **(D)** immersed in 3.5% NaCl solution after 240 h.

then the coating was quickly broken in a liquid nitrogen environment. Cross-section surfaces of different coatings were immediately treated with gold spraying to increase their conductivity (the thickness of the gold-plated layer was only 5–8 nm, which did not change the cross-section morphology of the prepared coatings), and at last the prepared cross-section surface samples were put in a vacuum chamber for SEM observation. The electrochemical test was performed at the electrochemical workstation (CHI-660E, China) using the three-electrode system. A platinum electrode was used as an auxiliary electrode, a calomel electrode was used as a reference electrode, and a carbon steel with 1 cm^2 exposed area was used as a working electrode. The corrosive medium was 3.5 wt% NaCl solution. The electrochemical impedance spectroscopy (EIS) curves after different immersion times were measured at an open circuit potential with an interference signal amplitude of 20 mV and a frequency range of 100,000–0.01 Hz. Electrochemical impedance fitting was performed using Zview software for data analysis. Three coating/electrode systems were prepared for each electrode, and the electrochemical test was repeated three times.

RESULTS AND DISCUSSION

Transformation Performance of PA on Rusty Carbon Steel

To investigate the transformation mechanism of PA on rusty carbon steel, infrared (IR) and XRD spectra of the rusty carbon steel, PA dropped on rusty carbon steel, and PA/G coating coated on rusty carbon steel are presented in **Figures 1**, **2**, respectively. In the IR spectrum of rusty carbon steel (**Figure 1A**), the peaks at 883 and 787 cm^{-1} belonged to the bending vibration of -OH in α-FeOOH. The band of 682 cm^{-1} belonged to the bending vibration of -OH in β-FeOOH, and the band around 745 cm^{-1} was due to the bending vibration of -OH in γ-FeOOH. When the 5 wt% PA solution was dropped on the rusty carbon steel for 4 h, the characteristic peaks of rusty carbon steel almost disappeared, and some new characteristic peaks located at 1,004 and 2,847 cm^{-1} appeared (**Figure 1B**), which corresponded to the P-O stretching vibration and the stretching vibration of OH in the P-OH group, indicating that PA could reacted with rust and has been absorbed on rusty carbon steel. When the PA/G/EP was coated on rusty carbon steel (**Figure 2C**), most of the characteristic peaks of rusty carbon steel cannot be detected. Some new absorption peaks at 1,657 and 1,543 cm^{-1} came from the carbon skeleton vibration of the G (Xu et al., 2021).

It can be found in the XRD (see **Figure 2A**) pattern that the rust mainly contained diffraction peaks of NaCl (PDF 05-0628), FeOCl (PDF 39-0612), Fe_2O_3 (PDF 16-0653), and Fe (PDF 50-1275). After adding PA, only NaCl characteristic peak was left, indicating that most rust was converted by PA (**Figure 2B**). No obvious rust characteristic peak was found in **Figure 2C**. In order to investigate the change of surface morphology of rusty carbon steel after the reaction between PA and rust, 5 wt% PA solution was directly dropped on the surface of rusty carbon steel. It could be seen that many corrosion pits appeared on the surface of rusty carbon steel (**Figure 3A**); when the PA reacted with the rust for 24 h, the corrosion pits almost disappeared and the surface roughness significantly decreased (**Figure 3B**), indicating that the PA has excellent rust conversion performance.

Generally, coatings with good physical barrier properties have excellent protective properties, and the dispersion state of fillers in composite coatings has a significant impact on the physical barrier properties of coatings (Liu et al., 2013b). In order to observe the dispersion state of G and PA in the composite coating, SEM was used to observe the dispersion performance of G in xylene solvent and the cross-section surface morphology of the coating, and the results are shown in **Figures 4**, **5**, respectively. **Figure 4** showed that the sheet structure of G was dispersed uniformly by polyo-phenylenediamine in xylene solvent, and no obvious agglomeration of G could be found.

The cross-section surface of pure EP was relatively smooth, and there were fluvial cracks parallel to the direction of crack propagation on the surface (**Figure 5A**), which was typical of brittle thermosetting polymers section characteristics. After adding PA in pure EP (**Figure 5B**), the crack of PA/EP coating section was reduced compared with that of pure EP, and some small holes were observed in the coating. When the PA and well-dispersed G slurry were added in EP (**Figure 5C**), the cross-section of the PA/G/EP coating was smooth; no obvious agglomeration of G or small holes could be observed, indicating that G could effectively improve the compactness of the EP coating.

Corrosion Performance of the G Modified Epoxy Surface Tolerant Coating

Figure 6 presents the open circuit potential (E_{OCP}) variation of rusty carbon steel, EPPA/EP, and PA/G/EP coated on rusty carbon steel as a function of immersion time in 3.5% NaCl solution. The E_{OCP} of rusty carbon steel was kept at −0.782 V and was basically unchanged. The E_{OCP} of all coatings decreased to different degrees after the

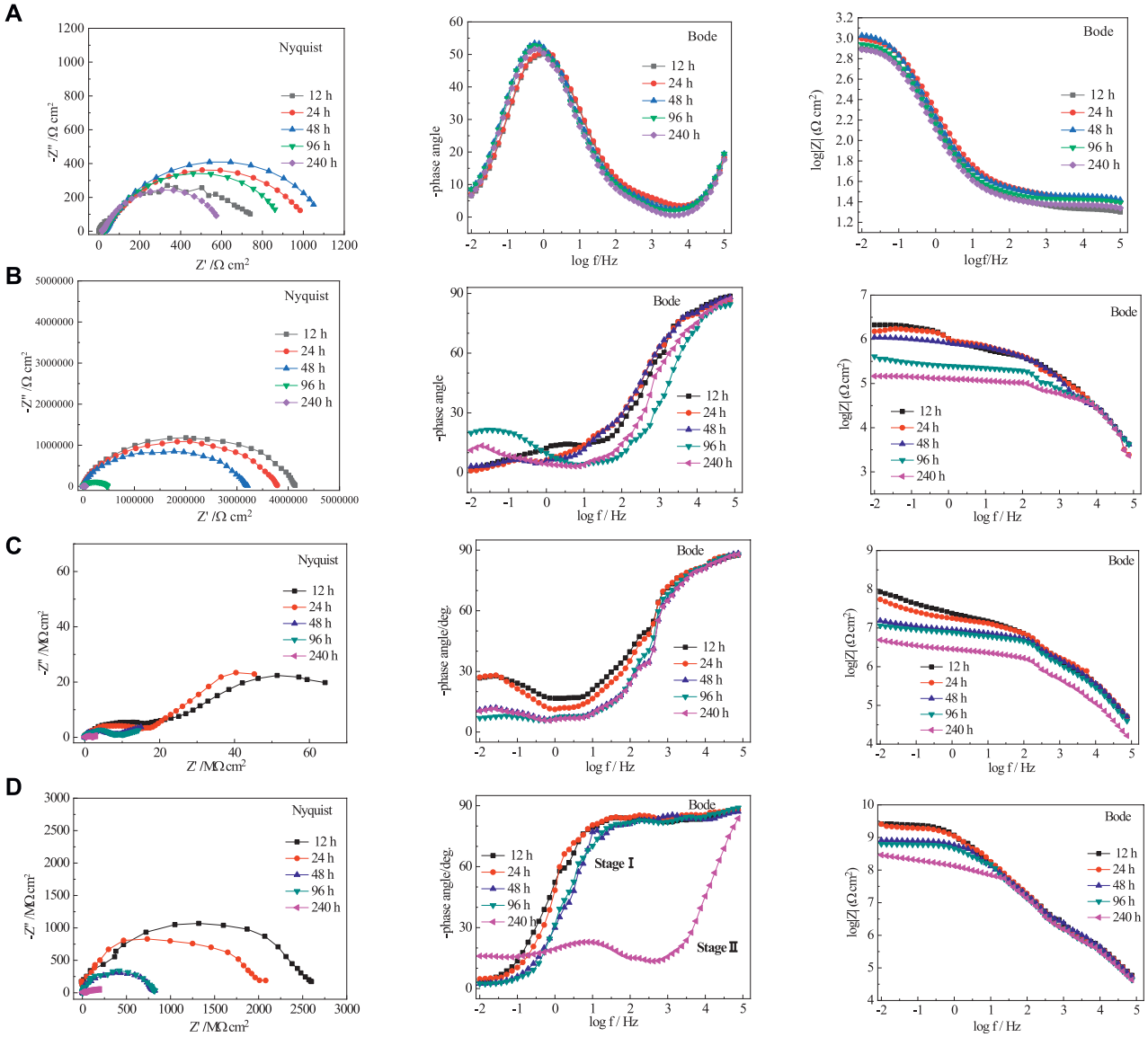

FIGURE 7 | The EIS of rusty carbon steel **(A)**, EP **(B)**, PA/EP **(C)**, and PA/G/EP **(D)** immersed in 3.5 wt% NaCl solution after different times.

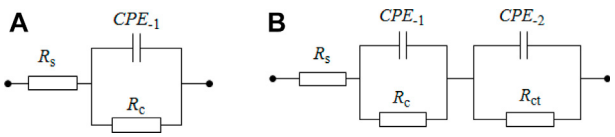

FIGURE 8 | The equivalent circuit used to fit the EIS data. **(A)** used for one time constant in EIS, **(B)** used for two time constants in EIS.

fluctuation at initial time and then remained basically unchanged after 240 h. Compared with pure EP, PA/EP and PA/G/EP exhibited much more enhanced E_{OCP}. After 288 h immersion, compared to EP, the positive shift of E_{OCP} as 0.11 V for PA/G/EP indicated that well-dispersed G has obvious corrosion inhibition, and this similar phenomenon has been reported by other researchers (Cui et al., 2019). In our previous research, we confirmed that commercial G without dispersion was found to have almost no corrosion inhibition (Liu et al., 2016).

Nyquist and Bode plots are shown in **Figure 7** for bare rusty carbon steel, EP, PA/EP, and PA/G/EP coated on rusty carbon steel after different immersion times in 3.5 wt% NaCl solution, as EIS is one of the most intensive and nondestructive testing techniques for investigation and prediction of the anticorrosion performance of organic coating in aqueous solution (Liu et al., 2013a; Liu et al., 2013b). To quantitative analyze the corrosion resistance of these four systems, two appropriate equivalent circuits (**Figure 8**) were used to fit the EIS data, and the fitting corrosion parameters are listed in **Table 1**; (Xia et al., 2020). In **Figure 6**, R_s is the solution resistance, and R_c and CPE_{-1} represent the coating resistance

TABLE 1 | Electrochemical corrosion parameters fitted from the equivalent circuit.

	Time hours	R_s	CPE_{-1}	n_1	R_c	CPE_{-2}	n_2	R_{ct}
		Ω	nF/S $^{(1-n1)}$ cm^2		MΩ cm^2	μF/S$^{(1-n2)}$ cm^2		MΩ cm^2
Rusty carbon steel	12	0.02	2,506	0.68	5.98×10^{-5}	235	0.89	1.12×10^{-3}
	24	0.01	3,512	0.85	5.12×10^{-5}	335	0.66	1.08×10^{-3}
	48	0.01	6,591	0.76	4.23×10^{-5}	285	0.86	9.56×10^{-4}
	96	0.03	6,562	0.56	3.12×10^{-5}	269	0.78	7.73×10^{-4}
	240	0.01	8,452	0.91	1.05×10^{-5}	398	0.96	6.32×10^{-4}
EP	12	0.03	50.2	0.70	0.86	0.56	0.69	4.56
	24	0.01	125	0.68	0.78	1.23	0.72	3.87
	48	0.04	886	0.61	0.65	5.68	0.85	3.46
	96	0.03	989	0.62	0.46	8.69	0.59	0.52
PA/EP	240	0.02	1,023	0.71	0.23	9.98	0.62	0.12
	12	0.01	19.7	0.95	18.6	0.0747	0.83	82.6
	24	0.01	125	0.93	16.8	0.0859	0.77	78.4
	48	0.03	234	0.91	11.3	0.161	0.82	15.2
	96	0.01	376	0.84	9.53	0.562	0.84	13.5
	240	0.02	758	0.88	7.56	0.983	0.79	3.56
PA/G/EP	12	0.03	0.126	0.78	2,685	—	—	—
	24	0.02	0.156	0.66	2,156	—	—	—
	48	0.02	0.254	0.85	781.3	—	—	—
	96	0.01	0.356	0.86	756.1	—	—	—
	240	0.02	4.95	0.95	53.16	0.364	0.46	235.6

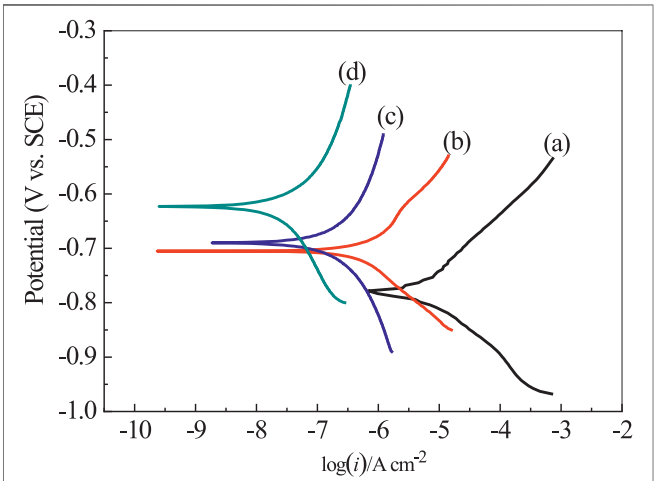

FIGURE 9 | The polarization curves of rusty carbon steel **(A)**, EP **(B)**, PA/EP **(C)**, and PA/G/EP **(D)** immersed in 3.5 wt% NaCl solution after 240 h.

TABLE 2 | Corrosion parameters of rusty carbon steel, EP, PA/EP, and PA/G/EP immersed in 3.5 wt% NaCl solution after 240 h.

	E_{corr}	i_{corr}	β_a mVdec^{-1}	$-\beta_c$ mVdec^{-1}
	V, vs.SCE	μA cm^{-2}		
Rusty carbon steel	−0.778	13.2	73.9	61.8
EP	−0.705	0.813	121.7	105.2
PA/EP	−0.685	0.195	270.8	220.7
PA/G/EP	−0.624	0.031	285.2	221.1

and coating capacitance, respectively. R_{ct} and CPE_{-2} represent the charge-transfer resistance and double-layer capacitance, respectively (Wang et al., 2021; Cui et al., 2018). **Figure 8A** was used to fit the EIS data for PA/G/EP during the 96-h immersion, and **Figure 8B** was used to fit the EIS data which have two time constants (Pan et al., 2020).

Generally, the impedance modulus at the lowest frequency ($|Z|_{0.01Hz}$) in Bode diagram can be used to evaluate the protective performance of the coatings. For the EIS results with two time constants, the time constant at the high frequencies corresponds to the capacitive behavior of the coating (or rust), and the time constant at the medium and low frequencies is assigned to the corrosion response of the metal substrates (Liu et al., 2012).

For the bare rusty carbon steel (**Figure 7A**), the radius of the two capacitive arcs decreased gradually, and the impedance modulus at low frequency domain $|Z|_{0.01Hz}$ decreased with time, indicating that the corrosion rate of rusty carbon steel increased in 3.5 wt% NaCl solution. Without coating protection, the rusty carbon steel would corrode and fail in a short time in 3.5% NaCl solution.

When the pure EP was coated on rusty carbon steel without surface treatment (**Figure 7B**), the porous rust in epoxy coating may reduce the compactness of paint film, form water-vapor channel, and then decrease its anticorrosion performance. The $|Z|_{0.01Hz}$ of pure EP was only $3.56 \times 10^5\ \Omega\ cm^2$ after 240 h immersion in 3.5 wt% NaCl solution. Due to the water penetration and ionic species movement through the pure EP, the EP coating conductivity increased. The coating capacitance (CPE_{-1}) increased from 50.22 to 1,023 nF cm^{-2}, and the coating resistance (R_c) decreased from 0.86 to 0.23 MΩ cm^2 during 240 h of immersion in 3.5% NaCl solution.

When the PA/EP is coated on rusty carbon steel (**Figure 7C**), the PA could react with rust, reduce the porosity and increase the adhesion of the coating to the rusty carbon steel, and then increase the compactness of paint film. The radius of two capacitive reactance arcs was doubled compared to pure EP.

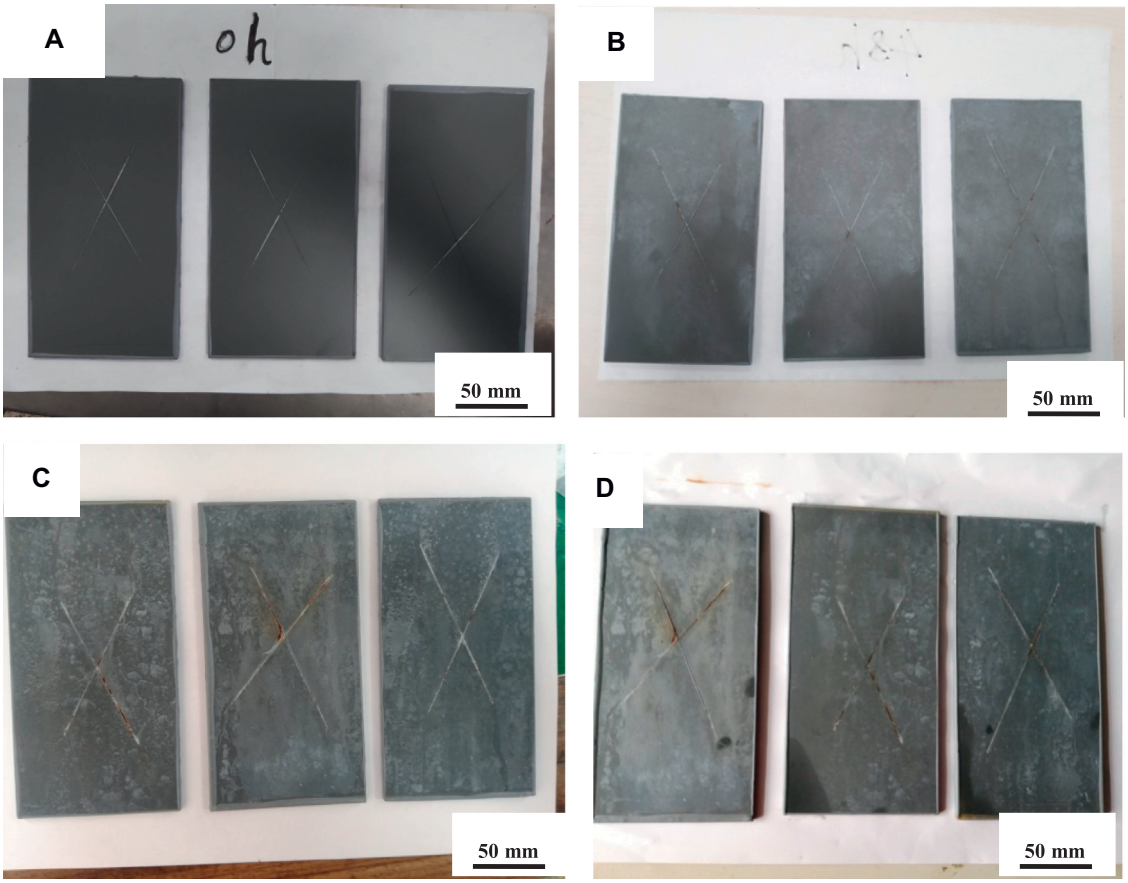

FIGURE 10 | Photographs of PA/G/EP coating immersed in salt spray chamber after different times. **(A)**: 0 h; **(B)**: 24 h; **(C)**: 120 h; **(D)**: 240 h.

However, there were still two time constants during the whole immersion times; the coating resistance (R_c) of PA/EP decreased from 18.6 to 1.56 MΩ cm^2 after 240 h immersion, indicating that water resistance of the PA/EP needs to be improved.

For PA/G/EP (**Figure 7D**), only one time constant was observed at the initial stage of 96 h immersion (Stage I), and then two time constants appeared after 240 h of immersion (Stage II). When the well-dispersed G is added into the EP, G can fill the structural and pinhole porosity of the EP and decrease the electrolyte diffusion towards the rusty carbon steel substrate, and the water diffusion coefficient is decreased greatly by the tortuous diffusion path (Liu et al., 2016). However, water molecules would gradually penetrate the coating with the extension of immersion time and accelerate the corrosion of the metal. Thus, two time constants (or two capacitive arcs) appeared after 240 h of immersion.

The pure EP and PA/EP coatings exhibit two time constants in short-term immersion, while the PA/G/EP remains one time constant in a high frequency range during 96-h immersion. The impedance modulus at low frequency ($|Z|_{0.01Hz}$) can represent the corrosion protection of coating/metal system, which is in inverse proportion to the corrosion rate. The $|Z|_{0.01Hz}$ of the PA/G/EP-coated rusty carbon electrode was $5.9 \times 10^8\ \Omega\ cm^2$ after 240-h immersion (**Figure 6D**), which was far larger than that of pure EP ($2.1 \times 10^5\ \Omega\ cm^2$) and PA/EP ($7.3 \times 10^6\ \Omega\ cm^2$) coated rusty carbon electrodes after 240-h immersion (**Figures 6B, C**). These results indicated that PA/G/EP exhibited better corrosion protection for the rusty carbon steel than other coatings. The increase in impedance for PA/G/EP can be attributed to the hydrophobicity and barrier effects of G well dispersed in EP. Moreover, PA/EP protects the rusty carbon steel against corrosion better than the pure EP does, mainly due to the passivation capabilities of the PA molecules.

Figure 9 presents the polarization curves of rusty carbon steel, EP, PA/EP, and PA/G/EP coated on rusty carbon steel immersed in 3.5 wt% NaCl solution after 240 h at room temperature (~25°C). The corrosion parameters calculated from the Tafel regions are listed in **Table 2** (Zhao et al., 2014). The corrosion current densities (i_{corr}) calculated from Tafel regions of rusty carbon steel, EP, PA/EP, and PA/G/EP were 13.2, 0.813, 0.195, and 0.031 μA cm^{-2}, respectively. Compared to the bare rusty carbon steel, when the EP, PA/EP, and PA/G/EP were coated on rusty carbon steel, both of the absolute values of β_a and β_c increased, suggesting that the anodic oxidation and cathodic reduction reaction of rusty carbon steel were inhibited. It is important to note that the PA/G/EP exhibited more positive potential (−0.624 V) as compared to the rusty carbon steel (−0.778 V), and the i_{corr} value of PA/G/EP (0.031 μA cm^{-2})

was almost two orders of magnitude less than that of the rusty carbon steel (3.2 μA cm^{-2}). The remarkably improved anticorrosion performance of PA/G/EP can be attributed to the synergistic effect of passivation performance of PA and physical barrier properties of G in the EP coatings.

Salt Spray Tests

Figure 10 shows photographs of PA/G/EP after different exposure times (0, 24, 120, and 240 h) in neutral salt spray chamber. To accelerate the damage of salt spray to the paint film, a single-edged knife was used to cut "×" on the surface of the coating. PA/G/EP compactly absorbed on the metal substrate and little corrosion was observed after 24 h (**Figure 10B**). It could be seen that some white sodium chloride deposited on the surface of the PA/G/EP film, and a few yellow rusty spots were observed near the scratches after 120 h (**Figure 10C**). After the PA/G/EP was kept in the salt spray chamber for 240 h (**Figure 10D**), yellow rust on the scratches increased; however, the PA/G/EP was intact without obvious corrosion or foaming phenomenon in the blank area. This phenomenon can be explained in that, on the one hand, G can improve the compactness of the PA/G/EP, making it difficult for the corrosion media (mainly including chloride ions and water molecules) to penetrate into the coating. On the other hand, the PA/G/EP has a good self-healing ability, the PA in the coating has a good rust conversion effect of the coating, and PA can inhibit metal corrosion even at the scratches of PA/G/EP. The salt spray test results indicated the good anticorrosion performance of PA/G/EP coating.

CONCLUSION

1) A graphene modified epoxy surface tolerant coating was prepared by adding G and PA in epoxy coating. Most of the rust was dissolved and transformed with the reaction of PA and rusty carbon steel. The well-dispersed G could inhibit the thermal shrinkage and improve the compactness of EP.
2) The $|Z|_{0.01Hz}$ of the PA/G/EP-coated rusty carbon electrode was $5.9 \times 10^8\ \Omega\ cm^2$ after 240-h immersion, which was far larger than that of pure EP ($2.1 \times 10^5\ \Omega\ cm^2$) and PA/EP ($7.3 \times 10^6\ \Omega\ cm^2$) coated rusty carbon electrodes after 240-h immersion.
3) When the PA/G/EP was coated on rusty carbon steel, both of the anodic oxidation and cathodic reduction reaction of rusty carbon steel were inhibited in 3.5 wt% NaCl solution. The salt spray test results indicated the good anticorrosion performance of PA/G/EP coating.

DATA AVAILABILITY STATEMENT

The original contributions presented in the study are included in the article/Supplementary Material; further inquiries can be directed to the corresponding authors.

AUTHOR CONTRIBUTIONS

Conceptualization, XG; methodology, HX; formal analysis, XG and JY; data curation, XG and JP; writing-original draft preparation, XG and SL; writing-review and editing, XG, CY, and SL; supervision, CY and SL; funding acquisition, JP. All authors have read and agreed to the published version of the manuscript.

FUNDING

The authors gratefully appreciate the financial support provided by National Science and Technology Major Project (2017-VII-0012-0107) and Zhejiang Key Research and Development Program (2019C03093).

REFERENCES

Arukalam, I. O., Oguzie, E. E., and Li, Y. (2018). Nanostructured Superhydrophobic Polysiloxane Coating for High Barrier and Anticorrosion Applications in marine Environment. *J. Colloid Interf. Sci.* 512, 674–685. doi:10.1016/j.jcis.2017.10.089

Bai, W., Ma, Y., Meng, M., and Li, Y. (2021). The Influence of Graphene on the Cathodic protection Performance of Zinc-Rich Epoxy Coatings. *Prog. Org. Coat.* 161, 106456. doi:10.1016/j.porgcoat.2021.106456

Chang, J., Wang, Z., Han, E.-H., Liang, X., Wang, G., Yi, Z., et al. (2021). Corrosion Resistance of Tannic Acid, D-Limonene and Nano-ZrO2 Modified Epoxy Coatings in Acid Corrosion Environments. *J. Mater. Sci. Tech.* 65, 137–150. doi:10.1016/j.jmst.2020.03.081

Cui, M., Ren, S., Pu, J., Wang, Y., Zhao, H., and Wang, L. (2019). Poly(o-phenylenediamine) Modified Graphene toward the Reinforcement in Corrosion protection of Epoxy Coatings. *Corrosion Sci.* 159, 108131. doi:10.1016/j.corsci.2019.108131

Cui, M., Ren, S., Zhao, H., Xue, Q., and Wang, L. (2018). Polydopamine Coated Graphene Oxide for Anticorrosive Reinforcement of Water-Borne Epoxy Coating. *Chem. Eng. J.* 335, 255–266. doi:10.1016/j.cej.2017.10.172

Díaz, B., Figueroa, R., Nóvoa, X. R., Pérez, C., and Pintos, A. (2020). The Corrosion protection Afforded by a Commercial Rust Converter Doped with Graphene Oxide. *Electrochimica Acta* 342, 136096. doi:10.1016/j.electacta.2020.136096

Feng, L., and Yuan, P. (2020). Corrosion protection Mechanism of Aluminum Triphosphate Modified by Organic Acids as a Rust Converter. *Prog. Org. Coat.* 140, 105508. doi:10.1016/j.porgcoat.2019.105508

Gu, L., Liu, S., Zhao, H., and Yu, H. (2015). Facile Preparation of Water-Dispersible Graphene Sheets Stabilized by Carboxylated Oligoanilines and Their Anticorrosion Coatings. *ACS Appl. Mater. Inter.* 7, 17641–17648. doi:10.1021/acsami.5b05531

Jiang, C., Zhang, X., Wang, D., Zhang, L., and Cheng, X. (2020). Phosphate Conversion Coatings on 35CrMnSi Steels Subjected to Different Heat Treatments. *Electrochemistry Commun.* 110, 106636. doi:10.1016/j.elecom.2019.106636

Lei, Y., Xiao, W., Peng, H., Yu, P., Cai, X., Luan, Z., et al. (2021). An Integrated Epoxy Rust Conversion Coating: Its Anticorrosion Properties and Rust Conversion Mechanism. *J. Alloys Comp.* 853, 157005. doi:10.1016/j.jallcom.2020.157005

Liao, K.-W., and Lee, Y.-T. (2016). Detection of Rust Defects on Steel Bridge Coatings *via* Digital Image Recognition. *Automation in Construction* 71, 294–306. doi:10.1016/j.autcon.2016.08.008

Liu, S., Gu, L., Zhao, H., Chen, J., and Yu, H. (2016). Corrosion Resistance of Graphene-Reinforced Waterborne Epoxy Coatings. *J. Mater. Sci. Tech.* 32, 425–431. doi:10.1016/j.jmst.2015.12.017

Liu, S., Gu, Y., Wang, S., Zhang, Y., Fang, Y., Johnson, D. M., et al. (2013b). Degradation of Organic Pollutants by a Co3O4-Graphite Composite Electrode in an electro-Fenton-like System. *Chin. Sci. Bull.* 58 (19), 2340–2346. doi:10.1007/s11434-013-5784-4

Liu, S., Sun, H., Sun, L., and Fan, H. (2012). Effects of pH and Cl− Concentration on Corrosion Behavior of the Galvanized Steel in Simulated Rust Layer Solution. *Corrosion Sci.* 65, 520–527. doi:10.1016/j.corsci.2012.08.056

Liu, S., Zhao, X.-R., Sun, H.-Y., Li, R.-P., Fang, Y.-F., and Huang, Y.-P. (2013a). The Degradation of Tetracycline in a Photo-Electro-Fenton System. *Chem. Eng. J.* 231, 441–448. doi:10.1016/j.cej.2013.07.057

Marano, C., Briatico-Vangosa, F., Marini, M., Pilati, F., and Toselli, M. (2009). Effects of Coating Composition and Surface Pre-treatment on the Adhesion of Organic-Inorganic Hybrid Coatings to Low Density Polyethylene (LDPE) Films. *Eur. Polym. J.* 45 (3), 870–878. doi:10.1016/j.eurpolymj.2008.11.028

Mu, J., Gao, F., Cui, G., Wang, S., Tang, S., and Li, Z. (2021). A Comprehensive Review of Anticorrosive Graphene-Composite Coatings. *Prog. Org. Coat.* 157, 106321. doi:10.1016/j.porgcoat.2021.106321

Oliveira, J. L., Skilbred, A. W. B., Loken, A., Henriques, R. R., and Soares, B. G. (2021). Effect of Accelerated Ageing Procedures and Flash Rust Inhibitors on the Anti-corrosive Performance of Epoxy Coatings: EIS and Dynamic-Mechanical Analysis. *Prog. Org. Coat.* 159, 106387. doi:10.1016/j.porgcoat.2021.106387

Pan, C., Wang, X., Behnamian, Y., Wu, Z., Qin, Z., Xia, D.-H., et al. (2020). Monododecyl Phosphate Film on LY12 Aluminum alloy: pH-Controlled Self-Assembly and Corrosion Resistance. *J. Electrochem. Soc.* 167, 161510. doi:10.1149/1945-7111/abd3bb

Wang, Q., Wang, W., Ji, X., Hao, X., Ma, C., Hao, W., et al. (2021). Self-Healing Coatings Containing Core-Shell Nanofibers with pH-Responsive Performance. *ACS Appl. Mater. Inter.* 13 (2), 3139–3152. doi:10.1021/acsami.0c18933

Xia, D.-H., Pan, C., Qin, Z., Fan, B., Song, S., Jin, W., et al. (2020). Covalent Surface Modification of LY12 Aluminum alloy Surface by Self-Assembly Dodecyl Phosphate Film towards Corrosion protection. *Prog. Org. Coat.* 143, 105638. doi:10.1016/j.porgcoat.2020.105638

Xu, H., Lu, G., Liu, S., Pu, J., Tian, S., Mao, C., et al. (2021). Anticorrosive Properties and Rust Conversion Mechanism of Phytic Acid-based Surface Tolerant Coating. *Asia-pac J. Chem. Eng.* 16, 2584. doi:10.1002/apj.2584

Ye, Y., Chen, H., Zou, Y., Ye, Y., and Zhao, H. (2020). Corrosion Protective Mechanism of Smart Graphene-Based Self-Healing Coating on Carbon Steel. *Corrosion Sci.* 174, 108825. doi:10.1016/j.corsci.2020.108825

Zhao, X., Liu, S., Wang, X., and Hou, B. (2014). Surface Modification of ZrO2 Nanoparticles with Styrene Coupling Agent and its Effect on the Corrosion Behaviour of Epoxy Coating. *Chin. J. Ocean. Limnol.* 32 (5), 1163–1171. doi:10.1007/s00343-014-3327-8

Zhu, Q., Li, E., Liu, X., Song, W., Li, Y., Wang, X., et al. (2020). Epoxy Coating with *In-Situ* Synthesis of Polypyrrole Functionalized Graphene Oxide for Enhanced Anticorrosive Performance. *Prog. Org. Coat.* 140, 105488. doi:10.1016/j.porgcoat.2019.105488

Conflict of Interest: Author JY is employed by Hubei Huaqiang Technology Co., Ltd.

The remaining authors declare that the research was conducted in the absence of any commercial or financial relationships that could be construed as a potential conflict of interest.

Publisher's Note: All claims expressed in this article are solely those of the authors and do not necessarily represent those of their affiliated organizations or those of the publisher, the editors and the reviewers. Any product that may be evaluated in this article, or claim that may be made by its manufacturer, is not guaranteed or endorsed by the publisher.

frontiers in Materials

ORIGINAL RESEARCH
published: 13 December 2021
doi: 10.3389/fmats.2021.794051

Carbon Source Starvation of a Sulfate-Reducing Bacterium–Elevated MIC Deterioration of Tensile Strength and Strain of X80 Pipeline Steel

*Zhong Li[1], Jike Yang[1,2], Huihua Guo[2], Sith Kumseranee[3], Suchada Punpruk[3], Magdy E. Mohamed[4], Mazen A. Saleh[4] and Tingyue Gu[1]**

[1]Department of Chemical and Biomolecular Engineering, Institute for Corrosion and Multiphase Technology, Ohio University, Athens, OH, United States, [2]Corrosion and Protection Center, University of Science and Technology Beijing, Beijing, China, [3]PTT Exploration and Production, Bangkok, Thailand, [4]Research and Development Center, Saudi Arabian Oil Company, Dhahran, Saudi Arabia

It is known that starved sulfate-reducing bacterial biofilms corrode carbon steel more aggressively because they use electrons from elemental iron oxidation as an alternative source of energy. This work used carbon source starvation to vary MIC (microbiologically influenced corrosion) severity for studying subsequent MIC impacts on the degradation of X80 carbon steel mechanical properties. X80 square coupons and dogbone coupons were immersed in ATCC 1249 culture medium (200 ml in 450-ml anaerobic bottles) inoculated with *Desulfovibrio vulgaris* for 3-day pre-growth and then for an additional 14 days in fresh media with adjusted carbon source levels for starvation testing. After the starvation test, the sessile cell counts (cells/cm^2) on the dogbone coupons in the bottles with carbon source levels of 0, 10, 50, and 100% (vs that in the full-strength medium) were 8.1×10^6, 3.2×10^7, 8.3×10^7, and 1.3×10^8, respectively. The pit depths from the X80 dogbone coupons were 1.9 µm (0%), 4.9 µm (10%), 9.1 µm (50%), and 6.4 µm (100%). The corresponding weight losses (mg/cm^2) from the square coupons were 1.9 (0%), 3.3 (10%), 4.4 (50%), and 3.7 (100%). The 50% carbon source level had the combination of carbon starvation without suffering too much sessile cell loss. Thus, both its pit depth and weight loss were the highest. The electrochemical tests corroborated the pit depth and weight loss trends. The tensile tests of the dogbone coupons after the starvation incubation indicated that sulfate-reducing bacteria (SRB) made X80 more brittle and weaker. Compared with the fresh (no-SRB-exposure) X80 dogbone coupon's ultimate tensile strain of 13.6% and ultimate tensile stress of 860 MPa, the 50% carbon source level led to the lowest ultimate tensile strain of 10.3% (24% loss when compared with the fresh dogbone) and ultimate tensile stress of 672 MPa (22% loss). The 100% carbon source level had a smaller loss in ultimate tensile strain than the 50% carbon source level, followed by 10% and then 0%. Moreover, the 100% carbon source level had a smaller loss in ultimate tensile strength than the 50%, followed by 10% and 0% in a tie. This outcome shows that even in the 17-day short-term test, significant degradation of the mechanical properties occurred and more severe MIC pitting caused more severe degradation.

Keywords: X80 steel, microbiologically influenced corrosion, mechanical property, sulfate-reducing bacteria, tensile test, starvation, biofilm

OPEN ACCESS

Edited by:
Qixin Zhou,
University of Akron, United States

Reviewed by:
Tao Liu,
Shanghai Maritime University, China
Chunguang Yang,
Institute of Metals Research (CAS), China

****Correspondence:***
Tingyue Gu
gu@ohio.edu

Specialty section:
This article was submitted to Environmental Degradation of Materials, a section of the journal Frontiers in Materials

Received: *13 October 2021*
Accepted: *15 November 2021*
Published: *13 December 2021*

Citation:
Li Z, Yang J, Guo H, Kumseranee S, Punpruk S, Mohamed ME, Saleh MA and Gu T (2021) Carbon Source Starvation of a Sulfate-Reducing Bacterium–Elevated MIC Deterioration of Tensile Strength and Strain of X80 Pipeline Steel. Front. Mater. 8:794051. doi: 10.3389/fmats.2021.794051

INTRODUCTION

Sulfate-reducing bacteria (SRB) are the most ubiquitous microorganisms in anaerobic environments, and they are the most important microbes in MIC (microbiologically influenced corrosion) in the oil and gas systems which are mostly anaerobic and often involve seawater containing sulfate (Little and Lee, 2007; Sheng et al., 2007; Xu et al., 2016; Jia et al., 2017; Jogdeo et al., 2017). SRB MIC can induce mechanical degradations of metallic materials (Abedi et al., 2007; AlAbbas et al., 2013; Al-Nabulsi et al., 2015; Wu et al., 2015). A failure of a X52 pipeline in the northern part of Iran was reported in 2004 due to SRB causing deterioration of the mechanical properties of the pipeline steel (Abedi et al., 2007). The deterioration of the mechanical properties is usually exhibited as losses of tensile stress and strain (Służalec, 1992).

The SRB are anaerobic bacteria that use sulfate as the terminal electron acceptor in their respiration (Dannenberg et al., 1992; Heidelberg et al., 2004; Lv and Du, 2018). When lactate is used as the organic carbon source, the following oxidation reaction occurs in the cytoplasm of the SRB under enzyme catalysis (Xu and Gu, 2011; Xu and Gu, 2014; Xu et al., 2016; Li et al., 2018; Dou et al., 2019; Gu et al., 2019):

TABLE 1 | Elemental composition of X80 steel (mass %).

C	Mn	Ni	Cu	Si	Mo	Cr	Nb	Ti	Fe
0.050	1.850	0.285	0.246	0.228	0.307	0.016	0.065	0.013	Balance

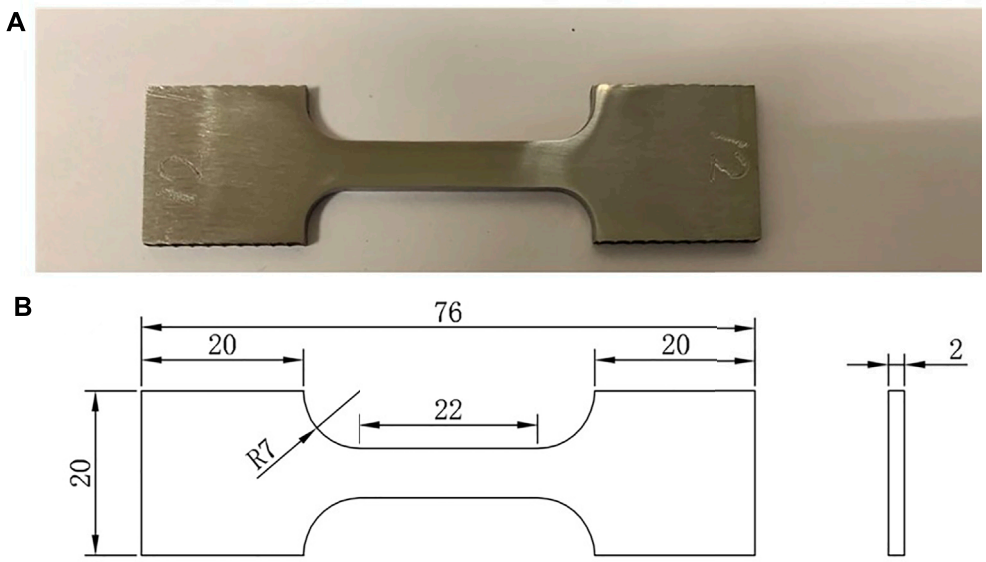

FIGURE 1 | (A) Dogbone of X80 carbon steel; **(B)** dimensions in millimeters.

TABLE 2 | Chemical composition of ATCC 1249 medium.

Component	Chemical	Amount
Component I	$MgSO4{\cdot}7H_2O$	4.1 g
	Sodium citrate	5.0 g
	$CaSO_4$	1.0 g
Component II	NH_4Cl	1.0 g
	Distilled water	400 ml
	K_2HPO_4	0.5 g
	Sodium lactate	4.5 ml
	Yeast extract	1.0 g
Component III	Distilled water	400 ml
Component IV	$Fe(NH_4)_2(SO_4)_2$	1.0 g

$$CH_3CHOHCOO^- + H_2O \rightarrow CH_3COO^- + CO_2 + 4H^+ + 4e^- \left(E^{\circ\prime} = -430\ \text{mV}\right) \quad (1)$$

$$\text{Reduction reaction}: SO_4^{2-} + 9H^+ + 8e^- \rightarrow HS^- + 4H_2O \left(E^{\circ\prime} = -217\ \text{mV}\right) \quad (2)$$

where the apostrophe in the reduction potential $E^{\circ\prime}$ of the two reactions indicates a pH of 7.0. When there is a lack of carbon source in the local environment such as at the bottom of the sulfate-reducing bacterial biofilm, elemental iron can provide the electrons for the SRB survival through extracellular Fe oxidation, as shown in **Eq. 2**. Fe like lactate can provide

energy according to the reduction potential values listed in **Eqs 1**, **3**. Like lactate, Fe oxidation can be coupled with sulfate reduction to provide energy for SRB (Biswas and Bose, 2005; Li et al., 2018). This means that carbon source starvation of a pre-existing sulfate-reducing bacterial biofilm accelerates SRB MIC of Fe (Xu and Gu, 2014; Dou et al., 2019):

$$\text{Oxidation reaction}: \mathrm{Fe} \rightarrow \mathrm{Fe}^{2+}+2\mathrm{e}^{-} \quad \left(E^{\circ\prime} = -447\ \mathrm{mV}\right) \quad (3)$$

Because elemental iron releases electrons extracellularly and the electrons are used in sulfate reduction inside the cytoplasm of the SRB, extracellular electron transfer (EET) is required. Thus, this kind of MIC is labeled as EET-MIC, which is the result of the demand of electroactive sessile cells for energy. The starved cells are more eager to harvest the extracellular electrons for energy production in order to survive, which can lead to more severe corrosion (Gu and Xu, 2013; Flemming et al., 2016; Liu et al., 2018).

In this work, carbon source starvation was used as a means to vary MIC severity in the study of the MIC impact on the degradation of X80 mechanical properties. Starvation also induced changes in dissolved H_2S and headspace H_2 levels, which were used to study their impact on the degradation as well.

Small X80 square coupons in anaerobic bottles were used for weight loss analysis after the starvation testing. They were also used as working electrodes in electrochemical glass cells for electrochemical tests. The X80 dogbone coupons were used for gas measurements, sessile cell counting, pitting analysis, and tensile testing.

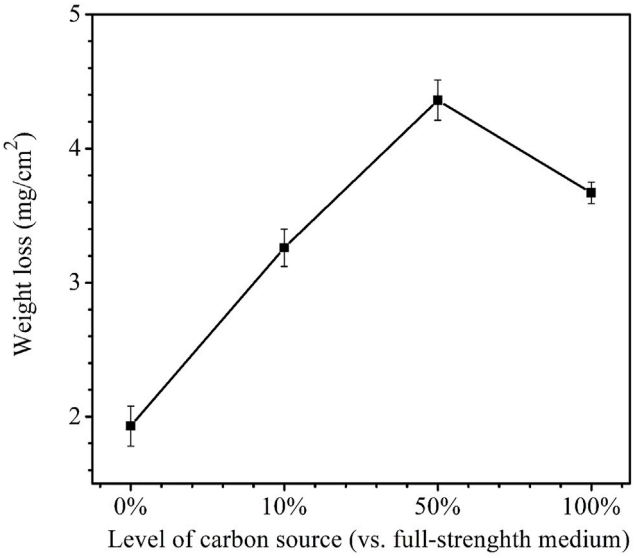

FIGURE 2 | Weight losses after 14-day starvation incubation in 450-ml anaerobic bottles with varied carbon source levels. (Each error bar represents a range of readings from three coupons in the same anaerobic bottle.).

EXPERIMENTAL

Materials

The composition of X80 carbon steel is listed in **Table 1**. Twenty X80 square coupons (with a 1-cm^2 exposed surface on the top) were used as weight loss samples (12 required) and working electrodes (eight required) in the electrochemical tests. X80 steel was also machined to create dogbone coupons for sulfate-reducing bacterial immersion and subsequent tensile testing. The dimensions of the dogbone coupons were based on the ASTM E8/E8M standard (ASTM-E8/E8M-13a, 2013) (**Figure 1**). Each dogbone coupon was painted with Teflon, except for a middle 2.5-cm section (with four sides unpainted), with a total exposed area slightly over 4 cm^2. The surfaces of the square coupons for weight losses and electrodes were sequentially polished with 180, 400, and 600 grit abrasive papers. The surfaces of the dogbone coupons were polished to 1,200 grit by the supplier prior to shipping. After painting, all the coupons were cleaned with pure isopropanol and dried under UV light for 20 min. The chemicals used in this work were purchased from Fisher Scientific (Pittsburgh, PA, United States) or Sigma-Aldrich (St Louis, MO, United States).

Culture Media and Inoculum

Desulfovibrio vulgaris (ATCC 7757) was selected in this research as a typical pure-strain SRB. The culture medium was an ATCC 1249 medium (composition in **Table 2**), which is a modified Baar's medium for sulfate reducers. The initial pH in each anaerobic bottle prior to each inoculation was adjusted to 7 by using HCl or NaOH solution as required before sterilization in an autoclave at 121°C for 40 min. After autoclaving, the SRB culture media were deoxygenated using filter-sterilized N_2 sparging for more than 45 min. About 100 ppm L-cysteine was then added to the culture media as an oxygen scavenger to reduce dissolved oxygen further and to mitigate possible oxygen leakage. All incubations were carried out at 37°C anaerobically. About 200 mL of the deoxygenated sterilized culture medium and 2 ml of SRB seed culture were put into each 450-ml anaerobic bottle for 3-day SRB pre-growth in the full-strength ATCC 1249 medium. Each bottle contained three square coupons (at the bottom) or one dogbone coupon (leaning on the wall at a 30° angle with the bottom). The dogbone was not pulled or stressed during incubation. This was compatible with the field situation in which a support beam normally under no load or of a small load is corroded by SRB. When a large load (e.g., a heavy truck on a bridge) finally comes, the beam fails. After the 3-day pre-growth, the square coupons, including the working electrode coupons (already in the epoxy resin), and the dogbone coupons were covered with mature biofilms. They were transferred into other 450-ml anaerobic bottles with fresh culture media containing different levels of the carbon source (0, 10, 50, and 100% vs the carbon source in the standard ATCC 1249 medium) for an additional 14-day carbon starvation incubation. Both lactate and citrate were adjusted to vary the carbon source levels in the ATCC 1249 medium, although only lactate is known to be utilized by *D. vulgaris* as a carbon source.

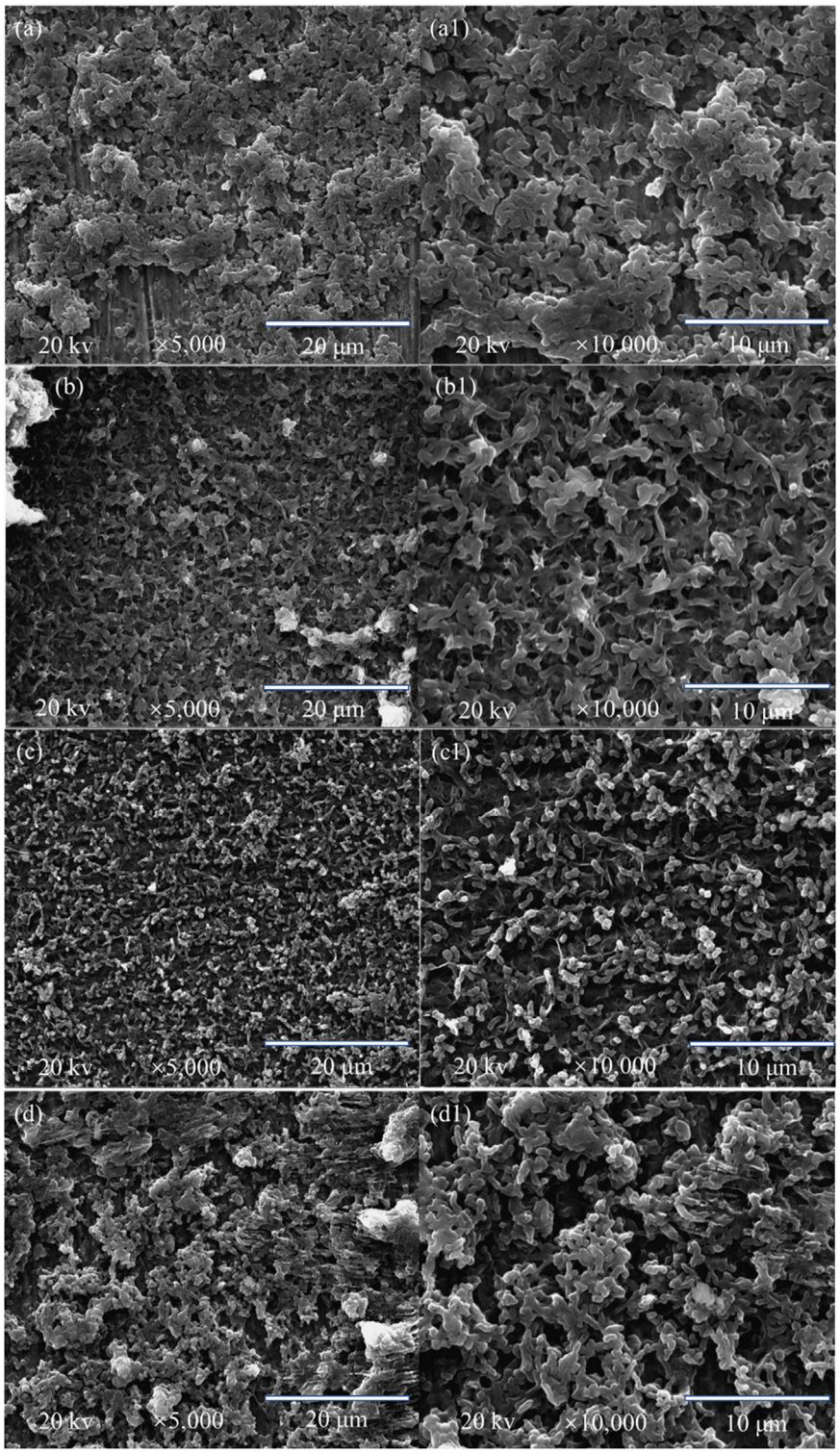

FIGURE 3 | SEM images of the square coupon surfaces after 14-day starvation incubation in anaerobic vials with 200 ml of *D. vulgaris* broth, 250 ml of headspace, and carbon source levels of 0% **(a,a1)**, 10% **(b,b1)**, 50% **(c,c1)**, and 100% **(d,d1)**.

Weight Loss

In this study, because the dogbone coupons were too heavy to obtain the milligram weight losses accurately, small X80 coupons with a 1-cm^2 exposed top surface were used for the weight loss analysis. After the starvation incubation, the square coupons were cleaned with fresh Clarke's solution to remove biofilms and

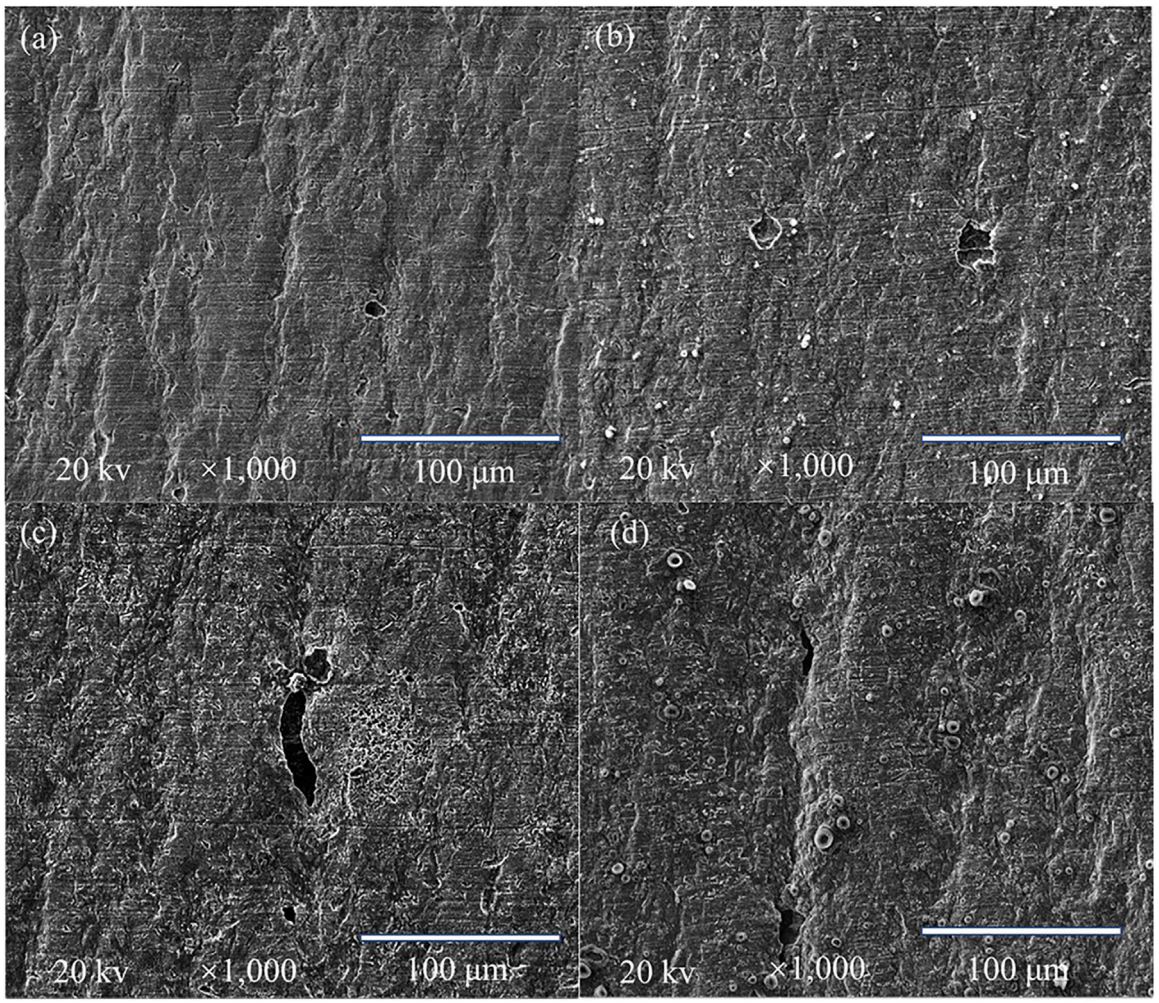

FIGURE 4 | SEM images for the X80 square coupons (with corrosion products removed) after 14-day starvation incubation in an anaerobic vial with 200 ml of *D. vulgaris* broth, 250 ml of headspace, and carbon source levels of 0% **(A)**, 10% **(B)**, 50% **(C)**, and 100% **(D)**.

corrosion products before weighing to obtain the weight loss data. Each weight loss data point was the average of three replicate coupons from the same anaerobic bottle.

Surface and Biofilm Analysis

After 14 days of starvation incubation, the X80 square coupons were retrieved. A scanning electron microscope (SEM) (FEI Quanta 250, Hillsboro, OR, United States) was used to observe the biofilm morphology on the square coupon surfaces. Before biofilm observation, the coupons were first cleaned with pH 7.40 phosphate-buffered saline (PBS) solution for 15 s, and then soaked in 2.5% (w/w) glutaraldehyde solution for 8 h at 10°C to fix the biofilm. Afterward, the coupons were dehydrated with 50% (v/v), 70%, 80%, 90%, and 95% ethanol sequentially for 10 min at each concentration and 100% ethanol for 30 min at the end (Cui et al., 2020). Then, the coupon surfaces were sputter coated with Au to provide surface conductivity. Subsequently, the same coupons were cleaned using Clarke's solution to remove biofilms and corrosion products before pit image analysis under the SEM and finally used for weight loss measurements.

Electrochemical Measurements

A VersaSTAT 3 potentiostat from Princeton Applied Research (Oak Ridge, TN, United States) was used to measure the electrochemical responses of the X80 working electrodes for varied carbon source levels in *D. vulgaris* broths. Each glass cell contained 200 ml of culture medium with a varied carbon source (0, 10, 50, and 100%) and 250 ml of headspace. It was inoculated with 2 ml of SRB seed culture before 3-day pre-growth incubation at 37°C. A saturated calomel electrode was used as the reference electrode, and a platinum plate (10 mm × 10 mm × 1 mm) was used as the counter electrode. Open circuit potential (OCP), linear polarization resistance (LPR), and potentiodynamic polarization analyses were performed. The LPR was scanned at a rate of 0.1667 mV/s in the range of −10 mV to +10 mV vs the OCP. Electrochemical impedance

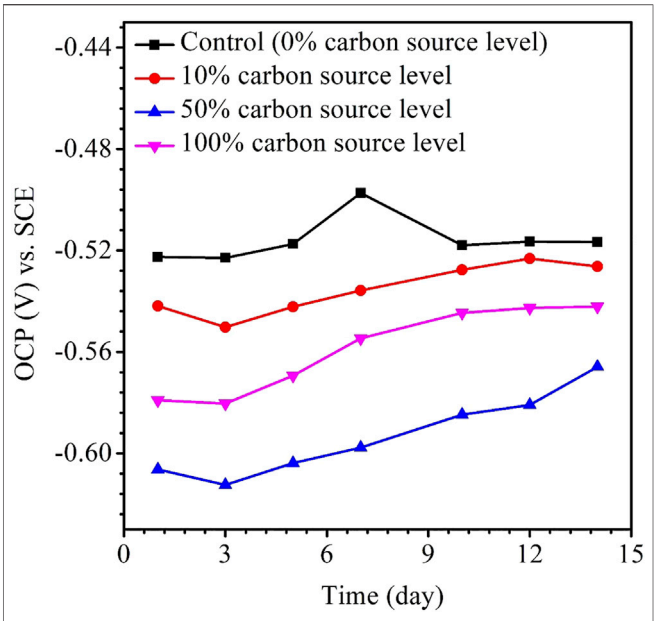

FIGURE 5 | Variations of the OCP vs. time for X80 during 14-days starvation incubation.

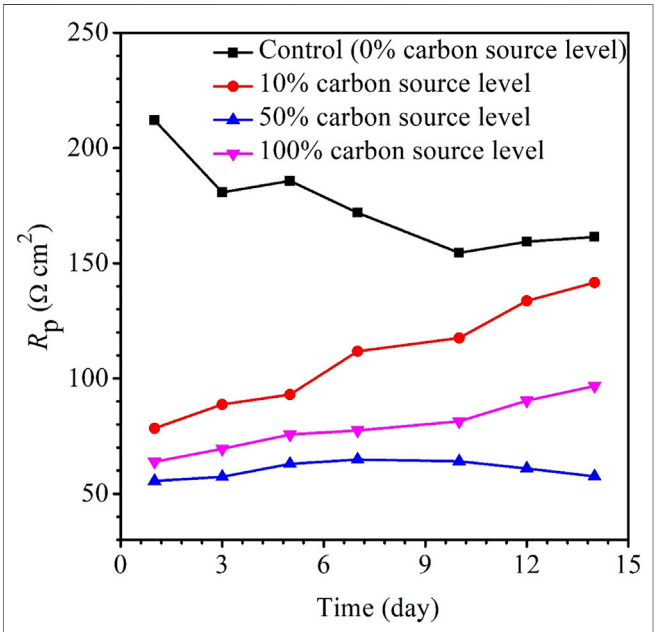

FIGURE 6 | Variations of R_p vs time for X80 during 14-days starvation incubation.

spectroscopy (EIS) was performed at the OCP by applying a sinusoidal signal of 10 mV (amplitude) in the frequency ranging from 10^4 to 10^{-2} Hz. Potentiodynamic polarization curves were scanned at the end of the 14-day starvation incubation from the OCP to −200 mV vs. the OCP using one working electrode, and from the OCP to +200 mV vs. the OCP using a replicate working electrode in a different glass cell at a rate of 0.1667 mV/s. The corrosion potential (E_{corr}), corrosion current density (i_{corr}), and anodic and cathodic Tafel slopes (β_a and β_c) were determined from the Tafel analysis of the polarization curves.

Gas Measurements, Sessile Cell Counts, Pit Depths, and Tensile Testing

After the starvation test, the concentrations of H_2S and H_2, as well as the total pressure in the headspace of each anaerobic bottle containing one dogbone coupon were measured using a portable H_2S sensor (GAXT-H-DL, BW Technologies, Calgary, Alberta, Canada), a portable H_2 sensor (BH-90A, Forensics Detectors, Palos Verdes Peninsula, CA, United States), and a digital manometer (Xplorer GLX-PS-2002, PASCO scientific, Roseville, CA, United States), respectively. The H_2S sensor has an upper detection limit of 100 ppm (v/v). If a headspace sample had a high concentration, dilution was required. A 125-ml bottle sealed with 1 atm air was injected with 10 ml of headspace gas for 12.5× dilution. After mixing, a syringe was used to flush and flood the sensor's sample port with 40 ml of the headspace gas before taking a meter reading.

The pH value of each SRB broth was measured for all dogbone bottles after the starvation incubation. After the starvation incubation, the dogbone coupons were taken out and rinsed three times in PBS of pH 7.40 to remove loosely attached planktonic cells and culture medium. Sessile cells on each dogbone coupon's exposed section were removed using a small disposable brush into 10 ml of PBS solution in a disposable plastic weighing dish. Then, the brush, the coupon, and 10 ml PBS solution were vortexed together in a 50-ml conical tube for 30 s.

After the sessile cell counting using a hemocytometer had been carried out (Li et al., 2015), each dogbone coupon was cleaned using Clarke's solution before it was scanned using an Infinite Focus Microscope (IFM) (Model ALC13, Alicona Imaging GmbH, Graz, Austria) to obtain the pit depth profiles.

Finally, all the dogbone coupons after SRB incubation and a fresh X80 dogbone coupon were subjected to tensile testing on an electromechanical universal testing machine (E44.304, MTS system, MN, United States) to obtain stress–strain curves. The strain rate used in the testing was 0.004 s^{-1}.

RESULTS AND DISCUSSION

Weight Loss Using Square Coupons

After the 14-day carbon starvation incubation, the coupon weight losses for the carbon source levels of 0, 10, 50, and 100% were obtained. They are shown in **Figure 2**. The highest weight loss was 4.4 mg/cm^2 for 50% carbon source and the lowest was 1.9 mg/cm^2 for 0% carbon source. The weight loss for 10% carbon source 3.3 mg/cm^2 and weight loss for 100% carbon source 3.7 mg/cm^2 were close. It is to be noted that 0% carbon source had the lowest weight loss instead of the highest. This was because the extreme starvation had led to much loss of sessile cells (Xu and Gu, 2014; Dou et al., 2019).

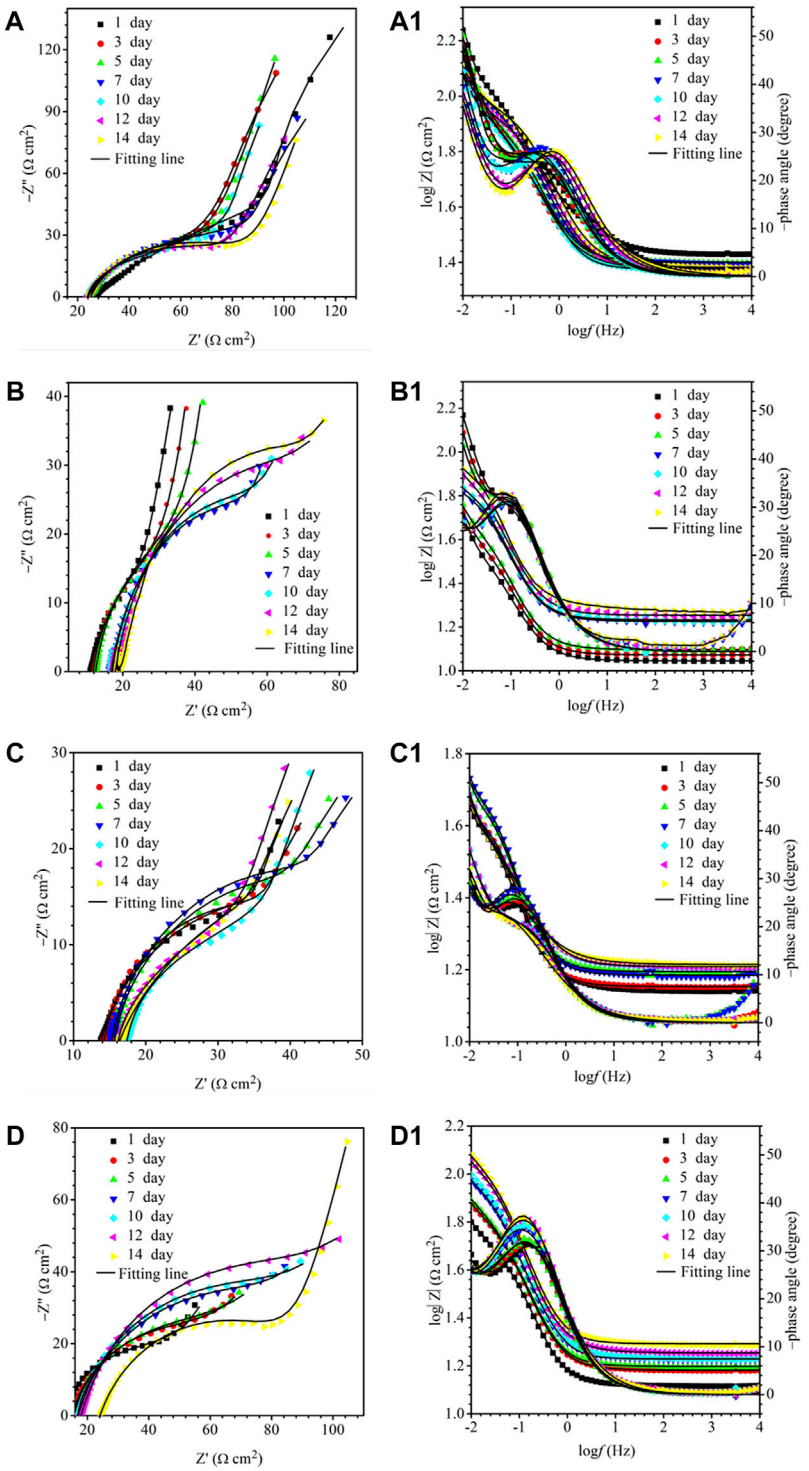

FIGURE 7 | Nyquist and Bode plots for X80 during 14-days incubation in an anaerobic vial with 200 ml of *D. vulgaris* broth, 250 ml of headspace, and carbon source levels of 0% **(a,a1)**, 10% **(b,b1)**, 50% **(c,c1)**, and 100% **(d,d1)**.

Surface and Biofilm Analyses Using Square Coupons

The SEM images in **Figure 3** depict the surface morphologies of the *D. vulgaris* biofilms under different carbon sources after 14-day carbon starvation incubation. The amount of sessile cells on their surfaces were increasing with increasing carbon source levels, from 0% carbon source level to 100% carbon source level as expected. The SEM images in **Figure 4** are consistent

TABLE 3 | Electrochemical parameters obtained from fitting EIS spectra in **Figure 7**.

Carbon source level	t (d)	R_s (Ω cm^2)	Q_{dl} (Ω^{-1} cm^{-2} s^n)	n_1	R_f (Ω cm^2)	Q_{dl} (Ω^{-1} cm^{-2} s^n)	n_2	R_{ct} (Ω cm^2)	*W-R* (Ω cm^2)	*W-T* (s)	*W-P*
0%	1	26.7	1.09×10^{-2}	0.63	31.2	1.03×10^{-2}	0.44	182	80.6	3.43	0.63
	3	23.8	1.61×10^{-2}	0.73	74.5	7.91×10^{-2}	0.96	110	1.26×10^{3}	68.4	0.64
	5	25.1	1.38×10^{-2}	0.79	65.5	7.50×10^{-2}	0.90	121	309	3.51	0.35
	7	25.1	9.56×10^{-3}	0.85	44.9	3.54×10^{-2}	0.56	131	38.4	2.21	0.61
	10	23.7	1.03×10^{-2}	0.87	33.9	4.10×10^{-2}	0.63	112	76.2	4.79	0.58
	12	23.9	9.62×10^{-3}	0.78	63.5	1.01×10^{-1}	0.78	82.1	215	2.74	0.63
	14	24.1	8.41×10^{-3}	0.76	73.9	1.26×10^{-1}	0.84	79.2	145	1.01	0.71
10%	1	11.1	8.43×10^{-2}	0.83	28.8	1.51×10^{-1}	0.80	49.1	101	3.93	0.63
	3	11.2	7.82×10^{-2}	0.85	36.7	2.52×10^{-1}	0.98	53.1	148	14.4	0.43
	5	12.5	7.30×10^{-2}	0.84	44.1	2.51×10^{-1}	0.97	45.9	106	7.91	0.42
	7	16.8	6.05×10^{-2}	0.83	53.1	5.41×10^{-1}	0.95	60.6	108	8.02	0.55
	10	17.1	5.81×10^{-2}	0.84	57.7	3.77×10^{-1}	0.82	63.9	182	8.99	0.64
	12	17.9	5.21×10^{-2}	0.83	61.2	1.48×10^{-1}	0.54	76.8	198	14.2	0.62
	14	18.9	4.97×10^{-2}	0.81	68.4	1.04×10^{-1}	0.43	79.8	195	14.3	0.65
50%	1	13.9	7.20×10^{-2}	0.83	10.8	4.60×10^{-2}	0.30	45.1	56.9	11.4	0.63
	3	14.2	7.04×10^{-2}	0.88	12.2	4.60×10^{-2}	0.28	42.3	48.3	9.81	0.63
	5	15.7	6.91×10^{-2}	0.88	15.7	4.91×10^{-2}	0.30	45.7	71.9	11.2	0.62
	7	15.3	6.63×10^{-2}	0.88	17.3	4.51×10^{-2}	0.26	48.9	78.6	12.2	0.63
	10	17.4	5.57×10^{-2}	0.82	23.3	2.05×10^{-1}	0.73	35.5	63.9	4.19	0.55
	12	16.2	7.07×10^{-2}	0.78	27.3	2.92×10^{-1}	0.96	32.8	59.8	10.6	0.42
	14	16.4	8.47×10^{-2}	0.70	28.3	9.06×10^{-2}	0.52	33.5	37.8	6.03	0.66
100%	1	13.1	3.80×10^{-2}	0.90	20.5	4.19×10^{-2}	0.43	43.5	224	96.2	0.73
	3	15.2	3.56×10^{-2}	0.87	25.5	2.56×10^{-2}	0.50	44.9	241	212	0.72
	5	15.8	3.41×10^{-2}	0.89	29.3	4.15×10^{-2}	0.63	47.3	364	359	0.76
	7	16.9	2.71×10^{-2}	0.93	31.5	3.62×10^{-2}	0.83	49.1	323	415	0.70
	10	17.0	3.25×10^{-2}	0.80	37.3	3.20×10^{-3}	0.99	50.7	405	592	0.71
	12	17.9	2.74×10^{-2}	0.84	44.8	9.72×10^{-3}	0.96	51.1	376	442	0.69
	14	19.6	9.03×10^{-1}	0.90	50.8	2.74×10^{-2}	0.80	49.1	425	552	0.63

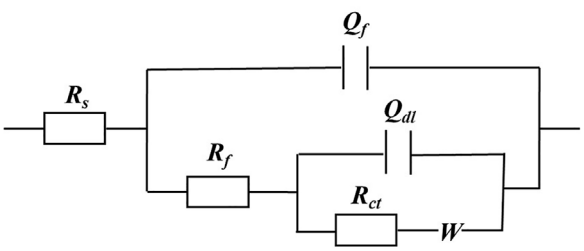

FIGURE 8 | Equivalent electrical circuit model for fitting EIS data in **Figure 7**.

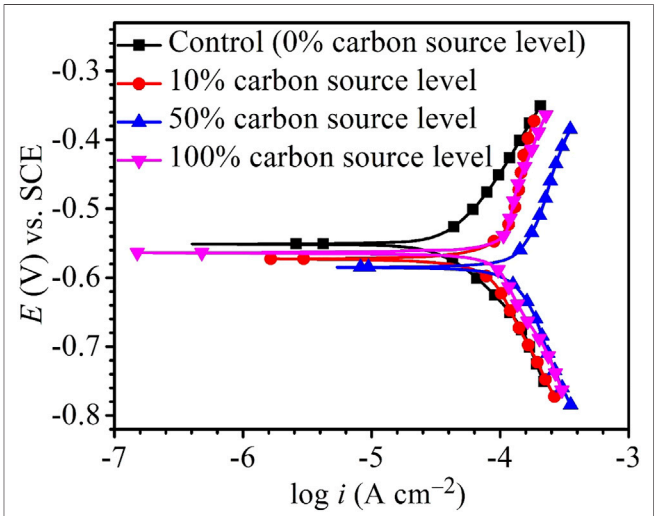

FIGURE 9 | Potentiodynamic polarization curves at the end of 14-days starvation incubation.

with the weight loss findings that 50% carbon source level caused the most severe corrosion and 0% the least.

Electrochemical Tests Using Square Coupons

The variations of the OCP during the 14-day carbon starvation are shown in **Figure 5**. A lower OCP indicates a higher tendency for the working electrode to lose electrons (i.e., undergoing oxidation) or be corroded. During the starvation period, 50% carbon source had the lowest OCP and 0% the highest, which is consistent with the weight loss trend. In MIC, sometimes, the OCP trends are not always correct because the OCP only indicates to a tendency without factoring in the actual corrosion speed. The kinetic electrochemical data on corrosion

TABLE 4 | Fitted electrochemical parameters from Tafel analysis of **Figure 9**.

Carbon source level (%)	i_{corr} (μA/cm^2)	E_{corr} (mV) vs SCE	β_a (mV/dec)	β_c (mV/dec)
0	41	−561	294	−187
10	84	−564	469	−348
50	145	−599	604	−525
100	98	−616	945	−364

TABLE 5 | Headspace gas concentrations and total pressure as well as calculated [H_2S] after 14-day carbon starvation incubation in dogbone bottles.

Carbon source level (vs full-strength medium	(%) Total pressure in headspace (bar)	H_2 concentration in headspace (10^3 ppm) (v/v)	H_2S concentration in headspace (10^3 ppm) (v/v)	Dissolved [H_2S] in liquid phase (10^{-4} M)
0	1.03	0.75	4.08	3.10
10	1.07	1.16	5.08	4.01
50	1.16	1.95	9.00	7.66
100	1.55	2.50	12.6	14.4

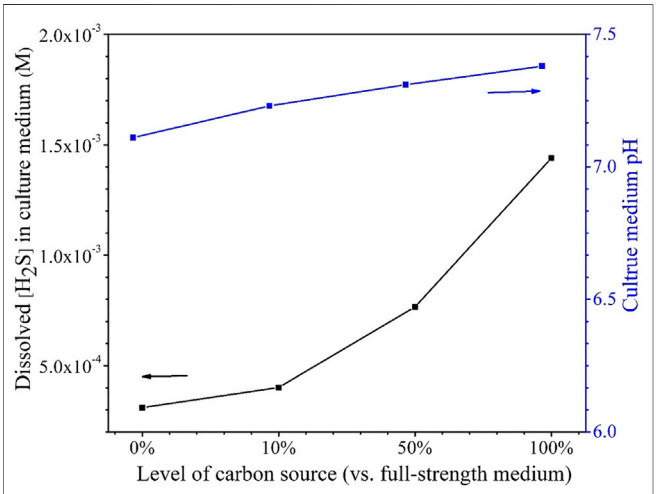

FIGURE 10 | Dissolved [H_2S] in the culture media and broth pH after 14-days starvation incubation in 450-ml anaerobic bottles.

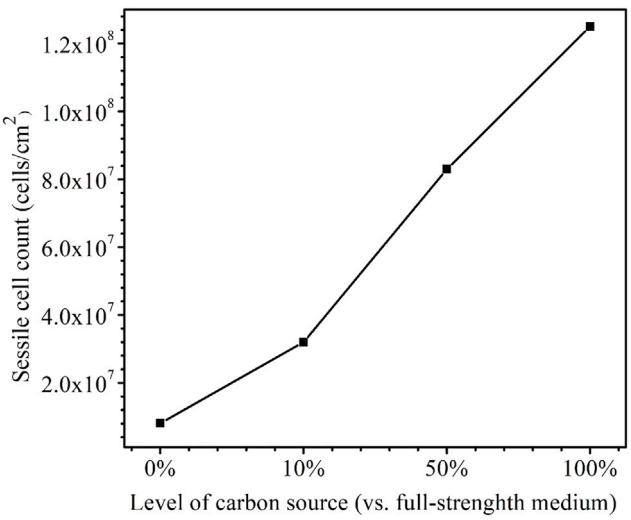

FIGURE 11 | Sessile cell counts on dogbone coupons after 14-days starvation incubation in 450-ml anaerobic bottles with varied carbon source levels.

resistance or corrosion current are more reliable (Jia et al., 2019). In corrosion kinetics, R_p is inversely proportional to the corrosion rate. **Figure 6** shows that the R_p for the 50% carbon source level is the lowest, corresponding to the highest corrosion rate, followed by 100, 10, and 0% carbon source levels. The $1/R_p$ here is consistent with the weight loss trend.

The EIS Nyquist and Bode plots of the X80 square coupons for different carbon source levels on different days during the 14-day starvation incubation are shown in **Figure 7**. The corresponding fitted parameters are listed in **Table 3**. The Nyquist plots of the square coupons indicate a capacitive behavior and a diffusion phenomenon. The equivalent circuit model is shown in **Figure 8**, in which R_s is solution resistance, R_f and Q_f are the resistance and constant-phase element of the biofilm, respectively. R_{ct} is the charge-transfer resistance, Q_{dl} the constant-phase element of the electric double layer, and W is the Warburg element describing the diffusion process. The presence of W in **Figures 7**, **8** and **Table 3** was caused by the mass transfer resistance effect exerted by the biofilm and corrosion product film on the X80 working electrode (Yin et al., 2018). The impedance spectra for different carbon source levels fitted well with the two-time constant circuit model. The 50% carbon source level had the smallest diameters of the semi-circles in the Nyquist plots (**Figure 7**) and the smallest value of (R_{ct} + R_b) (**Table 3**), which means that the 50% carbon source level exhibited the highest corrosion rate (Dou et al., 2019). The EIS results are consistent with the LPR results (**Figure 6**), supporting the weight loss trend (**Figure 2**).

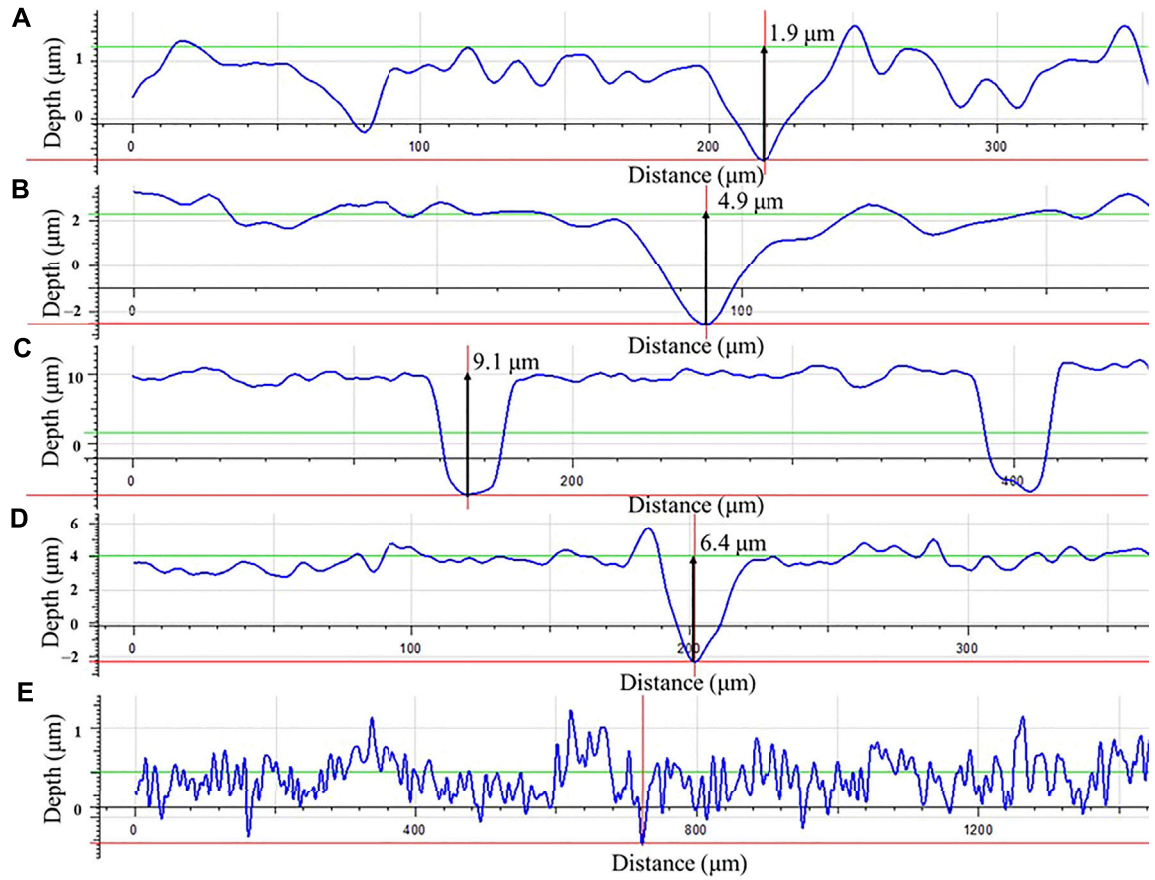

FIGURE 12 | Pit depth profiles for dogbone coupons after 14-days starvation incubation with the carbon source level of: **(A)** 0%, **(B)** 10%, **(C)** 50%, **(D)** 100%, and with **(E)** fresh dogbone (control).

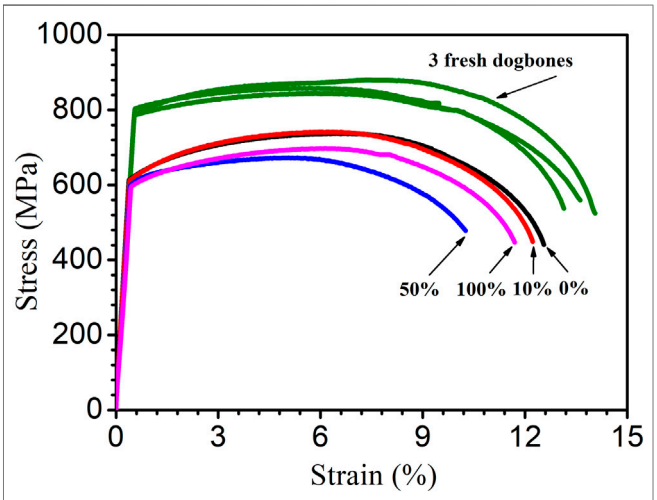

FIGURE 13 | Stress–strain curves for three fresh X80 dogbone coupons (three replicates) and dogbone coupons (with corrosion products removed) after 14-day starvation incubation in 450-ml anaerobic bottles with varied carbon source levels.

TABLE 6 | Ultimate tensile strength and ultimate tensile strain data from **Figure 13**.

Carbon source level	Ultimate tensile strength (MPa) (and loss)	Ultimate tensile strain (%) (and loss)
(No immersion)	860 ± 17.6 (control)	13.6 ± 0.5% (control)
0%	736 (14% loss)	12.7% (7% loss)
10%	741 (14% loss)	12.2% (10% loss)
50%	672 (22% loss)	10.3% (24% loss)
100%	697 (19% loss)	11.7% (14% loss)

The Tafel plots are shown in **Figure 9**. Because potentiodynamic polarization scans use a large voltage range, they may alter the surface of the working electrode. Thus, Tafel scans are usually performed only once at the end. In this work, they were performed at the end of the 14-day starvation period after all the other electrochemical measurements. The fitted Tafel parameters are listed in **Table 4**. The i_{corr} data here are consistent with the weight loss trend showing 50% carbon source having the highest value (145 μA/cm^2), followed by 100% carbon source (98 μA/cm^2), 10% carbon source (84 μA/cm^2), and 0% carbon source

(41 μA/cm^2). The i_{corr} trend here is consistent with the weight loss trend. This work showed that LPR, EIS, and Tafel scans, all confirmed the weight loss trend, suggesting that the electrochemical methods are valuable in MIC studies. Furthermore, the weight loss only reflects the cumulative corrosion outcome, but nondestructive LPR and EIS can provide transient corrosion behaviors.

Dogbone Bottles: H_2 Concentration, H_2S Concentration, Total Pressure

Table 5 shows that a higher carbon source level led to a higher concentration of H_2. This H_2 trend is reasonable because it is known that *D. vulgaris* produces H_2 during lactate oxidation, and later it consumes H_2 when there is a shortage of organic carbon (Wang et al., 2020).

$$CH_3CHOHCOO^- + H_2O \rightarrow CH_3COO^- (\text{acetate}) + 2H_2 + CO_2, \quad (4)$$

$$SO_4^{2-} + 4H_2 + H^+ \rightarrow HS^- + 4H_2O. \quad (5)$$

HS^- can absorb one proton to become H_2S or lose one proton to become S^{2-} as shown below (Gu and Xu, 2013):

$$HS^- + H^+ \rightarrow H_2S, \quad (6)$$

$$HS^- \rightarrow H^+ + S^{2-}. \quad (7)$$

The H_2S data in **Table 5** indicate that better SRB growth (as a result of a higher carbon source level) produced more H_2S from sulfate reduction. The dissolved H_2S concentrations in the liquid phases were estimated based on H_2S equilibrium at 37°C (Ning et al., 2014). The dissolved [H_2S] in the culture medium data was plotted together with broth pH data at the end of the 14-day starvation incubation as shown in **Figure 10**. **Figure 10** clearly indicates that a higher dissolved H_2S concentration corresponds to a higher pH. This contradicts the conventional thinking of more H_2S in a system for more acidic liquid pH (lower pH). This is because in abiotic H_2S corrosion testing, externally introduced H_2S acidifies the liquid phase due to H_2S dissociation, which releases protons. However, in the SRB broth, H_2S is as a reservoir of H^+, but its H^+ originally comes from the broth itself rather than being externally introduced. Thus, it is not rational to argue for acidification by biogenic H_2S in the SRB system. More dissolved H_2S in the SRB system results in a higher and not a lower pH.

It is known that sulfate respiration does not normally change scalar and vectorial protons (Peck, 1993). On the contrary, better SRB growth allows more H_2S to escape to the headspace, thus taking away more proton from the broth. This is why **Figure 10** shows a higher carbon source level leading to a higher broth pH (7.38 for 100% carbon source, 7.31 for 50% carbon source, 7.23 for 10% carbon source, and 7.11 for 0% carbon source). In fact, SRB are used to increase the pH of acid mine drainage for exactly the same reason as demonstrated here (Bai et al., 2013). The above 7.00 pH values in **Figure 10** also suggest that acid attack and H_2S attack were not important contributors to the MIC in this work (Wang et al., 2020).

Sessile Cell Counts on Dogbone Coupons

After the 14-day starvation incubation, the sessile cell count was found to be higher for a larger carbon source level as was expected (**Figure 11**). The cell counts on the dogbone coupons in the bottles with the carbon source levels of 0, 10, 50, and 100% were 8.1×10^6, 3.2×10^7, 8.3×10^7, and 1.3×10^8 cells/cm^2, respectively. The 0% carbon source bottle had the lowest sessile cell count due to extreme starvation (Dou et al., 2019). The sessile cell counts on the X80 dogbone coupons here are consistent with the SEM biofilm images on the X80 square coupons.

Pit Depths on Dogbone Coupons

Morphologies of MIC pits on the dogbone coupons after the 14-day carbon starvation incubation with biofilms and with corrosion products removed were examined under the IFM before tensile testing (**Figure 12**). The maximum pit depth was the highest for 50% carbon source (9.1 μm) followed by 100% carbon source (6.4 μm), 10% carbon source (4.9 μm), and 0% carbon source (1.9 μm). The pit depth trend here is consistent with the weight loss trend.

Tensile Testing Using Dogbone Coupons

Figure 13 shows the stress–strain curves of the dogbone coupons after the 14-day starvation incubation. Compared with the fresh X80 dogbone's ultimate strength of 879 MPa, all the biotic dogbone coupons had a lower ultimate tensile strength and ultimate tensile strain. **Table 6** shows a summary. It indicates that the trend of the degradation of the ultimate tensile strain followed the trend of MIC severity (in terms of weight loss and pit depth) and followed the following sequence (more to less): 50, 100, 10, and 0% carbon source levels. The degradation of the ultimate strength followed the same general trend (but with 10 and 0% having practically the same value). A lower ultimate tensile strain means a more brittle metal. Thus, the tensile strain data indicated that SRB MIC made X80 more brittle in addition to weakening its mechanical strength.

The 50% carbon source led to the highest reductions in both ultimate tensile strength (22% loss) and ultimate tensile strain (24% loss) compared with the fresh dogbone data. In this work, 50% carbon source caused the biggest MIC damages in terms of weight loss and pitting depth. As a result, it led to the most severe degradation of X80 mechanical properties. This trend could not be attributed to H_2 or H_2S because 50% source did not have the highest H_2 or H_2S level. In abiotic H_2S studies, externally introduced H_2S acidifies a liquid, which causes corrosion. But it was not the case in this study with biogenic H_2S production, which does not acidify the liquid phase. Thus, it was not surprising that the highest dissolved H_2S concentration (100% carbon source) did not result in the highest losses to ultimate strength and ultimate tensile strain.

CONCLUSIONS

(1) The weight loss data using square coupons indicated that 50% carbon source levels resulted in the highest weight loss. This was because 50% carbon had the combination of carbon starvation without suffering too much sessile cell loss. The weight loss trend was supported by the pit depth trend.
(2) The electrochemical results, including LPR, EIS, and Tafel scans, all supported the weight loss trend, confirming that the 50% carbon source level caused the most severe MIC.
(3) The SEM biofilm results agreed with the sessile cell count trend.
(4) The H_2S, H_2, and sessile cell count data for dogbone coupons were consistent in supporting the higher carbon source levels for better growth, exhibiting higher biogenic H_2S and H_2 concentrations.
(5) The tensile test results for the biotic coupons and the fresh X80 dogbone showed that more severe MIC led to larger degradations of ultimate tensile strain and ultimate tensile strength. The 50% carbon source led to the highest reductions in both ultimate tensile strength (22% loss vs fresh dogbone) and ultimate tensile strain (24% loss).
(6) A higher dissolved H_2S concentration at a nonacidic pH in this work did not result in higher losses in ultimate strength and ultimate tensile strain because it did not provide higher weight loss and pit depth.

DATA AVAILABILITY STATEMENT

The datasets generated for this study are available upon request to the corresponding author.

AUTHOR CONTRIBUTIONS

All authors listed have made a substantial, direct, and intellectual contribution to the work and have approved it for publication.

FUNDING

This project was funded by the Chinese Society for Corrosion and Protection (CSCP), PTTEP of Thailand and Saudi Aramco.

ACKNOWLEDGMENTS

The tensile testing part received support from Marc Singer, who works in the Institute for Corrosion and Multiphase Technology (ICMT) at Ohio University.

REFERENCES

Abedi, S. S., Abdolmaleki, A., and Adibi, N. (2007). Failure Analysis of SCC and SRB Induced Cracking of a Transmission Oil Products Pipeline. *Eng. Fail. Anal.* 14, 250–261. doi:10.1016/j.engfailanal.2005.07.024

Al-Nabulsi, K. M., Al-Abbas, F. M., Rizk, T. Y., and Salameh, A. E. M. (2015). Microbiologically Assisted Stress Corrosion Cracking in the Presence of Nitrate Reducing Bacteria. *Eng. Fail. Anal.* 58, 165–172. doi:10.1016/j.engfailanal.2015.08.003

AlAbbas, F. M., Williamson, C., Bhola, S. M., Spear, J. R., Olson, D. L., Mishra, B., et al. (2013). Influence of Sulfate Reducing Bacterial Biofilm on Corrosion Behavior of low-alloy, High-Strength Steel (API-5L X80). *Int. Biodeterioration Biodegradation* 78, 34–42. doi:10.1016/j.ibiod.2012.10.014

ASTM-E8/E8M-13a (2013). *Standard Test Methods for Tension Testing of Metallic Materials*. West Conshohocken, PA: ASTM International.

Bai, H., Kang, Y., Quan, H., Han, Y., Sun, J., and Feng, Y. (2013). Treatment of Acid Mine Drainage by Sulfate Reducing Bacteria with Iron in Bench Scale Runs. *Bioresour. Technology* 128, 818–822. doi:10.1016/j.biortech.2012.10.070

Biswas, S., and Bose, P. (2005). Zero-valent Iron-Assisted Autotrophic Denitrification. *J. Environ. Eng.* 131, 1212–1220. doi:10.1061/(ASCE)0733-937210.1061/(asce)0733-9372(2005)131:8(1212)

Cui, L. Y., Liu, Z. Y., Xu, D. K., Hu, P., Shao, J. M., Du, C. W., et al. (2020). The Study of Microbiologically Influenced Corrosion of 2205 Duplex Stainless Steel Based on High-Resolution Characterization. *Corrosion Sci.* 174, 108842. doi:10.1016/j.corsci.2020.108842

Dannenberg, S., Kroder, M., Dilling, W., and Cypionka, H. (1992). Oxidation of H2, Organic Compounds and Inorganic Sulfur Compounds Coupled to Reduction of O2 or Nitrate by Sulfate-Reducing Bacteria. *Arch. Microbiol.* 158, 93–99. doi:10.1007/BF00245211

Dou, W., Liu, J., Cai, W., Wang, D., Jia, R., Chen, S., et al. (2019). Electrochemical Investigation of Increased Carbon Steel Corrosion via Extracellular Electron Transfer by a Sulfate Reducing Bacterium under Carbon Source Starvation. *Corrosion Sci.* 150, 258–267. doi:10.1016/j.corsci.2019.02.005

Flemming, H.-C., Wingender, J., Szewzyk, U., Steinberg, P., Rice, S. A., and Kjelleberg, S. (2016). Biofilms: an Emergent Form of Bacterial Life. *Nat. Rev. Microbiol.* 14, 563–575. doi:10.1038/nrmicro.2016.94

Gu, T., Jia, R., Unsal, T., and Xu, D. (2019). Toward a Better Understanding of Microbiologically Influenced Corrosion Caused by Sulfate Reducing Bacteria. *J. Mater. Sci. Technology* 35, 631–636. doi:10.1016/j.jmst.2018.10.026

Gu, T., and Xu, D. (2013). *Why Are Some Microbes Corrosive and Some Not? CORROSION 2013*. Paper No. 2336. Orlando, FL: NACE International.

Heidelberg, J. F., Seshadri, R., Haveman, S. A., Hemme, C. L., Paulsen, I. T., Kolonay, J. F., et al. (2004). The Genome Sequence of the Anaerobic, Sulfate-Reducing Bacterium *Desulfovibrio Vulgaris* Hildenborough. *Nat. Biotechnol.* 22, 554–559. doi:10.1038/nbt959

Jia, R., Wang, D., Jin, P., Unsal, T., Yang, D., Yang, J., et al. (2019). Effects of Ferrous Ion Concentration on Microbiologically Influenced Corrosion of Carbon Steel by Sulfate Reducing Bacterium *Desulfovibrio Vulgaris*. *Corrosion Sci.* 153, 127–137. doi:10.1016/j.corsci.2019.03.038

Jia, R., Yang, D., Al-Mahamedh, H. H., and Gu, T. (2017). Electrochemical Testing of Biocide Enhancement by a Mixture of D-Amino Acids for the Prevention of a Corrosive Biofilm Consortium on Carbon Steel. *Ind. Eng. Chem. Res.* 56, 7640–7649. doi:10.1021/acs.iecr.7b01534

Jogdeo, P., Chai, R., Shuyang, S., Saballus, M., Constancias, F., Wijesinghe, S. L., et al. (2017). Onset of Microbial Influenced Corrosion (MIC) in Stainless Steel Exposed to Mixed Species Biofilms from Equatorial Seawater. *J. Electrochem. Soc.* 164, C532–C538. doi:10.1149/2.0521709jes

Li, H., Xu, D., Li, Y., Feng, H., Liu, Z., Li, X., et al. (2015). Extracellular Electron Transfer Is a Bottleneck in the Microbiologically Influenced Corrosion of C1018 Carbon Steel by the Biofilm of Sulfate-Reducing Bacterium *Desulfovibrio Vulgaris*. *PLoS One* 10, e0136183. doi:10.1371/journal.pone.0136183

Li, X., Lan, S.-m., Zhu, Z.-p., Zhang, C., Zeng, G.-m., Liu, Y.-g., et al. (2018a). The Bioenergetics Mechanisms and Applications of Sulfate-Reducing Bacteria in Remediation of Pollutants in Drainage: a Review. *Ecotoxicology Environ. Saf.* 158, 162–170. doi:10.1016/j.ecoenv.2018.04.025

Li, Y., Xu, D., Chen, C., Li, X., Jia, R., Zhang, D., et al. (2018b). Anaerobic Microbiologically Influenced Corrosion Mechanisms Interpreted Using Bioenergetics and Bioelectrochemistry: a Review. *J. Mater. Sci. Technology* 34, 1713–1718. doi:10.1016/j.jmst.2018.02.023

Little, B. J., and Lee, J. S. (2007). *Microbiologically Influenced Corrosion*. Hoboken, New Jersey, United States: John Wiley & Sons. doi:10.1002/9783527610426.bard040603

Liu, H., Gu, T., Zhang, G., Liu, H., and Cheng, Y. F. (2018). Corrosion of X80 Pipeline Steel under Sulfate-Reducing Bacterium Biofilms in Simulated CO2-saturated Oilfield Produced Water with Carbon Source Starvation. *Corrosion Sci.* 136, 47–59. doi:10.1016/j.corsci.2018.02.038

Lv, M., and Du, M. (2018). A Review: Microbiologically Influenced Corrosion and the Effect of Cathodic Polarization on Typical Bacteria. *Rev. Environ. Sci. Biotechnol.* 17, 431–446. doi:10.1007/s11157-018-9473-2

Ning, J., Zheng, Y., Young, D., Brown, B., and Nešić, S. (2014). Thermodynamic Study of Hydrogen Sulfide Corrosion of Mild Steel. *Corrosion* 70 (4), 375–389. doi:10.5006/0951

Peck, H. D. (1993). "Bioenergetic Strategies of the Sulfate-Reducing Bacteria," in *The Sulfate-Reducing Bacteria: Contemporary Perspectives*. Editors J. M. Odom and R. Singleton (New York, NY: Springer), 41–76. doi:10.1007/978-1-4613-9263-7_3

Sheng, X., Ting, Y.-P., and Pehkonen, S. O. (2007). The Influence of Sulphate-Reducing Bacteria Biofilm on the Corrosion of Stainless Steel AISI 316. *Corrosion Sci.* 49, 2159–2176. doi:10.1016/j.corsci.2006.10.040

Służalec, A. (1992). "Stress-Strain Curve," in *Introduction to Nonlinear Thermomechanics: Theory and Finite-Element Solutions*. London: Springer London, 45–47. doi:10.1007/978-1-4471-1906-7_5

Wang, D., Liu, J., Jia, R., Dou, W., Kumseranee, S., Punpruk, S., et al. (2020). Distinguishing Two Different Microbiologically Influenced Corrosion (MIC) Mechanisms Using an Electron Mediator and Hydrogen Evolution Detection. *Corrosion Sci.* 177, 108993. doi:10.1016/j.corsci.2020.108993

Wu, T., Yan, M., Zeng, D., Xu, J., Sun, C., Yu, C., et al. (2015). Stress Corrosion Cracking of X80 Steel in the Presence of Sulfate-Reducing Bacteria. *J. Mater. Sci. Technology* 31, 413–422. doi:10.1016/j.jmst.2014.08.012

Xu, D., and Gu, T. (2011). *Bioenergetics Explains when and Why More Severe MIC Pitting by SRB Can Occur*. CORROSION 2011, Paper No. 11426. Houston, TX: NACE International.

Xu, D., and Gu, T. (2014). Carbon Source Starvation Triggered More Aggressive Corrosion against Carbon Steel by the *Desulfovibrio Vulgaris* Biofilm. *Int. Biodeterioration Biodegradation* 91, 74–81. doi:10.1016/j.ibiod.204.03.01410.1016/j.ibiod.2014.03.014

Xu, D., Li, Y., and Gu, T. (2016). Mechanistic Modeling of Biocorrosion Caused by Biofilms of Sulfate Reducing Bacteria and Acid Producing Bacteria. *Bioelectrochemistry* 110, 52–58. doi:10.1016/j.bioelechem.2016.03.003

Yin, K., Liu, H., and Cheng, Y. F. (2018). Microbiologically Influenced Corrosion of X52 Pipeline Steel in Thin Layers of Solution Containing Sulfate-Reducing Bacteria Trapped under Disbonded Coating. *Corrosion Sci.* 145, 271–282. doi:10.1016/j.corsci.2018.10.012

Conflict of Interest: The authors declare that the research was conducted in the absence of any commercial or financial relationships that could be construed as a potential conflict of interest.

Publisher's Note: All claims expressed in this article are solely those of the authors and do not necessarily represent those of their affiliated organizations, or those of the publisher, the editors, and the reviewers. Any product that may be evaluated in this article, or claim that may be made by its manufacturer, is not guaranteed or endorsed by the publisher.

frontiers in Materials

ORIGINAL RESEARCH
published: 05 January 2022
doi: 10.3389/fmats.2021.804328

Active Corrosion Protection by Epoxy Coating on Li_2CO_3-Pretreated Anodized Aluminum Alloy 2024-T3

Badar Minhas, Sahib Dino, Luyao Huang and Dequan Wu*

Institute for Advanced Materials and Technology, University of Science and Technology Beijing, Beijing, China

The fast leaching and robust barrier property of inhibitors are the basic fundamentals for the formation of active protective coatings to protect aluminum alloys. Herein, an active protective surface was developed based on an epoxy coating and an underlying lithium carbonate (Li_2CO_3)-treated anodized aluminum alloy 2024-T3. The morphology of the Li-LDH layer was studied to know its formation mechanism. The electrochemical studies revealed that the fast and adequate leaching of lithium led to a substantial increment of corrosion resistance of the scratched coating in 3.5 wt% NaCl from 1 to 8 days. Time of flight secondary ion mass spectroscopy (ToF-SIMS) results indicated that Li was distributed in the lateral direction and covered the scratched area. The 3D images indicated that different lithium compounds were formed and 90% of the scratched area was covered with the lithium protective layer over immersion time. A combined approach of morphology observations, electrochemical measurements, and ToF-SIMS showed the lithium protective layer offered good corrosion resistance. On the contrary, lithium provided fast and adequate leaching from the coating, demonstrating good active protection for aluminum and its alloys.

Keywords: lithium inhibitors, aluminum alloy 2024-T3, coating, ToF-SIMS, corrosion protection

OPEN ACCESS

Edited by:
Xiaoqiang Fan,
Southwest Jiaotong University, China

Reviewed by:
Mahmood Aliofkhazraei,
Tarbiat Modares University, Iran
Han Yan,
Southwest Jiaotong University, China

****Correspondence:***
Badar Minhas
badar.minhas@outlook.com

Specialty section:
This article was submitted to Environmental Degradation of Materials, a section of the journal Frontiers in Materials

Received: *29 October 2021*
Accepted: *07 December 2021*
Published: *05 January 2022*

Citation:
Minhas B, Dino S, Huang L and Wu D (2022) Active Corrosion Protection by Epoxy Coating on Li_2CO_3-Pretreated Anodized Aluminum Alloy 2024-T3. Front. Mater. 8:804328. doi: 10.3389/fmats.2021.804328

INTRODUCTION

In the aerospace industries, the corrosion protection of aluminum alloys is of great significance (Buchheit et al., 1993; Kendig and Buchheit, 2003; Visser et al., 2018a), which is principally achieved by anodic oxidation incorporated with the Cr(VI) conversion process. However, this approach will be banned by regulatory authorities in the near future due to the hazardous and carcinogenic effects of chromate commercial coatings. 2024-T3 aluminum alloy, one of the most commonly used aluminum alloys, is prone to localized corrosion in the chloride-containing medium due to the presence of intermetallic particles (IMPs). The IMPs provide active sites for corrosion initiation and propagation with respect to the surrounding matrix (Yasakau et al., 2006). Kosari et al. (2020) and Kosari et al. (2021a) studied the initiation, propagation, and dealloying of IMPs in 0.01 M NaCl solution by liquid phase transmission electron microscopy (LP-TEM). *In situ* TEM images revealed that the main cause of corrosion initiation to the propagation of aluminum alloy was the S-phase (Al_2CuMg) and θ-phase (Al_2Cu). The S-phase was more electrochemically active than the θ-phase and showed fast local degradation upon exposure to corrosive media. Over time, different IMPs cause local corrosion on an aluminum alloy such as pitting, intergranular corrosion, and copper redistribution process. To eradicate the electrochemical reactions on IMPs, it is urgent to design eco-friendly, highly protective, and cost-effective coatings to replace chromate-based surface technologies.

In recent years, many breakthroughs related to Cr(VI)-free coatings have been reported, particularly for corrosion protection of 2024-T3 aluminum alloys. In particular, the active protective coatings possessing both the barrier property from the coating matrix and the inhibition effect from the incorporated corrosion inhibitors are shown to be more promising for corrosion protection than the regular barrier-type coatings (Zhang et al., 2018; Ma et al., 2021a; Ma et al., 2021b). In case of mechanical damages on the coating surface, the incorporated inhibitors in the coating will leach out and protect the damaged coating area. Lithium salts have been demonstrated to be excellent corrosion inhibitors toward aluminum and its alloys for active protection. For example, Drewien et al. (1996) introduced a lithium-based conversion layer by exposing the 1,100 aluminum alloy in Li_2CO_3 solution at different pH values. Visser et al. (2016), Visser et al. (2017), Visser et al. (2018a), Visser et al. (2018b), and Visser et al. (2019a) found another way of utilizing lithium inhibitors by adding them directly into the epoxy coating which was applied on the aluminum alloy surface. The lithium salts mixed in the coating could leach out under aggressive environments and establish an alkaline condition that enabled the generation of a protective film on the defective area in the coating, therefore successfully stifling the electrochemical process. In addition, a recent work of Visser et al. (2019b) demonstrated that lithium salt incorporated in an organic coating could leach out with high chemical throwing power over a broad width of an artificial coating defect. Kosari et al. (2021b) and Bouali et al. (2021) developed a lithium-based double hydroxide (LDH) layer on the aluminum alloy surface, and demonstrated that the immersion in alkaline solution induced the surface enrichment of Cu which favored the growth of the Li-LDH layer *via* aluminum and magnesium dissolution. Andressa et al. (Trentin et al., 2019) observed the effect of lithium on poly (methyl methacrylate) (PMMA) silica sol–gel coating. The addition of lithium resulted in a densified network of PMMA by reduction in the stacking defect and provided active protection as restoration of the system over a long immersion time. Many researchers performed the plasma electrolytic oxidation (PEO) and micro arc oxidation (MAO) on Mg and Al alloys to obtain the porous structure that solved the relative adhesion problems of polymer top coatings on the surfaces. Furthermore, the PEO and MAO surfaces acted as containers to store different inhibitors, and the pH changes provided active corrosion protection in the defect area and improved its barrier properties (Golabadi et al., 2017a; Yang et al., 2018a; Yang et al., 2018b; Pezzato et al., 2019; Toorani and Aliofkhazraei, 2019; Toorani et al., 2019; Toorani et al., 2020; Liu et al., 2021; Ostapiuk, 2021; Toorani et al., 2021; Zeng et al., 2021; Zhang et al., 2021). Golabadi et al. (2017b) showed that the compaction and cathodic disbondment of the epoxy coating were enhanced on the phosphated coating consisting of different additives.

In the present work, a new active protective coating was designed on the 2024-T3 aluminum alloy surface to protect it against localized corrosion. A concave anodic aluminum oxide (AAO) layer was first formed on the 2024-T3 aluminum alloy and was immersed in lithium carbonate solution to obtain a lithium-based protective layer (Li-AAO). To explore the active protective response, an epoxy coating was further applied onto Li-AAO and was scratched before immersion in a 3.5 wt% NaCl solution. The formation and growth mechanism of the lithium-based protective layer on aluminum alloy were studied by various analytical techniques including scanning electron microscopy (SEM), transmission electron microscopy (TEM), and time-of-flight–secondary ion mass spectroscopy (ToF-SIMS). The corrosion resistance property of the generated layers was investigated using electrochemical impedance spectroscopy (EIS) and potentiodynamic polarization.

EXPERIMENTAL SECTION

Materials and Coating Preparation

As received, aluminum alloy sheets 2024-T3 [12.7 cm (L) × 7.6 cm (W)] formed by cutting were used as the substrates. In order to introduce the concave AAO surfaces, an electrochemical polishing pretreatment was applied on the aluminum alloy prior to anodization (Montero-Moreno et al., 2007). First, electrochemical polishing was conducted at 20 V (vs. calomel reference electrode) in a potentiostatic mode at 0–5°C, in a mixture of ethanol (900 ml), perchloric acid (80 ml), and distilled water (20 ml), under continuous stirring for 1 min. Afterward, the substrate was etched in 10 wt% NaOH alkaline solution for 5 min at 55°C, followed by desmutting in 30 vol% HNO_3 at ambient temperature. The aforementioned steps were repeated once, followed by etching in a mixture of 6 wt% H_3PO_4 and 1.8 wt% CrO_3 for 1 min at 55°C. The polished substrates were thoroughly rinsed with distilled water for 2 min. Thereafter, a two-step anodization process was used (Zaraska et al., 2010; Elaish et al., 2018). The pretreated samples were anodized in an electrochemical cell at 32 V (vs. saturated calomel electrode) in 0.3 M H_2SO_4 for 1 h, with aluminum alloy as the anode and graphite as the cathode. The bath temperature was maintained at 0–5°C under continuous stirring. The first concave layer formed after anodization was removed by acid etching in the mixture of 6 wt% H_3PO_4 and 1.8 wt% CrO_3 for 5 min at 45°C. The second anodization was performed under the same condition. Finally, the samples were rinsed with distilled water and air-dried at room temperature.

In order to prepare the lithium-based protective coatings, the anodized aluminum surface was immersed in 0.1 M Li_2CO_3 solution at 25°C for 24 h. The Li-based film was formed by a coprecipitation reaction involving Al; therefore, a sacrificial aluminum substrate was also immersed in the solution and allowed to dissolve freely. The pH of the solution was controlled to be 11.5 during the reaction. Thereafter, the samples were taken out and air-dried, which were named Li-AAO substrate. The Li-AAO substrates were further coated with an epoxy coating and cured at 55°C for 24 h (denoted as Li-AAO/epoxy coating). The epoxy coating was applied with a bar coater to control a final thickness of ~25 μm (Visser et al., 2017). An artificially scratched area (1–1.5 mm in width) was made by a surgical knife on the Li-AAO epoxy coating surface before immersion in 3.5 wt% NaCl solution. For comparison, an AAO substrate without lithium inhibitor

treatment was also coated with an epoxy coating and named AAO/epoxy coating.

Electrochemical Measurements

The EIS measurements of the 1) AAO substrate, 2) Li-AAO substrate, 3) scratched AAO/epoxy coating, and 4) scratched Li-AAO/epoxy coating were conducted using Princeton applied research PARSTAT 2273 potentiostat after immersion in 3.5 wt% NaCl solution for 1, 3, 5, and 8 days. A classic three-electrode electrochemical cell was used, with the (coated) aluminum substrate as the working electrode, a platinum foil as the counter electrode, and a saturated calomel electrode (SCE) as the reference electrode (Visser et al., 2018a). EIS tests were executed in a frequency range 10^{-2}–10^{5} Hz with a perturbation of 10 mV. EIS data were fitted using suitable equivalent electric circuits (EECs) by ZSimpWin software. To ensure reproducibility, each measurement was repeated at least three times. Potentiodynamic polarizations were performed on the samples after 8 days of immersion in 3.5 wt% NaCl solution, with a scan rate of 1 mV/s.

Surface Analytical Measurements

The top and cross-sectional images of the AAO substrate and Li-AAO substrate were obtained by SEM (SU8200 Hitachi, Japan). The cross section of the Li-AAO substrate was prepared using focused ion beam (FIB) of Ga^{+} ion Zeiss Auriga Compact Cross Beam SEM (ZEISS 540) and was characterized by TEM observation (TALOS F200X).

ToF-SIMS Measurement

ToF-SIMS measurements were carried out using ToF-SIMS GmbH (ION-TOF, Germany), equipped with a 30 keV Bi^{+} primary ion beam source worked in a high-current mode to obtain the high-resolution mass spectra. Positive mass spectra were obtained over a mass range of 1–800 amu and computed with the known fragments. The exact mass of the fragments was measured (in ppm) by the absolute difference between the experimental and theoretical mass, and the obtained result was divided by experimental mass. The lithium-layered double hydroxide (Li-LDH), lithium with pseudoboehmite (Li-PB), and pseudoboehmite (PB) were acquired by rastering area in patches of 300 μm × 300 μm from the large image area. The analysis for each patch was done for 60 s at a pixel density of 250 pixel/mm. According to the method reported by Marcoen et al. (2018), a peak list with high-resolution spectra was established for the reference sample and finally applied to the attained spectra.

The ToF-SIMS data were analyzed by simsMVA software, and 3D images were produced by Epina Image lab software (Shi et al., 2020). Two functions were used in simsMVA. The first one was the normalization and Poisson scaling of all peak intensities based on the method reported in the literature (Trindade et al., 2018). The second one was the non-negative matrix factorization (NMF), which was used to identify the distribution and presence of pure compounds on the surface.

Reference materials were made for the composition analysis of the lithium protective layer in the scratched area. Specifically, aluminum alloy substrates were thoroughly cleaned and coated with epoxy coating. PB and Li–PB reference samples were prepared according to the method reported by Gorman et al. (2003). The samples were scratched and then exposed to the (i) deionized water or (ii) a 0.02 M LiCl solution at 95–100°C to acquire PB or Li–PB, respectively. The reference of the Al–Li LDH layer is prepared by following the work of Drewien et al. (1996). According to this method, the AA-2024T3 substrates were immersed in 0.1 M Li_2CO_3 solution for 15 min. Finally, the treated substrate was washed thoroughly with deionized water and air-dried at room temperature. All ToF-SIMS measurements were performed in the scratched area.

RESULTS AND DISCUSSION

Figure 1A shows the concaved AAO surface formed on the aluminum alloy 2024-T3 substrate. Unlike the hexagonal array of AAO on pure aluminum (Wu et al., 2019; Wu et al., 2021), the uneven morphology of the nanopores on the AAO surface obtained in this study can be attributed to the potential difference between IMPs and the alloy matrix (Abrahami et al., 2017). **Figures 1B,C** are the top and cross-sectional views of the AAO surface treated with Li_2CO_3 inhibitors (Li-AAO substrate), presenting a plate-like LDH layer with somewhat irregular spacing (Visser et al., 2016). This LDH layer is formed due to the intercalation of lithium into the aluminum hydroxide gel. The AAO and Li-AAO substrates were then cured at 55°C for 24 h to simulate their changes during the curing process when epoxy coating was applied. **Figures 1D,E** are the top and cross-sectional SEM images of the Li-AAO substrate cured at 55°C. **Figure 1D** shows that the LDH layer became smaller flakes after curing. From the cross-sectional image (**Figures 1E,F**), the Li-AAO substrate displayed three defined regions including the columnar, the porous, and the barrier layers from the top to the bottom (Visser et al., 2018a).

EIS Measurements

EIS measurements were conducted on the samples with and without lithium inhibitors, followed by epoxy top coating during the 8 days of immersion in a 3.5% NaCl solution (**Figure 2**). **Figures 2A–C** show the Nyquist and Bode plots of the uncoated AAO surfaces without lithium inhibitors. The semi-capacitive arcs in Nyquist plots become smaller due to pitting corrosion with the prolonging of immersion time. The low-frequency impedance value at 10^{-2} Hz ($|Z|_{0.01Hz}$), which is a common indicator of the corrosion resistance (Buchheit et al., 1993), decreased slightly from 16.2 kΩ cm^2 (1 day) to 11.5 kΩ cm^2 (8 days). In the phase plots of **Figure 2C**, two time constants were shown; the one at low frequency (10^{-2}–10^{-1} Hz) was related to the electrochemical activity on the aluminum alloy surface, and the second one at middle frequency (10^{1}–10^{3} Hz) was ascribed to the oxide layer (Visser et al., 2017). It was shown in **Figure 2C** that the active corrosion was observed as the immersion time increased on the uncoated AAO surface. The EIS spectra of the Li-AAO substrate are shown in **Figures 2D–F**. The capacitive arcs remained almost unchanged over 8 days, denoting that the lithium protective

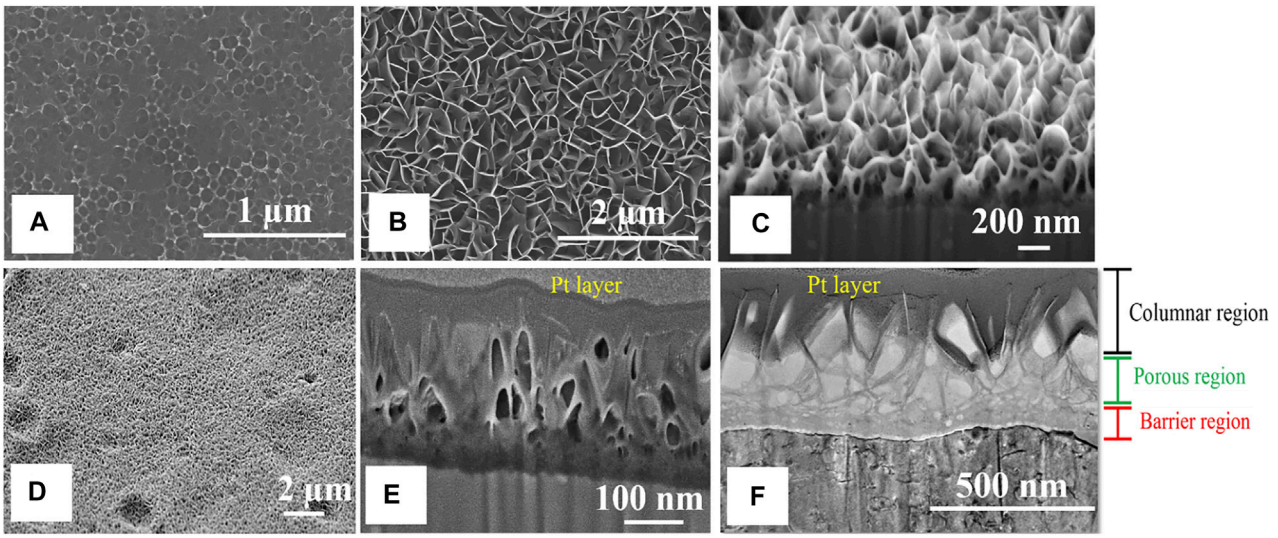

FIGURE 1 | SEM images of **(A)** the top view AAO surface on 2024-T3 substrate, **(B)** top view, and **(C)** cross-sectional view of the Li-AAO substrate; SEM images of **(D)** top view and **(E)** cross-sectional view of the Li-AAO substrate after curing at 55°C; **(F)** TEM image of the cross-sectional view of the Li-AAO substrate after curing at 55°C.

layer showed high interfacial resistance to the corrosion process (Visser et al., 2018a). In the Bode impedance plots, the $|Z|_{0.01Hz}$ values slightly increased from 1.0 MΩ cm^2 (day 1) to 1.3 MΩ (day 8). From the phase angle plots, three time constants were observed; the one at the low-frequency region (10^{-2}–10^{-1} Hz) represented corrosion on the metal surface, and the other two time constants overlapped in the broad middle frequency range and were attributed to the dense and porous regions of the lithium protective layer (Liu et al., 2016). The EIS spectra of Li-AAO illustrated that the lithium protective layer showed a significant corrosion protection as compared to the uncoated AAO substrate. The EIS spectra of the scratched AAO/epoxy coating are illustrated in **Figures 2G–I**. The Nyquist plots showed a decrease in size of the capacitive arcs after 1 day. In the Bode impedance plots, the $|Z|_{0.01Hz}$ displayed a small change within 8 days. The Nyquist and Bode plots of scratched Li-AAO/epoxy coating are presented in **Figures 2J–L**. The obvious increase in the size of capacitive arcs signified the growth of the protective layer in the scratched area. From the Bode impedance plots, the $|Z|_{0.01Hz}$ value changed from 0.6 MΩ cm^2 (1 day) to 2.2 MΩ cm^2 (8 days), determining that the corrosion protection property was improved. From the Bode phase plots, three time constants were observed. The time constant at low frequency (10^{-2} Hz) at day 1 was ascribed to the electrochemical activity. The second and third time constants were noticed at the middle frequency region (10^{1}–10^{3} Hz), which were referred to the dense and porous regions of the lithium protective layer (Visser et al., 2018a; Trentin et al., 2019). The time constant at the low frequency disappeared after 1 day of immersion. It should be noted the EIS spectra of Li-AAO in **Figures 2D–F** present slightly different results compared with those of the scratched Li-AAO/epoxy coating (**Figures 2J–L**). The main reason is associated with the lithium leaches from the complex network of the columnar region into the scratched area that further densified the porous and barrier regions next to the substrate. In contrast, the Li-AAO substrate shows the EIS measurements from the top surface with no scratched area. As a result, the corrosion protection of the scratched Li-AAO/epoxy coating was increased over time (Kosari et al., 2021b). The EIS spectra of scratched Li-AAO/epoxy coating showed that lithium leached from the lithium protective layer and provided active protection in the scratched area over the immersion time. Diping and their coworkers performed plasma electrolytic oxidation (PEO) on UNS A97075 Al alloy and further sealed this layer with silane. The corrosion property of PEO sealed with silane was measured by electrochemical impedance spectroscopy (EIS). The measured corrosion resistance of aluminum alloy was good but lower than that of the present study (Zeng et al., 2021).

The EIS measurements were fitted by the EECs in **Figure 3** to evaluate the electrochemical response of different substrates. **Figure 3A** displays an EEC with two time constants, which is used to describe the electrochemical response in the damaged area without the lithium inhibitors. In this circuit, R_{sol} describes the solution resistance; R_{oxide} and CPE_{oxide} represent the resistance and capacitance of the AAO layer; and R_{ct} and CPE_{dl} depict the electrochemical responses at the aluminum alloy surface *via* charge transfer resistance and double layer capacitance, respectively (Visser et al., 2018a; Visser et al., 2017). Generally, CPE is used instead of a pure capacitance to define the non-ideal capacitive behavior of elements, which is mainly attributed to the uneven growth of the generated layer (Hsu and Mansfeld, 2001). An EEC with three time constants in **Figure 3B** is used to fit the EIS data of AAO with lithium inhibitors. In this model, an additional time constant is contributed to the generated lithium-based protective layer, which is in good agreement with the SEM and TEM results in

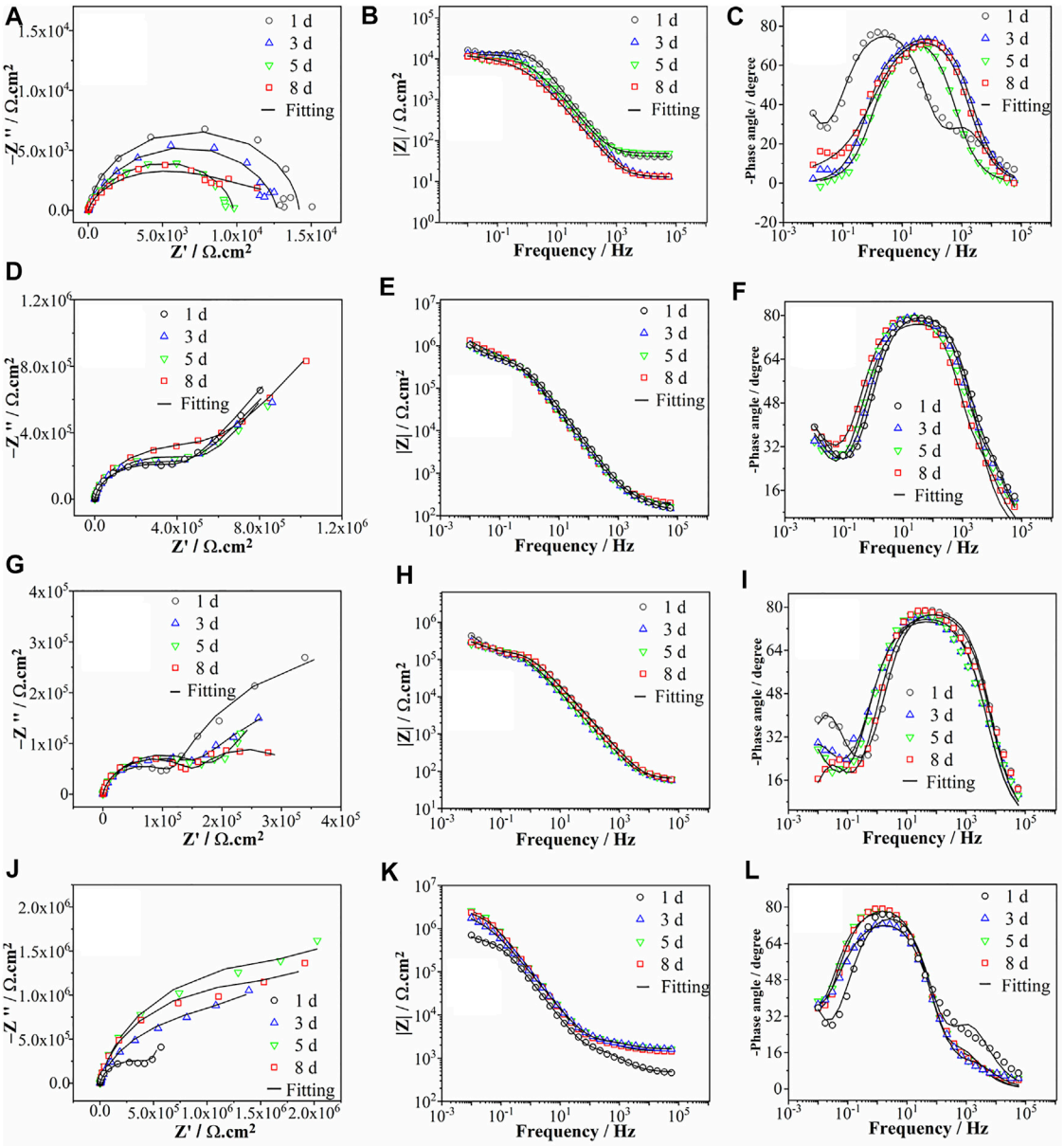

FIGURE 2 | EIS spectra of the **(A–C)** AAO substrate, **(D–F)** Li-AAO substrate, **(G–I)** scratched AAO/epoxy coating, and **(J–L)** scratched Li-AAO/epoxy coating during immersion in 3.5% NaCl solution from 1 to 8 days.

Figures 1E,F. R_{sol} describes the solution resistance, R_{porous} and CPE_{porous} represent the resistance and capacitance of the porous layer, respectively, and R_{oxide} and CPE_{oxide} refer to the capacitance and resistance of the combination of the AAO layer and dense layer, respectively. **Figure 3B** shows that an additional time constant attributed to the porous oxide layer formed on the barrier layer. The equivalent capacitance values of different elements in **Figures 3A,B** can be calculated by using CPE values (Q and n) with their respective resistance according to the following **Eq. 1** (Golabadi et al., 2017b).

$$C = Q^{1/n} R^{(1-n)/n}. \quad (1)$$

Figure 4A illustrates the variation of R_{oxide} with respect to the immersion time. For the AAO substrate, the R_{oxide} value was as low as ~100 kΩ cm^{-2} at the beginning of immersion (1 day), whereas the R_{oxide} value of the Li-AAO substrate was relatively high (2590 kΩ cm^{-2}) after 1 day. After application of the epoxy coating, the R_{oxide} of the scratched AAO/epoxy coating remained as low as ~463 kΩ cm^{-2} during the 8 days of immersion. The R_{oxide} of the scratched Li-AAO/epoxy coating was ~2500 kΩ cm^{-2} after 1 day, which increased to ~7,500 kΩ cm^{-2} after 5 days, and then decreased to 4,300 kΩ cm^{-2} after 8 days. The corresponding CPE_{oxide} values of different coatings are shown in **Figure 4B**. The CPE_{oxide} of the

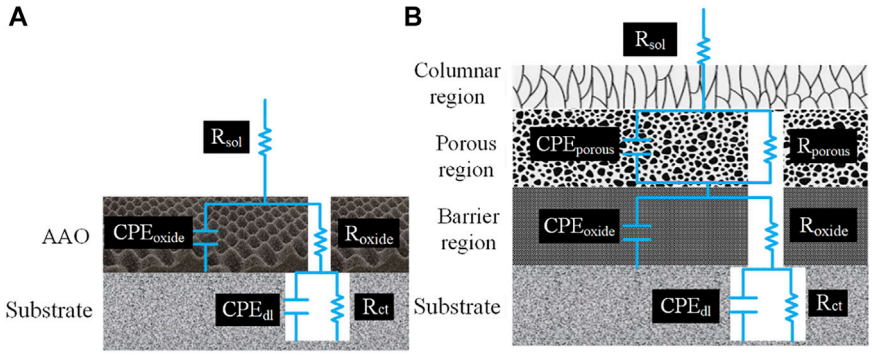

FIGURE 3 | Equivalent electric circuits used to fit EIS spectra **(A)** without inhibitors and **(B)** with inhibitors.

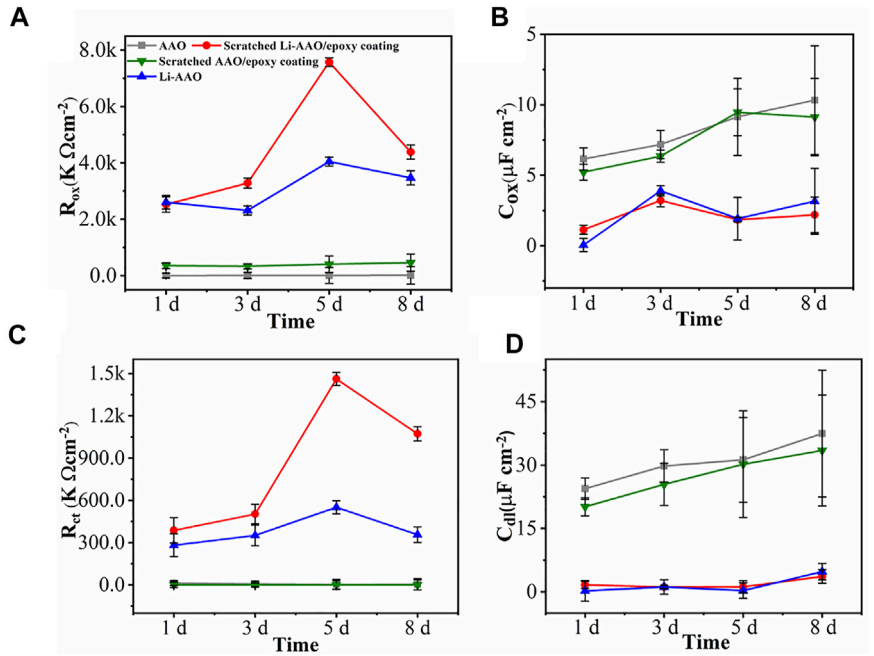

FIGURE 4 | Evolution of the **(A)** oxide resistance (R_{oxide}), **(B)** oxide capacitance (C_{oxide}), **(C)** charge transfer resistance (R_{ct}), and **(D)** double-layer capacitance (C_{dl}) of the AAO substrate, Li-AAO substrate, scratched AAO/epoxy coating, and scratched Li-AAO/epoxy coating.

AAO substrate and scratched AAO/epoxy coating showed an increase over time. The CPE_{oxide} values of the Li-AAO substrate and the scratched Li-AAO/epoxy coating were much lower, and a slight increase in the CPE_{oxide} was observed after 1 day, which was attributed to the development of the lithium-based protective layer. The corrosion rate of the surfaces can be estimated by R_{ct} values, which are shown in **Figure 4C**. The R_{ct} of samples without inhibitors showed much lower values throughout the entire immersion. R_{ct} was higher in case of the Li-AAO substrate, which was ~267 kΩ cm^{-2} after 1 day, and increased to ~552 kΩ cm^{-2} after 5 days, and then decreased to 363 kΩ cm^{-2} after 8 days. The R_{ct} of the scratched Li-AAO/epoxy coating was the highest, being 389 kΩ cm^{-2} after 1 day, and increased up to ~1,469 kΩ cm^{-2} after 5 days, and then slightly decreased to 1,075 kΩ cm^{-2} after 8 days. In **Figure 4D**, the variation of the CPE_{dl} values is in good agreement with that of the R_{ct} values for all samples. The samples containing Li inhibitors possess higher resistance values and smaller CPE values, demonstrating a better corrosion protection property. The active protection by the lithium protective layer was determined by the R_{oxide} and R_{ct} values. Comparing Li-AAOs with the uncoated AAO and scratched AAO/epoxy coating, the R_{oxide} and R_{ct} values showed a remarkable increment. A similar trend was observed in the CPE_{oxide} and C_{dl} values as compared to the oxide resistance (R_{oxide}) and charge transfer resistance (R_{ct}) values. The higher R_{ct} values of Li-AAOs after 1 day displayed that the lithium

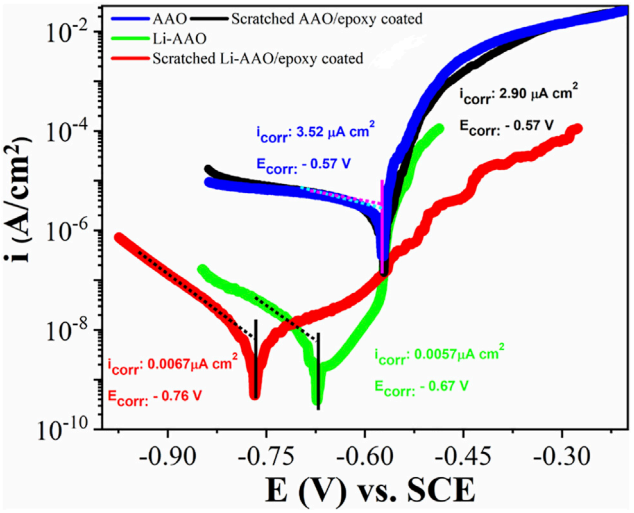

FIGURE 5 | Potentiodynamic polarization curves of the AAO substrate, Li-AAO substrate, scratched AAO/epoxy coating, and scratched Li-AAO/epoxy coating.

protective layer showed good barrier properties. Further increment in R_{ct} values from 3 to 8 days ascribed the lithium leaching from the lithium layer, providing active protection in the scratched area. Toorani et al. (2019) performed micro arc oxidation on AZ31-magnesium alloy, and the existing porous structure was closed by cerium oxide and was epoxy-coated further. The different nominal concentration of cerium oxide was used, and the corrosion property was observed at the defined scratched zone. The layer exhibited good corrosion protection and was much comparable with the present study (Toorani and Aliofkhazraei, 2019).

Potentiodynamic Polarization Measurements

Figure 5 shows the polarization measurements of the AAO substrate, Li-AAO substrate, scratched AAO/epoxy coating, and scratched Li-AAO/epoxy coating after 8 days of immersion in 3.5% NaCl solution. The curves of the AAO substrate and the scratched AAO/epoxy coating overlapped with each other. Both curves showed active corrosion during anodic polarization with respect to the open circuit potential (OCP). The cathodic branches exhibited higher current densities than the Li-AAO substrate, which were ascribed to the diffusion-limited reduction of dissolved oxygen (Visser et al., 2016; Visser et al., 2018a). In contrast, the Li-AAO substrate showed effective corrosion inhibition after 8 days of immersion. The anodic polarization of the Li-AAO substrate showed a small passive range from −670 to −570 mV. Unlike the Li-AAO substrate, the scratched Li-AAO/epoxy coating after 8 days of immersion in 3.5% NaCl solution showed passivation behavior in the anodic region (Visser et al., 2017). The anodic polarization exhibited the anodic passive range, with no sign of pitting corrosion as compared to the Li-AAO substrate. The cathodic branches of Li-AAOs showed lower current density, indicating the oxygen reduction reaction is suppressed. This shows that the cathodic inhibition of Li-AAOs is due to the leaching of lithium from the lithium protective layer. The corrosion current (i_{corr}) is measured by extrapolating the cathodic branch that has a linear Tafel region to intersect with OCP. By analyzing the electrochemical parameters in **Figure 5**, it can be deduced that the Li-AAO samples yield a corrosion inhibition effect as compared to the samples without inhibitors.

Li Distribution and Composition Tested by ToF-SIMS

Li is a low atomic number element that is very difficult to be detected using the typical surface analytical approaches (Marcoen et al., 2018). ToF-SIMS with high sensitivity to the lithium element was hence proposed to analyze the distribution and composition of the generated protective layer on AA2024-T3. ToF-SIMS measurements are performed in the scratched area with the omission of areas near the edges to eradicate the artefacts. A multivariant analysis method, that is, non-negative matrix factorization (NMF), was used to figure out the various elements present on the protective surface. The NMF function was applied to know the relative chemical composition of Li species after leaching in the scratched area with respect to the reference material. Three reference materials (Li-LDH, Li–PB, and PB)

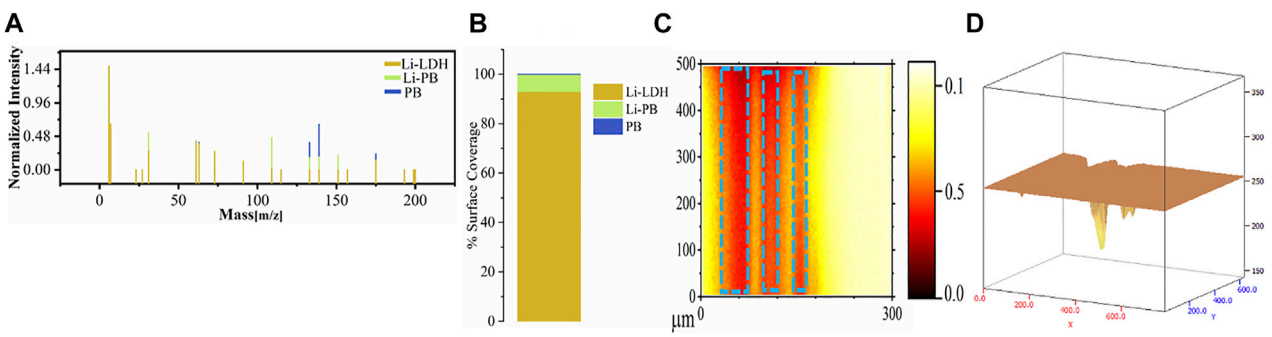

FIGURE 6 | Reference material data for ToF-SIMS analysis: **(A)** mass spectrum, **(B)** surface coverage, **(C)** ToF-SIMS, and **(D)** 3D image.

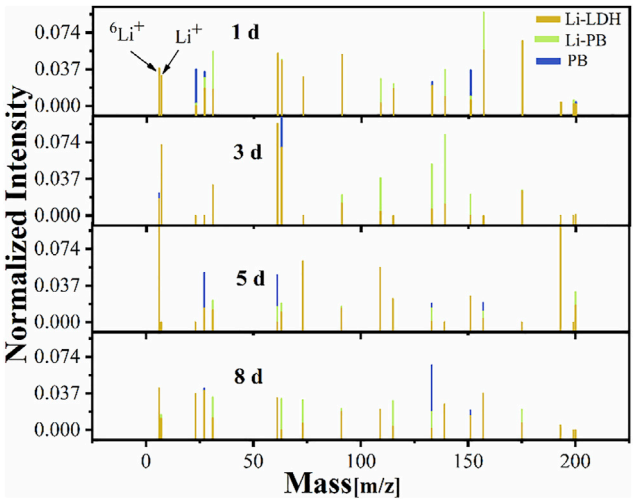

FIGURE 7 | Positive ToF-SIMS mass spectra data from PB, Li–PB, and Li-LDH; the mass spectra are normalized to the total ion intensity.

were prepared, and their respective data are shown in **Figures 6A–D** (Yang et al., 2018a; Visser et al., 2019b).

Figure 7 shows the NMF mapping of all spectra within 8 days of immersion and was produced by applying the method of Trindade et al. (2018). These maps showed fast leaching of Li^+ over a long immersion time in the scratched area. The NMF mapping was used to determine three chemical compositions in the scratched area. The major attention in the mass ranges was paid to two peaks located at 6 and 7 (*m/z*), which can be attributed to the minor isotope $^6Li^+$ and Li^+ ion, respectively. The presence of both peaks in each spectrum indicates that lithium was incorporated in the LDH structures. The maps for lithium distribution are monitored by the minor isotope $^6Li^+$ in the scratched area. Li^+ was found to saturate in the detector, and its natural abundance was reported to be 92.5%, and the remaining was minor isotope $^6Li^+$ ion (Marcoen et al., 2018). **Figure 8** discloses that the Li distribution covered the scratched area after 1 day. The inspected scratched areas of 3, 5, and 8 days of coatings revealed different amounts of $^6Li^+$ concentration, suggesting that the surface compositions are different. Furthermore, **Figure 7** shows that the maximum enrichment of Li was seen after 5 days. These results are in good agreement with the EIS data in **Figure 2**.

The 3D images in **Figure 9** show different compound formation in the scratched area over 8 days of immersion. The 3D images showed that different Li-LDH layers were found in the scratched area. The different compounds of lithium were observed due to changes in local pH values in the scratched area, and the leaching of lithium occurred from the lithium protective layer. **Figure 10** illustrates the percentage surface coverage of three different compounds in the scratched area, and the surface coverage data extracted from **Figure 9**. Two or three different regions were seen in the scratched area, indicating that the protective layers were made of different compounds. The formation of the Li-LDH layer depends on the higher pH values, and adequate amounts of $Al(OH)_4^-$, OH^-, CO_3^-, and Li^+ ions should be present in the scratched zone. In

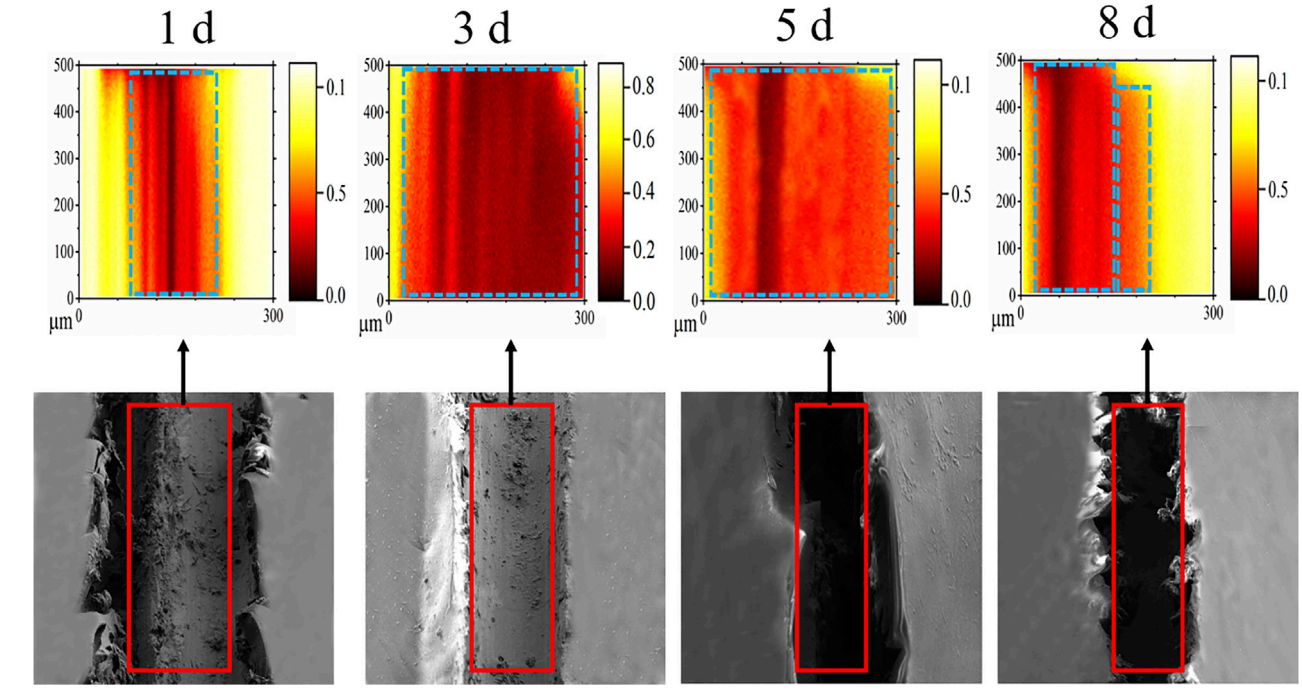

FIGURE 8 | ToF-SIMS and SEM images of the scratched Li-AAO/epoxy coating in the scratched area during immersion in 3.5% NaCl solution from 1 to 8 days; the ToF-SIMS images are normalized to the total ion intensity.

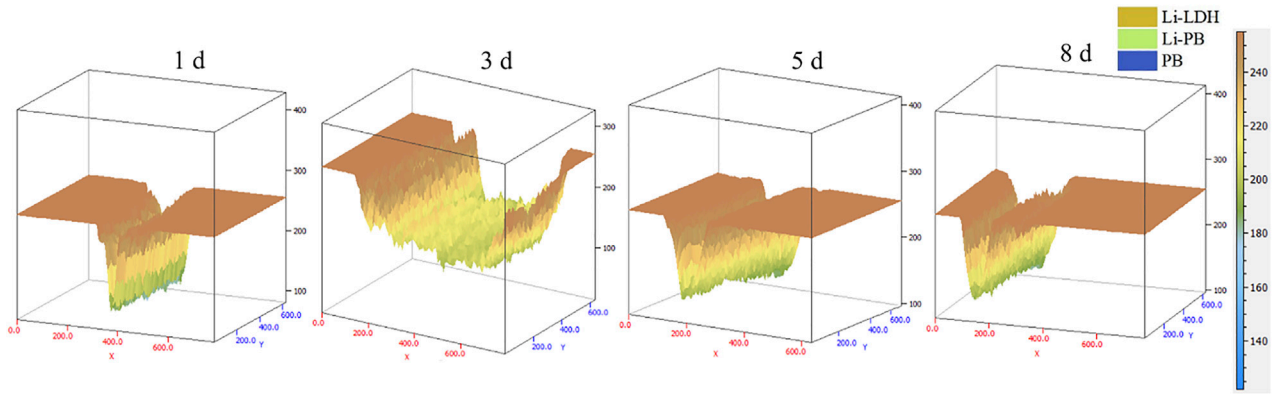

FIGURE 9 | 3D images of PB, Li–PB, and Li-LDH derived from ToF-SIMS data.

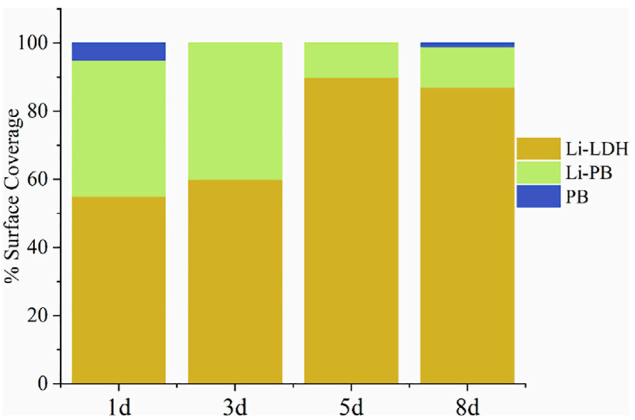

FIGURE 10 | Surface coverage percentage of PB, Li–PB, and Li-LDH derived from 3D images.

Figure 10, 1 and 8 days show three compounds formation, while 3 and 5 days display only two compounds in the scratched area. After 1 day, the leaching of lithium over the immersion time increased, and the main compound that covered the scratched area is Li-LDH. Due to changes in pH values, the Li–PB and PB regions are also observed in the scratched area.

Mechanism of Active Corrosion Inhibition

The mechanism of the lithium protective layer to achieve active corrosion protection in damaged coating can be described as follows based on the EIS, polarization, and ToF-SIMS results. As the scratched Li-AAO/epoxy coating is exposed to the chloride environment, the presence of IMPs on the exposed aluminum alloy substrate such as the S-phase is susceptible to more rapid corrosion. As a result, Al and Mg are dissolved, which leads to Cu enrichment. The oxygen reduction on the Cu develops the alkaline environment that triggers the leaching of lithium from the lithium-based protective layer. Meanwhile, uniform corrosion of Al also occurred, and Al_2O_3 is formed. As the immersion time increased, the continuous increment in the pH value accelerates the lithium leaching rate. It is reported that $Al(OH)_4^-$ was found on the Cu particles at higher pH values, and lithium is easily intercalated into aluminum hydroxide gel (Kosari et al., 2021b; Bouali et al., 2021). Therefore, the Li-LDH layer is observed in high amounts during the 8 days of immersion, gradually covering the scratched area. The pH values in the scratched area are different due to different alloying elements. At mild pH values, a small amount of PB is observed. At higher pH values, Li–PB is also found over the scratched area (Yan et al., 2020). The corrosion process of the scratched Li-AAO/epoxy coating slows down after 1 day, a dense barrier layer (Li-LDH and Li–PB) is formed, and active corrosion protection is thereby achieved as the immersion time prolonged.

CONCLUSION

In this work, a novel active protective surface was developed on anodized 2024-T3 with Li_2CO_3 inhibitors. The growth and barrier property of the lithium protective layer in 3.5 wt% NaCl solution was investigated by SEM and TEM analyses, electrochemical techniques, and ToF-SIMS. The main conclusions of the study are as follows:

1) The active protective coating on 2024-T3 aluminum alloy was formed as a result of precipitation by exposure of anodized 2024-T3 in Li_2CO_3 solution. The formed layer plays a significant role to provide active protection to 2024-T3 aluminum alloy.
2) The EIS results confirmed that the formed layer provided active corrosion protection through the leaching of lithium from the lithium-based layer in the scratched area over the immersion time. The ToF-SIMS analysis provided useful information about the Li distribution in the scratched area.
3) The 3D images of the scratched Li-AAO/epoxy coating showed that the leading compound in the scratched area was Li-LDH, and it can be observed after 1 day of immersion in chloride solution. Another lithium compound, namely, Li–PB, was also observed in the scratched area, and its amount decreased with the immersion time.

DATA AVAILABILITY STATEMENT

The original contributions presented in the study are included in the article/Supplementary Material; further inquiries can be directed to the corresponding author.

AUTHOR CONTRIBUTIONS

BM contributed to supervision, writing—review and editing, conceptualization, investigation, and writing—original draft. SD contributed to conceptualization, investigation, writing—original draft. LH contributed to conceptualization, investigation, and writing—original draft. DW contributed to conceptualization, investigation, material handling, and writing—original draft.

ACKNOWLEDGMENTS

The authors thank Professor Arjan Mol from Delft University of Technology for the helpful discussion.

REFERENCES

Abrahami, S. T., de Kok, J. M. M., Terryn, H., and Mol, J. M. C. (2017). Towards Cr(VI)-free Anodization of Aluminum Alloys for Aerospace Adhesive Bonding Applications: A Review. *Front. Chem. Sci. Eng.* 11, 465–482. doi:10.1007/s11705-017-1641-3

Bouali, A. C., Iuzviuk, M. H., Serdechnova, M., Yasakau, K. A., Drozdenko, D., Lutz, A., et al. (2021). Mechanism of LDH Direct Growth on Aluminum Alloy Surface: A Kinetic and Morphological Approach. *J. Phys. Chem. C* 125, 11687–11701. doi:10.1021/acs.jpcc.1c02281

Buchheit, R. G., Bode, M. D., and Stoner, G. E. (1993). *Talc Coat. Aluminum* 850, 205–214.

Drewien, C. A., Eatough, M. O., Tallant, D. R., Hills, C. R., and Buchheit, R. G. (1996). Lithium-aluminum-carbonate-hydroxide Hydrate Coatings on Aluminum Alloys: Composition, Structure, and Processing bath Chemistry. *J. Mater. Res.* 11, 1507–1513. doi:10.1557/jmr.1996.0188

Elaish, R., Curioni, M., Gowers, K., Kasuga, A., Habazaki, H., Hashimoto, T., et al. (2018). Effect of Fluorozirconic Acid on Anodizing of Aluminium and AA 2024-T3 alloy in Sulphuric and Tartaric-Sulphuric Acids. *Surf. Coat. Technol.* 342, 233–243. doi:10.1016/j.surfcoat.2018.02.096

Golabadi, M., Aliofkhazraei, M., Toorani, M., and Rouhaghdam, A. S. (2017). Evaluation of La Containing PEO Pretreatment on Protective Performance of Epoxy Coating on Magnesium. *Prog. Org. Coat.* 105, 258–266. doi:10.1016/j.porgcoat.2017.01.010

Golabadi, M., Aliofkhazraei, M., Toorani, M., and Sabour Rouhaghdam, A. (2017). Corrosion and Cathodic Disbondment Resistance of Epoxy Coating on Zinc Phosphate Conversion Coating Containing Ni 2+ and Co 2+. *J. Ind. Eng. Chem.* 47, 154–168. doi:10.1016/j.jiec.2016.11.027

Gorman, J. D., Hughes, A. E., Jamieson, D., and Paterson, P. J. K. (2003). Oxide Formation on Aluminium Alloys in Boiling Deionised Water and NaCl, CeCl3 and CrCl3 Solutions. *Corrosion Sci.* 45, 1103–1124. doi:10.1016/s0010-938x(02)00209-3

Hsu, C. H., and Mansfeld, F. (2001). Technical Note: Concerning the Conversion of the Constant Phase Element Parameter Y0 into a Capacitance. *Corrosion* 57, 747–748. doi:10.5006/1.3280607

Kendig, M. W., and Buchheit, R. G. (2003). Corrosion Inhibition of Aluminum and Aluminum Alloys by Soluble Chromates, Chromate Coatings, and Chromate-free Coatings. *Corrosion* 59, 379–400. doi:10.5006/1.3277570

Kosari, A., Ahmadi, M., Tichelaar, F., Visser, P., Gonzalez-Garcia, Y., Zandbergen, H., et al. (2021). Editors' Choice-Dealloying-Driven Cerium Precipitation on Intermetallic Particles in Aerospace Aluminium Alloys. *J. Electrochem. Soc.* 168, 041505. doi:10.1149/1945-7111/abf50d

Kosari, A., Tichelaar, F., Visser, P., Zandbergen, H., Terryn, H., and Mol, J. M. C. (2020). Dealloying-driven Local Corrosion by Intermetallic Constituent Particles and Dispersoids in Aerospace Aluminium Alloys. *Corrosion Sci.* 177, 108947. doi:10.1016/j.corsci.2020.108947

Kosari, A., Tichelaar, F., Visser, P., Zandbergen, H., Terryn, H., and Mol, J. M. C. (2021). Laterally-resolved Formation Mechanism of a Lithium-Based Conversion Layer at the Matrix and Intermetallic Particles in Aerospace Aluminium Alloys. *Corrosion Sci.* 190, 109651. doi:10.1016/j.corsci.2021.109651

Liu, C., Lu, X., Li, Y., Chen, Q., Zhang, T., and Wang, F. (2021). Influence of post-treatment Process on Corrosion and Wear Properties of PEO Coatings on AM50 Mg alloy. *J. Alloys Comp.* 870, 159462. doi:10.1016/j.jallcom.2021.159462

Liu, Y., Visser, P., Zhou, X., Lyon, S. B., Hashimoto, T., Curioni, M., et al. (2016). Protective Film Formation on AA2024-T3 Aluminum Alloy by Leaching of Lithium Carbonate from an Organic Coating. *J. Electrochem. Soc.* 163. C45–C53. doi:10.1149/2.0021603jes

Ma, L., Ren, C., Wang, J., Liu, T., Yang, H., Wang, Y., et al. (2021). Self-reporting Coatings for Autonomous Detection of Coating Damage and Metal Corrosion: A Review. *Chem. Eng. J.* 421, 127854. doi:10.1016/j.cej.2020.127854

Ma, L., Wang, J., Zhang, D., Huang, Y., Huang, L., Wang, P., et al. (2021). Dual-action Self-Healing Protective Coatings with Photothermal Responsive Corrosion Inhibitor Nanocontainers. *Chem. Eng. J.* 404, 127118. doi:10.1016/j.cej.2020.127118

Marcoen, K., Visser, P., Trindade, G. F., Abel, M.-L., Watts, J. F., Mol, J. M. C., et al. (2018). Compositional Study of a Corrosion Protective Layer Formed by Leachable Lithium Salts in a Coating Defect on AA2024-T3 Aluminium Alloys. *Prog. Org. Coat.* 119, 65–75. doi:10.1016/j.porgcoat.2018.02.011

Montero-Moreno, J. M., Sarret, M., and Müller, C. (2007). Influence of the Aluminum Surface on the Final Results of a Two-step Anodizing. *Surf. Coat. Technol.* 201, 6352–6357. doi:10.1016/j.surfcoat.2006.12.003

Ostapiuk, M. (2021). Corrosion Resistance of PEO and Primer Coatings on Magnesium alloy. *J. Asian Ceram. Soc.* 9, 17–29. doi:10.1080/21870764.2020.1847424

Pezzato, L., Rigon, M., Martucci, A., Brunelli, K., and Dabalà, M. (2019). Plasma Electrolytic Oxidation (PEO) as Pre-treatment for Sol-Gel Coating on Aluminum and Magnesium Alloys. *Surf. Coat. Technol.* 366, 114–123. doi:10.1016/j.surfcoat.2019.03.023

Shi, L., Liu, X., Shi, L., Stinson, H. T., Rowlette, J., Kahl, L. J., et al. (2020). Mid-infrared Metabolic Imaging with Vibrational Probes. *Nat. Methods* 17, 844–851. doi:10.1038/s41592-020-0883-z

Toorani, M., Aliofkhazraei, M., Mahdavian, M., and Naderi, R. (2020). Effective PEO/Silane Pretreatment of Epoxy Coating Applied on AZ31B Mg alloy for Corrosion protection. *Corrosion Sci.* 169, 108608. doi:10.1016/j.corsci.2020.108608

Toorani, M., Aliofkhazraei, M., Mahdavian, M., and Naderi, R. (2021). Superior Corrosion protection and Adhesion Strength of Epoxy Coating Applied on AZ31 Magnesium alloy Pre-treated by PEO/Silane with Inorganic and Organic Corrosion Inhibitors. *Corrosion Sci.* 178, 109065. doi:10.1016/j.corsci.2020.109065

Toorani, M., Aliofkhazraei, M., and Naderi, R. (2019). Ceria-embedded MAO Process as Pretreatment for Corrosion protection of Epoxy Films Applied on AZ31-magnesium alloy. *J. Alloys Comp.* 785, 669–683. doi:10.1016/j.jallcom.2018.12.257

Toorani, M., and Aliofkhazraei, M. (2019). Review of Electrochemical Properties of Hybrid Coating Systems on Mg with Plasma Electrolytic Oxidation Process as Pretreatment. *Surf. Inter.* 14, 262–295. doi:10.1016/j.surfin.2019.01.004

Trentin, A., Harb, S. V., Uvida, M. C., Pulcinelli, S. H., Santilli, C. V., Marcoen, K., et al. (2019). Dual Role of Lithium on the Structure and Self-Healing Ability of PMMA-Silica Coatings on AA7075 Alloy. *ACS Appl. Mater. Inter.* 11, 40629–40641. doi:10.1021/acsami.9b13839

Trindade, G. F., Abel, M.-L., Lowe, C., Tshulu, R., and Watts, J. F. (2018). A Time-Of-Flight Secondary Ion Mass Spectrometry/Multivariate Analysis (ToF-SIMS/MVA) Approach to Identify Phase Segregation in Blends of Incompatible but Extremely Similar Resins. *Anal. Chem.* 90, 3936–3941. doi:10.1021/acs.analchem.7b04877

Visser, P., Gonzalez-Garcia, Y., Mol, J. M. C., and Terryn, H. (2018). Mechanism of Passive Layer Formation on AA2024-T3 from Alkaline Lithium Carbonate Solutions in the Presence of Sodium Chloride. *J. Electrochem. Soc.* 165, C60–C70. doi:10.1149/2.1011802jes

Visser, P., Liu, Y., Terryn, H., and Mol, J. M. C. (2016). Lithium Salts as Leachable Corrosion Inhibitors and Potential Replacement for Hexavalent Chromium in Organic Coatings for the protection of Aluminum Alloys. *J. Coat. Technol. Res.* 13413, 557–566. doi:10.1007/s11998-016-9784-6

Visser, P., Marcoen, K., Trindade, G. F., Abel, M.-L., Watts, J. F., Hauffman, T., et al. (2019). The Chemical Throwing Power of Lithium-Based Inhibitors from Organic Coatings on AA2024-T3. *Corrosion Sci.* 150, 194–206. doi:10.1016/j.corsci.2019.02.009

Visser, P., Meeusen, M., Gonzalez-Garcia, Y., Terryn, H., and Mol, J. M. C. (2017). Electrochemical Evaluation of Corrosion Inhibiting Layers Formed in a Defect from Lithium-Leaching Organic Coatings. *J. Electrochem. Soc.* 164, C396–C406. doi:10.1149/2.1411707jes

Visser, P., Terryn, H., and Mol, J. M. C. (2019). Active Corrosion protection of Various Aluminium Alloys by Lithium-leaching Coatings. *Surf. Interf. Anal.* 51, 1276–1287. doi:10.1002/sia.6638

Visser, P., Terryn, H., and Mol, J. M. C. (2018). On the Importance of Irreversibility of Corrosion Inhibitors for Active Coating protection of AA2024-T3. *Corrosion Sci.* 140, 272–285. doi:10.1016/j.corsci.2018.05.037

Wu, D., Ma, L., Liu, B., Zhang, D., Minhas, B., Qian, H., et al. (2021). Long-term Deterioration of Lubricant-Infused Nanoporous Anodic Aluminium Oxide Surface Immersed in NaCl Solution. *J. Mater. Sci. Technol.* 64, 57–65. doi:10.1016/j.jmst.2019.12.008

Wu, D., Zhang, D., Ye, Y., Ma, L., Minhas, B., Liu, B., et al. (2019). Durable Lubricant-Infused Anodic Aluminum Oxide Surfaces with High-Aspect-Ratio Nanochannels. *Chem. Eng. J.* 368, 138–147. doi:10.1016/j.cej.2019.02.163

Yan, Y. M., Maltseva, A., Zhou, P., Li, X. J., Zeng, Z. R., Gharbi, O., et al. (2020). On the *In-Situ* Aqueous Stability of an Mg-Li-(Al-Y-Zr) alloy: Role of Li. *Corros. Sci.* 164, 1–36. doi:10.1016/j.corsci.2019.108342

Yang, J., Blawert, C., Lamaka, S. V., Snihirova, D., Lu, X., Di, S., et al. (2018). Corrosion protection Properties of Inhibitor Containing Hybrid PEO-Epoxy Coating on Magnesium. *Corrosion Sci.* 140, 99–110. doi:10.1016/j.corsci.2018.06.014

Yang, J., Di, S., Blawert, C., Lamaka, S. V., Wang, L., Fu, B., et al. (2018). Enhanced Wear Performance of Hybrid Epoxy-Ceramic Coatings on Magnesium Substrates. *ACS Appl. Mater. Inter.* 10, 30741–30751. doi:10.1021/acsami.8b10612

Yasakau, K. A., Zheludkevich, M. L., Lamaka, S. V., Lamaka, Mario. G. S. Ferreira., and Ferreira, M. G. S. (2006). Mechanism of Corrosion Inhibition of AA2024 by Rare-Earth Compounds. *J. Phys. Chem. B* 110, 5515–5528. doi:10.1021/jp0560664

Zaraska, L., Sulka, G. D., Szeremeta, J., and Jaskuła, M. (2010). Porous Anodic Alumina Formed by Anodization of Aluminum alloy (AA1050) and High Purity Aluminum. *Electrochimica Acta* 55, 4377–4386. doi:10.1016/j.electacta.2009.12.054

Zeng, D., Liu, Z., Bai, S., and Zhao, J. (2021). Preparation and Characterization of a Silane Sealed Peo Coating on Aluminum alloy. *Coatings* 11. doi:10.3390/coatings11050549

Zhang, F., Ju, P., Pan, M., Zhang, D., Huang, Y., Li, G., et al. (2018). Self-healing Mechanisms in Smart Protective Coatings: A Review. *Corrosion Sci.* 144, 74–88. doi:10.1016/j.corsci.2018.08.005

Zhang, G., Wu, L., Serdechnova, M., Tang, A., Wang, C., Blawert, C., et al. (2021). *In-situ* LDHs Growth on PEO Coatings on AZ31 Magnesium alloy for Active protection: Roles of PEO Composition and Conversion Solution. *J. Magnesium Alloys* 11, 1–14. doi:10.1016/j.jma.2021.09.001

Conflict of Interest: The authors declare that the research was conducted in the absence of any commercial or financial relationships that could be construed as a potential conflict of interest.

Publisher's Note: All claims expressed in this article are solely those of the authors and do not necessarily represent those of their affiliated organizations, or those of the publisher, the editors, and the reviewers. Any product that may be evaluated in this article, or claim that may be made by its manufacturer, is not guaranteed or endorsed by the publisher.

frontiers in Materials

ORIGINAL RESEARCH
published: 07 January 2022
doi: 10.3389/fmats.2021.820721

Microstructure Refinement on Crevice Corrosion of High-Speed Rail Steel U75V Visualized by an *In Situ* Monitoring System

Jian Wang[1,2,3], *Binbin Zhang*[1,2,4], *Weichen Xu*[1,2,4]*, *Jie Zhang*[1,2,4]*, *Lihui Yang*[1,2,4], *Zhongbo Peng*[3] and *Baorong Hou*[1,2,4]

[1]Key Laboratory of Marine Environmental Corrosion and Bio-Fouling, Institute of Oceanology, Chinese Academy of Sciences, Qingdao, China, [2]Open Studio for Marine Corrosion and Protection, Pilot National Laboratory for Marine Science and Technology (Qingdao), Qingdao, China, [3]School of Shipping and Naval Architecture, Chongqing Jiaotong University, Chongqing, China, [4]Center for Ocean Mega-Science, Chinese Academy of Sciences, Qingdao, China

Rail foot covered by a fastener will suffer from crevice corrosion, leading to thinning and localized attack of crevice interior posing a risk of failure. This work investigated crevice corrosion behavior of a typical pearlitic high-speed rail steel U75V, focusing for the first time on the effect of pearlitic microstructure refinement achieved by heat treatment with different cooling rates 2, 5, and 10°C/s. Under anodic polarization, localized dissolved spots presented on the as-received sample, where crevice corrosion mostly initiated from. For cooling rates 2 and 5°C/s, localized dissolved spots were also observed but crevice corrosion was mostly presented as general corrosion instead of from local spots, ascribed to enhanced tendency of uniform dissolution due to microstructure refinement and homogenization. For cooling rate 10°C/s, crevice corrosion expanded flocculently, ascribed to preferential dissolution of pearlitic nodules with entangled cementite due to over refinement. Crevice corrosion was obviously accelerated by microstructure refinement. Cooling rates 5 and 10°C/s led to the fastest and slowest expansion of the corroded area, respectively, while the corrosion depth was just the opposite based on the same amount of metal loss. This work provides important information regarding the effect of pearlitic microstructure refinement on crevice corrosion and introduces a facile method for *in situ* monitoring of crevice corrosion.

Keywords: microstructure, crevice corrosion, pearlite, cooling rate, U75V rail steel, interlamellar spacing

OPEN ACCESS

Edited by:
Changdong Gu,
Zhejiang University, China

Reviewed by:
Jichao Li,
the Ohio State University, United States
Liya Guo,
Shanghai University, China

***Correspondence:**
Weichen Xu
w.xu@qdio.ac.cn
Jie Zhang
zhangjie@qdio.ac.cn

Specialty section:
This article was submitted to Environmental Degradation of Materials, a section of the journal Frontiers in Materials

Received: *23 November 2021*
Accepted: *13 December 2021*
Published: *07 January 2022*

Citation:
Wang J, Zhang B, Xu W, Zhang J, Yang L, Peng Z and Hou B (2022) Microstructure Refinement on Crevice Corrosion of High-Speed Rail Steel U75V Visualized by an In Situ Monitoring System. Front. Mater. 8:820721. doi: 10.3389/fmats.2021.820721

INTRODUCTION

Rapid development of the high-speed railway industry requires high reliability and durability of materials. Wear, contact–impact, fatigue (or rolling contact fatigue, i.e., RCF), and corrosion are the main reasons for material degradation in rail tracks (Hernandez et al., 2007; Shurpali et al., 2012; Hernandez-Valle et al., 2013; Shariff et al., 2013; Safa et al., 2015; Zhao et al., 2015; Yazici and Yilmaz, 2018; Liu et al., 2019). Among these issues, corrosion attracts far less attention than the others while its damage is no less (Xu et al., 2021). This is because damage of materials caused by corrosion is unobservable from the beginning, but corrosion, especially localized corrosion, is usually an important precursor for accident or failure (Hill and Lillard, 2006; Li et al., 2017). Corrosion of rail tracks induces huge economic loss, and it has been reported that direct cost resulted from rail

track corrosion (railcar excluded), including replacement of corroded components, maintenance regarding corrosion mitigation, and application of corrosion protection technologies, was 18.88 billion RMB (Hou et al., 2017).

Corrosion occurred on the large surface of rails (e.g., on rail head, where wear and contact–impact are much more severe) is not crucial since it tends to develop into general corrosion instead of growing deep (Xu et al., 2021), and frequent contact between the rail and wheel inhibits the formation of an electrolyte layer as a precursor of localized corrosion. However, severe corrosion problems very often take place near the rail base and rail foot, resulting in thinning of specific section and instability of rail, thus inducing a potential risk of displacement, large stress, or even severe engineering failure (Xu et al., 2021). Due to the special structure between the fastener system and rail foot section, the crevice corrosion issue on the rail track has been reported by Panda et al. (2008), Panda et al. (2009) and has been recently investigated in details by the authors of this work, especially under conditions of varying gap size (Xu et al., 2022).

Pearlitic steels are widely applied as rail track steels due to their excellent mechanical properties, while the corrosion issue was usually overlooked (Hernandez et al., 2007). Microstructures strongly influence electrochemical dissolution behaviors (Haisch et al., 2002). The microstructure of various carbon steels has been studied, and the close relationship between pearlitic lamellar structure and initiation of localized corrosion was proposed (Clover et al., 2005), mostly stemmed from different electrochemical potentials between ferrite and cementite leading to galvanic coupling (Panda et al., 2008; Katiyar et al., 2018).

The microstructure of pearlite, especially interlamellar spacing, is closely related to corrosion resistance (Toribio and Ovejero, 2001; Katiyar et al., 2018; Wu et al., 2020). Ren et al. (2012) compared two kinds of pearlitic steels and found that smaller interlamellar spacing and more uniform structure resulted in higher resistance to atmospheric corrosion. Refinement of microstructure and the decrease of interlamellar spacing resulted in an improvement of polarization resistance and mechanical properties (toughness, strength, and hardness) and also a decrease of the corrosion rate (Panda et al., 2008; Katiyar et al., 2018), but further refinement led to entanglement of cementite lamellae and an increase of the corrosion rate (Katiyar et al., 2018). Ren (2012) also reported an increase of corrosion resistance due to the decrease of interlamellar spacing of pearlitic steels, and the dispersion degree (uniformity) of the interlamellar spacing was found to be inversely related to corrosion resistance. It seems that the lamellar structure of pearlite is often the weakness regarding corrosion (coarser structure generally resulted in lower localized corrosion resistance) (Al-Rubaiey et al., 2013). However, the appearance of pearlite was recently reported to act as a cathode and help suppress corrosion of a multi-phase rail steel (Neetu et al., 2021). Therefore, the effect of the pearlitic phase on corrosion depends on different factors, and a consistent conclusion cannot be simply drawn.

A study on crevice corrosion of pearlitic steel is very few. Preferential dissolution of pearlite nodules with larger interlamellar spacing between ferrite and cementite has been reported to initiate crevice corrosion and induce a corrosion defect with the sharp tip at the crevice interior, posing a risk of cracking (Xu et al., 2022). The boundary of ferrite and cementite has been observed to dissolve preferentially, resulting in threatening crack-like trenches (Murase et al., 2021). Moreover, localized (crevice) corrosion coupled with stress can potentially lead to cracking (Hernandez et al., 2009; Li et al., 2017; Li et al., 2020). Crevice corrosion of pearlitic steel was observed to start from oval-like spots ascribed to preferential dissolution of specific pearlitic nodules (Xu et al., 2022), while the effect of interlamellar spacing on the initiation and development of crevice corrosion of pearlitic steels is still unclear.

In this work, the effect of interlamellar spacing between ferrite and cementite lamellae on crevice corrosion behaviors of typical pearlitic high-speed rail track steel U75V has been investigated for the first time. Since crevice corrosion was usually difficult to be visualized, a self-made monitoring system was applied to observe initiation and development of crevice corrosion *in situ* under a transparent glass crevice former.

MATERIALS AND METHODS

Heat Treatment

U75V high-speed rail steel was cut into discs (diameter 6 mm) from the rail foot section. The chemical composition of as-received U75V steel is listed in **Table 1**. Variation of interlamellar spacing was obtained by heat treatment with different cooling processes. Heat treatments were performed by using a Gleeble-3500 thermal mechanical simulator (Dynamic Systems Inc.). U75V discs were heated from room temperature to 950°C in 5°C/s and kept for 10 min and then cooled to below 200°C at different cooling rates 2, 5, and 10°C/s.

After heat treatment, the disc surface was mirror polished until scratches were not observable via an optical microscope. The surface was etched by 4% nital for 4–6 s, washed with ethanol, and air-dried for further microstructural analysis.

Electrochemical Tests

U75V discs, after heat treatment, were welded with the electric cable and embedded in an epoxy resin with the exposed surface area of 0.283 cm^2. The surface was ground with SiC sand papers 600, 1,000, 1,500, 2,000, and 3,000 successively. Both crevice-free and crevice corrosion measurements were carried out.

For crevice-free tests, the samples were immersed in 0.1 M NaCl after grinding. Open circuit potential was always measured first until its change with time was less than 3 mV/min ($\Delta OCP/\Delta t < 3$ mV/min, ca. 40 min from the start of immersion), and then polarization tests were carried out. The electrochemical workstation Ivium Vertex.C.EIS (Ivium Technologies BV, The Netherlands) was used for all electrochemical tests. The reference electrode was a saturated calomel electrode (SCE), and the counter electrode was a platinum foil (2 cm × 2 cm) connected to a Teflon rod.

For crevice corrosion investigation, a self-designed device was applied for electrochemical tests and *in situ* monitoring of

TABLE 1 | Chemical composition (wt%) of U75V steel (the balance is Fe).

C	Si	Mn	P	S	Cr	Al	V	H	O	N
0.65–0.76	0.15–0.58	0.70–1.20	<0.030	<0.025	<0.15	<0.010	<0.030	<2e-4	<0.003	<0.009

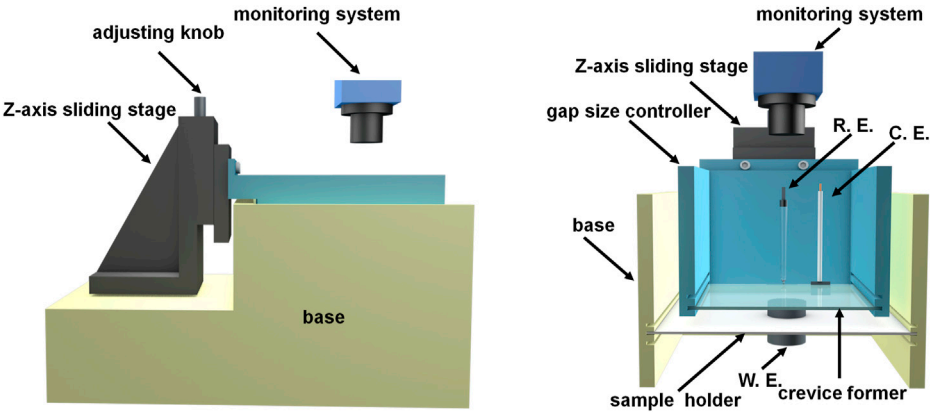

FIGURE 1 | Schematic diagram of the self-designed *in situ* monitoring device.

corrosion morphology development. A piece of transparent glass was used as a crevice former, fixed in a frame with grooves, and connected to a *Z*-axis sliding stage (with a micrometer) as a crevice gap size controller, so that the gap size can be adjusted as required. The combination of electrochemical methods and real-time corresponding images is important, so this device incorporated an optical system with a vertically placed Navitar microscope, coupled using a CCD camera connected to a computer. The lens was above the surface of the working electrode (working distance ca. 7 cm) and fixed on a stage which allowed movement in *X* and *Y* directions. A ring illuminator was fixed around the lens. The magnification was 50X–400X. A schematic diagram illustrating this device is shown in **Figure 1**. The disc samples were immersed in 0.1 M NaCl after grinding with a 50 μm crevice gap. Considering surface roughness and machining tolerance regarding the contact surface between the rail foot and fastener (Xu et al., 2021), a gap size of 50 μm is regarded as a reasonable value in this work. Similarly, open circuit potential was measured to achieve stable OCP ($\Delta OCP/\Delta t <$ 3 mV/min, ca. 50 min from the start of immersion), and polarization tests were carried out afterward when required.

Morphology Analysis

Besides the self-designed device, a scanning electron microscope (HITACHI Regulus 8100) was applied for corrosion morphology investigation after etching or electrochemical measurements. A 3D measuring laser scanning microscope (Olympus LEXT OLS5000) was applied after electrochemical tests, and LEXT analysis software was used for comparison of the surface profile.

RESULTS AND DISCUSSION

Metallographic Structure

The SEM micrographs of the etched surface of disc samples after heat treatment are shown in **Figure 2**. The interlamellar spacing was noticeably decreased with the increasing cooling rate, except that it was not as remarkable if 2 and 5°C/s are compared. Furthermore, the thickness of both ferrite lamella and cementite lamella was decreased after heat treatment and decreased with the increasing cooling rate.

Electrochemical Tests Under Crevice-Free Condition

After OCP was stabilized under free immersion conditions, four different samples were dynamically polarized in 0.1 M NaCl without crevice (anodic and cathodic polarizations were carried out separately; scan rate 0.1667 mV/s). From cathodic polarization curves (**Figure 3A**), the difference between four samples was not obvious except the difference on OCP, indicating similar behavior of oxygen reduction regardless of microstructure. From anodic polarization curves, there were noticeable differences in the weak polarization region (presenting a "shoulder" for AR, 2, and 10°C/s, while 5°C/s was less obvious due to its higher OCP) representing the early stage of anodic dissolution. According to the classic Evans diagram, when the cathodic reaction remains the same, OCP increases with the suppressed anodic reaction. Therefore, the anodic dissolution rate of samples related to the cooling rate 2 and 5°C/s in the early stage was lower than that of the as-received sample, while that for 10°C/s was the highest. This well agrees to Katiyar et al. (2018) who reported that refined microstructure was

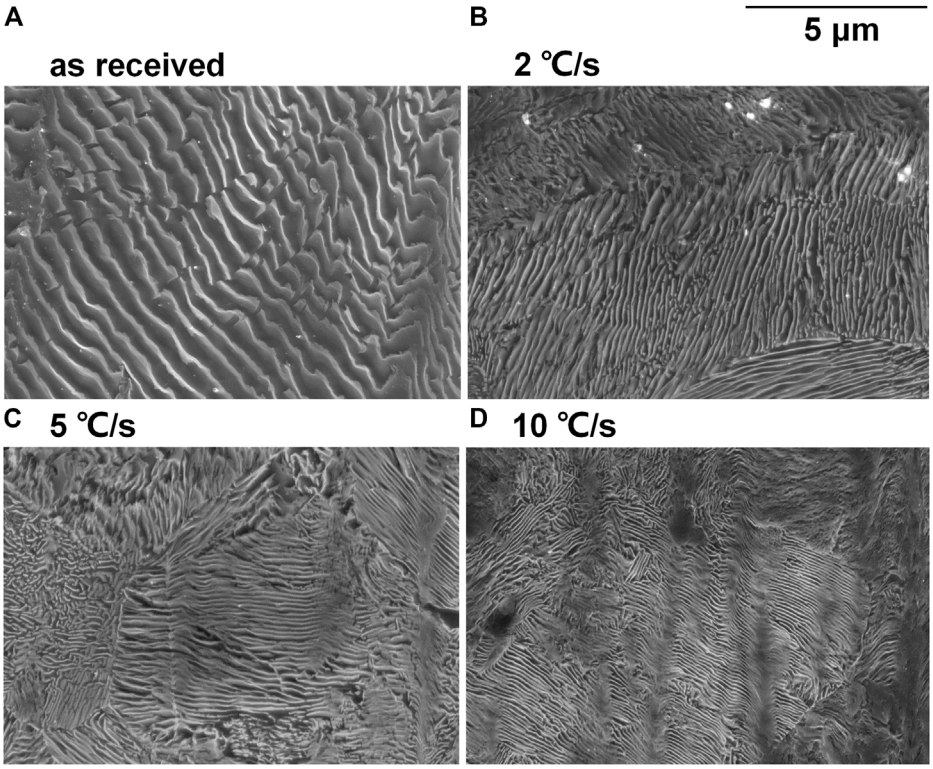

FIGURE 2 | SEM micrographs of the etched surface of the **(A)** as-received sample and the samples after heat treatment with cooling rates **(B)** 2°C/s, **(C)** 5°C/s, and **(D)** 10°C/s.

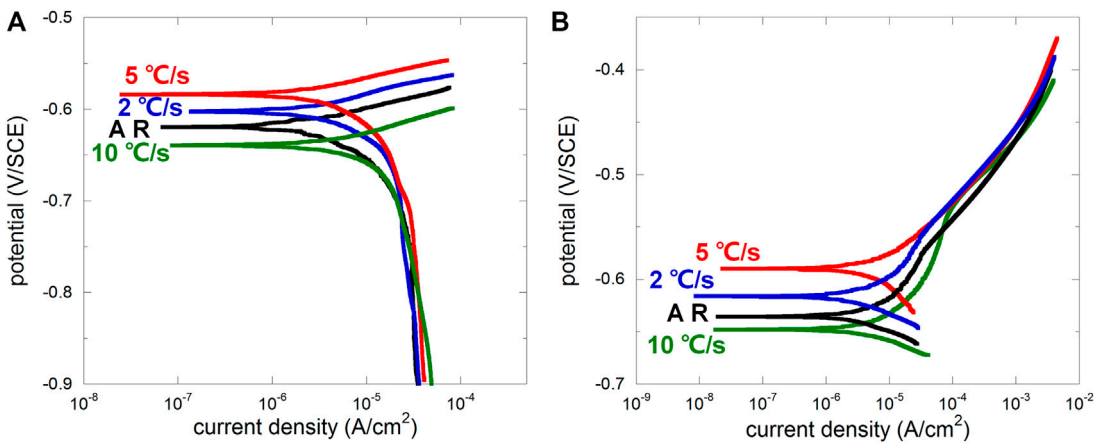

FIGURE 3 | Cathodic **(A)** and anodic **(B)** polarization curves of the as-received sample (AR) and the samples after heat treatment with cooling rates 2°C/s, 5°C/s, and 10°C/s.

helpful on decreasing the corrosion rate, but further refinement may lead to accelerated corrosion again. The development of corrosion morphology was very quick due to the absence of inhibition of metal ions diffusion, and the surface quickly turned dark for all four samples, making it difficult for taking successive macrographs of the changing surface.

Generally, the ferrite lamella acts anodically, and the cementite lamella acts cathodically (Murase et al., 2021). Interlamellar spacing distribution was usually scattered for the as-received sample (Ren, 2012), and corrosion usually initiated from pearlitic nodules with larger interlamellar spacing and larger area of ferrite lamellae (more local ferrite implies higher possibility to be locally dissolved under

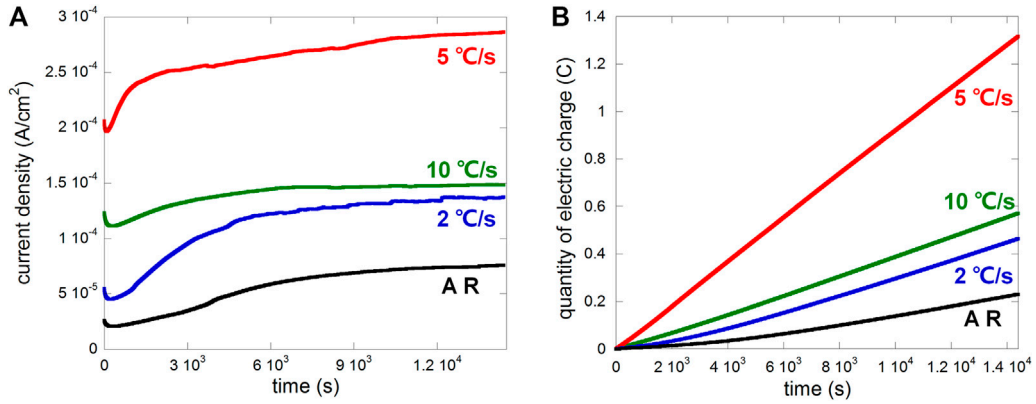

FIGURE 4 | Plots of **(A)** current density vs. time and **(B)** electric charge vs. time of different samples (AR, i.e., as-received, and samples after heat treatment with cooling rates 2°C/s, 5°C/s, and 10°C/s) anodically polarized at 0.15 V vs. OCP in 0.1 M NaCl with a 50 μm crevice gap.

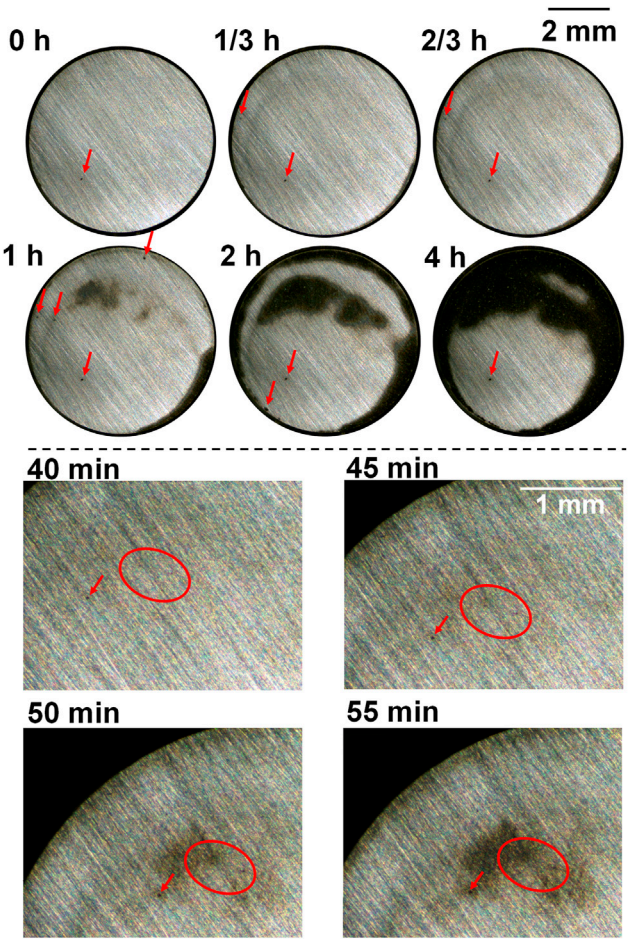

FIGURE 5 | Macrographs of the surface of the as-received sample presenting crevice corrosion development at 0.15 V vs. OCP in 0.1 M NaCl, taken by the self-designed device (lower part shows upper left of the surface).

both free immersion and anodic polarization conditions) (Xu et al., 2022). After microstructure refinement, interlamellar spacing distribution tended to be homogenized, decreasing the amount of potential anodic initiation sites, and thus the amount of pearlitic nodules contributing to the anodic current would be less, leading to increased OCP according to the Evans diagram. However, the over-high cooling rate may lead to entanglement of the cementite lamella (Katiyar et al., 2018), resulting in more disordered microstructure and more potential anodic initiation site. The cooling rate 10°C/s may be the case, raising the anodic branch and decreasing OCP according to the Evans diagram. This is further discussed regarding crevice corrosion behaviors in following sections.

Electrochemical Tests Under Crevice Corrosion Condition

The samples were anodically polarized in 0.1 M NaCl at a potential of 0.15 V vs. OCP with a 50 μm crevice gap after OCP stabilized. The plot of anodic current density vs. time is shown in **Figure 4A**, and the calculated electric charge (linearly representing metal loss) is shown in **Figure 4B**. Heat treatment obviously promoted the anodic current for crevice corrosion, especially after the cooling rate 5°C/s, while cooling rates 2 and 10°C/s were similar, consistently higher than that of the as-received sample.

The macrographs of the as-received sample and after heat treatment with cooling rates 2, 5, and 10°C/s, taken during the anodic polarization process shown in **Figure 4** using a self-designed *in situ* monitoring device (see **Figure 1**), are presented in **Figures 5–8** respectively, with some local sites compared. 0 h means the start point of anodic polarization after free immersion (stable OCP was achieved).

For the as-received sample (**Figure 5**), there were only a few spots that were preferentially dissolved at the end of free immersion (0 h). From the start of anodic polarization, more spots were gradually observed, which can be seen in the local sites presented in the lower part of **Figure 5** (showing upper left of

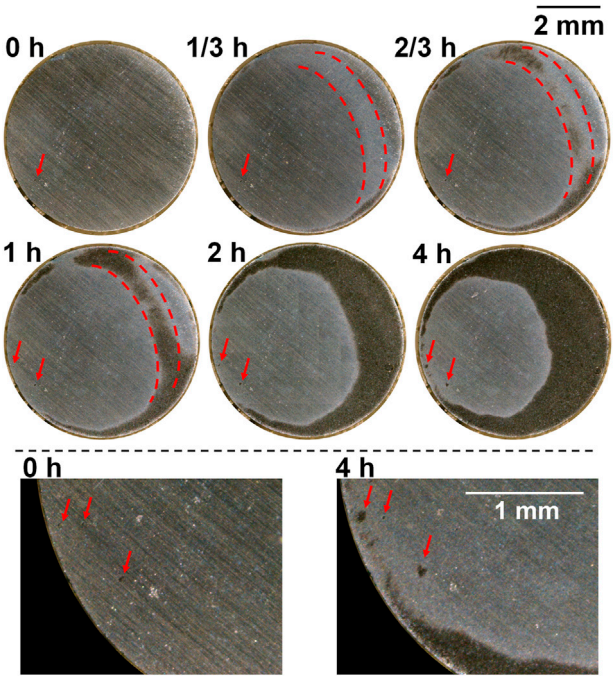

FIGURE 6 | Macrographs of the surface of the sample after heat treatment with the cooling rate 2°C/s presenting crevice corrosion development at 0.15 V vs. OCP in 0.1 M NaCl, taken by the self-designed device (lower part shows bottom left of the surface).

the sample surface), and these spots gradually developed into an enlarged dissolving area turning dark. This agrees to the previous work of the authors reporting the oval-like spots as initiation sites of crevice corrosion (Xu et al., 2022). There were corroded areas at the edge which was common for crevice corrosion because the diffusion of metal ions from the edge of crevice is the most readily. However, it is clearly noticed that some preferentially dissolved sites as shown in the lower part of **Figure 5** were neither at the edge nor at the center, but at some area between the edge and center, which was suggested to be ascribed to the combination effect of interfacial potential and local chloride and/or proton accumulation (Xu et al., 2022). In the end of polarization (4 h), coalescence of different dark areas took place, and some part was still not corroded.

For the sample after heat treatment with the cooling rate 2°C/s (**Figure 6**), a few preferentially dissolved spots were observed and expanded slightly during polarization (see the lower part of **Figure 6** showing bottom left of the sample surface), but newly formed spots during polarization was not clearly noticed. However, unlike the as-received sample, most of the dissolved area was not from these local spots, but from general corrosion on the relatively larger area (clearly shown on the macrograph taken at 1/3 h in the area marked by dashed red line), which turned light first and then dark. This area was also between the edge and center and coalesced with the edge area at the end.

For the sample after heat treatment with the cooling rate 5°C/s (**Figure 7**), preferentially dissolved spots were observed to be more than those observed in 2°C/s (**Figure 6**). The size of these spots did not grow noticeably till the end of anodic polarization, except that the periphery turned dark when the general corrosion area was about to cover the spots (see the lower part of **Figure 7** showing bottom left of the sample surface). Instead, the development of crevice corrosion was mainly based on general corrosion, and some preferentially dissolved spots presented at the end of free immersion (**Figure 7**, 0 h, marked with red arrows) were still observable at 1 h, although the dark-dissolved area already covered these spots, indicating small dissolved depth of general corrosion. After 2 h, the whole surface was totally dissolved, which was obviously faster than the other samples, also proved by metal loss shown in **Figure 4B**. In addition, a bubble was observed after 2/3 h which was believed to be hydrogen gas since the crevice interior was already acidified and interfacial potential should allow its formation.

For the sample after heat treatment with the cooling rate 10°C/s (**Figure 8**), preferentially dissolved spots were also observed, especially near the edge, and did not grow noticeably during polarization (see the lower part of **Figure 8** showing bottom left and right of the sample surface). In addition, newly formed spots were not observed during polarization. The dissolution behavior was totally different from that of the other samples. The dissolved area was neither initiated from formerly dissolved spots (**Figure 5**) nor like general corrosion (**Figures 6**, **7**); instead, it expanded from the edge to center flocculently (or reticularly).

Crevice corrosion behaviors of the four samples described previously under free immersion conditions were similar,

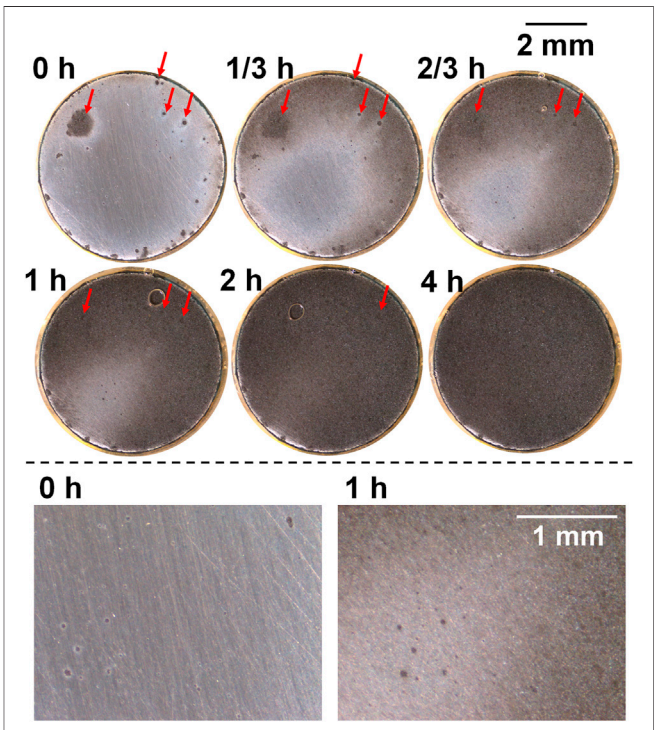

FIGURE 7 | Macrographs of the surface of the sample after heat treatment with cooling rate 5°C/s presenting crevice corrosion development at 0.15 V vs. OCP in 0.1 M NaCl, taken by the self-designed device (lower part shows bottom left of surface).

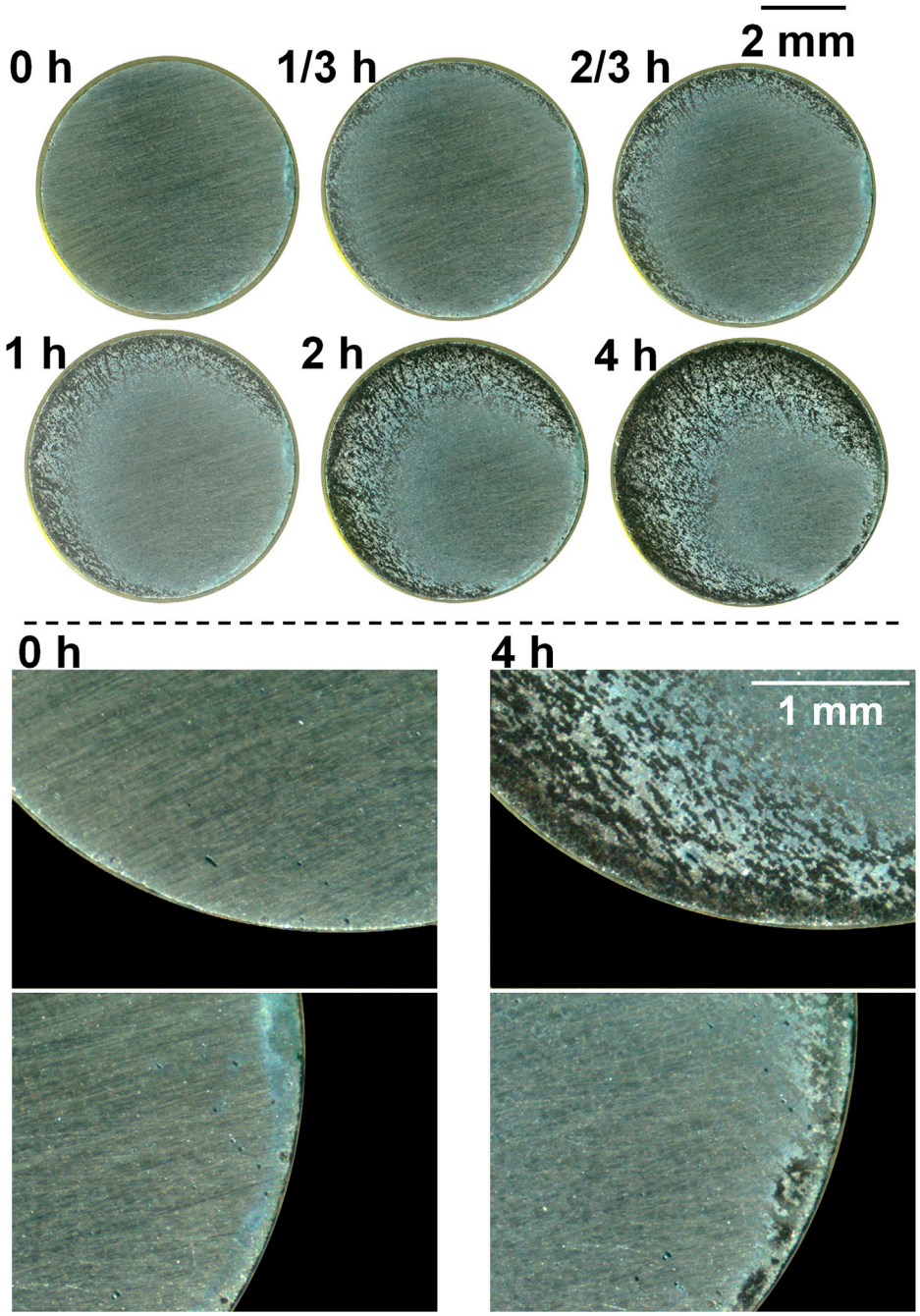

FIGURE 8 | Macrographs of the surface of the sample after heat treatment with the cooling rate 10°C/s presenting crevice corrosion development at 0.15 V vs. OCP in 0.1 M NaCl, taken by the self-designed device (lower part shows bottom left and right of the surface).

presented with preferentially dissolved local sites, but differed noticeably under anodic polarization conditions. The tendency of general corrosion within crevice for samples after heat treatment was largely due to the refinement of microstructure. Dissolution of cementite is a kinetic process, and its dissolution rate is much lower than that of ferrite under anodic polarization conditions (Xu et al., 2015; Xu et al., 2017). When the interlamellar spacing was large (as-received sample), preferentially dissolved ferrite was very likely to act as a local site for corrosion initiation, and dissolved ferrite was separated by adjacent cementite. If the interlamellar spacing was decreased, accompanied with thickness decrease of both ferrite and cementite lamellae, preferentially dissolved ferrite lamellae were more easily to coalesce because the distance between the ferrite lamella was

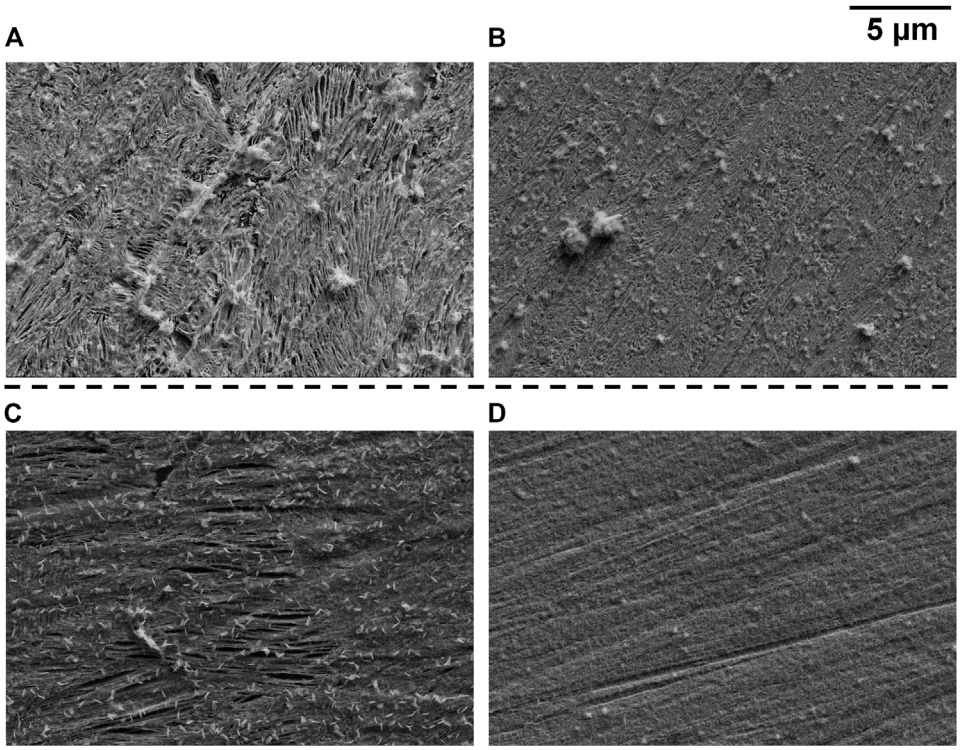

FIGURE 9 | SEM micrographs taken on samples after heat treatment with cooling rates 2°C/s [**(A)** fully dissolved/dark area; **(B)** boundary area] and 5°C/s [**(C)** fully dissolved/dark area; **(D)** boundary area].

decreased and thinner cementite lamellae were more easily to detach. Therefore, general corrosion more readily took place for refined microstructure.

Investigation on Micrographs Inside Crevice

Micrographs of some typical local sites after identical anodic polarization tests (crevice gap 50 μm) were obtained by SEM to further investigate crevice corrosion behaviors of different samples. During the expansion of the creviced area, there were basically three areas according to the macrographs shown previously, i.e., fully dissolved area (appeared dark), non-corroded area, and the boundary between the two (presented as light color before turning dark, clear in **Figures 6**, **7**). Therefore, SEM images of the fully dissolved area and boundary area of samples after heat treatment with cooling rates 2 and 5°C/s are shown in **Figure 9**. **Figure 9A** (fully dissolved area for 2°C/s) clearly shows the cementite skeleton due to preferential dissolution of ferrite. In the boundary area (**Figure 9B**), preferential dissolution of ferrite can also be observed but not as clear as **Figure 9A**; in addition, the scratches due to grinding still appear which is not presented in **Figure 9A**. Therefore, the generalized corrosion for 2°C/s was still based on preferential dissolution of ferrite. In comparison, **Figure 9C** (fully dissolved area for 5°C/s) does not show the typical pattern of the cementite skeleton but only some elongated cavity (ferrite lamella dissolution), and the scratches due to grinding can still be seen. The boundary area (**Figure 9D**) also does not show the typical pattern of the cementite skeleton. Therefore, the dissolution depth of 5°C/s was generally less than that of 2°C/s, although the expansion rate of the dissolved area (dark area) for 5°C/s was obviously higher than that of other samples (**Figures 5–8**). This is related to the observation that those dark spots formed during free immersion can still be seen even after the expanding corroded area crossing them (**Figure 7**, 1 h). The appearance of dark color on the dissolved area (observed in macrographs) was mainly due to cementite, either detached from the surface or remained as a skeleton, which has been reported before on localized corrosion of industrial pure iron (Xu et al., 2017) and carbon steel (Xu et al., 2019).

Figure 10 shows SEM images of the sample after heat treatment with the cooling rate 10°C/s. The flocculent dissolution behavior described regarding **Figure 8** is more clearly presented in **Figure 10A**. Corrosion depth was different on the surface leading to different heights. The higher part shows some elongated cavities which was probably due to ferrite dissolution, and scratches due to grinding can still be seen. In comparison, the lower part shows the cementite skeleton where scratches disappeared (**Figure 10B**). It has

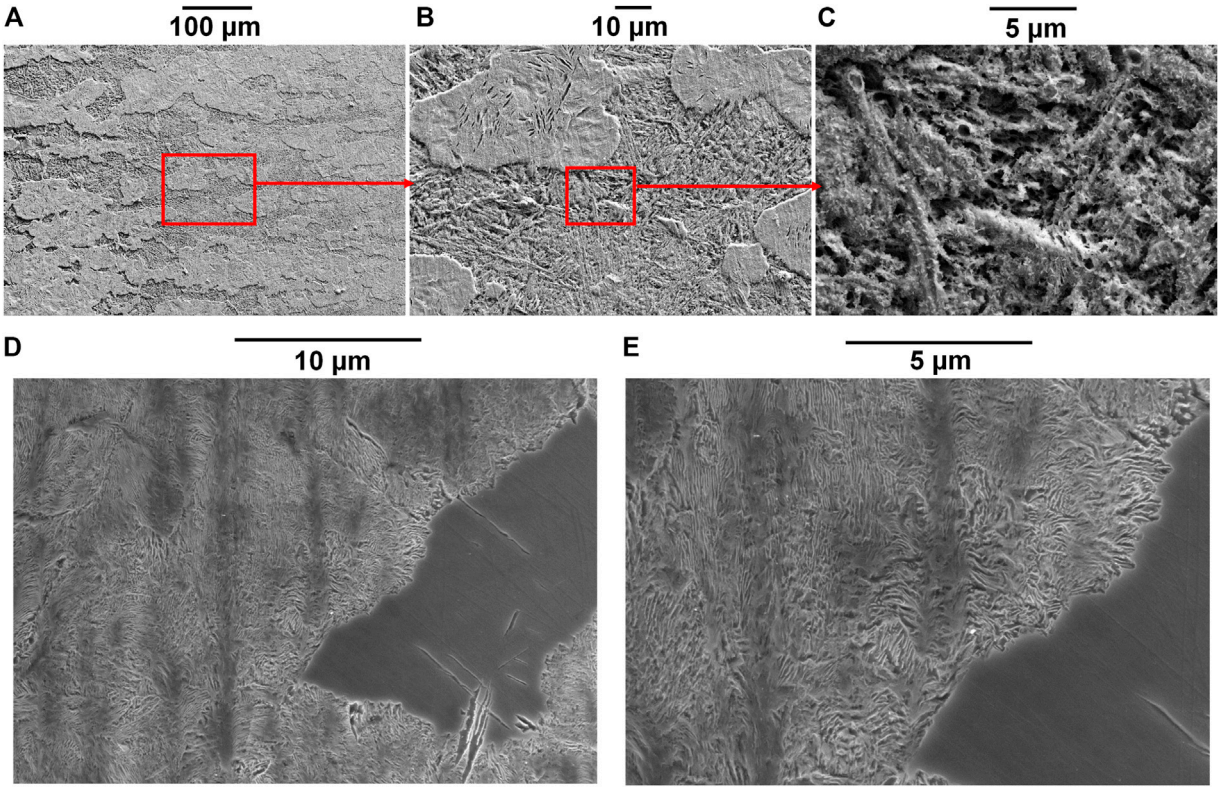

FIGURE 10 | SEM micrographs of samples after heat treatment with the cooling rate 10°C/s [**(A)** after anodic polarization at 0.15 V vs. OCP with a crevice gap of 50 μm; **(B)** magnification of A; **(C)** magnification of B; **(D)** etched surface of the same sample as **Figure 2D**; **(E)** magnification of D].

been suggested by Katiyar et al. (2018) that the over-high cooling rate of heat treatment on pearlitic steel may lead to entanglement of cementite lamellae (typical of quasi-pearlitic structure) which decreases polarization resistance. It agrees with our study, and the entanglement was observed in **Figure 10C**. This kind of entanglement may also lead to connection of different cementite lamellae separating ferrite, which is a type of less-ordered microstructure than that of typical pearlite, forming a "big cathode and small anode" in certain local sites. The pearlitic nodules with more entangled cementite lamella were preferentially dissolved while the less entangled remained, resulting in the special flocculent corrosion pattern. A similar phenomenon was also observed on the etched surface as shown in **Figure 10D**, where dissolved and less-dissolved areas are clearly presented. Entanglement of the cementite lamella is noticeable, especially near the boundary of dissolved and less-dissolved areas (**Figure 10E**).

By comparing the crevice-free and crevice corrosion behaviors, it is known that the two conditions did not agree with each other. Generally, microstructure refinement is able to improve corrosion resistance of pearlitic steel based on the literature (Ren, 2012; Ren et al., 2012; Al-Rubaiey et al., 2013; Katiyar et al., 2018). It is mostly ascribed to the microstructural homogenization [mainly regarding homogenous distribution of the micro-galvanic cell between the ferrite and cementite lamella (Katiyar et al., 2018)] ruling out less-ordered metallographic structure, which is often responsible for corrosion initiation. Corrosion normally initiates from local sites, and corrosion resistance can be improved due to statistically less initiation site. However, when it comes to crevice corrosion, an occlusive geometry increases corrosiveness of the crevice interior because steels are active in neutral NaCl and metal ions are inevitably dissolved and accumulated in crevice. Corrosion can take place auto-catalytically when the environment is corrosive enough, and refined microstructure alone is unable to effectively inhibit corrosion initiation. Homogenous microstructure tends to equalize corrosion initiating possibility of each local site on a certain region in which interfacial potential and chloride/proton distribution are almost homogenous. In this region, many tiny local sites (probably certain pearlitic nodules in the close range) have the equal possibility to be dissolved, which can quickly and easily coalesce before they can be observed as generalized dissolution of large area. In comparison, inhomogeneous microstructure results in preferential localized dissolution of bigger but more separated pearlitic nodules in a certain region even interfacial potential and chloride/proton distribution were homogenous in this region; so, the phenomenon of crevice corrosion initiating from some local spots can be more easily observed before it develops into dissolution of large area.

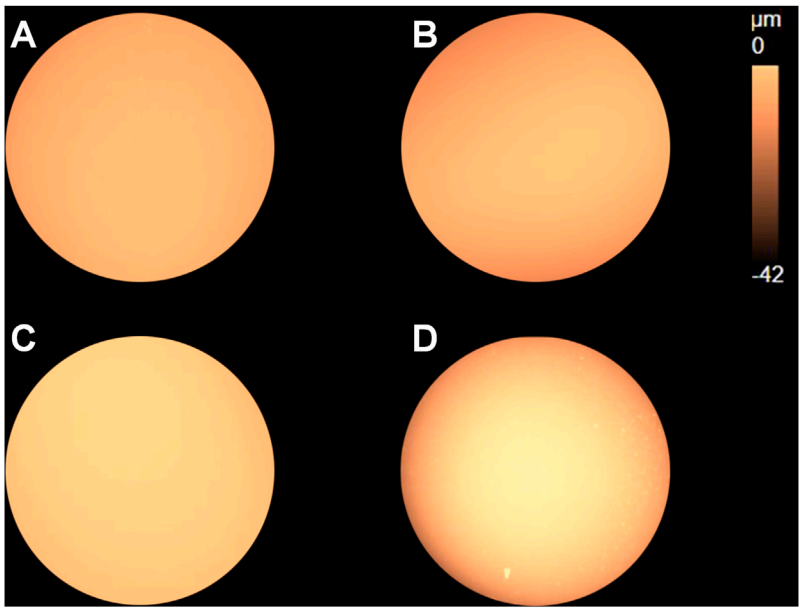

FIGURE 11 | Surface profile mappings of the **(A)** as-received sample and samples after heat treatment with cooling rates **(B)** 2°C/s, **(C)** 5°C/s, and **(D)** 10°C/s after anodic polarization at 0.15 V vs. OCP stopped when the electric charge reached 0.2 C.

Surface Profiles Based on the Same Amount of Metal Loss

Since the rate of metal loss varied substantially between different samples, surface profiles need to be compared based on the same amount of metal loss instead of time. According to **Figure 4B**, the electric charge 0.2°C was a reasonable value (the surface would not be completely dissolved for all four samples), so the potentiostatic polarization at 0.15 V vs. OCP was carried out on each of the four samples and stopped when the electric charge reached 0.2°C. The surface profile mappings presenting dissolution depth and height information are shown in **Figure 11**.

Distribution of the surface profile for the cooling rate 5°C/s appears to be uniform, indicating small dissolution depth. It agrees with the results shown in **Figures 7**, **9**, where preferentially dissolved local spots and scratches due to grinding were still observed, respectively, in the dissolved area. As to the sample regarding the cooling rate 10°C/s, the edge region of the disc clearly shows darker color, indicating large dissolution depth near the edge. In addition, flocculent dissolution behavior can also be observed since some bright spots appear in the darker region near the edge.

To show the difference more clearly, **Figure 12** presents surface profile data including sq (standard deviation of surface height, presenting the degree of surface height uniformity) and sz (maximum height difference between the peak and valley, representing the largest corrosion depth). The most uniform height distribution and smallest height difference between the peak and valley regarding the cooling rate 5°C/s should be resulted from small corrosion depth and generalized corrosion. In comparison, the least uniform height of the surface and biggest height difference between the peak and valley regarding the cooling rate 10°C/s should be resulted from the seriously corroded region near the edge, and the expansion of the dissolved area was slow (metal loss was mainly concentrated near the edge). This phenomenon was also observed in **Figure 8**, where the flocculently dissolved area was still near the edge until about 2 h (the whole surface was completely dissolved in 2 h as shown in **Figure 7**). The difference between the as-received sample and the sample after heat treatment with the cooling rate 2°C/s was negligible. It implies that the dissolved area based

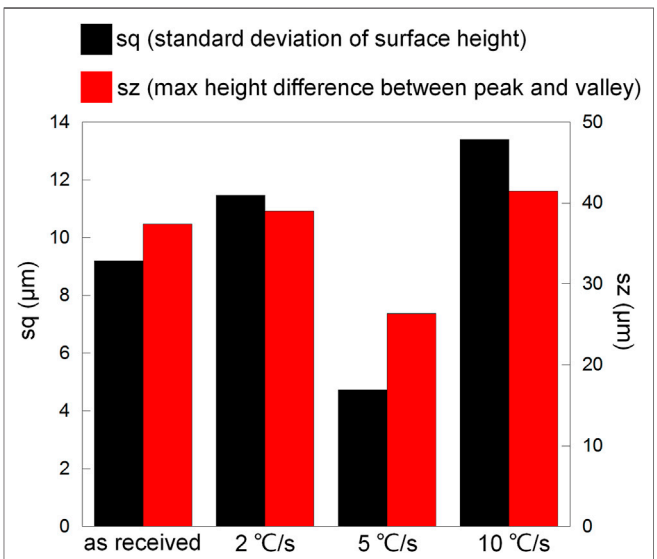

FIGURE 12 | Surface profile data (sq and sz) regarding **Figure 11**.

on the same amount of metal loss should be the biggest for 5°C/s and smallest for 10°C/s. Therefore, microstructure refinement tended to cause general corrosion of the whole crevice surface but further refinement led to corrosion concentrated near the crevice mouth (the edge).

Although microstructure refinement led to accelerated corrosion, it was mainly based on general corrosion with a small corrosion depth, which may cause uniform thinning of the rail foot. However, if microstructure is over refined, the corrosion rate was lowered but corrosion tended to be deep and non-uniform due to entangled cementite. The non-uniform dissolution area may act as a stress concentrator in the case of rail foot, suffering from strong downforce of the fastener. Therefore, although microstructure refinement is often applied for improvement of mechanical properties and corrosion resistance, one should be careful with the condition where crevice corrosion may occur.

CONCLUSION

The effect of pearlitic microstructure refinement (heat treatment with cooling rates 2, 5, and 10°C/s) on crevice corrosion has been studied on a typical high-speed rail steel U75V *via* facile *in situ* monitoring during electrochemical measurement. The main conclusions are as follows:

(1) The crevice corrosion rate increased after microstructure refinement, and the medium cooling rate 5°C/s resulted in the highest corrosion rate and expansion rate of the dissolved area.
(2) Dissolution of crevice interior developed from local spots for the as-received sample but tended to be generalized on the large area after microstructure refinement with cooling rates 2 and 5°C/s, ascribed to homogenization of pearlitic microstructure.
(3) Further refinement with the cooling rate 10°C/s resulted in entanglement of cementite, leading to preferential dissolution (appeared as flocculent expansion) on pearlitic nodules with entangled cementite. Dissolution largely concentrated on the preferentially dissolved region, lowering the expansion rate of the dissolved area.
(4) Based on the same amount of metal loss, uniformity of surface height was the highest and corrosion depth was the smallest for 5°C/s, while for 10°C/s it was vice versa..

DATA AVAILABILITY STATEMENT

The raw data supporting the conclusion of this article will be made available by the authors upon request, without undue reservation.

AUTHOR CONTRIBUTIONS

JW carried out most of the experimental work. BZ, WX, and JZ contributed to the conception and design of the study. WX wrote the draft of the manuscript and guided experimental work. LY and ZP helped on analysis of experimental data. BH helped on improvement of discussions in the manuscript. All authors contributed to manuscript revision and read and approved the submitted version.

FUNDING

This work was funded by the Shandong Provincial Natural Science Foundation, China (Grant No. ZR2019QEM011) and National Natural Science Foundation of China (Grant No. 41827805) and also supported by the Shandong Key Laboratory of Corrosion Science, China.

ACKNOWLEDGMENTS

The authors appreciate the help of Mr. Yu Deng on SEM analysis.

REFERENCES

Al-Rubaiey, S. I., Anoon, E. A., and Hanoon, M. M. (2013). The Influence of Microstructure on the Corrosion Rate of Carbon Steels. *Eng. Technol. J.* 31 (10), 1825–1836.

Clover, D., Kinsella, B., Pejcic, B., and De Marco, R. (2005). The Influence of Microstructure on the Corrosion Rate of Various Carbon Steels. *J. Appl. Electrochem.* 35 (2), 139–149. doi:10.1007/s10800-004-6207-7

Haisch, T., Mittemeijer, E. J., and Schultze, J. W. (2002). On the Influence of Microstructure and Carbide Content of Steels on the Electrochemical Dissolution Process in Aqueous NaCl-Electrolytes. *Mater. Corrosion* 53 (10), 740–755. doi:10.1002/1521-4176(200210)53:10<740:aid-maco740>3.0.co;2-j

Hernandez, F. C. R., Demas, N. G., Davis, D. D., Polycarpou, A. A., and Maal, L. (2007). Mechanical Properties and Wear Performance of Premium Rail Steels. *Wear* 263, 766–772. doi:10.1016/j.wear.2006.12.021

Hernandez, F. C. R., Plascencia, G., and Koch, K. (2009). Rail Base Corrosion Problem for North American Transit Systems. *Eng. Fail. Anal.* 16 (1), 281–294. doi:10.1016/j.engfailanal.2008.05.011

Hernandez-Valle, F., Edwards, R. S., Clough, A. R., Rosli, M. H., and Dutton, B. (2013). "Laser Generation and Detection for Surface Wave Interaction with Different Defect Geometries," in *Review of Progress in Quantitative Nondestructive Evaluation*. Editors D.O. Thompson and D.E. Chimenti (Melville: Amer Inst Physics), 32a and 32b, 324–329.

Hill, M. A., and Lillard, R. S. (2006). Methods for Accessing Pitting Damage in Carbon Steel Exposed to Alkaline Chloride Waste Environments. *Corrosion* 62 (9), 801–810. doi:10.5006/1.3278305

Hou, B., Li, X., Ma, X., Du, C., Zhang, D., Zheng, M., et al. (2017). The Cost of Corrosion in China. *Npj Mater. Degrad.* 1 (1), 4. doi:10.1038/s41529-017-0005-2

Katiyar, P. K., Misra, S., and Mondal, K. (2018). Effect of Different Cooling Rates on the Corrosion Behavior of High-Carbon Pearlitic Steel. *J. Materi Eng. Perform.* 27 (4), 1753–1762. doi:10.1007/s11665-018-3256-3

Li, Y., Guo, X., and Zhang, G. (2017). Synergistic Effect of Stress and Crevice on the Corrosion of N80 Carbon Steel in the CO 2 -Saturated NaCl Solution Containing Acetic Acid. *Corrosion Sci.* 123, 228–242. doi:10.1016/j.corsci.2017.05.005

Li, Y., Wang, X., and Zhang, G. (2020). Corrosion Behaviour of 13Cr Stainless Steel under Stress and Crevice in 3.5 wt.% NaCl Solution. *Corrosion Sci.* 163, 108290. doi:10.1016/j.corsci.2019.108290

Liu, J. P., Zhou, Q. Y., Zhang, Y. H., Liu, F. S., Tian, C. H., Li, C., et al. (2019). The Formation of Martensite during the Propagation of Fatigue Cracks in Pearlitic Rail Steel. *Mater. Sci. Eng. A* 747, 199–205. doi:10.1016/j.msea.2019.01.049

Murase, Y., Masuda, H., and Katayama, H. (2021). Corrosion Resistance of Finer/Coarser Pearlitic Structures of Carbon Steel. *J. Electrochem. Soc.* 168 (4), 041501. doi:10.1149/1945-7111/abf185

Neetu, V., Katiyar, P. K., Sangal, S., and Mondal, K. (2021). Effect of Various Phase Fraction of Bainite, Intercritical Ferrite, Retained Austenite and Pearlite on the Corrosion Behavior of Multiphase Steels. *Corrosion Sci.* 178, 109043. doi:10.1016/j.corsci.2020.109043

Panda, B., Balasubramaniam, R., and Dwivedi, G. (2008). On the Corrosion Behaviour of Novel High Carbon Rail Steels in Simulated Cyclic Wet-Dry Salt Fog Conditions. *Corrosion Sci.* 50 (6), 1684–1692. doi:10.1016/j.corsci.2008.02.021

Panda, B., Balasubramaniam, R., Mahapatra, S., and Dwivedi, G. (2009). Fretting and Fretting Corrosion Behavior of Novel Micro Alloyed Rail Steels. *Wear* 267 (9-10), 1702–1708. doi:10.1016/j.wear.2009.06.035

Ren, A. C., Zhou, H., Zhu, M., and Yuan, Z. X. (2012). Comparative Study on the Cyclic Corrosion Test of Rail Steel U68CuCr and U75V. *Adv. Mater. Res.* 616-618, 1059–1062. doi:10.4028/www.scientific.net/AMR.616-618.1059

Ren, A. (2012). PhD Thesis: Research on High-Strength and Corrosion Resistance Rail. PhD thesis. Wuhan: Wuhan University of Science and Technology.

Safa, M., Sabet, A., Ghahremani, K., Haas, C., and Walbridge, S. (2015). Rail Corrosion Forensics Using 3D Imaging and Finite Element Analysis. *Int. J. Rail Transportation* 3 (3), 164–178. doi:10.1080/23248378.2015.1054622

Shariff, S. M., Pal, T. K., Padmanabham, G., and Joshi, S. V. (2013). Influence of Chemical Composition and Prior Microstructure on Diode Laser Hardening of Railroad Steels. *Surf. Coat. Technol.* 228, 14–26. doi:10.1016/j.surfcoat.2013.03.046

Shurpali, A. A., Van Dam, E., Edwards, J. R., Lange, D. A., and Barkan, C. P. L. (2012). *Laboratory Investigation of the Abrasive Wear Mechanism of concrete Crosstie Rail Seat Deterioration (Rsd)*. New York: Amer Soc Mechanical Engineers.

Toribio, J., and Ovejero, E. (2001). Microstructure-Based Modelling of Localized Anodic Dissolution in Pearlitic Steels. *Mater. Sci. Eng. A* 319-321, 308–311. doi:10.1016/s0921-5093(01)01009-7

Wu, S., Liu, L., and Peng, J. (2020). Influence of Pearlite Interlamellar Spacing on Initial Corrosion of U71Mn Heavy Rail Steel. *Trans. Mater. Heat Treat.* 41 (11), 87–93. doi:10.13289/j.issn.1009-6264.2020-0209

Xu, W., Street, S. R., Amri, M., Mosselmans, J. F. W., Quinn, P. D., Rayment, T., et al. (2015). *In-Situ* Synchrotron Studies of the Effect of Nitrate on Iron Artificial Pits in Chloride Solutions. (Ii). On the Effect of Carbon. *J. Electrochem. Soc.* 162 (6), C243–C250. doi:10.1149/2.0591506jes

Xu, W., Rayment, T., and Davenport, A. (2017). The Effect of Carbon within Corrosion Pits of Iron in Chloride Solutions. *Corrosion Eng. Sci. Technol.* 52 (5), 383–390. doi:10.1080/1478422x.2017.1304618

Xu, W., Zhang, B., Yang, L., Li, T., and Li, Y. (2019). Liquid-Air Interface Corrosion of A537 Steel in High Level Liquid Radioactive Waste Simulant in a Sealed Container. *J. Electrochem. Soc.* 166 (2), C33–C41. doi:10.1149/2.0421902jes

Xu, W., Zhang, B., Deng, Y., Wang, Z., Jiang, Q., Yang, L., et al. (2021). Corrosion of Rail Tracks and Their protection. *Corrosion Rev.* 39 (1), 1–13. doi:10.1515/corrrev-2020-0069

Xu, W., Deng, Y., Zhang, B., Zhang, J., Peng, Z., Hou, B., et al. (Forthcoming 2022). Crevice Corrosion of U75V High-speed Rail Steel with Varying Crevice Gap Size by *In-Situ Monitoring. J. Mater. Res. Technol.* doi:10.1016/j.jmrt.2021.12.116

Yazici, O., and Yilmaz, S. (2018). Investigation of Effect of Various Processing Temperatures on Abrasive Wear Behaviour of High Power Diode Laser Treated R260 Grade Rail Steels. *Tribology Int.* 119, 222–229. doi:10.1016/j.triboint.2017.11.006

Zhao, X., Fan, Y., Liu, Y., Wang, H., and Dong, P. (2015). Evaluation of Fatigue Fracture Mechanism in a Flash Butt Welding Joint of a U75V Type Steel for railroad Applications. *Eng. Fail. Anal.* 55, 26–38. doi:10.1016/j.engfailanal.2015.05.001

Conflict of Interest: The authors declare that the research was conducted in the absence of any commercial or financial relationships that could be construed as a potential conflict of interest.

Publisher's Note: All claims expressed in this article are solely those of the authors and do not necessarily represent those of their affiliated organizations, or those of the publisher, the editors, and the reviewers. Any product that may be evaluated in this article, or claim that may be made by its manufacturer, is not guaranteed or endorsed by the publisher.

frontiers in Materials

ORIGINAL RESEARCH
published: 26 January 2022
doi: 10.3389/fmats.2022.839948

Eco-Friendly Anticorrosion Superhydrophobic Al_2O_3@PDMS Coating With Salt Deliquescence Self-Coalescence Behaviors Under High Atmospheric Humidity

Binbin Zhang[1,2,3], Jiayang Yan[1], Weichen Xu[1], Teng Yu[1], Zhuoyuan Chen[4] and Jizhou Duan[1,2,3]*

[1]CAS Key Laboratory of Marine Environmental Corrosion and Bio-fouling, Institute of Oceanology, Chinese Academy of Sciences, Qingdao, China, [2]Open Studio for Marine Corrosion and Protection, Pilot National Laboratory for Marine Science and Technology (Qingdao), Qingdao, China, [3]Center for Ocean Mega-Science, Chinese Academy of Sciences, Qingdao, China, [4]School of Materials Science and Hydrogen Energy, Foshan University, Foshan, China

Bio-inspired superhydrophobic coatings have been demonstrated to be promising anticorrosion materials. However, developing robust superhydrophobic coatings through simple one-step fluorine-free procedures to meet various functional requirements remains a major challenge. In this study, we fabricated an eco-friendly superhydrophobic Al_2O_3@PDMS composite coating with mechanical robustness based on Al_2O_3 NPs, PDMS, and spray coating technique. To characterize surface morphologies, chemical compositions, surface wettability, and anticorrosion properties, FE-SEM, EDS, XPS, contact angle meter, electrochemical impendence spectroscopy, and potentiodynamic polarization techniques were employed. The electrochemical results show that $|Z|_{0.01\ Hz}$ and R_{ct} values of the superhydrophobic Al_2O_3@PDMS coating were four orders of magnitude higher than bare Q235 carbon steel, indicating a significant improvement in corrosion resistance. Furthermore, the deliquescence behaviors of NaCl salt particles and the instantaneous self-coalescence phenomenon were recorded under high atmospheric humidity to suggest that a superhydrophobic surface with Cassie–Baxter interfacial contacts can serve as an efficient barrier to suppress the formation of saline liquid thin films and protect the underlying substrate from corrosion. This robust superhydrophobic Al_2O_3@PDMS coating is expected to be easily applied to a variety of substrates and to find potential applications for liquid repellency, self-cleaning, corrosion resistance, and other properties.

Keywords: anticorrosion, superhydrophobic, fluorine-free, salt deliquescence, atmospheric corrosion

OPEN ACCESS

Edited by:
Changdong Gu,
Zhejiang University, China

Reviewed by:
Sudagar J.,
VIT-AP University, India
Liang Wu,
Chongqing University, China

****Correspondence:***
Binbin Zhang
zhangbinbin11@mails.ucas.ac.cn

Specialty section:
This article was submitted to Environmental Degradation of Materials, a section of the journal Frontiers in Materials

Received: *20 December 2021*
Accepted: *10 January 2022*
Published: *26 January 2022*

Citation:
Zhang B, Yan J, Xu W, Yu T, Chen Z and Duan J (2022) Eco-Friendly Anticorrosion Superhydrophobic Al_2O_3@PDMS Coating With Salt Deliquescence Self-Coalescence Behaviors Under High Atmospheric Humidity. Front. Mater. 9:839948. doi: 10.3389/fmats.2022.839948

INTRODUCTION

Carbon steels are widely used for structural applications in industrial and engineering constructions because of their high specific strength, weldability, machinability, and low cost (Oguzie et al., 2010; Zhang S. et al., 2020; Tan et al., 2020). However, the aggressive nature of different service environments causes serious corrosion and degradation of exposed carbon

steels, resulting in massive economic loss and inevitable safety accidents. Extensive studies indicate that the use of multifunctional protective coatings is one of the most effective strategies for reducing the tendency of metallic corrosion (Ye et al., 2020; Panda et al., 2021). In recent years, the development of bio-inspired superhydrophobic coatings has become one of the anticorrosion research hot spots because it can provide a non-wetting physical barrier between the metallic surface and the surrounding environments (Du and Chen, 2020; Zhang ZQ et al., 2020; Jena et al., 2020; Darband et al., 2020; Zhang and Xu, 2021; Zhang ZQ et al., 2021; Zhang B et al., 2021).

Nature-inspired superhydrophobicity refers to the surface with a static water contact angle greater than 150° and a sliding angle less than 10° (Esmaeili et al., 2020). Micro-/nano-/binary rough structures and low surface energy are the two essential parameters for designing superhydrophobic materials. To develop superhydrophobic surfaces, a variety of technologies including chemical etching (Zhang et al., 2019b; Lan et al., 2021), anodization (Mokhtari et al., 2017; Zhang et al., 2019a), hydrothermal (Wang and Guo, 2018; Zhang B et al., 2021), and laser processing (Boinovich et al., 2018; Sataeva et al., 2020) have been introduced. Despite significant advances in scientific community, many limitations remain in large-scale fabrication and widespread practical applications, such as strict experimental conditions, complicated preparation procedures, and fluorine-containing toxic compounds (Anitha et al., 2018; Wang and Zhang, 2020). Given these concerns, it is particularly significant to design and develop facile one-step, low cost, and fluorine-free eco-friendly superhydrophobic coatings for efficient anticorrosion applications.

Thus, in this study, fluorine-free PDMS with intrinsic hydrophobicity and Al_2O_3 nanoparticles (Al_2O_3 NPs) were employed to design and fabricate the superhydrophobic Al_2O_3@PDMS composite coating through a facile one-step spray coating technique. The evolution of surface wettability with different Al_2O_3 NPs/PDMS mass ratios was investigated. The dynamic water droplet contacting process, surface morphologies, chemical compositions, anticorrosion properties, NaCl salt deliquescence behaviors, and mechanical stability were systematically studied. The results show that this substrate-independent superhydrophobic Al_2O_3@PDMS composite coating exhibits superior adaptability and corrosion suppression performance.

EXPERIMENTAL SECTION

Materials and Reagents

Q235 carbon steel substrates (size: 40 mm × 40 mm × 1 mm) were purchased from Shandong Shengxin Technology Co., Ltd. Hydrophilic aluminum oxide nanoparticles (Al_2O_3 NPs, 99.9%, 30 nm) were purchased from Shanghai Macklin Biochemical Co., Ltd. Polydimethylsiloxane (PDMS, Sylgard 184) and silicone elastomer curing agent were obtained from Dow Corning Corporation. Other reagents including n-hexane (C_6H_{14}, 97.0%), ethanol absolute (C_2H_6O, 99.7%), sodium chloride (NaCl, 99.5%), and methylene blue trihydrate ($C_{16}H_{18}ClN_3S{\cdot}3H_2O$, 99.5%) were supplied by Sinopharm Chemical Reagent Co., Ltd, and 3 M VHB tape was supplied by 3 M China Limited. Silicon carbide abrasive paper (2000 grit) was provided by Suisun Co., Ltd. All chemical reagents were used as received without further purification.

Fabrication of Superhydrophobic Al_2O_3@PDMS Coating

A total of 1 g PDMS, 0.1 g curing agent, and different amounts of Al_2O_3 NPs were ultrasonically and magnetically dissolved in 10 ml n-hexane to obtain a milk-like suspension. Different mass ratios of Al_2O_3 NPs/PDMS (1:4, 1:2, 3:4, 1:1, 5:4, and 3:2) were used to achieve Al_2O_3@PDMS composite coatings. Prior to the spray coating process, Q235 carbon steel substrates were sanded and cleaned with ethanol absolute solution. A spraying gun with a nozzle diameter of 1 mm and a spraying pressure of 0.3-MPa was employed for spray coating treatment. The spray-coated Al_2O_3 NPs/PDMS composite coatings were cured at 100°C for 1 h after spraying. Various substrates including glass, aluminum alloy, 3D foam material, polyurethane plastic, wood, filter paper, and concrete block were used to prepare superhydrophobic Al_2O_3@PDMS coating according to the same procedure of Q235 carbon steel. The schematic illustration of the preparation process of the superhydrophobic Al_2O_3@PDMS composite coating is shown in **Figure 1**.

Characterizations

The micro-/nano-morphologies of different samples were observed by using a field-emission scanning electron microscope (FE-SEM, FEI Nova Nano SEM450) equipped with energy-dispersive X-ray spectroscopy (EDS, Oxford X-MaxN50). X-ray photoelectron spectroscopy (XPS, Thermo Scientific Escalab 250Xi) was employed to analyze the chemical compositions of the fabricated superhydrophobic Al_2O_3@PDMS composite coating. The static water contact angles and sliding angles of Al_2O_3@PDMS composite coatings with different Al_2O_3/PDMS mass ratios were measured by a contact angle meter (Dataphysics OCA25) with 4 μL deionized water droplets.

Electrochemical Tests

The electrochemical tests of different samples were carried out using an electrochemical workstation (CorrTest CS2350H) in a typical three-electron cell. Platinum sheet, saturated calomel electrode, and testing samples were used as the counter electrode, the reference electrode, and the working electrode, respectively. The electrochemical impendence spectroscopy (EIS) and the potentiodynamic polarization of bare Q235 carbon steel and superhydrophobic Al_2O_3@PDMS composite coating were measured in 3.5 wt.% NaCl aqueous solution under open circuit potential with an amplitude of 10 mV. The testing

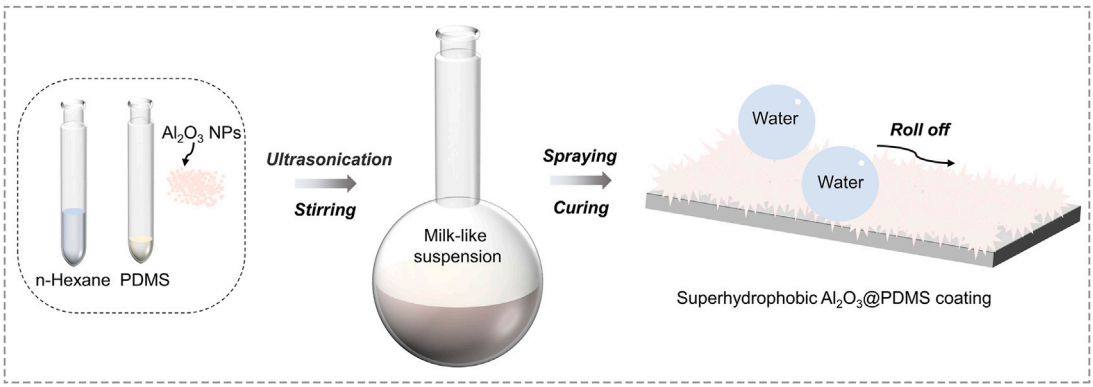

FIGURE 1 | Schematic illustration of the preparation procedure of the superhydrophobic Al_2O_3@PDMS composite coating.

frequency range of EIS is from 100 kHz to 10 mHz. The obtained EIS data were fitted with equivalent electrical circuit (EEC) using *Zsimwin* software. Potentiodynamic polarization curves were measured with respect to OCP in both the anodic and cathodic directions with a scanning speed of 0.167 mV/s. The corrosion current density (I_{corr}) and corrosion potential (E_{corr}) were calculated by extrapolating the linear portion of the curves with *CS Studio* software.

Mechanical Robustness Test

The mechanical robustness of the fabricated superhydrophobic Al_2O_3@PDMS composite coating was assessed using the tape-peeling test and sandpaper abrasion tests. The prepared superhydrophobic coating was pressed with 3 M tape loaded with 100 g for 30 s to ensure a uniform contact between the 3 M tape and coating for the tape-peeling test. After that, the 3 M tape was completely peeled away from the surface. This press-peeling process was defined as one testing cycle. The abrasion test was carried out by orienting the as-fabricated superhydrophobic coating toward the 2,000-grit sandpaper and placing a weight of 100 g on top of it. The superhydrophobic coating was then subjected to unidirectional drift with a speed of 1 cm/s. One abrasion cycle was defined as the reciprocating pulling of the sample in the horizontal direction over a distance of 20 cm. After various tape-peeling and sandpaper abrasion cycles, the water contact angles and sliding angels of the samples were measured using a contact angle meter.

RESULTS AND DISCUSSIONS

Surface Wettability

The surface wettability of spray-coated Al_2O_3@PDMS composite coatings was investigated to understand and validate the optimal parameters. **Figure 2** depicts the variation of water contact angles and sliding angles of Al_2O_3@PDMS composite coatings with

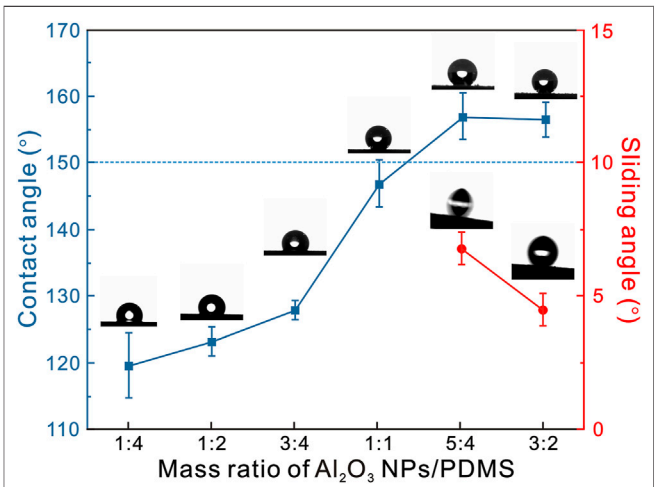

FIGURE 2 | Variation of water contact angles and sliding angles of the Al_2O_3@PDMS composite coatings with different Al_2O_3/PDMS mass ratios.

different Al_2O_3/PDMS mass ratios including 1:4, 1:2, 3:4, 1:1, 5:4, and 3:2. It can be seen that the water contact angles of the coatings gradually increased as the Al_2O_3/PDMS mass ratio increased. The contact angle of the Al_2O_3@PDMS composite coating was 119.6 ± 4.8°, 123.2 ± 2.2°, 127.9 ± 1.5°, and 146.9 ± 3.5°, corresponding to the Al_2O_3/PDMS mass ratios of 1:4, 1:2, 3:4, and 1:1, respectively. When the Al_2O_3/PDMS mass ratio is increased to 5:4, the water contact angle and sliding angle of the surface are 157.0 ± 3.5° and 6.7 ± 0.5°, respectively, displaying a typical superhydrophobic property. The water contact angle and the sliding angle are 156.5 ± 2.6° and 4.5 ± 0.5° when the Al_2O_3/PDMS mass ratio is 3:2. Surface superhydrophobicity was achieved through the combination of Al_2O_3 NP–induced roughness and low–surface energy PDMS molecules. The optimal Al_2O_3/PDMS mass ratio for developing superhydrophobic Al_2O_3@PDMS composite coating is 5:4, which was used to fabricate superhydrophobic samples for the characterizations and performance evaluations listed as follows.

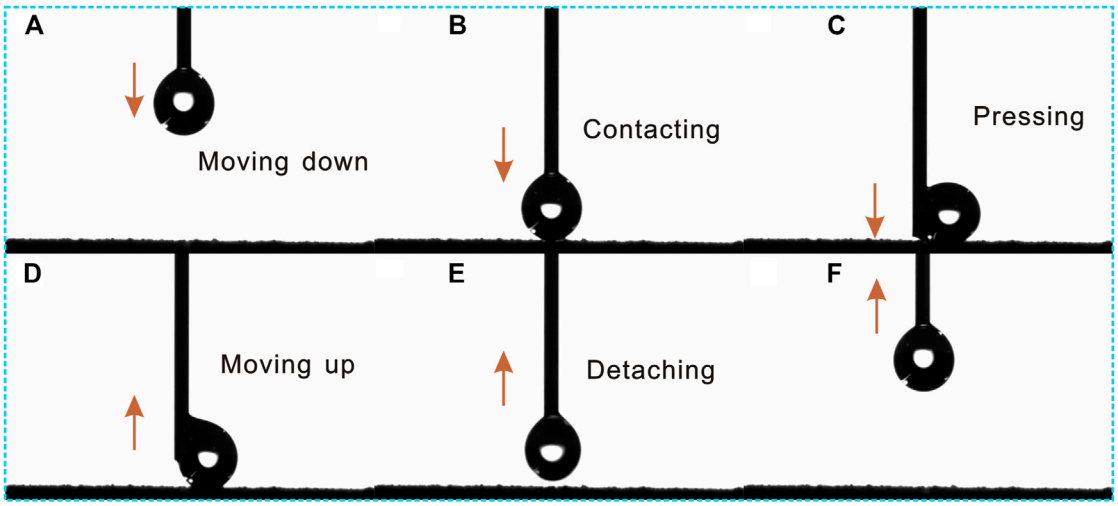

FIGURE 3 | (A–F) Dynamic contacting process of water droplet on the as-prepared superhydrophobic Al_2O_3@PDMS composite coating.

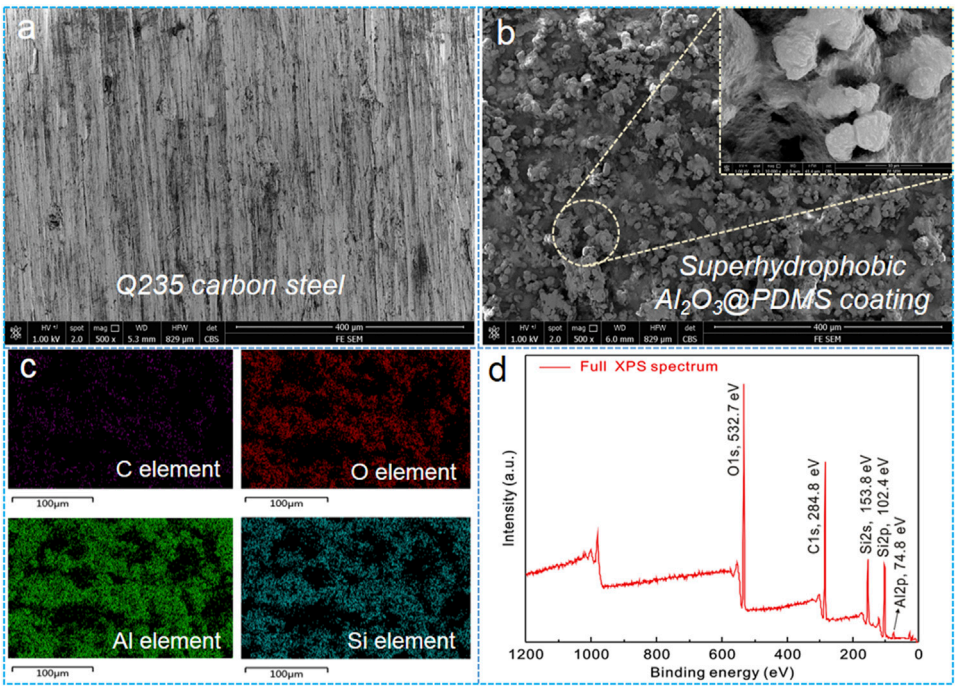

FIGURE 4 | (A,B) FE-SEM images of the bare Q235 carbon steel and the superhydrophobic Al_2O_3@PDMS coating, **(C)** EDS mappings, and **(D)** full XPS spectrum of the as-prepared superhydrophobic Al_2O_3@PDMS coating.

The dynamic contacting process of a water droplet on the as-prepared superhydrophobic Al_2O_3@PDMS composite coating is depicted in **Figure 3**. As the water droplet moves down from the microsyringe, it gradually closes and contacts with the as-prepared superhydrophobic Al2O3@PDMS composite coating (**Figures 3A,B**). As it is pressed further, the water droplet is pushed up and moved up along the neck of the microsyringe (**Figure 3C**). The water droplet detached and separated from the superhydrophobic Al_2O_3@PDMS coating as the microsyringe moved up, eventually hanging on the needlepoint of the microsyringe (**Figures 3D–F**). Throughout the dynamic process, the superhydrophobic surface remains non-wetting with no water traces remaining. As a result, the adhesion force between the superhydrophobic surface and the water droplet is

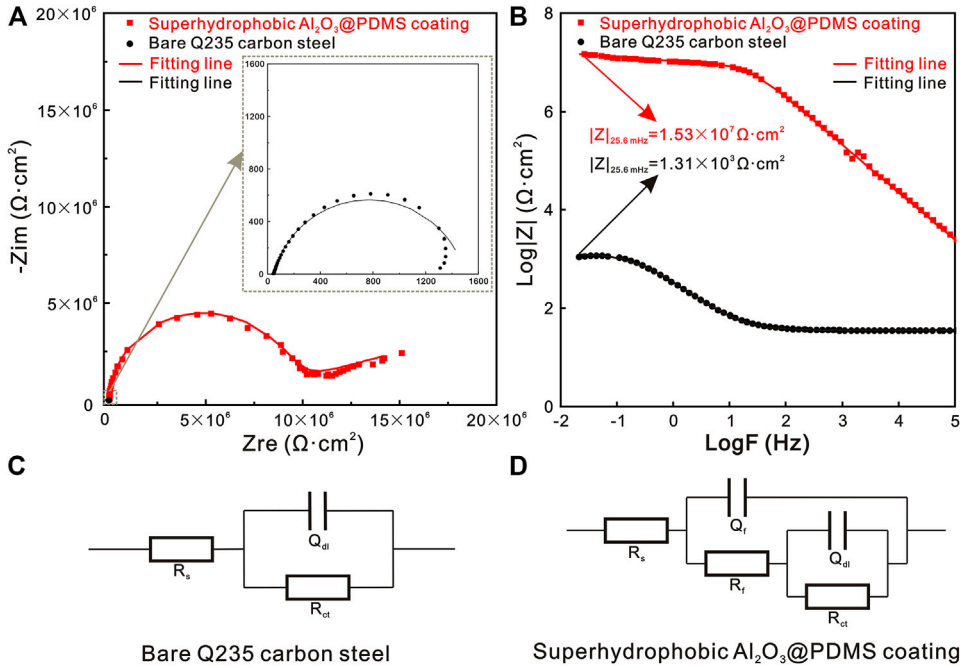

FIGURE 5 | (A) Nyquist plots, **(B)** Bode plots of log |Z| vs. log frequency, and **(C,D)** equivalent circuit models of the bare Q235 carbon steel and superhydrophobic Al_2O_3@PDMS coating.

extremely low, which contributes to the easy rolling behavior of liquids on the as-fabricated superhydrophobic Al_2O_3@PDMS coating.

Surface Morphologies and Chemical Compositions

FE-SEM, EDS, and XPS techniques were used to observe the micro-/nano-structures and chemical compositions of the samples. **Figures 4A,B** present the SEM images of the bare Q235 carbon steel and superhydrophobic Al_2O_3@PDMS coating. The surface morphology of bare Q235 carbon steel is relatively smooth, with few sandpaper polishing marks, while for the superhydrophobic Al_2O_3@PDMS coating (shown in **Figure 4B**), some micro-sized clusters and protrusions with nano-sized particles (**Figure 4B** inset) were packed on the coating surface, resulting in a remarkably improved surface roughness. Theses micro- and nano-hierarchical structures can trap air to form an extremely thin layer of air cushion. The air cushion can significantly reduce the contacting area between the superhydrophobic Al_2O_3@PDMS coating and water droplets, which is crucial for the non-wetting Cassie–Baxter air–liquid–solid contact. As a result, the water droplets barely penetrate the as-fabricated superhydrophobic Al_2O_3@PDMS coating, demonstrating stable water-repellent superhydrophobicity.

Besides, the two-dimensional EDS mapping result of the fabricated superhydrophobic Al_2O_3@PDMS coating is presented in **Figure 4C**. According to the EDS mappings, the C, O, Al, and Si elements of the spray-coated superhydrophobic Al_2O_3@PDMS coating showed a uniform distribution. **Figure 4D** shows the full XPS spectrum of the as-prepared superhydrophobic Al_2O_3@PDMS coating. In this elemental analysis, five peak signals of Al2p, Si2p, Si2s, C1s, and O1s can be clearly observed in the XPS survey at the binding energies of 74.8, 102.4, 153.8, 284.8, and 532.7 eV, respectively. The results of the elemental testing indicate that the Al_2O_3 NPs@PDMS composite coating with superhydrophobicity was successfully produced.

Anticorrosion Performance

The corrosion resistance behaviors of bare Q235 carbon steel and the as-prepared superhydrophobic Al_2O_3@PDMS coating in 3.5 wt.% NaCl aqueous solution were evaluated from the electrochemical points of view. Electrochemical impedance spectroscopy (EIS) is one of the most common techniques applied for the evaluation and analysis of the protective properties of coatings for metallic materials (Jeyaram et al., 2020; Mei et al., 2020). **Figure 5** presents the EIS plots and the equivalent circuit models of bare Q235 carbon steel and the superhydrophobic Al_2O_3@PDMS coating. **Figure 5A** and its inset image display the Nyquist plots of the Q235 carbon steel and superhydrophobic Al_2O_3@PDMS coating. The diameter of the capacitance arcs of the superhydrophobic Al_2O_3@PDMS coating is significantly larger than that of the bare Q235 carbon steel, demonstrating a superior anticorrosion properties. **Figure 5B** shows the Bode plots of log |Z| vs. log frequency of the Q235 carbon steel and superhydrophobic Al_2O_3@PDMS coating. The impedance modulus data at low frequency ($|Z|_{0.01\ Hz}$) are commonly used as an intuitive index of the anticorrosion

TABLE 1 | Electrochemical parameters for the EIS fitting results of bare Q235 carbon steel and superhydrophobic Al_2O_3@PDMS coating.

Parameter	Bare Q235 carbon steel	Superhydrophobic Al_2O_3@PDMS coating
R_s ($\Omega \cdot cm^2$)	43.4	32.5
Q_f ($\Omega^{-1} \cdot cm^{-2} \cdot s^{n1}$)	—	8.8×10^{-10}
n_1	—	0.97
R_f ($\Omega \cdot cm^2$)	—	8.4×10^3
Q_{dl} ($\Omega^{-1} \cdot cm^{-2} \cdot s^{n2}$)	4.5×10^{-4}	2.3×10^{-7}
n_2	0.84	0.79
R_{ct} ($\Omega \cdot cm^2$)	1.5×10^3	3.3×10^7

barrier performance of protective coatings (Mishra et al., 2020; Wiering et al., 2021). According to the Bode plots of log |Z| vs. log frequency, the $|Z|_{0.01\ Hz}$ of the superhydrophobic Al_2O_3@PDMS coating is $1.53 \times 10^7\ \Omega \cdot cm^2$, which is four orders of magnitude higher than bare Q235 carbon steel ($1.31 \times 10^3\ \Omega \cdot cm^2$), indicating that the superhydrophobic Al_2O_3@PDMS coating can lead to excellent corrosion protection properties.

To perform a quantitative comparison, the EIS data were fitted using equivalent circuit models. **Figures 5C,D** show the equivalent circuit model of the bare Q235 carbon steel and the superhydrophobic Al_2O_3@PDMS coating. The $R_s(Q_{dl}R_{ct})$ equivalent circuit model was used for the EIS fitting of bare Q235 carbon steel. R_s, Q_{dl}, and R_{ct} refer to solution resistance, constant phase element of the electric double layer, and charge transfer resistance at Q235 carbon steel/electrolyte interface, respectively. As a comparison, the $R_s\{Q_f[R_f(Q_{dl}R_{ct})]\}$ equivalent circuit model was employed for the as-prepared superhydrophobic Al_2O_3@PDMS coating, in which Q_f and R_f represent the constant phase element and film resistance of superhydrophobic Al_2O_3@PDMS coating, respectively. The corresponding fitting parameters are provided in **Table 1**. The lower Q_{dl} and higher R_{ct} values of the superhydrophobic Al_2O_3@PDMS coating suggest a conspicuously reduced corrosion rate.

Generally, a lower corrosion current density (I_{corr}) or a higher corrosion potential (E_{corr}) in a typical potentiodynamic polarization curve corresponds to a lower corrosion rate and higher corrosion resistance (Mishra and Balasubramaniam, 2004; Liu et al., 2016). **Figure 6** shows the potentiodynamic polarization curves of bare Q235 carbon steel and the as-prepared superhydrophobic Al_2O_3@PDMS coating in 3.5 wt.% NaCl aqueous solution. The corrosion potential (E_{corr}) and corrosion current density (I_{corr}) of the as-prepared superhydrophobic Al_2O_3@PDMS coating are −0.52 V and 3.74×10^{-10} A/cm^2, respectively, indicating a remarkable difference from that of the bare Q235 carbon steel (E_{corr} = −0.80 V, $I_{corr} = 4.66 \times 10^{-6}$ A/cm^2). The E_{corr} of the as-fabricated superhydrophobic Al_2O_3@PDMS coating shifted toward the positive direction by 0.27 V and the I_{corr} decreased by more than four orders of magnitude. The significant positive shift of the E_{corr} could be attributed to the improved protective performance of the as-fabricated superhydrophobic Al_2O_3@PDMS coating. The corresponding corrosion inhibition efficiency (η) could be calculated using the equation as follows (Liu et al., 2020; Ma et al., 2020):

$$\eta = \frac{I_{corr}^{bare} - I_{corr}^{coating}}{I_{corr}^{bare}} \times 100\%. \quad (1)$$

According to **Eq. 1**, the η value of the as-fabricated superhydrophobic Al_2O_3@PDMS coating was calculated to be 99.992%, supporting the conclusion that the spray-coated superhydrophobic Al_2O_3@PDMS coating provides an effective barrier for corrosion suppression.

Deliquescence Behaviors of NaCl Salt Particles

Atmospheric corrosion of metallic materials is a spontaneous degradation process resulting from interactions with its surrounding environment (Pei et al., 2020). More frequently, the atmospheric corrosion processes are initiated by surface wetting due to the moisture condensation and hygroscopic properties of salts and pollutants deposited on the surface (Koushik et al., 2021). Thus, understanding the interaction and relationship between NaCl salt particles and the atmospheric environment with high relative humidity remains a major challenge. To address this issue, the hygroscopic and deliquesce behaviors of single and double NaCl salt particles were investigated, as shown in **Figure 7**.

Figures 7A–D depict the deliquescence process of a single NaCl particle on a horizontally placed superhydrophobic Al_2O_3@PDMS coating in an atmospheric condition with 80 ± 2% relative humidity. Water vapor condensed on the surface of the solid NaCl particle during the deliquesce process, forming a saline solution. The solid NaCl particle was completely dissolved after deliquesce for 95 min, presenting a spherical saline liquid droplet. Owing to the liquid-repellent superhydrophobicity, the saline solution could not spread and wet the coating, resulting in a good protective performance against NaCl salt deliquesce–induced atmospheric corrosion attack. In addition, the deliquesce

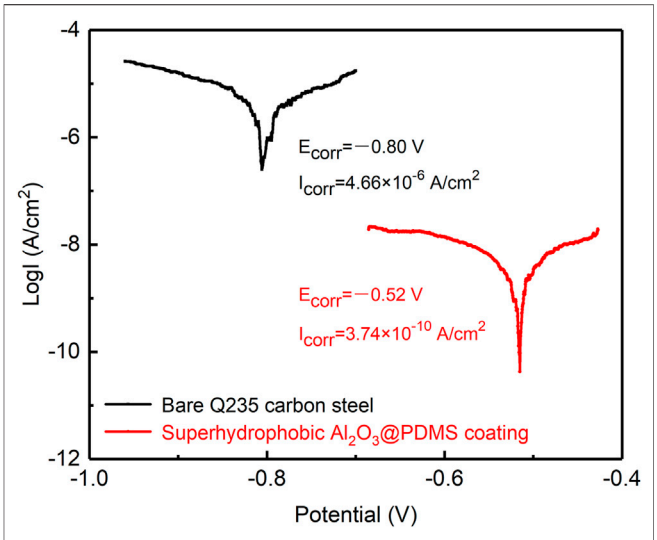

FIGURE 6 | Potentiodynamic polarization curves of the bare Q235 carbon steel and the as-prepared superhydrophobic Al_2O_3@PDMS coating with a scanning rate of 0.167 mV/s.

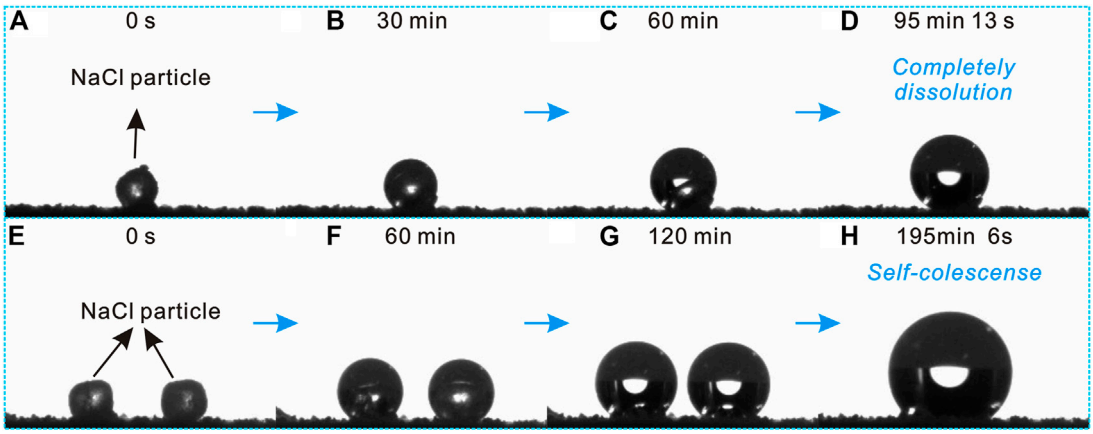

FIGURE 7 | Deliquescence behaviors of **(A–D)** single and **(E–H)** double NaCl salt particles on the prepared superhydrophobic Al_2O_3@PDMS coating under relative humidity environment of 80 ± 2%.

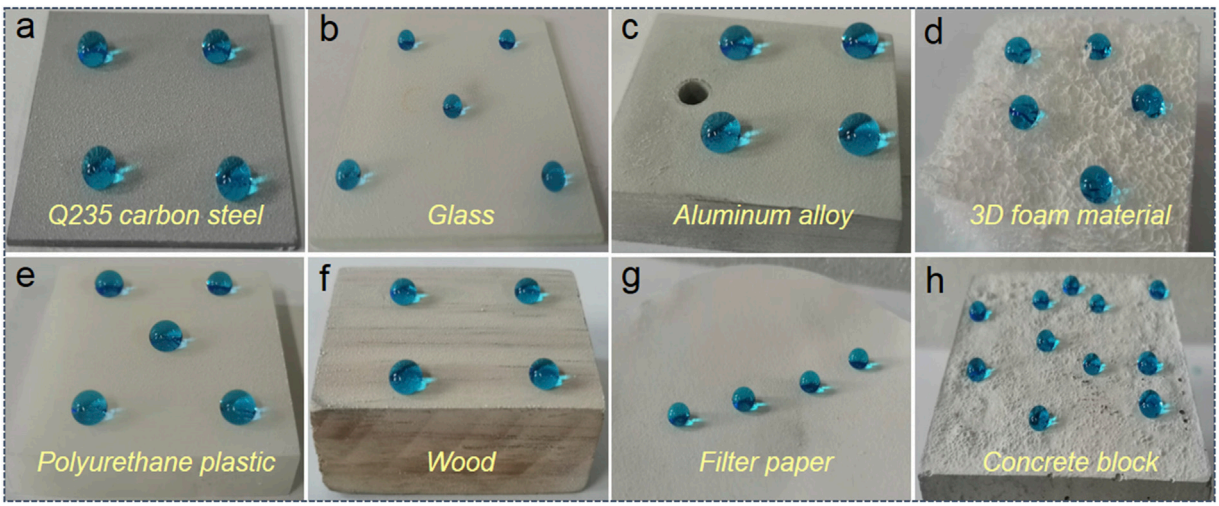

FIGURE 8 | Optical images of superhydrophobic Al_2O_3@PDMS coating on different substrates including **(A)** Q235 carbon steel, **(B)** glass, **(C)** aluminum alloy, **(D)** 3D foam material, **(E)** polyurethane plastic, **(F)** wood, **(G)** filter paper, and **(H)** concrete block.

behavior of double NaCl salt particles on the prepared superhydrophobic Al_2O_3@PDMS coating was first carried out and studied, as depicted in **Figures 7E–H**. At the beginning of the deliquescence process, the evolution of the double NaCl particles was similar to that of the single NaCl salt deliquesce. The solution film formed over the double NaCl particles, resulting in larger spherical droplets as deliquescence time passed. With the deliquescence time prolonged to 195 min 6 s (**Figure 7H**), it is worth noting that the two saline solution droplets self-coalesced instantaneously and eventually became a single saline droplet. The self-coalescence–induced salt deliquescence behavior of the as-fabricated superhydrophobic Al_2O_3@PDMS coating demonstrates that the Cassie–Baxter interfacial phase contacts of the superhydrophobic surface can serve as an efficient barrier to suppress the formation of thin saline liquid electrolyte film and protect the underlying substrate from being corroded under the atmospheric service environments with high relative humidity.

Adaptability and Mechanical Robustness

The adaptability of superhydrophobic coatings is critical for real-world applications. The preparation procedure should be adaptable to various substrates. To demonstrate the substrate-independent property of the as-fabricated superhydrophobic Al_2O_3@PDMS coating, eight typical substrates were used to study the large-scale adaptability performance, including Q235 carbon steel, glass, aluminum alloy, 3D foam material, polyurethane plastic, wood, filter paper, and concrete block. **Figures 8A–H** show the optical images of the spray-coated superhydrophobic Al_2O_3@PDMS coating on different substrates. The dyed blue water droplets maintained a spherical shape on each spray-coated substrate, illustrating a typical Cassie–Baxter

TABLE 2 | Water contact angles and sliding angles of the obtained superhydrophobic coating on different substrates.

Substrate	Contact angles	Sliding angles
Q235 carbon steel	157.0 ± 3.5°	6.7 ± 0.5°
Glass	156.2 ± 3.0°	5.4 ± 0.5°
Aluminum alloy	155.6 ± 2.5°	5.7 ± 1.0°
3D foam material	157.8 ± 2.0°	7.0 ± 0.5°
Polyurethane plastic	156.5 ± 3.0°	6.0 ± 1.0°
Wood	158.3 ± 2.5°	4.5 ± 1.5°
Filter paper	158.0 ± 3.0°	5.0 ± 2.0°
Concrete block	159.1 ± 3.5°	6.5 ± 1.0°

interfacial phase contact. The water contact angles and sliding angles of the obtained superhydrophobic coating on different substrates are presented in **Table 2**. The contact angles were all greater than 150° with sliding angles less than 8°, indicating excellent superhydrophobicity. It is noteworthy that the facile and substrate-independent spray coating method and the fluorine-free superhydrophobic Al_2O_3@PDMS coating will provide a suitable large-scale technique that can be easily applied to various substrates and has potential applications for water repellency, self-cleaning, corrosion resistance, and so on.

Mechanical robustness plays a key role for functional applications. Tape peeling and sandpaper abrasion tests are commonly conducted to evaluate the mechanical robustness and durability of superhydrophobic materials. **Figures 9A,B** present the variations of water contact angles and sliding angles of the superhydrophobic Al_2O_3@PDMS coating after different cycles in the tape peeling and sandpaper abrasion tests. After 32 tape peeling cycles, the as-prepared superhydrophobic Al_2O_3@PDMS coating remained its superhydrophobic property with a contact angle of 152.4 ± 2.2° and a sliding angle of 9.8 ± 0.6°. The sandpaper abrasion test was performed to confirm the mechanical durability. As shown in **Figure 9B**, the contact angles of the superhydrophobic Al_2O_3@PDMS coating decrease by only 5° after 20 abrasion cycles (i.e., 400 cm length) with a contact angle of 153.6 ± 1.8°. The results of the tape peeling and sandpaper abrasion tests show that the fabricated superhydrophobic Al_2O_3@PDMS coating possesses excellent mechanical robustness and durability. The cross-linked PDMS can firmly bind the Al_2O_3 NPs and contribute to the improvement of the mechanical strength of the coating.

CONCLUSION

In summary, eco-friendly and robust superhydrophobic Al_2O_3@PDMS coating was fabricated through a facile one-step substrate-independent spray coating approach without the use of hazardous fluorochemicals. The Al_2O_3 NP–induced micro-/nano-roughness and PDMS with low surface energy both contribute to the achievement of water-repellent superhydrophobicity. The optimal Al_2O_3/PDMS mass ratio for developing superhydrophobic Al_2O_3@PDMS composite coating is 5:4. The as-prepared superhydrophobic coating exhibits extremely low adhesion force between the water droplet and the solid surface. The $|Z|_{0.01\ Hz}$ value of Bode plots of the superhydrophobic Al_2O_3@PDMS coating is $1.53 \times 10^7\ \Omega{\cdot}cm^2$, which is four orders of magnitude higher than that of the bare Q235 carbon steel ($1.31 \times 10^3\ \Omega{\cdot}cm^2$), indicating excellent corrosion protection properties. Furthermore, the E_{corr} of the superhydrophobic Al_2O_3@PDMS coating shifted toward the positive direction by 0.27 V and the I_{corr} reduced by more than four orders of magnitude. The deliquescence behaviors of the single and double NaCl salt particles on the as-fabricated superhydrophobic Al_2O_3@PDMS coating present spherical saline droplets and instantaneous self-coalescence phenomenon, indicating that the Cassie–Baxter interfacial phase contacts of the superhydrophobic surface can serve as an efficient barrier to suppress the atmospheric corrosion in high relative humidity marine and industrial environments.

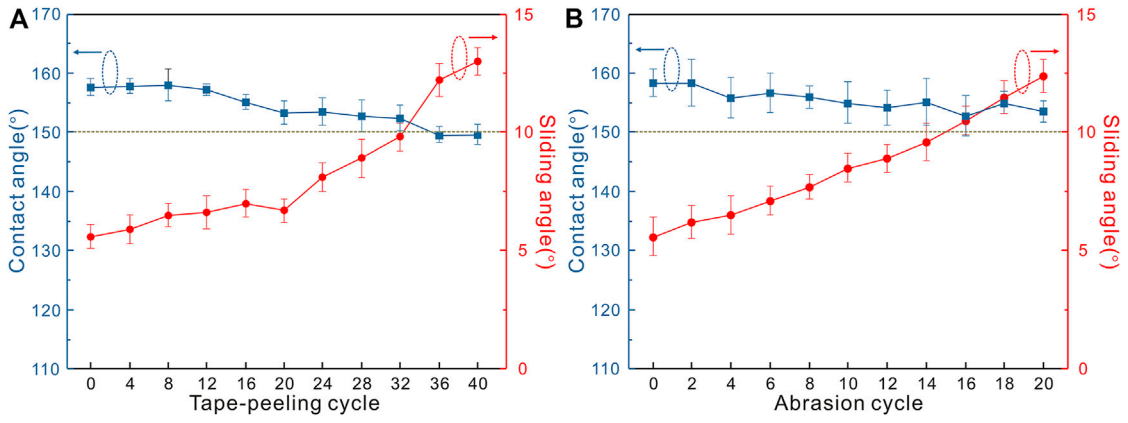

FIGURE 9 | Variations of water contact angles and sliding angles of the superhydrophobic Al_2O_3@PDMS coating after different **(A)** tape peeling and **(B)** sandpaper abrasion cycles.

DATA AVAILABILITY STATEMENT

The original contributions presented in the study are included in the article/Supplementary Material; further inquiries can be directed to the corresponding author.

AUTHOR CONTRIBUTIONS

BZ contributed to conceptualization, methodology, writing-original draft, funding acquisition, and supervision; JY contributed to data curation, formal analysis, and software; WX contributed to software; TY contributed to data curation; ZC contributed to writing—review and editing; and JD contributed to writing—review and editing. All authors have read and approved the submitted article version for publication.

ACKNOWLEDGMENTS

The authors acknowledge the financial supports from the Project of Innovation Development Joint Funds supported by the Shandong Provincial Natural Science Foundation (No. ZR2021LFG004); the Youth Innovation Promotion Association Chinese Academy of Sciences (No. 2021207); and the 2020 Open Projects (No. KLATM202006) of Key Laboratory of Advanced Technologies of Materials, Ministry of Education China, Southwest Jiaotong University.

REFERENCES

Anitha, C., Syed Azim, S., and Mayavan, S. (2018). Influence of Particle Size in Fluorine Free Corrosion Resistance Superhydrophobic Coating - Optimization and Stabilization of Interface by Multiscale Roughness. *J. Alloys Compd.* 765, 677–684. doi:10.1016/j.jallcom.2018.06.214

Boinovich, L. B., Emelyanenko, K. A., Domantovsky, A. G., and Emelyanenko, A. M. (2018). Laser Tailoring the Surface Chemistry and Morphology for Wear, Scale and Corrosion Resistant Superhydrophobic Coatings. *Langmuir* 34, 7059–7066. doi:10.1021/acs.langmuir.8b01317

Darband, G. B., Aliofkhazraei, M., Khorsand, S., Sokhanvar, S., and Kaboli, A. (2020). Science and Engineering of Superhydrophobic Surfaces: Review of Corrosion Resistance, Chemical and Mechanical Stability. *Arabian J. Chem.* 13, 1763–1802. doi:10.1016/j.arabjc.2018.01.013

Du, X. Q., and Chen, Y. (2020). Corrosion Inhibition by a Superhydrophobic Surface on Aluminum that Was Prepared with a Facile Electrochemical Route. *Mater. Res. Express* 7, 056405. doi:10.1088/2053-1591/ab9253

Esmaeili, A. R., Mir, N., and Mohammadi, R. (2020). A Facile, Fast, and Low-Cost Method for Fabrication of Micro/nano-Textured Superhydrophobic Surfaces. *J. Colloid Interf. Sci.* 573, 317–327. doi:10.1016/j.jcis.2020.04.027

Jena, G., Thinaharan, C., George, R. P., and Philip, J. (2020). Robust Nickel-Reduced Graphene Oxide-Myristic Acid Superhydrophobic Coating on Carbon Steel Using Electrochemical Codeposition and its Corrosion Resistance. *Surf. Coat. Techn.* 397, 125942. doi:10.1016/j.surfcoat.2020.125942

Jeyaram, R., Elango, A., Siva, T., Ayeshamariam, A., and Kaviyarasu, K. (2020). Corrosion protection of Silane Based Coatings on Mild Steel in an Aggressive Chloride Ion Environment. *Surf. Inter.* 18, 100423. doi:10.1016/j.surfin.2019.100423

Koushik, B. G., Van den Steen, N., Mamme, M. H., Van Ingelgem, Y., and Terryn, H. (2021). Review on Modelling of Corrosion under Droplet Electrolyte for Predicting Atmospheric Corrosion Rate. *J. Mater. Sci. Techn.* 62, 254–267. doi:10.1016/j.jmst.2020.04.061

Lan, X., Zhang, B., Wang, J., Fan, X., and Zhang, J. (2021). Hydrothermally Structured Superhydrophobic Surface with superior Anti-corrosion, Anti-bacterial and Anti-icing Behaviors. *Colloids Surf. A Physicochem. Eng. Aspects* 624, 126820. doi:10.1016/j.colsurfa.2021.126820

Liu, W., Xu, Q., Han, J., Chen, X., and Min, Y. (2016). A Novel Combination Approach for the Preparation of Superhydrophobic Surface on Copper and the Consequent Corrosion Resistance. *Corrosion Sci.* 110, 105–113. doi:10.1016/j.corsci.2016.04.015

Liu, X., Zhang, T. C., He, H., Ouyang, L., and Yuan, S. (2020). A Stearic Acid/CeO2 Bilayer Coating on AZ31B Magnesium alloy with Superhydrophobic and Self-Cleaning Properties for Corrosion Inhibition. *J. Alloys Compd.* 834, 155210. doi:10.1016/j.jallcom.2020.155210

Ma, Y., Fan, B., Liu, H., Fan, G., Hao, H., and Yang, B. (2020). Enhanced Corrosion Inhibition of Aniline Derivatives Electropolymerized Coatings on Copper: Preparation, Characterization and Mechanism Modeling. *Appl. Surf. Sci.* 514, 146086. doi:10.1016/j.apsusc.2020.146086

Mei, D., Lamaka, S. V., Lu, X., and Zheludkevich, M. L. (2020). Selecting Medium for Corrosion Testing of Bioabsorbable Magnesium and Other Metals - A Critical Review. *Corrosion Sci.* 171, 108722. doi:10.1016/j.corsci.2020.108722

Mishra, R., and Balasubramaniam, R. (2004). Effect of Nanocrystalline Grain Size on the Electrochemical and Corrosion Behavior of Nickel. *Corrosion Sci.* 46, 3019–3029. doi:10.1016/j.corsci.2004.04.007

Mishra, P., Yavas, D., Bastawros, A. F., and Hebert, K. R. (2020). Electrochemical Impedance Spectroscopy Analysis of Corrosion Product Layer Formation on Pipeline Steel. *Electrochim. Acta* 346, 136232. doi:10.1016/j.electacta.2020.136232

Mokhtari, S., Karimzadeh, F., Abbasi, M. H., and Raeissi, K. (2017). Development of Super-hydrophobic Surface on Al 6061 by Anodizing and the Evaluation of its Corrosion Behavior. *Surf. Coat. Techn.* 324, 99–105. doi:10.1016/j.surfcoat.2017.05.060

Oguzie, E. E., Enenebeaku, C. K., Akalezi, C. O., Okoro, S. C., Ayuk, A. A., and Ejike, E. N. (2010). Adsorption and Corrosion-Inhibiting Effect of *Dacryodis Edulis* Extract on Low-Carbon-Steel Corrosion in Acidic media. *J. Colloid Interf. Sci.* 349, 283–292. doi:10.1016/j.jcis.2010.05.027

Panda, J. N., Wong, B. C., Medvedovski, E., and Egberts, P. (2021). Enhancement of Tribo-Corrosion Performance of Carbon Steel through Boronizing and BN-Based Coatings. *Tribology Int.* 153, 106666. doi:10.1016/j.triboint.2020.106666

Pei, Z., Zhang, D., Zhi, Y., Yang, T., Jin, L., Fu, D., et al. (2020). Towards Understanding and Prediction of Atmospheric Corrosion of an Fe/Cu Corrosion Sensor via Machine Learning. *Corrosion Sci.* 170, 108697. doi:10.1016/j.corsci.2020.108697

Sataeva, N. E., Boinovich, L. B., Emelyanenko, K. A., Domantovsky, A. G., and Emelyanenko, A. M. (2020). Laser-assisted Processing of Aluminum alloy for the Fabrication of Superhydrophobic Coatings Withstanding Multiple Degradation Factors. *Surf. Coat. Techn.* 397, 125993. doi:10.1016/j.surfcoat.2020.125993

Tan, J., Guo, L., Yang, H., Zhang, F., and El Bakri, Y. (2020). Synergistic Effect of Potassium Iodide and Sodium Dodecyl Sulfonate on the Corrosion Inhibition of Carbon Steel in HCl Medium: a Combined Experimental and Theoretical Investigation. *RSC Adv.* 10, 15163–15170. doi:10.1039/D0RA02011G

Wang, F., and Guo, Z. (2018). Insitu Growth of Durable Superhydrophobic Mg-Al Layered Double Hydroxides Nanoplatelets on Aluminum Alloys for Corrosion Resistance. *J. Alloys Compd.* 767, 382–391. doi:10.1016/j.jallcom.2018.07.086

Wang, C.-X., and Zhang, X.-F. (2020). A Non-particle and Fluorine-free Superhydrophobic Surface Based on One-step Electrodeposition of Dodecyltrimethoxysilane on Mild Steel for Corrosion protection. *Corrosion Sci.* 163, 108284. doi:10.1016/j.corsci.2019.108284

Wiering, L., Qi, X., and Battocchi, D. (2021). Corrosion Performance of High-Temperature Organic Coatings Subjected to Heat Treatments. *Prog. Org. Coat.* 159, 106418. doi:10.1016/j.porgcoat.2021.106418

Ye, Y., Chen, H., Zou, Y., Ye, Y., and Zhao, H. (2020). Corrosion Protective Mechanism of Smart Graphene-Based Self-Healing Coating on Carbon Steel. *Corrosion Sci.* 174, 108825. doi:10.1016/j.corsci.2020.108825

Zhang, B., Xu, W., Zhu, Q., Sun, Y., and Li, Y. (2019a). Mechanically Robust Superhydrophobic Porous Anodized AA5083 for marine Corrosion protection. *Corrosion Sci.* 158, 108083. doi:10.1016/j.corsci.2019.06.031

Zhang, B., Xu, W., Zhu, Q., Yuan, S., and Li, Y. (2019b). Lotus-inspired Multiscale Superhydrophobic AA5083 Resisting Surface Contamination and marine Corrosion Attack. *Materials* 12, 1592. doi:10.3390/ma12101592

Zhang B, B., Wang, J., and Zhang, J. (2020). One-pot Fluorine-free Superhydrophobic Surface towards Corrosion Resistance and Water Droplet Bouncing. *Mater. Corrosion* 71, 2011–2020. doi:10.1002/maco.202011787

Zhang S, S., Hou, L., Du, H., Wei, H., Liu, B., and Wei, Y. (2020). A Study on the Interaction between Chloride Ions and CO2 towards Carbon Steel Corrosion. *Corrosion Sci.* 167, 108531. doi:10.1016/j.corsci.2020.108531

Zhang ZQ, Z.-Q., Zeng, R.-C., Yan, W., Lin, C.-G., Wang, L., Wang, Z.-L., et al. (2020). Corrosion Resistance of One-step Superhydrophobic Polypropylene Coating on Magnesium Hydroxide-Pretreated Magnesium alloy AZ31. *J. Alloys Compd.* 821, 153515. doi:10.1016/j.jallcom.2019.153515

Zhang, B., and Xu, W. (2021). Superhydrophobic, Superamphiphobic and SLIPS Materials as Anti-corrosion and Anti-biofouling Barriers. *New J. Chem.* 45, 15170–15179. doi:10.1039/D1NJ03158A

Zhang B, B., Duan, J., Huang, Y., and Hou, B. (2021). Double Layered Superhydrophobic PDMS-Candle Soot Coating with Durable Corrosion Resistance and thermal-mechanical Robustness. *J. Mater. Sci. Techn.* 71, 1–11. doi:10.1016/j.jmst.2020.09.011

Zhang ZQ, Z.-Q., Wang, L., Zeng, M.-Q., Zeng, R.-C., Lin, C.-G., Wang, Z.-L., et al. (2021). Corrosion Resistance and Superhydrophobicity of One-step Polypropylene Coating on Anodized AZ31 Mg alloy. *J. Magnesium Alloys* 9, 1443–1457. doi:10.1016/j.jma.2020.06.011

Conflict of Interest: The authors declare that the research was conducted in the absence of any commercial or financial relationships that could be construed as a potential conflict of interest.

Publisher's Note: All claims expressed in this article are solely those of the authors and do not necessarily represent those of their affiliated organizations, or those of the publisher, the editors, and the reviewers. Any product that may be evaluated in this article, or claim that may be made by its manufacturer, is not guaranteed or endorsed by the publisher.

frontiers in Materials

ORIGINAL RESEARCH
published: 02 March 2022
doi: 10.3389/fmats.2022.843522

Imidazo [1,2-a] Pyrimidine Derivatives as Effective Inhibitor of Mild Steel Corrosion in HCl Solution: Experimental and Theoretical Studies

*Kun Cao, Wenheng Huang, Xi Huang and Jie Pan**

School of Chemistry and Chemical Engineering, Neijiang Normal University, Neijaing, China

The inhibitory performance of imidazole [1,2-a] pyrimidine derivatives, namely, 2,4-diphenylbenzo [4,5]imidazo [1,2-a]pyrimidine (DPIP) and 2-(4-octylphenyl)-4-phenylbenzo [4,5]imidazo [1,2-a]pyrimidine (OPIP), against mild steel corrosion in 1 mol L^{-1} HCl solution was studied by weight loss at different temperatures, potentiodynamic polarization curves (PDP), electrochemical impedance spectroscopy (EIS), and surface analysis technology. The two corrosion inhibitors showed an outstanding inhibition performance, and the inhibition efficiency achieved 91.9% for OPIP and 90.5% for DPIP at a concentration of 0.1 mmol L^{-1}. Electrochemical methods showed that DPIP and OPIP behaved as mixed-type inhibitors. Density function theory (DFT) and molecular dynamic simulation (MD) were approached to theoretically study the relationship of the inhibitor structure and anti-corrosion performance, which were also compatible with the weight loss and electrochemical observations.

Keywords: corrosion, imidazo pyrimidine, inhibitor, EIS, dynamic simulation

OPEN ACCESS

Edited by:
Binbin Zhang,
Institute of Oceanology (CAS), China

Reviewed by:
Yujie Qiang,
University of Science and Technology Beijing, China
Lei Guo,
Tongren University, China

****Correspondence:***
Jie Pan
figock01@163.com

Specialty section:
This article was submitted to Environmental Degradation of Materials, a section of the journal Frontiers in Materials

Received: *26 December 2021*
Accepted: *20 January 2022*
Published: *02 March 2022*

Citation:
Cao K, Huang W, Huang X and Pan J (2022) Imidazo [1,2-a] Pyrimidine Derivatives as Effective Inhibitor of Mild Steel Corrosion in HCl Solution: Experimental and Theoretical Studies. Front. Mater. 9:843522. doi: 10.3389/fmats.2022.843522

1 INTRODUCTION

Mild steel is widely used in transportation, construction, medical equipment, and other fields, which has an extremely important impact on human life and social production. Unfortunately, Q235 steel is susceptible to corrosion in harsh work environments, and it is prone to breakage after being corroded, which not only causes enormous economic losses but also threatens people's lives. Hence, the corrosion protection of metal materials is particularly important. A corrosion inhibitor is one of the best ways to inhibit metal corrosion in a harsh corrosive environment such as salt solution or acid solution through surface adsorption. Due to the moderate price of these products, this method is easy to carry out and cheap. A large number of studies conducted in the past 50 years have produced inorganic, organic, or plant extract products suitable for specific corrosion systems (metal/corrosive media) (Li et al., 2021). The organic corrosion inhibitor needs at least polar groups, through which molecules can combine the metal surface, such as the functional group(s) with a heteroatom(s) (N, P, O, or S) containing lone pair electrons; the combination between the molecule and the metal surface can also achieved through the interaction between the delocalized "π" electron of the double bond or aromatic ring and the "d" orbital of the metal. In addition, the shape or size of the corrosion inhibitor molecule has a great impact on its performance (El Azzouzi et al., 2016; Zarrouk et al., 2016; Salim et al., 2019; Meeusen et al., 2020; Mishra et al., 2020). As seen previously, heterocyclic compounds have been studied by many researchers such as benzimidazoles, quinoxaline, oxazole, imidazole,

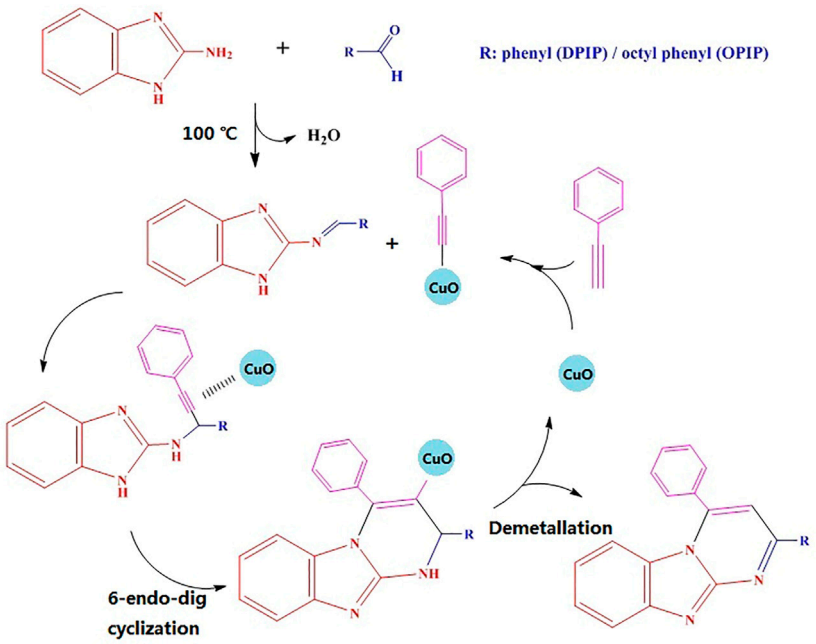

FIGURE 1 | Mechanism for synthesis of imidazo [1,2-a] pyrimidine compounds.

quinoline, and tetrazole (Zhang et al., 2019a; Zhang et al., 2019b; El-Hajjaji et al., 2019; Qiang et al., 2020; Qiang et al., 2021). In addition, with the increase in the number of unsaturated bonds in the molecules, the corrosion inhibition performance of these compounds is improved. Imidazole pyrimidine and its derivatives are commonly used as antibacterial, antiviral, anti-inflammatory, and antitumor drugs. It has heterocyclic groups such as imidazole and pyrimidine and is a potential corrosion inhibitor to protect steel from environmental corrosion (Anejjar et al., 2015; Ech-chihbi et al., 2017).

In this work, we mainly aimed to investigate the two imidazole pyrimidine derivatives as potential corrosion inhibitors for mild steel in an acidic environment and the corrosion inhibition mechanism. Understanding of the mechanism can allow for the most profitable use of these corrosion inhibitors and the optimization of more effective compounds. Therefore, the anti-corrosion properties of the inhibitors were investigated by weight loss, electrochemical methods, and the characterization of the metal surface treated by scanning electron microscopy (SEM), atomic force microscopy (AFM), and X-ray photoelectron spectroscopy (XPS). A correlation between inhibitory activity and molecular structures was investigated using the density functional theory (DFT) method and dynamic molecular simulation.

2 EXPERIMENTAL

2.1 Chemical Synthesis of Organic Compounds

The route for the synthesis of the two imidazo pyrimidine compounds is shown in **Figure 1**. Briefly, 0.5 mmol 2-aminobenzimidazole, 0.5 mmol benzaldehyde (or 4-Octylbenzaldehyde), 0.5 mmol phenylacetylene, and 10 mg copper oxide nanoparticles were stirred at 100°C under solvent-free condition until the consumption of 2-aminobenzimidazole. After completion of the reaction, ethanol was added to the reaction mixture, and then the catalyst was separated by centrifugation. The organic layer was concentrated under rotary evaporation to afford the crude product, which was purified by column chromatography. For 2,4-diphenylbenzo [4,5] imidazo [1,2-a]pyrimidine (DPIP), ^{1}H NMR (CDCl3, 400 MHz) δ 8.24 (br, 2H), 7.91 (d, 1H), 7.66–7.37 (m, 9H), 7.19 (s, 1H), 6.96 (t, 1H, J = 8.24 Hz), 6.62 (d, 1H, J = 8.4 Hz); For 2-(4-octylphenyl)-4-phenylbenzo [4,5]imidazo [1,2-a]pyrimidine (OPIP), ^{1}H NMR (CDCl3, 400 MHz) δ 8.23 (d, J = 8.24 Hz, 2H), 7.95–7.97 (m, 1H), 7.63–7.72 (m, 5H), 7.44 (t, J = 7.33 Hz, t), 7.34 (d, J = 8.24 Hz, 2H), 7.24 (s, 1H), 7.01 (t, J = 8.01 Hz, 1H), 6.66–6.68 (m, 1H), 2.69 (t, J = 7.79 Hz, 2H), 1.26–1.69 (m, 12H), 0.91 (t, J = 7.33 Hz, 3H);

2.2 Material and Solution Preparation

The mild steel samples used in this study have a chemical composition (% by weight) Fe = 99.13, S = 0.07, P = 0.10, Si = 0.39, Al = 0.02, Mn = 0.07, and C = 0.22. All mild steel samples in this work were polished using 200–2000 grand SiC paper and 0.5 μm Al_2O_3 powder, washed with distilled water, degreased with acetone, and dried in the cool air. HCl solution (1 mol L^{-1}) is obtained by dilution of 37% hydrochloride acid using distilled water. Inhibitor stock solution (1 mmol/L) was prepared by dissolving DPIP and OPIP in a 30% by volume of ethyl alcohol in 1 mol L^{-1} HCl solution, and the required concentration of inhibitors were prepared by dilution using 1 mol L^{-1} HCl

solution. The amount of ethyl alcohol in all aqueous solution in the presence and the absence of the investigated nutmeg oil were kept constant to remove the effect of the ethyl alcohol on the inhibition efficiency.

2.3 Weight Loss Experiment

A weight loss experiment is a simple method to determine the corrosion rate (CR) of mild steel. The mild steel samples with rectangle shape (50 mm × 25 mm × 2 mm) were immersed in 1 mol L^{-1} HCl in the absence and presence of each of the studied corrosion inhibitors with different concentrations (from 0.001 to 0.1 mmol L^{-1}) for a period of 3 h at 298, 308, and 318 K. The inhibition performance (η_W %) and surface coverage (θ) were calculated using **Eqs. 1** and **2** (Singh et al., 2016):

$$\eta_W(\%) = \frac{CR_0 - CR}{CR_0} \times 100 \quad (1)$$

$$\theta = \frac{CR_0 - CR}{CR_0} \quad (2)$$

where CR_0 and CR are the CRs without and with different concentrations of DPIP and OPIP, respectively; θ is the degree of surface coverage of DPIP and OPIP.

2.4 Electrochemical Evaluation

The electrochemical measurements were carried out with an Ivium workstation; this device is connected to a cell with three electrodes: a working electrode (mild steel sample) with exposure area 1 cm^2, a reference electrode (saturated calomel electrode), and a counter electrode (platinum sheet). Before the electrochemical test, soak the working electrode in the test solution for 30 min to stabilize the corrosion potential. For potentiodynamic polarization study, the potential sweep ranges from −600 to −100 mV (*vs.* SCE) with a scan rate of 0.5 mV s^{-1}. Electrochemical parameters such as corrosion potential (E_{corr}), corrosion current densities (i_{corr}), and Tafel slopes (β_c, β_a) can be derived by extrapolation of the linear Tafel segments of the polarization curves. Electrochemical impedance spectroscopy (EIS) tests were made in the frequency range of 10^5–0.01 Hz with an excitation signal of 10 mV.

2.5 Mild Steel Surface Analyses

Corroded mild steel surface obtained after 3 h immersion in the HCl solution with and without the optimal concentration of 0.1 mmol L^{-1} inhibitors was analyzed using TESCAN VEGA three SBH scanning electron microscope. The accelerating voltage is 20 kV. AFM was done using a Bruker MULTIMODE eight instrument. AFM was conducted using a tapping mode and a 2.5 Hz scan rate. XPS spectra were obtained using the PHI5000-VersaProbe system using Mg Kα radiation as the excitation source.

2.6 Computational Details

2.6.1 Toxicity Prediction

First, the toxicity and solubility of DPIP and OPIP were predicted. The toxicity assessment was carried out in T.E.S.T. software, which is based on the quantitative structure–activity relationship (QSAR) model, a mathematical approach exploited to solve toxicity prediction in light of the physical characteristics of molecular structure (Raevsky et al., 2011).

2.6.2 DFT Calculations

The quantum chemical parameters were calculated by DFT using Gaussian 09W to analyze the corrosion inhibition mechanism of DPIP and OPIP. The optimized molecular structure and its molecular orbital [highest occupied molecular orbital (HOMO) and lowest unoccupied molecular orbital (LUMO)] were obtained by the b3lyp/6–31G method, which is considered an efficient and reliable method to deal with quantum chemical problems (Rahmani et al., 2019a). All parameters such as E_{HOMO}, E_{LUMO}, the energy gap ($\Delta E = E_{HOMO} - E_{LUMO}$), the dipole moment ($\mu$), and the fraction of electrons transferred (ΔN) of the studied compounds in neutral forms were calculated and discussed (El-Hajjaji et al., 2018).

The local reactivity of corrosion inhibitors can be acquired by analyzing the Fukui functions (Parr and Yang, 1984). The Fukui function f_k is defined as follows. N is the number of electrons, $\rho(r)$ is the electronic density, and $\nu(r)$ is the constant external potential (Khaled, 2010):

$$f_k = \left(\frac{\partial \rho(r)}{\partial N}\right)_{\nu(r)} \quad (3)$$

The Fukui function can be obtained by calculating the Milliken charges distribution of the atoms of a molecule.

The Fukui function is represented by finite difference approximations as follows:

$$f_k^+ = q_k(N+1) - q_k(N) \quad (\text{for nucleophilic attack}) \quad (4)$$

$$f_k^- = q_k(N) - q_k(N-1) \quad (\text{for electrophilic attack}) \quad (5)$$

where $q_k(N)$, q_k $(N + 1)$, and q_k $(N - 1)$ are the charges of the neutral, cationic, and anionic species, respectively. N is the number of electrons in the neutral species. In this work, Fukui functions for DPIP and OPIP were calculated with the Multiwfn software (Fan et al., 2015).

As it is known, the concept of generalized philicity has been introduced (Parthasarathi et al., 2004); they defined a local quantity called philicity associated with a site k in a molecule with the assistance of corresponding condensed-to-atom variants of Fukui function. The local softness $\sigma_k^{\pm}$ (σ_k^+ and σ_k^-) and electrophilicity $\omega_k^{\pm}$ (ω_k^+ and ω_k^-) are related to the electrophilic and nucleophilic attacks, respectively. Also, $\sigma_k^{\pm}$ and $\omega_k^{\pm}$ can be calculated according to **Eqs 6**, **7** (Lee et al., 1988).

$$\sigma_k^{\pm} = \sigma f_k^{\pm} \quad (6)$$

$$\omega_k^{\pm} = \omega f_k^{\pm} \quad (7)$$

where σ_k^+ and σ_k^- denote the local softness for the nucleophilic and electrophilic attacks, respectively. ω_k^+ and ω_k^- are the local electrophilicity for the nucleophilic and electrophilic attacks, respectively.

Further, it was affirmed that the dual local descriptors such as dual Fukui $\Delta f(k)$ (difference between the nucleophilic and electrophilic Fukui functions), dual local softness $\Delta\sigma_k$

(difference between the nucleophilic and electrophilic local softness), and the philicity $\Delta\omega_k$ (difference between the nucleophilic and electrophilic philicity functions) are more accurate and consistent tools than the aforementioned local reactivity indices (Morell et al., 2006; Padmanabhan et al., 2006). In addition, $\Delta f(k)$, $\Delta\sigma_k$, and $\Delta\omega_k$ are calculated according to the following **Eqs 8–10**.

$$\Delta f\,(k) = f_k^{\pm} - f_k^{-} \tag{8}$$

$$\Delta\sigma_k = \sigma_k^{+} - \sigma_k^{-} \tag{9}$$

$$\Delta\omega_k = \omega_k^{+} - \omega_k^{-} \tag{10}$$

If $\Delta\omega_k$ (or $\Delta f(k)$) > 0, the site k is favored for a nucleophilic attack, whereas if $\Delta\omega_k$ (or $\Delta f(k)$) < 0, the site k may be favored for an electrophilic attack.

2.6.3 Molecular Dynamic Simulation Details

Molecular dynamic (MD) simulation is usually used to study the interaction and adsorption between corrosion inhibitors and metal surfaces. This method can better understand the molecular interaction mechanism of corrosion inhibitors (El Faydy et al., 2019; Laabaissi et al., 2019; Benhiba et al., 2020). In this work, the adsorption processes of DPIP and OPIP on mild steel surfaces were investigated by Materials Studio eight software. The simulation of the Fe (1 1 0) surface was implemented by placing the surface crystal in a cell (32.27 × 32.27 × 30.13 Å^3). The liquid phase contained 5 Cl^-, 5 H_3O^+, and 495 H_2O. A 40 Å vacuum layer was established on the liquid layer to avoid the interaction between the surface and periodic repeating planes. The simulations were implemented at 298 K controlled by NVT ensemble with Andersen thermostat. The simulation was performed by Forcite code in a COMPASS force field for 200 ps with a time step of 0.1 fs (Andersen, 1980; Sun, 1998). The diffusions of Cl^-, H_3O^+, and H_2O in the inhibitor membranes were also simulated.

3 RESULTS AND DISCUSSIONS

3.1 Toxicity of Inhibitors

Some important toxicity endpoints involving developmental toxicity potential (DTP) and mutagenicity (M) were chosen to represent the toxicities. Generally, predicted values from 0.00 to 0.50 represent low toxicity probabilities, while predicted values >0.50 indicate high toxicity probabilities. The LD_{50} value should be greater than 300 mg/kg (**Supplementary Table S1**) (Alhaffar, et al., 2019). With careful inspection of the obtained probability values in **Supplementary Figure S1**, we can affirm that the toxic level of DPIP and OPIP is in the safe area. The probability for biodegradability (B) is 0.595 and 0.610, respectively, which implies that this substance is biodegradable and environmentally friendly.

3.2 Weight Loss Measurement

The inhibitory performance of the studied imidazo pyrimidine derivatives was realized by the weight loss method after 3 h immersions in 1 mol L^{-1} HCl solution in the presence and absence of the corrosion inhibitors at different temperatures. **Table 1** gives the values of the CR and the inhibition efficiency (η_W %).

From **Table 1**, the results showed that DPIP and OPIP have good corrosion inhibition properties for mild steel in the 1 mol L^{-1} HCl solution. The anti-corrosion performance gets better with increase in inhibitor concentration. At a concentration of 0.1 mmol L^{-1}, the inhibition efficiency of OPIP and DPIP reached the maximum 94.1% and 93.4%, respectively. This may be because the corrosion process of mild steel in a corrosion solution could be retarded by the adsorption of corrosion inhibitor molecules on the mild steel surface. The high anti-corrosion property of DPIP and OPIP is probably explained by the adsorption of the electron-rich imidazo pyrimidine group and improved with the carbon chain on the benzene ring.

Table 1 clearly shows that the corrosion degree increases with the increase of temperature. The corrosion inhibition efficiency of DPIP and OPIP decreases, which can be interpreted to mean that organic corrosion inhibitor molecules are easier to desorb from the metal surface with the rise of temperature.

3.3 Potentiodynamic Polarization Study

The polarization curves without and with different concentrations of OPIP and DPIP in the 1 mol L^{-1} HCl solution at 298 K are presented in **Figure 2**. The electrochemical parameters are reported in **Table 2**.

By analyzing the cathodic and anodic polarization curves in **Figure 2**, the corrosion inhibitor has a significant impact on the anodic and cathodic processes of corrosion reaction after adding DPIP and OPIP. A decrease in the cathodic current densities can be explained by the reduction of the exposed surface area caused by the adsorption of inhibitor molecules which leads to a reduction of hydrogen evolution reaction, while the decrease in anodic current density is caused by reduced dissolution reaction of mild steel. The inhibition performance of DPIP and OPIP is related to the adsorption on the working electrode surface and the formation of the barrier film (Monticelli et al., 2019). It is well known that the reduction of hydrogen ions needs two consecutive steps (Singh and Quraishi, 2010; El-Taib Heakal et al., 2012). In this work, the cathodic curves conform to the form of the Tafel curve, and the hydrogen evolution reaction on the mild steel surface is carried out based on the pure activation mechanism.

There is no defined trend for the shift of E_{corr} value. However, if the E_{corr} value deviates more than ±85 mV from the blank E_{corr} value, the inhibitor can be classified as a cathodic or anodic inhibitor; otherwise, it can be regarded as a mixed inhibitor affecting cathodic reaction (hydrogen evolution) and anodic reaction (metal dissolution) (Anusuya et al., 2017; Haque et al., 2017; Ouici et al., 2017; Salhi et al., 2017). In this study, the addition of different concentrations of corrosion inhibitors will lead to a slight change in the E_{corr} value, which is no more than 85 mV compared with the blank E_{corr} value. Therefore, the undefined trend shift of E_{corr} for DPIP and OPIP showed a mixed inhibition behavior.

TABLE 1 | Weight loss data of the mild steel with DPIP and OPIP in 1 mol·L^{-1} HCl at different temperatures.

Inhibitor	C (mmol·L^{-1})	298K			308K			318K		
		Δw (mg)	CR (mg·cm^{-2}·h^{-1})	η_w (%)	Δw (mg)	CR (mg·cm^{-2}·h^{-1})	η_w (%)	Δw (mg)	CR (mg·cm^{-2}·h^{-1})	η_w (%)
Blank	0	62.4	0.91	—	70.9	1.04	—	76.3	1.12	—
DPIP	0.001	12.8	0.19	79.5	21.2	0.31	70.1	25.1	0.37	67.1
	0.005	11.4	0.17	81.7	18.8	0.27	73.5	23.4	0.34	69.3
	0.01	8.34	0.12	86.6	14.1	0.21	80.1	19.1	0.28	75.0
	0.05	6.13	0.09	90.2	10.7	0.16	84.9	16.8	0.25	78.0
	0.1	4.09	0.06	93.4	8.69	0.13	87.7	11.7	0.17	84.7
OPIP	0.001	13.1	0.19	79.0	20.5	0.30	71.1	25.2	0.37	67.0
	0.005	10.8	0.16	82.7	18.3	0.27	74.2	22.9	0.33	70.0
	0.01	7.59	0.11	87.8	13.2	0.19	81.4	19.2	0.28	74.8
	0.05	5.83	0.09	90.7	9.52	0.14	86.6	16.5	0.24	78.4
	0.1	3.71	0.05	94.1	7.91	0.12	88.8	11.5	0.16	85.6

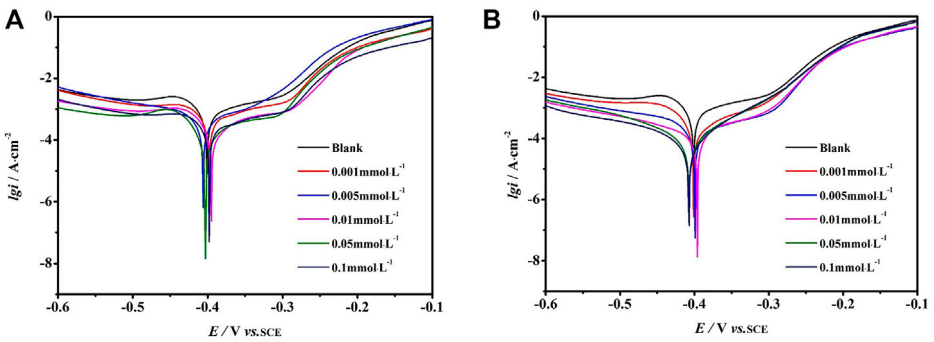

FIGURE 2 | Polarization curves for the mild steel in 1 mol L^{-1} HCl containing different concentrations of DPIP **(A)** and OPIP **(B)** at 298 K.

TABLE 2 | Polarization curve parameters of mild steel in 1 mol L^{-1} HCl with various concentrations of inhibitors (DPIP and PIP) at 298K.

Inhibitors	C (mmol·L^{-1})	-E_{corr} (mV)	β_a (mV·dec^{-1})	-β_c (mV·dec^{-1})	i_{corr} (μA·cm^{-2})	η_i (%)
Blank	0	401	151	178	735	—
DPIP	0.001	398	87	172	312	57.6
	0.005	406	89	163	222	69.8
	0.01	395	74	150	184	75.0
	0.05	403	75	155	143	80.5
	0.1	398	79	151	103	86.0
OPIP	0.001	403	83	174	302	58.9
	0.005	399	85	167	225	69.4
	0.01	396	81	154	186	74.7
	0.05	407	72	152	132	82.0
	0.1	409	78	143	97.5	86.7

The inhibition efficiencies calculated by the corrosion current density without and with inhibitors at different concentrations are shown in **Eq. 11**:

$$\eta_i(\%) = \frac{i^0_{corr} - i_{corr}}{i^0_{corr}} \times 100 \quad (11)$$

where i^0_{corr} and i_{corr} are the corrosion current density without and with DPIP and OPIP, respectively. The results give kinetic information of cathodic and anodic reactions. Also, the results match the weight loss method.

3.4 EIS Measurements

EIS was used to obtain information about the mechanism of charge transfer, diffusion, and adsorption between the electrode surface and the studied corrosion inhibitors. Nyquist diagrams of the mild steel immersed in 1 mol L^{-1} HCl without and with

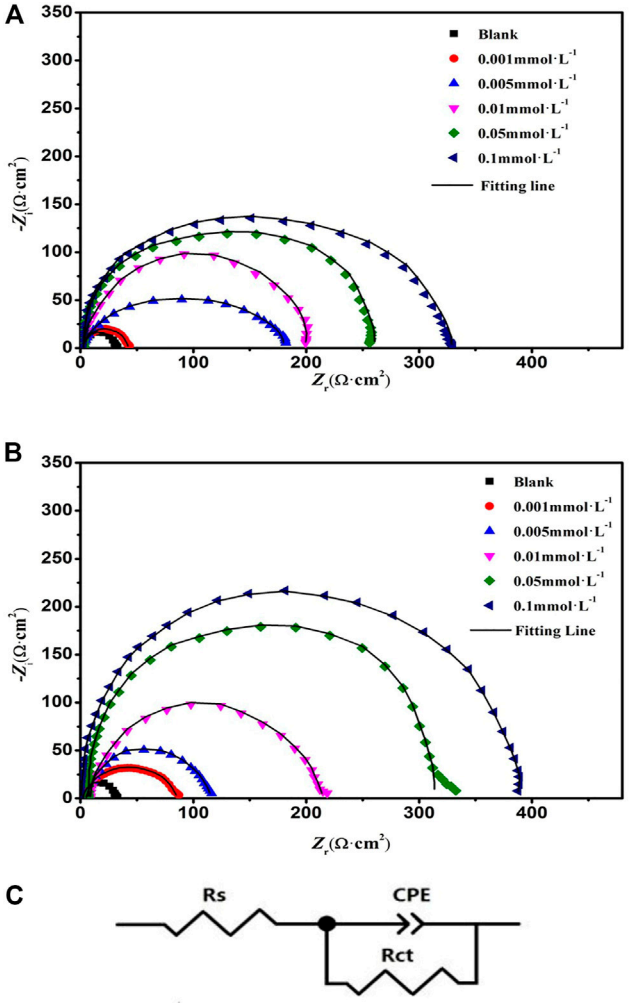

FIGURE 3 | Nyquist plots of DPIP **(A)**, OPIP **(B)** and equivalent circuit **(C)** for mild steel in 1 mol L^{-1} HCl containing different concentrations at 298K.

different concentrations of DPIP and OPIP are presented in **Figure 3**.

It is noted from the Nyquist graphs that the impedance spectra consist of single depressed semicircle capacitive loops, which are caused by the frequency dispersion and the heterogeneity of the electrode surface (Khadiri et al., 2018; El Faydy et al., 2018). The shape of impedance spectra obtained in different electrolyte solutions (containing different concentrations of corrosion inhibitor and blank) are the same, which suggests that the corrosion mechanism of mild steel has not changed, and the radius of capacitive loops increases significantly after increasing the corrosion inhibitor concentration. The behavior of the impedance can be illustrated by adapting an electrochemical equivalent circuit (**Figure 3**) including a solution resistance (R_s), constant phase element (*CPE*), and the charge transfer resistance (R_{ct}) (Pan et al., 2020). The electrochemical parameters are listed in **Table 3**.

CPE values are calculated using **Eq. 12** (Zhang et al., 2012):

$$Z_{CPE} = Q^{-1}(iw)^{-n} \tag{12}$$

where Q, w, i, and n stand for *CPE* constant, the angular frequency, imaginary root, and the deviation indicator related to the homogeneity of the work electrode surface, respectively. In addition, double-layer capacitance (C_{dl}) values are defined using **Eq. 13** (Brug et al., 1984):

$$c_{dl} = Q^{1/n}\left(\frac{R_s R_{ct}}{R_s + R_{ct}}\right)^{(1-n)/n} \tag{13}$$

The inhibition efficiency was evaluated using the following expression:

$$\eta_R(\%) = \frac{R_{ct} - R_{ct}^0}{R_{ct}} \times 100 \tag{14}$$

where R_{ct}^0 and R_{ct} mean the charge transfer resistance of blank electrolyte and electrolyte with inhibitors, respectively.

It is observed that the highest R_{ct} [329.2 ($\Omega\cdot cm^2$) for DPIP and 387.8 ($\Omega\cdot cm^2$) for OPIP] has been obtained at 0.1 mmol L^{-1}. With the increase of inhibitor concentration in the corrosive medium, the adsorption of inhibitor molecules on the surface of mild steel increases, which means that the exposed surface area of mild steel decreases, the charge transfer resistance increases, and the inhibition efficiency improves. On the other hand, the increase of R_{ct} value coincides with the decrease of C_{dl} value of the inhibitors, which can be explained as replacing Cl^- ions and H_2O molecules from the mild steel surface with inhibitor molecules. This process reduced the surface reaction of mild steel in the corrosive medium, increasing the resistance to charge and mass transfer (McCafferty and Hackerman, 1972).

3.5 Adsorption Studies

The adsorption isotherm gives the chance to better understand the interaction between the inhibitor molecules and the metal surface. Langmuir, Temkin, Freundlich, Flory Huggins, and El Awady adsorption isotherms (**Eqs 15–20**) are employed to obtain more information about adsorption behavior and the relationship between surface coverage and inhibitor concentration. The values of surface coverage are obtained from the weight loss data.

$$\frac{C}{\theta} = \frac{1}{K_{ads}} + C \quad \text{Langmuir} \tag{15}$$

$$\ln\left(\frac{\theta}{1-\theta}\right) = \ln K + y \ln C \ \ (K_{ads} = K^{1/y}) \quad \text{El} - \text{Awady} \tag{16}$$

$$\mathrm{n}\left(\frac{\theta}{C}\right) = \ln K_{ads} + x \ln(1-\theta) \quad \text{Flory} - \text{Huggins} \tag{17}$$

$$\ln\theta = \ln K_{ads} + Z \ln C \quad \text{Freundlich} \tag{18}$$

$$\ln\left[\left(\frac{\theta}{1-\theta}\right) \times \left(\frac{1}{C}\right)\right] = -\ln K_{ads} + 2d\theta \quad \text{Frumkin} \tag{19}$$

$$\theta = -\frac{1}{2a}\ln K_{ads} - \frac{1}{2a}\ln C \quad \text{Temkin} \tag{20}$$

Analysis of the different isotherms shows that the fitting provided by the Langmuir isotherm has a regression coefficient R^2 of 0.999 for DPIP and OPIP at 298 K

TABLE 3 | EIS parameters of mild steel in 1 mol L^{-1} HCl containing various concentrations of DPIP and OPIP.

Inhibitors	C (mmol·L^{-1})	R_s (Ω·cm^2)	CPE_{dl}		R_{ct} (Ω·cm^2)	η_R (%)
			C_{dl} (μF·cm^{-2})	n		
Blank	0	2.485	446	0.89	31.2	—
DPIP	0.001	2.571	338.4	0.88	43.4	28.1
	0.005	2.978	287.6	0.85	180.5	82.7
	0.01	2.764	203.8	0.86	199.8	84.4
	0.05	2.756	153.8	0.88	256.5	87.8
	0.1	2.525	112.5	0.88	329.2	90.5
OPIP	0.001	2.144	288.9	0.83	85.9	63.7
	0.005	2.426	267.2	0.86	116.4	73.2
	0.01	2.518	213.8	0.85	211.6	85.3
	0.05	2.913	123.1	0.85	327.6	90.5
	0.1	2.651	108.5	0.80	387.8	91.9

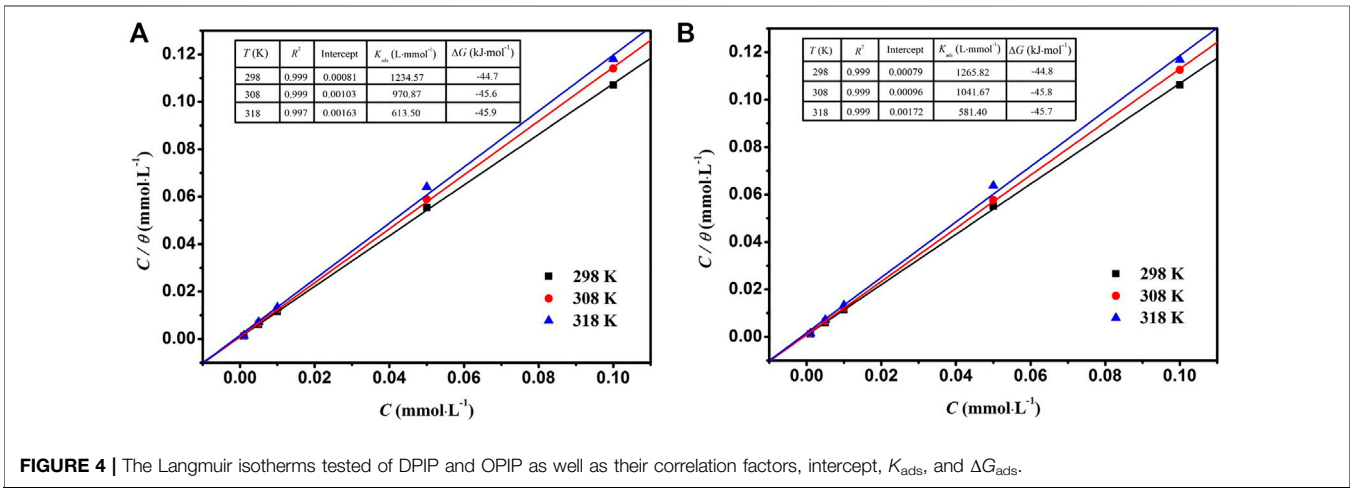

FIGURE 4 | The Langmuir isotherms tested of DPIP and OPIP as well as their correlation factors, intercept, K_{ads}, and ΔG_{ads}.

(**Figure 4**). The slope of the adsorption isotherm equation is slightly greater than 1 due to the inhomogeneity of the surface.

The values of the adsorption equilibrium constant K_{ads} can be accessed from the values of the standard free adsorption energies ΔG_{ads} by the following equality (Zhao et al., 2020):

$$\Delta G_{ads} = -RT \ln(55.5 \times K_{ads}) \tag{21}$$

where C_{H2O} is 55.5 mol L^{-1} in the solution; R is the constant of gases, and T is the temperature.

As we all know, if the value of ΔG_{ads} is near −20 kJ mol^{-1} or more positive, it can be regarded as physical adsorption. However, when the value of ΔG_{ads} is equal to or less than −40 kJ mol^{-1}, it is thought to be chemisorption through the interaction between lone pair electrons in inhibitor molecules and metal surface (Nahle et al., 2018; Rahmani et al., 2019b; Farhadian et al., 2021). In the present work, the values of ΔG_{ads} are less than −40 kJ mol^{-1}, which shows that the inhibitor molecules are adsorbed on the mild steel surface by strong chemical bonds. Chemical bindings with Fe unfilled orbitals are through the combination of donating lone electron pairs and/or π-electrons of the DPIP and OPIP molecules and Fe empty orbitals (chemical adsorption).

3.6 Thermodynamic Activation Parameters for DPIP and OPIP

From the weight loss measurement, the inhibitory performance decreased with rising temperature, so in this part, the effort of temperature on the inhibition performance of DPIP and OPIP was studied. The corrosion kinetic process of mild steel in the corrosive solution without and with inhibitors was described by the Arrhenius equation as follows (Khadraoui et al., 2016):

$$CR = k \exp\left(\frac{-E_a}{RT}\right) \tag{22}$$

where k is the frequency factor and E_a is the activation energy. The value of E_a of metal dissolution in the inhibitor-free or inhibitor-containing solution is based on the slope ($-E_a/R$) of the plot of $\ln CR \sim 1/T$ (**Figure 5**).

The thermodynamic parameters such as enthalpy and entropy were described by the transition state equation (Khadraoui et al., 2016):

$$CR = \frac{RT}{N_a h} \exp\left(\frac{\Delta S}{R}\right) \exp\left(\frac{-\Delta H}{RT}\right) \tag{23}$$

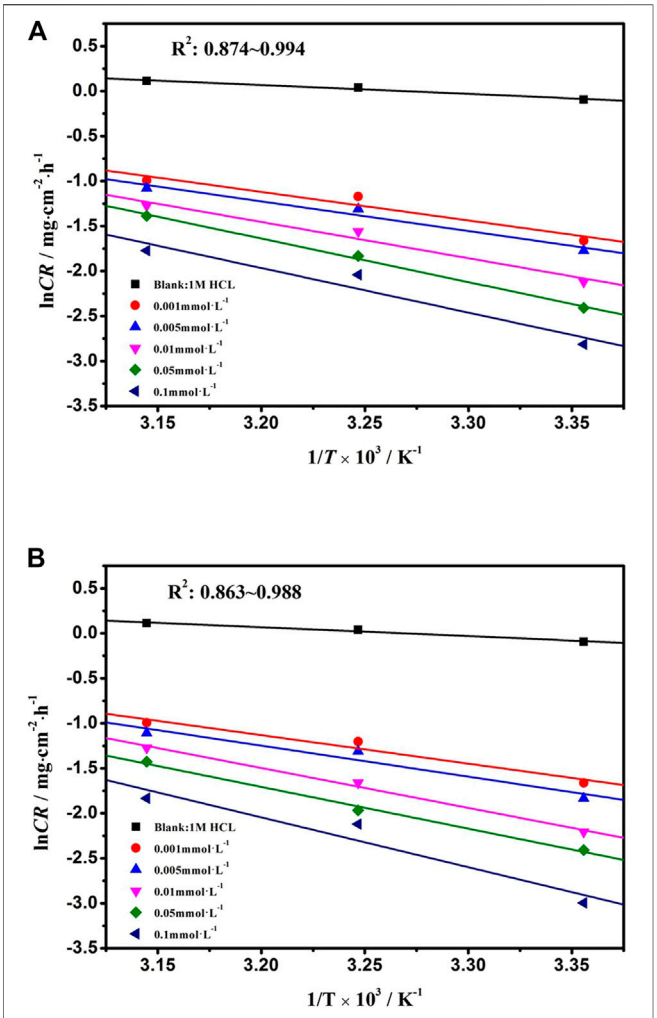

FIGURE 5 | ln*CR* versus 1,000/T for mild steel corrosion in 1 mol L^{-1} HCl with various concentrations of DPIP and OPIP.

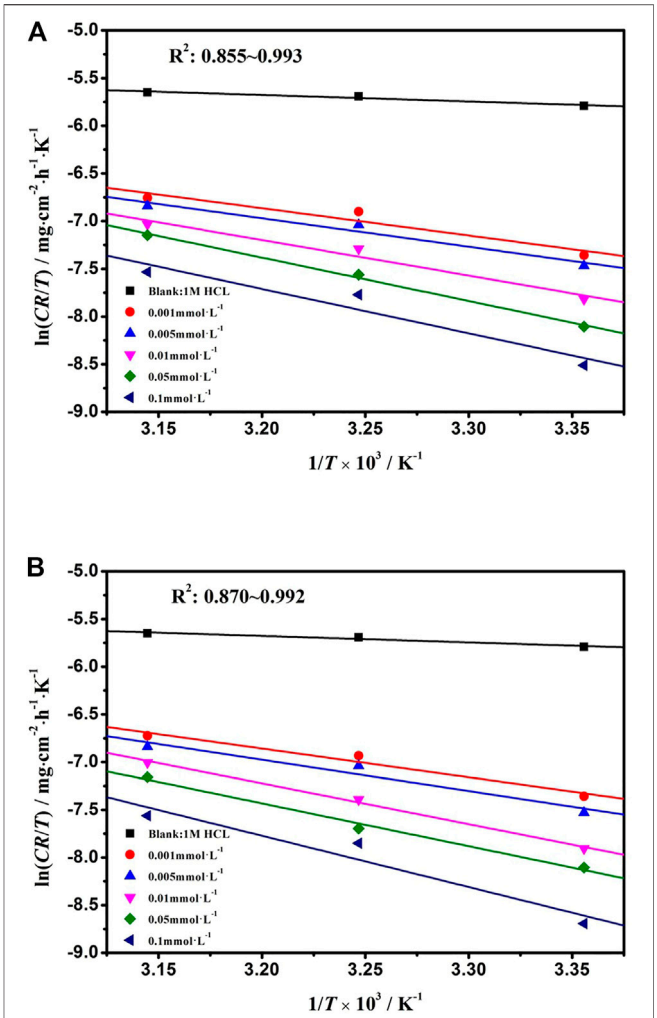

FIGURE 6 | ln [*CR*/*T*] versus 1,000/T for mild steel corrosion in 1 mol L^{-1} HCl with various concentrations of DPIP and OPIP.

where ΔH, ΔS, N_a, and h are enthalpy, entropy, Avogadro number, and Planck's constant, respectively. The relationship of ln [*CR*/*T*] ~ 1/*T* is showed in **Figure 6**. The values of ΔH and ΔS were obtained with the slope and intercept of the fitted line. The corrosion kinetic process of mild steel in the absent or present inhibitors solutions was described by the Arrhenius equation. The values of ΔH, ΔS, and E_a are listed in **Table 4**.

As showed in **Table 4**, the value of E_a for the mild steel in the inhibited solution is higher than that obtained for the uninhibited solution. The value of E_a in the inhibited solution (at least 26.38 kJ mol^{-1} for DPIP and 26.35 kJ mol^{-1} for OPIP) is higher than that in the blank solution and is 8.2 kJ mol^{-1}. It is well known that a higher value of the E_a than without inhibitors means that the inhibitors offer a thin adsorption film on the mild steel surface that creates a physical barrier for charge and mass transfer (Kannan et al., 2014). In addition, the activation energy was augmented with the increased inhibitors concentration, indicating that the dissolution rate of mild steel decreased in the corrosive medium (Sliem et al., 2019). The positive value of ΔH reflects that the dissolution process of mild steel in the studied solution is endothermic. Moreover, the difference between E_a and ΔH being greater than 0 also showed that gaseous reduction reaction (hydrogen evolution) occurred in the corrosion process (Zhang et al., 2021). Further analysis found that the average value of $E_a - \Delta H$ is about 2.56 kJ mol^{-1}, which is basically consistent with the value of RT (2.57 kJ mol^{-1}), indicating that the corrosion process is a unimolecular reaction (Gomma and Wahdan, 1995). Negative values of ΔS indicate the decrease in disorder. The adsorption process goes from the reagents to the activated complex, and complex compound formation was associated with the rate-determining step (Saady et al., 2021).

3.7 Surface Characterizations

3.7.1 SEM Analysis

SEM analysis provides two-dimensional visual information about the corrosion resistance of inhibitors to metal, which is a powerful supplement to the results of weight loss analysis and electrochemical

TABLE 4 | Activation parameters values in the nonexistence and existence of DPIP and OPIP solution.

Inhibitors	C (mmol·L^{-1})	ΔH (kJ·mol^{-1})	ΔS (J·mol^{-1}·K^{-1})	E_a (kJ·mol^{-1})	E_a-dh (kJ·mol^{-1})
Blank	0	5.64	−226.68	8.20	2.56
DPIP	0.001	23.82	−178.39	26.38	2.56
	0.005	24.84	−176.01	27.39	2.56
	0.01	30.92	−158.43	33.48	2.56
	0.05	37.73	−138.19	40.29	2.56
	0.1	38.67	−137.90	41.23	2.56
OPIP	0.001	25.04	−174.44	26.35	2.56
	0.005	27.33	−168.07	28.65	2.56
	0.01	35.55	−143.84	36.86	2.56
	0.05	37.27	−140.08	38.58	2.56
	0.1	44.74	−118.98	46.05	2.56

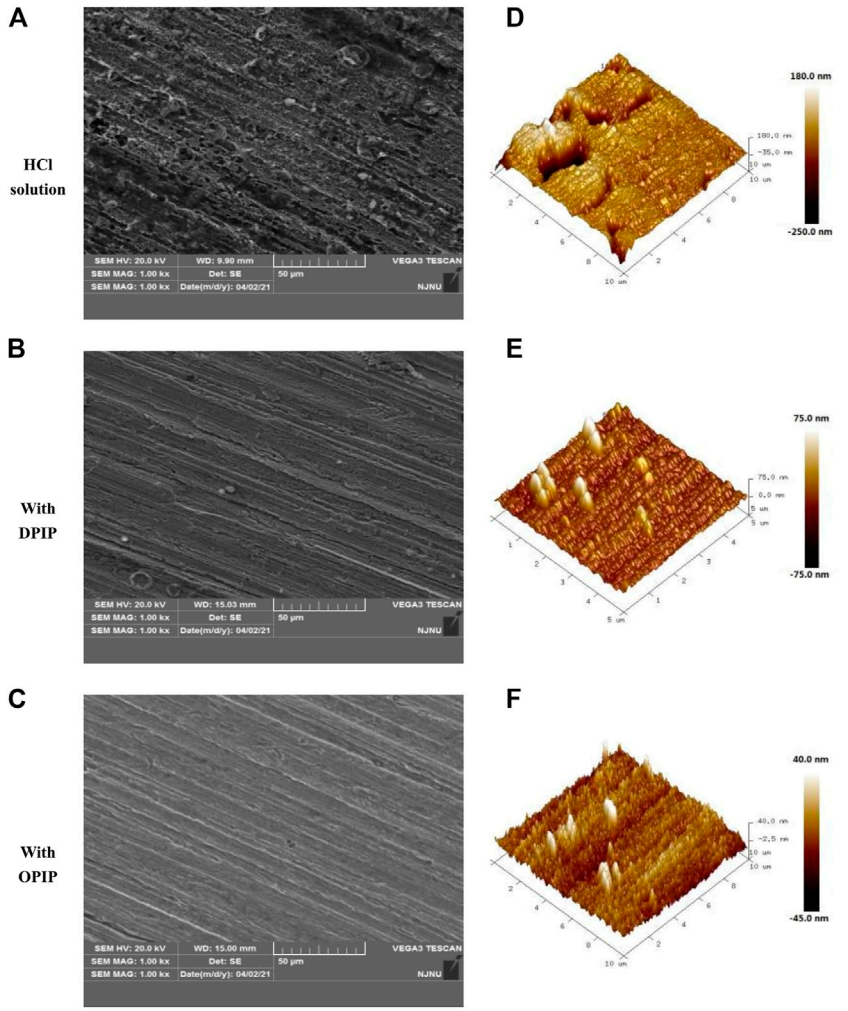

FIGURE 7 | SEM **(A–C)** and AFM **(D–F)** images of mild steel in 1 mol L^{-1} HCl without and with 0.1 mmol L^{-1} DPIP/OPIP after 3 h immersion.

research. The morphology of mild steel immersed in 1 mol L^{-1} HCl acid solution without and with 0.1 mmol L^{-1} of DPIP/OPIP for 3 h was studied, as showed in **Figures 7A–C**.

It is clear from **Figure 7** that the surface of mild steel is seriously damaged in the uninhibited acidic solution, reflecting a strong metal dissolution. The surface of mild

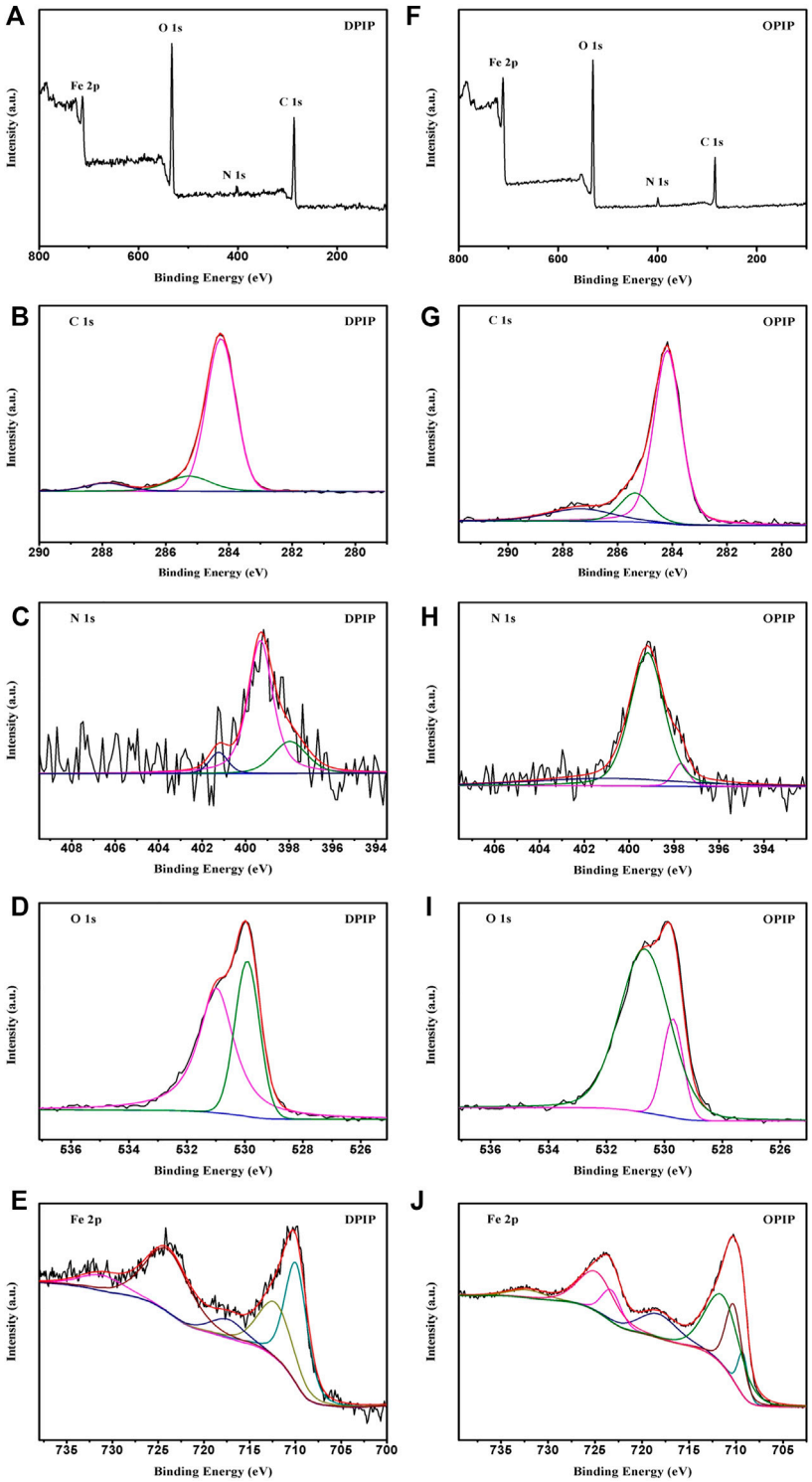

FIGURE 8 | XPS spectra of mild steel surface in 1 mol L^{-1} HCl without and with 0.1 mmol L^{-1} DPIP/OPIP after 3 h immersion: wide spectra, C 1s, N 1s, O 1s, and Fe 2p.

steel is rough and porous, and the hole is wide and deep. After adding DPIP/OPIP in the corrosive environment, the inhibitor molecules are adsorbed on the metal surface and cover the exposed surface to decrease the contact between the corrosive medium and the metal and delay the dissolution of the sample.

3.7.2 AFM Analysis

With the rapid development of high-resolution spatial characterization technology, AFM has been successfully implemented in the field of corrosion and protection. **Figure 7** shows the 3D morphology and roughness of mild steel surface with and without corrosion inhibitors in 1 mol L^{-1} HCl acidic medium. As shown in the figures, the surface of mild steel sample without corrosion inhibitor shows serious damage, with an average roughness of 33.7 nm. Compared with the sample without corrosion inhibitors, the metal surface of the sample with corrosion inhibitors is more uniform, and its roughness (RA) is lower. The average roughness of mild steel soaked in DPIP and OPIP solutions is 11 and 12 nm, respectively. AFM morphology further confirmed that the existence of corrosion inhibitors can effectively inhibit the corrosion of mild steel.

3.7.3 XPS Analysis

The composition of organic adsorption layer on mild steel surface in 1 mol L^{-1} hydrochloric acid corrosion medium with corrosion inhibitors was studied by XPS. The results demonstrate that the surface film is generally composed of ferric oxide and carbonaceous organic matter. In this way, the high-resolution peaks for C 1s, O 1s, N 1s, and Fe 2p for mild steel surface after 3 h of immersion in 1 mol L^{-1} HCl solution containing 0.1 mmol L^{-1} of DPIP and OPIP are recorded and shown in **Figure 8**.

The C 1s spectra of DPIP and OPIP show three peaks (287.9, 285.3, and 284.3) and (287.4, 285.4, and 284.2), respectively. The largest peak can be ascribed to the C–C and C=C aromatic bonds with the characteristic binding energy of 284.3 eV, with the peak at 284.2 eV in OPIP as well. Peaks at 285.3 or 285.4 eV referred to the C–H, and those at 287.9 or 287.4 eV referred to the C–N and C=N, respectively (Wagner et al., 1979; Watts and Wolstenholme, 2003; Yamashita and Hayes, 2008). The O 1s spectrum envelops were fitted by two peaks. The first peak located at 529.9 eV was attributed to Fe_2O_3 and/or Fe_3O_4 oxides. The second peak located at 530.8 eV (530.7 eV for OPIP) is attributed to the oxygen in hydrous iron oxides, such as FeOOH and/or $Fe(OH)_3$ (Temesghen and Sherwood, 2002). The peaks of the N 1s of the steel sample treated by DPIP may be fitted into three peaks located at 401.3, 399.3, and 398.0 eV corresponding to the quaternary nitrogen ($=N^+$-) atom of the imidazo pyrimidine ring (Tang et al., 2013), coordinated nitrogen atom, and C-N-metal bond (Weng et al., 1995; Finsgar et al., 2009), respectively. In the case of OPIP, these peaks are noted at 401.1, 399.2, and 397.7 eV.

The Fe 2p spectra were fitted to two doublets, 711.7 eV or 712.7 (Fe 2p3/2) and 724.3 eV or 724.6 (Fe 2p1/2), with an associated ghost structure. The peak is attributable to the Fe–N, which is reported to appear at 710.3 eV (711.7 eV for OPIP) (Ciampi and Di castro, 1995; Zhang et al., 2016). The peak located at 711.7 or 712.7 eV was assigned to ferric compounds such as FeOOH (i.e., oxyhydroxide), Fe_2O_3 (i.e., Fe^{3+} oxide), and/or Fe_3O_4 (i.e., Fe^{2+}/Fe^{3+} mixed oxide) (Pech-Canul and Bartolo-Perez, 2004; Bouanis et al., 2009); the peak observed at 718.6 or 718.7 eV may be ascribed to the satellite of Fe(III) (Ciampi and Di castro, 1995). Based on the previous observations, the XPS results support the presence of adsorbed inhibitors on the mild steel surface.

3.8 Quantum Chemical Calculations

3.8.1 DFT

Quantum chemistry research is often used to determine the correlation between the molecular structure and anti-corrosion performance of corrosion inhibitors (Zhao et al., 2014). DFT is a very powerful tool for calculating molecular electron descriptors and analyzing inhibitor/surface interaction. In this work, the HOMO and the LUMO were obtained by using Gaussian 09 software and given in **Figures 9A**–F (Xia et al., 2020).

It is worth noting that the frontier molecular orbitals of inhibitor molecules play a major role in predicting the contribution and acceptance of electrons. **Figure 9** shows that HOMO and LUMO orbitals of DPIP and OPIP molecules are distributed on the surfaces of pyrimidine and imidazole parts. It can be noted that heteroatoms, such as N atoms, and benzene rings related to the above groups are very active. This means that the above sites are more involved in the inhibitor–metal interaction in the donor–acceptor process (Qiang et al., 2017). In addition to graphical representation, different quantum chemical parameters such as E_{HOMO}, E_{LUMO} ΔE, and ΔN were calculated to further explain the reactivity of corrosion inhibitors and their adsorption capacity on mild steel surface. **Table 5** summarizes the most important quantum chemical descriptors obtained after geometry optimization in the neutral form for each molecule in the aqueous phase.

Generally speaking, the reactivity of inhibitor molecules can be forecast by the energy of molecular orbitals: high HOMO energy represents the tendency of molecules to give electrons, and high LUMO energy represents the tendency to accept electrons. Therefore, the corrosion inhibitor with higher HOMO and the lower LUMO energy can be expected to have high anti-corrosion performance. In this work, it can be seen that the HOMO energy of OPIP is higher than that of DPIP, which has a stronger electron supplying ability, while the LUMO orbital energy of DPIP is higher, which shows a stronger electron receiving ability. This result cannot directly be used to judge the anti-corrosion performance of the corrosion inhibitors but also needs to be compared through the energy gap of the molecule. The corrosion inhibitor with high reaction activity has a lower value of energy gap (Kozlica et al., 2021).

From **Table 5**, The ΔE values of OPIP (3.528 eV) is lower than DPIP (3.534 eV), indicating that OPIP molecules are more likely to react with the mild steel surface.

In addition, the dipole moment of OPIP (6.166 D) is also higher than DPIP (6.099), reflecting a better reactivity, which is well correlated to the ΔE. On the other hand, Lukovits have found theoretically that If $\Delta N < 3.6$, ΔN indicates the ability to provide electrons to the metal surface (Lukovits et al., 2001; Qiang et al., 2018). In the present work, the ΔN values of the corrosion inhibitors studied are less than 3.6, which indicates that the molecules of the inhibitors are the electron donor and the metal surface is an acceptor.

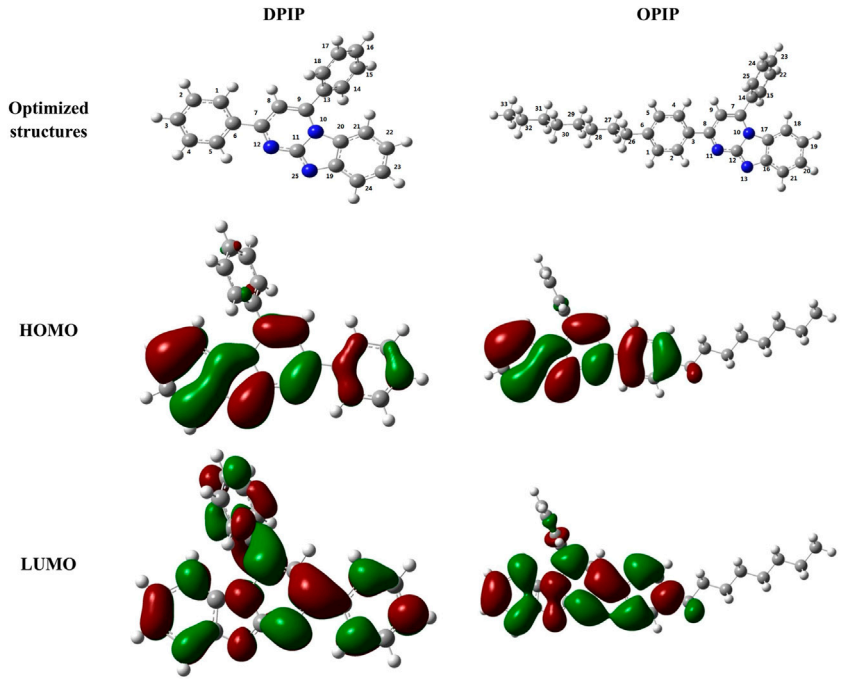

FIGURE 9 | Optimized structures, HOMO, and LUMO of DPIP and OPIP molecules obtained at B3LYP/6–31G level in aqueous solution.

TABLE 5 | Quantum chemical descriptors and MD data of DPIP and OPIP.

Inhibitors	E_{HOMO} (eV)	E_{LUMO} (eV)	ΔE (eV)	μ (D)	ΔN	$E_{interaction}$ (kJ·mol^{-1})	$E_{binding}$ (kJ·mol^{-1})
DPIP	−5.587	−2.053	3.534	6.099	0.2830	−534.67	534.67
OPIP	−5.518	−1.990	3.528	6.166	0.3022	−593.25	593.25

3.8.2 Fukui Index

Fukui index was used to understand the reactivity of DPIP and OPIP inhibitor molecules by identifying the electrophilic and nucleophilic attack sites (f_k^+ and f_k^-). **Supplementary Table S2** shows the Fukui index of corrosion inhibitors in an optimized form calculated in the neutral state in the aqueous phases.

It can be observed that the inhibitor molecule has multiple active donor–acceptors. The preferred sites for electrophilic attacks of the two inhibitors are found mainly on the benzene ring, imidazo ring, and pyrimidine ring, while the preferred sites for nucleophilic attacks are located on the imidazo ring and pyrimidine ring. According to the analysis above, the imidazo [1,2 a] pyrimidine group could be the main reactive site, which suggests that the imidazo [1,2 a] pyrimidine group has a stronger tendency to donate electrons to Fe^{2+} or Fe^{3+} on the Fe (110) surface. This indicates that these sites are liable to be the preferred sites for corrosion inhibitor molecules to adsorb on the mild steel surface.

Further, instead of analyzing the data of the Fukui functions ((f_k^+ and f_k^-), the local softness ($\sigma_k^{\pm}$), and the electrophilicity ($\omega_k^{\pm}$), the results of the dual Fukui function (Δf_k), the dual local softness ($\Delta\sigma_k$), and the dual local philicity ($\Delta\omega_k$) are analyzed and investigated; the graphical representation of the dual local descriptors (Δf_k, $\Delta\sigma_k$, and $\Delta\omega_k$) of the most representative active sites are presented in **Supplementary Figure S2** and **Supplementary Table S2**.

It was reported that if the dual local descriptors (Δf_k, $\Delta\sigma_k$, and $\Delta\omega_k$) are less than 0, the process is favored for an electrophilic attack; however, if (Δf_k, $\Delta\sigma_k$, and $\Delta\omega_k$) > 0, the process is favored for a nucleophilic attack (Geerlings et al., 2012). As results in **Supplementary Table S2** show, the three descriptors Δf_k, $\Delta\sigma_k$, and $\Delta\omega_k$ are lower than 0, which suggests that the two corrosion inhibitors studied have many active centers and have the ability to accept electrons from the metal, while the sites with the Δf_k, $\Delta\sigma_k$, and $\Delta\omega_k$ higher than 0 suggest electrophilic centers (Cuan et al., 2005; Domingo et al., 2016). As results in **Supplementary Table S2** show, the most active sites for electron accepting centers for DPIP and OPIP have the following trend: C14 > C6 > C2 > C17 > C18 > C19 > C24 > C20 > C22 > C11 > C9 > N25 > N10 > N12 > C21 > C8 > C7 > C13 and C14 > C6 > C2 > C17 > C18 > C26 > C19 > C24 > C20 > C22 > N11 > C9 > C25 > N10 > C12 > C21 > C8 > C7 > N13, respectively. However, the most active sites donating active centers for DPIP and OPIP can be arranged as follows: C5 > C3 > C1 > C23 > C15 > C16 > C4 and C5 > C3 > C28 > C1 > C29 > C30 > C27 > C31 > C32 > C33 > C23 > C15 > C16 > C4, respectively.

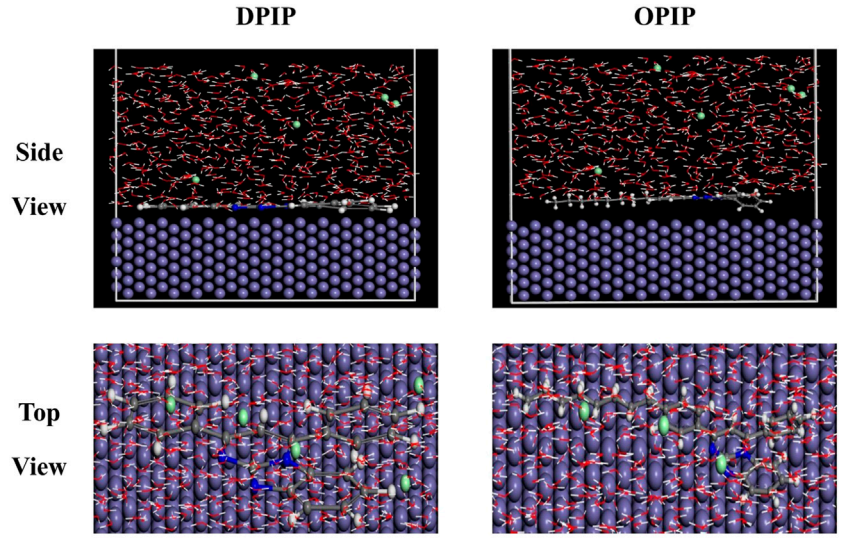

FIGURE 10 | Top and side views of the stable adsorption configuration of DPIP **(A)** and OPIP **(B)** obtained by molecular dynamic simulations on Fe (110).

3.9 MD Simulation Results

The performances of the studied molecules to the migration of corrosive species like Cl^-, H_3O^+, and H_2O are investigated with the help of diffusion coefficient values. The MSD is a microscopic parameter that is involved, defined as:

$$MSD(t) = \left[\frac{1}{N}\sum_{i=1}^{N}|R_i(t) - R_i(0)|^2\right] \quad (24)$$

$$D = \frac{1}{6}\lim_{t\to\infty}\frac{d}{dx}\sum_{i}^{N}\left[|R_i(t) - R_i(0)|^2\right] \quad (25)$$

where $|R_i(t) - R_i(0)|^2$ and N represents the MSD number of target molecules, respectively. The positions of corrosive particles at time t and 0 are given by $R_i(t)$ and R_i (0), respectively.

The MSD curves of Cl^-, H_3O^+, and H_2O in the protective film of DPIP and OPIP are shown in **Supplementary Figure S3**. The magnitude of diffusion coefficients for Cl^-, H_3O^+, and H_2O are 0.3222, 0.7830, and 2.3920 × 10^{-9} m^2/s, respectively (Ehteshamzade et al., 2006). However, the calculated diffusion coefficients for Cl^-, H_3O^+, and H_2O decrease significantly in the film of DPIP and OPIP (**Supplementary Table S3**). This observation reveals that the addition of DPIP and OPIP into the corrosive media generates a protective film over the mild steel surface and creates hindrance in the migration of corrosive species. The reduction in the diffusion coefficient values of OPIP is higher as compared to DPIP, which suggests more protective film formation in the case of OPIP over the metal surface than DPIP. This result further reinforces the superior performance of OPIP than DPIP and supports the experimental finding.

Figure 10 gives the top and side views of the stable adsorption configuration of DPIP and OPIP molecules on the Fe (1 1 0) surface in the presence of chloride ions with the temperatures of 298 K. It can be seen from the figure that the molecules of DPIP and OPIP are adsorbed on the Fe (1 1 0) surface in parallel in the presence of H_2O, H_3O, and Cl^-. This is due to a high number of active electron donor units in the imidazopyrimidine group, which is easier to adsorb with surface atoms on the mild steel substrate (Hsissou et al., 2020).

The interaction energy ($E_{interaction}$) and adsorption energy ($E_{binding}$) are employed to measure the interaction and adsorption capacity of DPIP and OPIP with the very fine surface of Fe (1 1 0), respectively. $E_{interaction}$ and $E_{binding}$ values are calculated according to the following two equations and listed in **Table 5** (Asadi et al., 2019):

$$E_{interaction} = E_{total} - (E_{surface+solution} + E_{inhibitor}) \quad (26)$$

$$E_{binding} = -E_{interaction} \quad (27)$$

The high absolute value of interaction and binding energy indicates the ability to replace the corrosive ions and H_2O molecules to form a protective layer against the corrosive medium (Guo et al., 2017; Rbaa et al., 2019). In this work, the interactions with the Fe (1 1 0)/OPIP interface are greater compared to interactions with the Fe (1 1 0)/DPIP interface, which is due to the carbon chain effect, so that leads to an increase in interactions at the interface. The data in **Table 5** show that the $E_{binding}$ value of OPIP is higher than that of DPIP, indicating the higher adsorption capacity of the compound.

4 CONCLUSION

The use of corrosion inhibitors is one of the important methods for surface modification of mild steel to prevent

corrosion. The synthesized DPIP and OPIP have high corrosion inhibition performance for mild steel in 1 mol L^{-1} HCl solution. Electrochemical test results show that the inhibition efficiency increases with increasing concentration. Both the inhibitors are mixed-type inhibitors in 1 mol L^{-1} HCl solution, and EIS data showed that the corrosion inhibitors played their role by adsorption on the mild steel surface. The adsorption of DPIP and OPIP on the mild steel obeys the Langmuir adsorption isotherm model. The addition of inhibitors leads to an increase in the activation energy of corrosion, indicating that the inhibitor adsorption on the metallic surface increased the energy barrier for the corrosion process. The theoretical calculations by the DFT method reveal that the adsorption of DPIP and OPIP is a chemical adsorption mainly through the bonding of N atoms or aromatic ring to the Fe surface, which is supported by MD simulation.

DATA AVAILABILITY STATEMENT

The original contributions presented in the study are included in the article/**Supplementary Material**, further inquiries can be directed to the corresponding author.

AUTHOR CONTRIBUTIONS

All authors listed have made a substantial, direct, and intellectual contribution to the work and approved it for publication.

SUPPLEMENTARY MATERIAL

The Supplementary Material for this article can be found online at: https://www.frontiersin.org/articles/10.3389/fmats.2022.843522/full#supplementary-material

REFERENCES

Alhaffar, M. T., Umoren, S. A., Obot, I. B., Ali, S. A., and Solomon, M. M. (2019). Studies of the Anticorrosion Property of a Newly Synthesized Green Isoxazolidine for API 5L X60 Steel in Acid Environment. *J. Mater. Res. Techn.* 8, 4399–4416. doi:10.1016/j.jmrt.2019.07.051

Andersen, H. C. (1980). Molecular Dynamics Simulations at Constant Pressure And/or Temperature. *J. Chem. Phys.* 72, 2384–2393. doi:10.1063/1.439486

Anejjar, A., Salghi, R., Zarrouk, A., Zarrok, H., Benali, O., Hammouti, B., et al. (2015). Investigation of Inhibition by 6-Bromo-3-Nitroso-2-Phenylimidazol [1,2-A]pyridine of the Corrosion of C38 Steel in 1 M HCl. *Res. Chem. Intermed* 41, 913–925. doi:10.1007/s11164-013-1244-7

Anusuya, N., Saranya, J., Sounthari, P., Zarrouk, A., and Chitra, S. (2017). Corrosion Inhibition and Adsorption Behaviour of Some Bis-Pyrimidine Derivatives on Mild Steel in Acidic Medium. *J. Mol. Liquids* 225, 406–417. doi:10.1016/j.molliq.2016.11.015

Asadi, N., Ramezanzadeh, M., Bahlakeh, G., and Ramezanzadeh, B. (2019). Utilizing Lemon Balm Extract as an Effective green Corrosion Inhibitor for Mild Steel in 1M HCl Solution: a Detailed Experimental, Molecular Dynamics, Monte Carlo and Quantum Mechanics Study. *J. Taiwan Inst. Chem. Eng.* 95, 252–272. doi:10.1016/j.jtice.2018.07.011

Benhiba, F., Serrar, H., Hsissou, R., Guenbour, A., Bellaouchou, A., Tabyaoui, M., et al. (2020). Tetrahydropyrimido-Triazepine Derivatives as Anti-corrosion Additives for Acid Corrosion: Chemical, Electrochemical, Surface and Theoretical Studies. *Chem. Phys. Lett.* 743, 137181. doi:10.1016/j.cplett.2020.137181

Bouanis, F. Z., Bentiss, F., Traisnel, M., and Jama, C. (2009). Enhanced Corrosion Resistance Properties of Radiofrequency Cold Plasma Nitrided Carbon Steel: Gravimetric and Electrochemical Results. *Electrochimica Acta* 54, 2371–2378. doi:10.1016/j.electacta.2008.10.068

Brug, G. J., Van Den Eeden, A. L. G., Sluyters-Rehbach, M., and Sluyters, J. H. (1984). The Analysis of Electrode Impedances Complicated by the Presence of a Constant Phase Element. *J. Electroanalytical Chem. Interfacial Electrochemistry* 176, 275–295. doi:10.1016/0368-1874(84)83477-210.1016/s0022-0728(84)80324-1

Ciampi, S., and Di castro, V. (1995). XPS Study of the Growth and Reactivity of FeMnO Thin Films. *Surf. Sci.* 331, 294–299. doi:10.1016/0039-6028(95)00190-5

Cuán, A., Galván, M., and Chattaraj, P. K. (2005). A Philicity Based Analysis of Adsorption of Small Molecules in Zeolites. *J. Chem. Sci.* 117, 541–548. doi:10.1007/BF02708360

Domingo, L., Ríos-Gutiérrez, M., and Pérez, P. (2016). Applications of the Conceptual Density Functional Theory Indices to Organic Chemistry Reactivity. *Molecules* 21, 748. doi:10.3390/molecules21060748

Ech-chihbi, E., Belghiti, M. E., Salim, R., Oudda, H., Taleb, M., Benchat, N., et al. (2017). Experimental and Computational Studies on the Inhibition Performance of the Organic Compound "2-phenylimidazo [1,2-A] pyrimidine-3-Carbaldehyde" against the Corrosion of Carbon Steel in 1.0 M HCl Solution. *Surf. Inter.* 9, 206–217. doi:10.1016/j.surfin.2017.09.012

Ehteshamzade, M., Shahrabi, T., and Hosseini, M. G. (2006). Inhibition of Copper Corrosion by Self-Assembled Films of New Schiff Bases and Their Modification with Alkanethiols in Aqueous Medium. *Appl. Surf. Sci.* 252, 2949–2959. doi:10.1016/j.apsusc.2005.05.003

El Azzouzi, M., Aouniti, A., Tighadouin, S., Elmsellem, H., Radi, S., Hammouti, B., et al. (2016). Some Hydrazine Derivatives as Corrosion Inhibitors for Mild Steel in 1.0M HCl: Weight Loss, Electrochemichal, SEM and Theoretical Studies. *J. Mol. Liquids* 221, 633–641. doi:10.1016/j.molliq.2016.06.007

El Faydy, M., Benhiba, F., Lakhrissi, B., Touhami, M. E., Warad, I., Bentiss, F., et al. (2019). The Inhibitive Impact of Both Kinds of 5-Isothiocyanatomethyl-8-Hydroxyquinoline Derivatives on the Corrosion of Carbon Steel in Acidic Electrolyte. *J. Mol. Liquids* 295, 111629. doi:10.1016/j.molliq.2019.111629

El Faydy, M., Touir, R., Ebn Touhami, M., Zarrouk, A., Jama, C., Lakhrissi, B., et al. (2018). Corrosion Inhibition Performance of Newly Synthesized 5-Alkoxymethyl-8-Hydroxyquinoline Derivatives for Carbon Steel in 1 M HCl Solution: Experimental, DFT and Monte Carlo Simulation Studies. *Phys. Chem. Chem. Phys.* 20, 20167–20187. doi:10.1039/C8CP03226B

El-Hajjaji, F., Messali, M., Aljuhani, A., Aouad, M. R., Hammouti, B., Belghiti, M. E., et al. (2018). Pyridazinium-based Ionic Liquids as Novel and green Corrosion Inhibitors of Carbon Steel in Acid Medium: Electrochemical and Molecular Dynamics Simulation Studies. *J. Mol. Liquids* 249, 997–1008. doi:10.1016/j.molliq.2017.11.111

El-Hajjaji, F., Messali, M., Martínez de Yuso, M. V., Rodríguez-Castellón, E., Almutairi, S., Bandosz, T. J., et al. (2019). Effect of 1-(3-phenoxypropyl) Pyridazin-1-Ium Bromide on Steel Corrosion Inhibition in Acidic Medium. *J. Colloid Interf. Sci.* 541, 418–424. doi:10.1016/j.jcis.2019.01.113

El-Taib Heakal, F., Tantawy, N. S., and Shehata, O. S. (2012). Influence of Cerium (III) Ions on Corrosion and Hydrogen Evolution of Carbon Steel in Acid Solutions. *Int. J. Hydrogen Energ.* 37, 19219–19230. doi:10.1016/j.ijhydene.2012.10.037

Fan, C., Zhang, B., Li, Y., Liang, Y., Xue, X., and Feng, Y. (2015). Application-oriented Computational Studies on a Series of D-π-A Structured Porphyrin Sensitizers with Different Electron-Donor Groups. *Phys. Chem. Chem. Phys.* 17, 30624–30631. doi:10.1039/C5CP05625J

Farhadian, A., Varfolomeev, M. A., Rahimi, A., Mendgaziev, R. I., Semenov, A. P., Stoporev, A. S., et al. (2021). Gas Hydrate and Corrosion Inhibition Performance of the Newly Synthesized Polyurethanes: Potential Dual Function Inhibitors. *Energy Fuels* 35, 6113–6124. doi:10.1021/acs.energyfuels.1c00101

Finšgar, M., Fassbender, S., Hirth, S., and Milošev, I. (2009). Electrochemical and XPS Study of Polyethyleneimines of Different Molecular Sizes as Corrosion Inhibitors for AISI 430 Stainless Steel in Near-Neutral Chloride media. *Mater. Chem. Phys.* 116, 198–206. doi:10.1016/j.matchemphys.2009.03.010

Geerlings, P., Ayers, P. W., Toro-Labbé, A., Chattaraj, P. K., and De Proft, F. (2012). The Woodward-Hoffmann Rules Reinterpreted by Conceptual Density Functional Theory. *Acc. Chem. Res.* 45, 683–695. doi:10.1021/ar200192t

Gomma, G. K., and Wahdan, M. H. (1995). Schiff Bases as Corrosion Inhibitors for Aluminium in Hydrochloric Acid Solution. *Mater. Chem. Phys.* 39, 209–213. doi:10.1016/0254-0584(94)01436-K

Guo, L., Kaya, S., Obot, I. B., Zheng, X., and Qiang, Y. (2017). Toward Understanding the Anticorrosive Mechanism of Some Thiourea Derivatives for Carbon Steel Corrosion: a Combined DFT and Molecular Dynamics Investigation. *J. Colloid Interf. Sci.* 506, 478–485. doi:10.1016/j.jcis.2017.07.082

Haque, J., Srivastava, V., Verma, C., and Quraishi, M. A. (2017). Experimental and Quantum Chemical Analysis of 2-amino-3-((4-((S)-2-Amino-2-Carboxyethyl)-1h-Imidazol-2-Yl)thio) Propionic Acid as New and green Corrosion Inhibitor for Mild Steel in 1 M Hydrochloric Acid Solution. *J. Mol. Liquids* 225, 848–855. doi:10.1016/j.molliq.2016.11.011

Hsissou, R., Benhiba, F., Dagdag, O., El Bouchti, M., Nouneh, K., Assouag, M., et al. (2020). Development and Potential Performance of Prepolymer in Corrosion Inhibition for Carbon Steel in 1.0 M HCl: Outlooks from Experimental and Computational Investigations. *J. Colloid Interf. Sci.* 574, 43–60. doi:10.1016/j.jcis.2020.04.022

Kannan, P., Jithinraj, P., and Natesan, M. (2014). Multiphasic Inhibition of Mild Steel Corrosion in H2S Gas Environment. *Arab. J. Chem.* 11, 388–404. doi:10.1016/j.arabjc.2014.10.032

Khadiri, A., Ousslim, A., Bekkouche, K., Aouniti, A., Warad, I., Elidrissi, A., et al. (2018). 4-(2-(2-(2-(2-(Pyridine-4-yl)ethylthio)ethoxy)ethylthio)ethyl)pyridine as New Corrosion Inhibitor for Mild Steel in 1.0 M HCl Solution: Experimental and Theoretical Studies. *J. Bio. Tribo Corros.* 4, 64. doi:10.1007/s40735-018-0179-3

Khadraoui, A., Khelifa, A., Hadjmeliani, M., Mehdaoui, R., Hachama, K., Tidu, A., et al. (2016). Extraction, Characterization and Anti-corrosion Activity of Mentha Pulegium Oil: Weight Loss, Electrochemical, Thermodynamic and Surface Studies. *J. Mol. Liquids* 216, 724–731. doi:10.1016/j.molliq.2016.02.005

Khaled, K. F. (2010). Experimental, Density Function Theory Calculations and Molecular Dynamics Simulations to Investigate the Adsorption of Some Thiourea Derivatives on Iron Surface in Nitric Acid Solutions. *Appl. Surf. Sci.* 256, 6753–6763. doi:10.1016/j.apsusc.2010.04.085

Kozlica, D. K., Kokalj, A., and Milošev, I. (2021). Synergistic Effect of 2-mercaptobenzimidazole and Octylphosphonic Acid as Corrosion Inhibitors for Copper and Aluminium - an Electrochemical, XPS, FTIR and DFT Study. *Corrosion Sci.* 182, 109082. doi:10.1016/j.corsci.2020.109082

Laabaissi, T., Benhiba, F., Rouifi, Z., Missioui, M., Ourrak, K., Oudda, H., et al. (2019). New Quinoxaline Derivative as a green Corrosion Inhibitor for Mild Steel in Mild Acidic Medium: Electrochemical and Theoretical Studies. *Int. J. Corros. Scale Inhib.* 8, 241–256. doi:10.17675/2305-6894-2019-8-2-6

Lee, C., Yang, W., and Parr, R. G. (1988). Local Softness and Chemical Reactivity in the Molecules CO, SCN− and H2CO. *J. Mol. Struct. THEOCHEM* 163, 305–313. doi:10.1016/0166-1280(88)80397-X

Li, H., Zhang, S., and Qiang, Y. (2021). Corrosion Retardation Effect of a green Cauliflower Extract on Copper in H2SO4 Solution: Electrochemical and Theoretical Explorations. *J. Mol. Liquids* 321, 114450. doi:10.1016/j.molliq.2020.114450

Lukovits, I., Kálmán, E., and Zucchi, F. (2001). Corrosion Inhibitors-Correlation between Electronic Structure and Efficiency. *Corrosion* 57, 3–8. doi:10.5006/1.3290328

McCafferty, E., and Hackerman, N. (1972). Double Layer Capacitance of Iron and Corrosion Inhibition with Polymethylene Diamines. *J. Electrochem. Soc.* 119, 146–154. doi:10.1149/1.2404150

Meeusen, M., Zardet, L., Homborg, A. M., Lekka, M., Andreatta, F., Fedrizzi, L., et al. (2020). The Effect of Time Evolution and Timing of the Electrochemical Data Recording of Corrosion Inhibitor protection of Hot-Dip Galvanized Steel. *Corrosion Sci.* 173, 108780. doi:10.1016/j.corsci.2020.108780

Mishra, A., Aslam, J., Verma, C., Quraishi, M. A., and Ebenso, E. E. (2020). Imidazoles as Highly Effective Heterocyclic Corrosion Inhibitors for Metals and Alloys in Aqueous Electrolytes: A Review. *J. Taiwan Inst. Chem. Eng.* 114, 341–358. doi:10.1016/j.jtice.2020.08.034

Monticelli, C., Balbo, A., Esvan, J., Chiavari, C., Martini, C., Zanotto, F., et al. (2019). Evaluation of 2-(salicylideneimino) Thiophenol and Other Schiff Bases as Bronze Corrosion Inhibitors by Electrochemical Techniques and Surface Analysis. *Corrosion Sci.* 148, 144–158. doi:10.1016/j.corsci.2018.12.017

Morell, C., Grand, A., and Toro-Labbé, A. (2006). Theoretical Support for Using the Δf(r) Descriptor. *Chem. Phys. Lett.* 425, 342–346. doi:10.1016/j.cplett.2006.05.003

Nahle, A., El-Hajjaji, F., Ghazoui, A., Benchat, N.-E., Taleb, M., Saddik, R., et al. (2018). Effect of Substituted Methyl Group by Phenyl Group in Pyridazine Ring on the Corrosion Inhibition of Mild Steel in 1.0 M HCl. *Acmm* 65, 87–96. doi:10.1108/acmm-03-2017-1769

Ouici, H., Tourabi, M., Benali, O., Selles, C., Jama, C., Zarrouk, A., et al. (2017). Adsorption and Corrosion Inhibition Properties of 5-amino 1,3,4-Thiadiazole-2-Thiol on the Mild Steel in Hydrochloric Acid Medium: Thermodynamic, Surface and Electrochemical Studies. *J. Electroanalytical Chem.* 803, 125–134. doi:10.1016/j.jelechem.2017.09.018

Padmanabhan, J., Parthasarathi, R., Subramanian, V., and Chattaraj, P. K. (2006). Chemical Reactivity Indices for the Complete Series of Chlorinated Benzenes: Solvent Effect. *J. Phys. Chem. A.* 110, 2739–2745. doi:10.1021/jp056630a

Pan, C., Song, Y., Jin, W., Qin, Z., Song, S., Hu, W., et al. (2020). Enhancing the Stability of Passive Film on 304 SS by Chemical Modification in Alkaline Phosphate-Molybdate Solutions. *Trans. Tianjin Univ.* 26, 135–141. doi:10.1007/s12209-020-00238-8

Parr, R. G., and Yang, W. (1984). Density Functional Approach to the Frontier-Electron Theory of Chemical Reactivity. *J. Am. Chem. Soc.* 106, 4049–4050. doi:10.1021/ja00326a036

Parthasarathi, R., Padmanabhan, J., Elango, M., Subramanian, V., and Chattaraj, P. K. (2004). Intermolecular Reactivity through the Generalized Philicity Concept. *Chem. Phys. Lett.* 394, 225–230. doi:10.1016/j.cplett.2004.07.002

Pech-Canul, M. A., and Bartolo-Pérez, P. (2004). Inhibition Effects of N-phosphono-methyl-glycine/Zn2+ Mixtures on Corrosion of Steel in Neutral Chloride Solutions. *Surf. Coat. Techn.* 184, 133–140. doi:10.1016/j.surfcoat.2003.11.018

Qiang, Y., Guo, L., Li, H., and Lan, X. (2021). Fabrication of Environmentally Friendly Losartan Potassium Film for Corrosion Inhibition of Mild Steel in HCl Medium. *Chem. Eng. J.* 406, 126863. doi:10.1016/j.cej.2020.126863

Qiang, Y., Li, H., and Lan, X. (2020). Self-assembling Anchored Film Basing on Two Tetrazole Derivatives for Application to Protect Copper in Sulfuric Acid Environment. *J. Mater. Sci. Techn.* 52, 63–71. doi:10.1016/j.jmst.2020.04.005

Qiang, Y., Zhang, S., Guo, L., Zheng, X., Xiang, B., and Chen, S. (2017). Experimental and Theoretical Studies of Four Allyl Imidazolium-Based Ionic Liquids as green Inhibitors for Copper Corrosion in Sulfuric Acid. *Corrosion Sci.* 119, 68–78. doi:10.1016/j.corsci.2017.02.021

Qiang, Y., Zhang, S., Tan, B., and Chen, S. (2018). Evaluation of Ginkgo Leaf Extract as an Eco-Friendly Corrosion Inhibitor of X70 Steel in HCl Solution. *Corrosion Sci.* 133, 6–16. doi:10.1016/j.corsci.2018.01.008

Raevsky, O. A., Grigor'ev, V. Y., Liplavskaya, E. A., and Worth, A. P. (2011). Prediction of Acute Rodent Toxicity on the Basis of Chemical Structure and Physicochemical Similarity. *Mol. Inf.* 30, 267–275. doi:10.1002/minf.201000145

Rahmani, H., Alaoui, K. I., Azzouzi, M. E., Benhiba, F., Hallaoui, A. E., Rais, Z., et al. (2019a). Corrosion Assessement of Mild Steel in Acid Environment Using Novel Triazole Derivative as a Anti-corrosion Agent: A Combined Experimental and Quantum Chemical Study. *Chem. Data Collections* 24, 100302. doi:10.1016/j.cdc.2019.100302

Rahmani, H., Alaoui, K. I., Emran, K. M., El Hallaoui, A., Taleb, M., El Hajji, S., et al. (2019b). Experimental and DFT Investigation on the Corrosion Inhibition of Mild Steel by 1, 2, 3- Triazole Regioisomers in 1M Hydrochloric Acid Solution. *Int. J. Electrochem. Sci.* 14, 985–998. doi:10.20964/2019.01.80

Rbaa, M., Benhiba, F., Obot, I. B., Oudda, H., Warad, I., Lakhrissi, B., et al. (2019). Two New 8-hydroxyquinoline Derivatives as an Efficient Corrosion Inhibitors for Mild Steel in Hydrochloric Acid: Synthesis, Electrochemical, Surface Morphological, UV-Visible and Theoretical Studies. *J. Mol. Liquids* 276, 120–133. doi:10.1016/j.molliq.2018.11.104

Saady, A., Rais, Z., Benhiba, F., Salim, R., Ismaily Alaoui, K., Arrousse, N., et al. (2021). Chemical, Electrochemical, Quantum, and Surface Analysis Evaluation on the Inhibition Performance of Novel Imidazo[4,5-B] Pyridine Derivatives against Mild Steel Corrosion. *Corrosion Sci.* 189, 109621. doi:10.1016/j.corsci.2021.109621

Salhi, A., Tighadouini, S., El-Massaoudi, M., Elbelghiti, M., Bouyanzer, A., Radi, S., et al. (2017). Keto-enol Heterocycles as New Compounds of Corrosion

Inhibitors for Carbon Steel in 1 M HCl: Weight Loss, Electrochemical and Quantum Chemical Investigation. *J. Mol. Liquids* 248, 340–349. doi:10.1016/j.molliq.2017.10.040

Salim, R., Ech-chihbi, E., Oudda, H., El Hajjaji, F., Taleb, M., and Jodeh, S. (2019). A Review on the Assessment of Imidazo[1,2-A]pyridines as Corrosion Inhibitor of Metals. *J. Bio. Tribo Corros.* 5, 14. doi:10.1007/s40735-018-0207-3

Singh, A. K., and Quraishi, M. A. (2010). Effect of Cefazolin on the Corrosion of Mild Steel in HCl Solution. *Corrosion Sci.* 52, 152–160. doi:10.1016/j.corsci.2009.08.050

Singh, D. K., Kumar, S., Udayabhanu, G., and John, R. P. (2016). 4(N,N-dimethylamino) Benzaldehyde Nicotinic Hydrazone as Corrosion Inhibitor for Mild Steel in 1 M HCl Solution: An Experimental and Theoretical Study. *J. Mol. Liquids* 216, 738–746. doi:10.1016/j.molliq.2016.02.012

Sliem, M. H., Afifi, M., Bahgat Radwan, A., Fayyad, E. M., Shibl, M. F., Heakal, F. E.-T., et al. (2019). AEO7 Surfactant as an Eco-Friendly Corrosion Inhibitor for Carbon Steel in HCl Solution. *Sci. Rep.* 9, 2319. doi:10.1038/s41598-018-37254-7

Sun, H. (1998). COMPASS: An Ab Initio Force-Field Optimized for Condensed-phase ApplicationsOverview with Details on Alkane and Benzene Compounds. *J. Phys. Chem. B* 102, 7338–7364. doi:10.1021/jp980939v

Tang, Y., Zhang, F., Hu, S., Cao, Z., Wu, Z., and Jing, W. (2013). Novel Benzimidazole Derivatives as Corrosion Inhibitors of Mild Steel in the Acidic media. Part I: Gravimetric, Electrochemical, SEM and XPS Studies. *Corrosion Sci.* 74, 271–282. doi:10.1016/j.corsci.2013.04.053

Temesghen, W., and Sherwood, P. (2002). Analytical Utility of Valence Band X-ray Photoelectron Spectroscopy of Iron and its Oxides, with Spectral Interpretation by Cluster and Band Structure Calculations. *Anal. Bioanal. Chem.* 373, 601–608. doi:10.1007/s00216-002-1362-3

Wagner, C. D., Riggs, W. M., Davis, L. E., Moulder, J. F., and Muilenberg, G. E. (1979). *Handbook of X-Ray Photoelectron Spectroscopy*. USA: Perking-Elmer Corporation, Physical Electronics Division.

Watts, J. F., and Wolstenholme, J. (2003). *An Introduction to Surface Analysis by XPS and AES*. UK: John Wiley & Sons.

Weng, L. T., Poleunis, C., Bertrand, P., Carlier, V., Sclavons, M., Franquinet, P., et al. (1995). Sizing Removal and Functionalization of the Carbon Fiber Surface Studied by Combined TOF SIMS and XPS. *J. Adhes. Sci. Techn.* 9, 859–871. doi:10.1163/156856195X00743

Xia, D.-H., Pan, C., Qin, Z., Fan, B., Song, S., Jin, W., et al. (2020). Covalent Surface Modification of LY12 Aluminum alloy Surface by Self-Assembly Dodecyl Phosphate Film towards Corrosion protection. *Prog. Org. Coat.* 143, 105638. doi:10.1016/j.porgcoat.2020.105638

Yamashita, T., and Hayes, P. (2008). Analysis of XPS Spectra of Fe2+ and Fe3+ Ions in Oxide Materials. *Appl. Surf. Sci.* 254, 2441–2449. doi:10.1016/j.apsusc.2007.09.063

Zarrouk, A., Zarrok, H., Ramli, Y., Bouachrine, M., Hammouti, B., Sahibed-dine, A., et al. (2016). Inhibitive Properties, Adsorption and Theoretical Study of 3,7-Dimethyl-1-(prop-2-Yn-1-Yl)quinoxalin-2(1h)-One as Efficient Corrosion Inhibitor for Carbon Steel in Hydrochloric Acid Solution. *J. Mol. Liquids* 222, 239–252. doi:10.1016/j.molliq.2016.07.046

Zhang, F., Tang, Y., Cao, Z., Jing, W., Wu, Z., and Chen, Y. (2012). Performance and Theoretical Study on Corrosion Inhibition of 2-(4-Pyridyl)-Benzimidazole for Mild Steel in Hydrochloric Acid. *Corrosion Sci.* 61, 1–9. doi:10.1016/j.corsci.2012.03.045

Zhang, G. A., Hou, X. M., Hou, B. S., and Liu, H. F. (2019a). Benzimidazole Derivatives as Novel Inhibitors for the Corrosion of Mild Steel in Acidic Solution: Experimental and Theoretical Studies. *J. Mol. Liquids* 278, 413–427. doi:10.1016/j.molliq.2019.01.060

Zhang, Q. H., Hou, B. S., Li, Y. Y., Zhu, G. Y., Lei, Y., Wang, X., et al. (2021). Dextran Derivatives as Highly Efficient green Corrosion Inhibitors for Carbon Steel in CO2-saturated Oilfield Produced Water: Experimental and Theoretical Approaches. *Chem. Eng. J.* 424, 130519. doi:10.1016/j.cej.2021.130519

Zhang, S. D., Wu, J., Qi, W. B., and Wang, J. Q. (2016). Effect of Porosity Defects on the Long-Term Corrosion Behaviour of Fe-Based Amorphous alloy Coated Mild Steel. *Corrosion Sci.* 110, 57–70. doi:10.1016/j.corsci.2016.04.021

Zhang, W., Li, H.-J., Wang, M., Wang, L.-J., Pan, Q., Ji, X., et al. (2019b). Tetrahydroacridines as Corrosion Inhibitor for X80 Steel Corrosion in Simulated Acidic Oilfield Water. *J. Mol. Liquids* 293, 111478. doi:10.1016/j.molliq.2019.111478

Zhao, H., Zhang, X., Ji, L., Hu, H., and Li, Q. (2014). Quantitative Structure-Activity Relationship Model for Amino Acids as Corrosion Inhibitors Based on the Support Vector Machine and Molecular Design. *Corrosion Sci.* 83, 261–271. doi:10.1016/j.corsci.2014.02.023

Zhao, Z., Sun, J., Tang, H., and Yan, X. (2020). Experimental and Theoretical Studies of Cinnamyl Alcohol as a Novel Corrosion Inhibitor for Copper Foils in Rolling Oil. *Mater. Corrosion* 72, 534–542. doi:10.1002/maco.202011887

Conflict of Interest: The authors declare that the research was conducted in the absence of any commercial or financial relationships that could be construed as a potential conflict of interest.

Publisher's Note: All claims expressed in this article are solely those of the authors and do not necessarily represent those of their affiliated organizations or those of the publisher, the editors and the reviewers. Any product that may be evaluated in this article, or claim that may be made by its manufacturer, is not guaranteed or endorsed by the publisher.

frontiers in Materials

ORIGINAL RESEARCH
published: 04 March 2022
doi: 10.3389/fmats.2022.852731

pH-Responsive Allicin-Based Coatings With Antibacterial and Antifouling Effects in Marine Environments

Xiangping Hao[1,2†], *Weilu Yan*[1,2†], *Ziqing Sun*[1], *Jingzhi Yang*[1,2], *Yun Bai*[1,2], *Hongchang Qian*[1,2], *Thee Chowwanonthapunya*[3,2*] *and Dawei Zhang*[1,2*]

[1]National Materials Corrosion and Protection Data Center, Institute for Advanced Materials and Technology, University of Science and Technology Beijing, Beijing, China, [2]BRI Southeast Asia Network for Corrosion and Protection (MOE), Shunde Graduate School of University of Science and Technology Beijing, Foshan, China, [3]Faculty of International Maritime Studies, Kasetsart University, Chonburi, Thailand

In this work, we report the design of pH-controlled releasing behaviors of polydopamine/tannic acid-allicin@chitosan (PDA/TA-ALL@CS) multilayer coatings to realize antibacterial and antifouling effects. The pH-responsive ALL@CS capsules were prepared using the microemulsion method with about 262–452 nm diameter. The bacteriostasis of ALL@CS microcapsules against *E. coli*, *S. aureus*, and *P. aeruginosa* all exceeded 94% as evaluated using the colony counting method. Because of the protonation in acid environments and deprotonation in alkaline environments for the amino groups of CS, ALL as biocides can be released from the nanocapsules and exert outstanding antibacterial properties. Confirmed by the plate colony counts, the ALL@CS capsules possessed an outstanding antibacterial effect for *E. coli* in acid solutions but were less effective in alkaline solutions. The PDA/TA-ALL@CS-7 coatings showed durable pH-responsive antibacterial activities with an efficiency of ~87% after immersion in pH 8 solutions for seven days. The PDA/TA-ALL@CS coating with controlled release performance and antibacterial properties may provide a new solution for developing antifouling coating applications in the marine environment.

Keywords: antibacterial, antifouling, pH-responsive, nanocapsules, marine environment

OPEN ACCESS

Edited by:
Xiaoqiang Fan,
Southwest Jiaotong University, China

Reviewed by:
Helena P. Felgueiras,
University of Minho, Portugal
Wei Wang,
Ocean University of China, China

***Correspondence:**
Dawei Zhang
dzhang@ustb.edu.cn
Thee Chowwanonthapunya
thee.c@ku.th

†These authors have contributed equally to this work

Specialty section:
This article was submitted to Environmental Degradation of Materials, a section of the journal Frontiers in Materials

Received: *11 January 2022*
Accepted: *11 February 2022*
Published: *04 March 2022*

Citation:
Hao X, Yan W, Sun Z, Yang J, Bai Y, Qian H, Chowwanonthapunya T and Zhang D (2022) pH-Responsive Allicin-Based Coatings With Antibacterial and Antifouling Effects in Marine Environments. Front. Mater. 9:852731. doi: 10.3389/fmats.2022.852731

INTRODUCTION

Biofouling issue in the marine environment brings a series of problems such as decreasing the speed of vehicles, increasing economic losses, and triggering the invasion of exotic species (Lejars et al., 2012). The conventional method comprises painted antifouling coatings containing biocides to restrain the biofouling process of the substrate underwater (Yebra et al., 2004; Banerjee et al., 2011; Bagley et al., 2015; Hao et al., 2016; Jia et al., 2017; Bloecher et al., 2021; Liu et al., 2021). The antifouling property of the coatings is realized through releasing of the antifoulant from the coating, so the releasing rate of the antifoulant is an important issue when designing coatings. Generally, the speed of vehicles has a huge impact on the releasing rate of the antifoulant, and the releasing rate is virtually much higher at high speed (Hao et al., 2020). At the anchor state, the coatings often cannot protect the substrates completely because the microorganism colonization occurs easily, but antifoulant release is more difficult. Hence, exploring antifouling coatings that release

antifoulant as required, especially at low-speed and at anchor states, is a critical guide for the future. Because the secretions such as acetic acid and lactic acid produced by bacterial metabolisms can decrease the pH of the microenvironment to acidic (Qian et al., 2007a; Traba and Liang, 2015; Hao et al., 2019; Saadouli et al., 2021), pH-responsive antifouling coatings have attracted increasing attention and developed rapidly in recent years (Hao et al., 2019; Hao et al., 2020; Huang et al., 2020; Xu et al., 2020).

Chitosan (CS) as a cationic natural polysaccharide not only possesses antibacterial properties but also is a proper candidate for preparing pH-responsive nanocapsules as a shell material because of the protonation and deprotonation of the amino groups (Chen et al., 2021; Hosseini et al., 2022; Tian et al., 2022). Wang et al. and Andrew et al. provided that CS can help to control drug-releasing behaviors by adjusting diffusion, swelling, and stimulus response (Arifin et al., 2006; Lin and Metters, 2006). Cheng et al. designed biodegradable pH-responsive hollow mesoporous silica nanoparticles for the delivery of pheophorbide and doxorubicin. These carriers demonstrated pH-sensitive drug delivery because of the GM/CS capping layer (Yan et al., 2020). Arash et al. prepared a smart drug delivery system using CS nanocapsule-mounted cellulose nanofibrils, and the optimal release of metronidazole molecules was pH 5.8 (Yunessnia lehi et al., 2019). In addition to the wide application in drug delivery and biomedical fields, CS as a representative has also been used to design pH-responsive antifouling systems to acquire smart and controlled releasing of antifoulants. When the bacteria colonize and reproduce near the motionless substrates, the pH of microenvironments will change from alkaline to acidic, and trigger protonation of the amino groups on the side chain of CS, leading to the swelling of the nanocapsules and accelerated releasing of the biocides. Chen et al. had used CS as a capped layer to encapsulate capsaicin, and the amount of released capsaicin was five times higher in a pH 4 environment than that in pH 8.5 (Wang et al., 2018). The abovementioned studies show that precise releasing of antifoulants in the marine environment can be realized by virtue of the pH-responsive character of CS, thus preventing the substrates from biofouling at anchor states and extending the longevity of antifouling coatings.

With the development of low copper and copper-free antifoulants, synthetic and natural biocides have been extensively studied as alternatives to prepare antifouling coating with excellent bactericidal performance (Qian et al., 2007b; Huang et al., 2019; Qian et al., 2019; Yang et al., 2021). Allicin (ALL), as one of the active components of freshly crushed garlic homogenates, has many advantages like broad-spectrum antibacterial effect at low concentrations, anticancer activity, and being less likely to develop bacterial drug resistance (Ankri and Mirelman, 1999; Bhatwalkar et al., 2021; Greef et al., 2021). In addition, Rajaneesh et al. demonstrated that garlic and its compounds have a positive effect on human beings by inhibiting reactive oxygen species, radical scavenging, and preventing DNA damage (Cao et al., 2014; Zhang et al., 2020; Bhatwalkar et al., 2021). Moreover, Breyer showed that garlic compound (ALL) can eliminate mortality on rainbow trout infected with *Aeromonas hydrophila* (Breyer, 2013). These kinds of literature prove that the ALL as an antifoulant is not only harmless to human beings but also has no side effect on marine vertebrates. However, the low stability and solubility of ALL restrict its applications. The disulfide bond, which is the main resource of the antibacterial properties in ALL, is particularly prone to rupture under alkaline conditions (Wills, 1956). One popular approach to solve this problem is to encapsulate allicin with proper encapsulation (Lawson and Hughes, 1992; Janská et al., 2021). For example, Malgorzata et al. designed oil-core nanocapsules based on a derivative of hyaluronic acid to protect garlic oil active components, resulting in preventing sulfur oxidation and maintaining antibacterial activities (Janik-Hazuka et al., 2021). Based on the previous discussion, it is believed that encapsulation of ALL in pH-responsive microcapsules could effectively improve the stability of ALL and achieve the purpose of a pH-controlled releasing process of the antifoulant.

Herein, the pH-responsive ALL@CS nanocapsules which were prepared by microemulsions were mixed with tannic acid (TA) as an anionic polyelectrolyte, followed by alternating deposition with polydopamine (PDA) which has an outstanding film-forming ability to acquire the pH-responsive PDA/TA-ALL@CS-n antifouling coatings. The ALL@CS nanocapsules with different diameters were obtained by adjusting the weight ratio of ALL and CS, and the PDA/TA-ALL@CS-n were prepared by adjusting the doping ratio of ALL@CS nanocapsules in TA solutions. The composite and size of the nanocapsules were evaluated using Fourier transform infrared spectroscopy (FTIR) and dynamic light scattering (DLS). The pH-responsive antibacterial properties of the nanocapsules were detected using DLS and the plate colony method. The composition, morphology, and thickness of the coatings were characterized using FTIR and scanning electron microscope (SEM). The antifouling and antibacterial performance of the PDA/TA-ALL@CS-n coatings were evaluated using the colony counting method and live/dead fluorescence. The ALL releasing behavior in different pH environments was measured using an ultraviolet–visible spectrophotometer (UV-Vis), and the pH-responsive antibacterial properties of the coatings were characterized using the colony counting method.

EXPERIMENTAL SECTION

Materials

CS with a low viscosity <200 mPa S and Tris (hydroxymethyl) aminomethane were provided by Aladdin Chemistry Co. Ltd. (China). ALL with a purity >95%, lecithin with a purity >98%, and dopamine hydrochloride were purchased from Shanghai Macklin Biochemical Co. Ltd. (China). TA was purchased from Sigma-Aldrich (United States). Different pH phosphate-buffered saline (PBS) solutions were stored after sterilization. Live/dead® BacLight TM Bacterial Viability Kit (L13152) was obtained from Thermo Fisher Scientific (America). The *E. coli* (ATCC 8739), *S. aureus* (ATCC 6538), and *P. aeruginosa* (MCCC 1A00099) were purchased from the Institute of Microbiology, Chinese Academy of Sciences, Beijing, China.

Preparation of ALL@CS Nanocapsules

The ALL@CS nanocapsules were synthesized using the microemulsion method (Wang et al., 2018). Different volumes of ALL (60, 35, and 10 μL) were added into the lecithin-containing ethyl alcohol solution. 10 mg of CS was mixed with an aqueous solution with 1% v/v acetic acid. These two solutions were mixed and stirred at room temperature for 2 h, followed by dialysis, to eliminate free ALL and freeze-drying.

Preparation of PDA/TA-ALL@CS-n Coatings

The 316L stainless steel substrates were abraded to 1200 grit with silicon carbide papers and cleaned with acetone, ethanol, and distilled water in ultrasonic baths. After drying with N_2, the coupons were immersed in dopamine hydrochloride (2 mg/ml) with Tris buffer (100 mM, pH 8.5) for 15 min at room temperature in a dark place, and then washed with distilled water smoothly, followed by immersion in different TA-ALL@CS solutions for another 15 min. The volume ratio of TA solution (2 mg/ml) and ALL@CS suspension (1 mg/ml) was 6:4, 7:3, and 8:2. The substrates were alternately dopped in these two solutions according to the abovementioned process about 20 times and dried with N_2.

Antimicrobial Properties of ALL@CS Nanocapsules

The colony counting method was applied to evaluate the antimicrobial ability of the ALL@CS nanocapsules. The initial concentration of each bacterium was about ~10^8 CFU/ml. Every 1 ml of *E. coli* or *S. aureus* suspensions was transformed into 50 ml Luria broth (LB) and incubated at 37°C for 18 h, and 1 ml *P. aeruginosa* suspensions were transformed into 2216 E medium culture and incubated at 30°C for 18 h. Afterward, 200 μL cultivated bacterial suspension was inoculated into 10 ml LB or 2216 E culture medium containing 1 mg/ml CS, ALL, or ALL@CS nanocapsules, and incubated for another 18 h at 37°C or 30°C. 20 μL suspension of each bacterial tube was diluted with physiological saline and spread on a solid medium plate, incubating overnight at corresponding temperature conditions.

pH-Responsive Performance and Antibacterial Properties of ALL@CS Nanocapsules

The ALL releasing behavior in different pH environments was evaluated initially. The dialysis bags with ALL@CS nanocapsule suspension were dialyzed at different pH PBS (pH 5, 6, 7, and 8) solutions for 4 h. The size of the ALL@CS nanocapsules was detected using DLS.

The pH-responsive properties of such nanocapsules were further measured using the colony plate method. The *E. coli* suspension was inoculated into 10 ml PBS solutions (pH 5, 6, 7, and 8) and LB with a 1:1 volume ratio containing ALL@CS nanocapsules, respectively. After incubation for 4 h, 20 μL diluted bacterial suspension was spread on the top of the solid medium and cultivated at 37°C for 18 h.

Antifouling and Antibacterial Properties of PDA/TA-ALL@CS-n Coatings

The colony counting method and live/dead fluorescence analysis were used to evaluate the antimicrobial ability of the PDA/TA-ALL@CS-n coatings. The initial concentration of each bacterium was about ~10^8 CFU/ml. Every 1 ml of *E. coli* or *S. aureus* suspensions was transformed into 50 ml LB and incubated at 37°C for 18 h, and 1 ml *P. aeruginosa* suspension was transformed into 2216E medium culture and incubated at 30°C for 18 h. Thereafter, 200 μL cultivated bacterial suspension was inoculated in a 10-ml sterile tube with different PDA/TA-ALL@CS-n-coated substrates. After incubation for 18 h, 20 μL diluted bacterial suspensions were spread on the top of the solid medium at 37°C or 30°C for 18 h.

The antibacterial and antifouling performances of the PDA/TA-ALL@CS-n coatings were detected using a confocal laser scanning microscope using a Live/dead® BacLight TM Bacterial Viability Kit. Each coated coupon was immersed in different bacterial suspensions for 18 h, and surfaces of the coupons were dyed at a 6-well plate for 20 min at dark places.

pH-Responsive Properties of PDA/TA-ALL@CS-n Coatings

The coated substrates were immersed in 0.1 M different PBS environments with pH values of 5–8 in a static environment. The concentrations of released ALL in different PBS solutions were measured spectroscopically at around 210 nm by UV-Vis after immersion for one, three, five, and seven days (Hathout et al., 2018). The coated coupons were collected, washed with diluted water, and dried with N_2 to detect the antibacterial properties.

The collected coupons were sterilized and taken into the sterile tube containing 200 μL *S. aureus* or *P. aeruginosa* in 10 ml LB or 2216 E culture medium. The suspensions were shaken at 120 rpm and incubated at 37°C or 30°C for 18 h, and each 20 μL diluted bacterial suspension was taken for colony counting by spreading on the solid medium plate and incubating overnight at different temperature conditions.

Characterization

The size and zeta potential of the ALL@CS nanocapsules were detected using Zetasizer Nano ZS90 (Malvern Instrument, Britain). The FTIR VERTEX70 was manufactured by Burker (Germany). The thickness and the morphology of the PDA/TA-ALL@CS-n coatings were demonstrated using SEM (Jeol JSM-F100, Japan). The UV-Vis used was manufactured by Thermo Biomates 3S (Thermo, America). The CLSM (Zeiss Observer Z1, Germany) was applied to determine the fluorescent assay.

RESULTS AND DISCUSSION

Characterization of the Prepared ALL@CS Nanocapsules

FTIR spectra of the CS, ALL, and the product we prepared are evaluated and demonstrated in **Figure 1**. On the ALL spectrum,

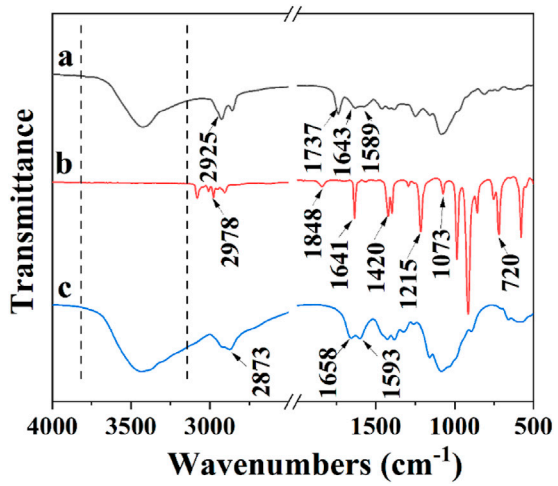

FIGURE 1 | FTIR spectra of ALL@CS **(A)**, ALL **(B)**, and CS **(C)**.

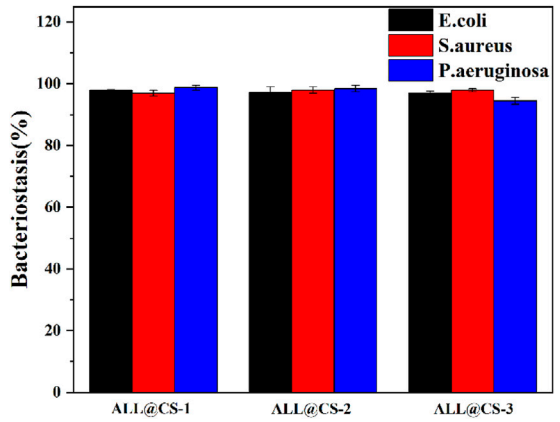

FIGURE 2 | Bacteriostasis of different ALL@CS nanocapsules against *E. coli*, *S. aureus*, and *P. aeruginosa*.

TABLE 1 | Mean hydrodynamic diameter, PDI, and zeta potential of nanocapsules made using different proportions of CS and ALL.

No	CS (mg)	ALL (μL)	Size (nm)	PDI	Zeta potential (mV)
1	10	60	261.7 ± 3.9	0.54 ± 0.07	7.7 ± 1.1
2	10	35	333.8 ± 3.5	0.32 ± 0.07	32.8 ± 1.6
3	10	10	452.3 ± 1.5	0.33 ± 0.01	40.6 ± 0.2
4	10	/	/	/	41.7 ± 0.4
5	/	60	/	/	−25.9 ± 0.7

the peaks at 2978 cm^{-1} and 1420 cm^{-1} belong to C-H stretching (Zhou et al., 2021). 1641 cm^{-1} and 1073 cm^{-1} peaks are associated with the C=C stretching vibration and S=O stretching vibration, respectively. The peaks at 1215 cm^{-1} and 720 cm^{-1} are attributed to S-S single bond (Kumar et al., 2021; Zhou et al., 2021). As for the spectrum of products, it is similar to the CS spectrum. The broad peak at 3300–3200 cm^{-1} can be seen in these two spectra which are contributed with the O-N and N-H stretching vibration (Lawrie et al., 2007). 2873 cm^{-1} peak on CS spectrum and 2925 cm^{-1} on product spectrum are associated with the C-H stretching vibration. The peaks located at 1658 cm^{-1} and 1593 cm^{-1} which belong to the N-H bending vibration of the amino group appear on the spectrum a at 1643 cm^{-1} and 1589 cm^{-1} (Wang et al., 2018). In addition, the new peak appears at 1737 cm^{-1} on the spectrum a because of the H-bond between CS and ALL (Gu et al., 2018). The 1848 cm^{-1} on the ALL curve is disappeared in spectrum a, indicating the inclusion interaction between ALL and CS attenuated the absorption of the guest molecular moiety (Zhou et al., 2021).

Table 1 summarizes the mean diameter, polydispersity index (PDI), and zeta potential of the ALL@CS nanocapsules synthesized at different weight ratios with CS and ALL. The zeta potential is positive for CS but is negative for pure ALL. The nanocapsules are all positively charged like CS, suggesting that the negative surface charge of free ALL is completely covered by cationic CS. This result agrees well with the FTIR result. Moreover, the ratio of CS and ALL impacts the zeta potential and diameter of the ALL@CS nanocapsules. With the decrease of the ratio, the size of the nanocapsules increases from 261.7 ± 3.9 nm to 452.3 ± 1.5 nm and the zeta potential increases from 7.7 ± 1.1 mV to 40.6 ± 0.2 mV. According to the DLVO theory, the stability of the system becomes lower as the size of the ALL@CS nanocapsules decreases because the balance between the Van der Waals force and the electrostatic repulsive force is broken (Hao et al., 2019). It means the ALL@CS-1 nanocapsule systems are not stable, and the zeta potential data also support this conclusion.

Antibacterial Properties and pH-Responsive Mechanism of ALL@CS Nanocapsules

E. coli and *S. aureus* were selected as representative Gram-negative bacterium and Gram-positive bacterium, and *P. aeruginosa* was selected as the marine bacteria representative strain. The antibacterial properties of three kinds of ALL@CS nanocapsules were evaluated using the colony counting method to choose the optimal preparation parameter. In **Figure 2**, all of these nanocapsules exhibit outstanding antibacterial effects, with the bacteriostasis rates ranging from 94.5 to 98.7%. The antibacterial properties of All@CS-3 nanocapsules are relatively poor of the three different diameter nanocapsules, and the bacteriostasis rates of *E. coli*, *S. aureus*, and *P. aeruginosa* are about 97.0, 98.0, and 94.5%, respectively. ALL@CS-1 and All@CS-2 nanocapsules show similar antibacterial properties, which surpass 97.03% against these three different bacterial strains. Considering the stability of the nanocapsules shown in **Table 1** and the ALL dosage, ALL@CS-2 nanocapsules were selected in the following study.

The antibacterial properties of pure CS, ALL, and ALL@CS nanocapsules were further evaluated using the colony counting method. Generally, CS and ALL have excellent antibacterial properties, and the antibacterial effect improves after synthesis

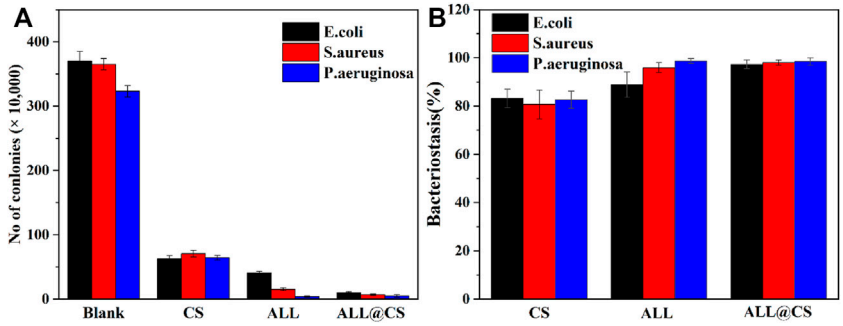

FIGURE 3 | Number of *E. coli*, *S. aureus*, and *P. aeruginosa* colonies in LB and 2216E medium for 18 h with pure CS, ALL, and ALL@CS nanocapsules **(A)**. The bacteriostasis of these three different bacteria strains corresponding to each counting result **(B)**.

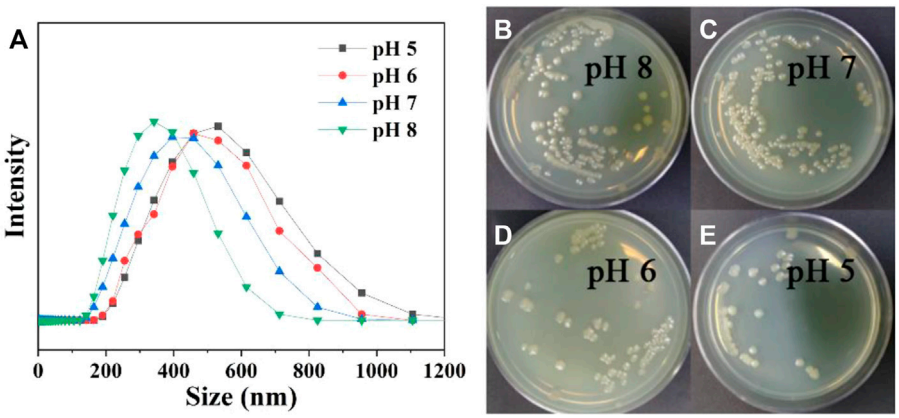

FIGURE 4 | Size of ALL@CS nanocapsules in different pH PBS solutions **(A)**. The plate colony images of ALL@CS incubating with *E. coli* for about 4 h **(B–E)**.

of ALL@CS as shown in **Figure 3**. In **Figure 3A**, after incubation for 18 h, the colonies of *E. coli* on the solid medium are about 370 CFU for the control group, and there are about 63, 41, and 10 CFU after incubation with the pure CS, ALL, and ALL@CS nanocapsules. According to **Figure 3B**, the bacteriostasis rate of ALL@CS against *E. coli* is 97.3%, which is increased by ~14.3 and ~8.4% compared with that of pure CS and ALL. The bacteriostasis rates of pure CS, ALL, and ALL@CS nanocapsules against *S. aureus* are 80.6, 95.9, and 98.0%, respectively. Regarding the antibacterial effects on *P. aeruginosa*, there are approximately 323 CFU for the control group and 5 CFU of the group with ALL@CS; that is, the bacteriostasis rate of ALL@CS is ~98.5%. The results revealed that the antibacterial properties of the ALL after encapsulating CS were almost unaffected or even slightly improved.

The pH-responsive properties of the ALL@CS nanocapsules were evaluated using DLS and the colony plate method. In **Figure 4A**, with the pH of the PBS environment decreasing from 8 to 5, the size of the ALL@CS increases from about 342.0 to 531.2 nm because of the protonation of the amino group CS. Under acidic conditions (i.e., pH 5 and 6), the ALL@CS nanocapsules exhibit swelling behaviors because the internal electrostatic repulsion of the system increased resulting from the NH_2 transformation to NH_3^+ (Lee and Mooney, 2012; Hao et al., 2019). However, the nanocapsules can remain at a smaller diameter which is about 396.1 and 342.0 nm in a neutral and alkaline environment, respectively. Meanwhile, the antibacterial performance against *E. coli* under different pH environments is different. **Figures 4B–E** demonstrate that after being treated with pH 8 and 7 solutions, the number of colonies is more than that with the pH 6 and 5 counterparts, and the colony count is minimal on the solid medium after incubation in pH 5 PBS environments, indicating that the ALL@CS nanocapsules have better antibacterial properties in acidic environments. Combined with the DLS results, the ALL@CS nanocapsules are swollen under an acidic environment, leading to the increased amount of released ALL and thus the stronger antibacterial effect. On the contrary, under the neutral and alkaline environment, the nanocapsules present a smaller diameter which restricts the releasing of ALL and leads to an inhibited antibacterial property. Hence, the ALL can be kept in the nanocapsules under alkaline conditions such as marine environments, and kill bacteria when the pH value drops due to bacteria reproduction under the anchoring state.

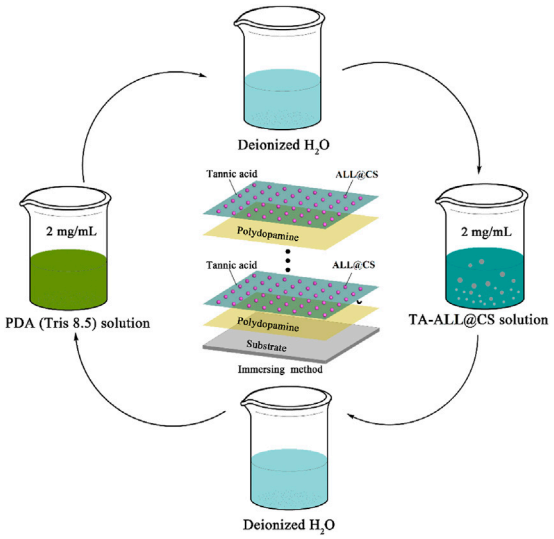

FIGURE 5 | Schematic diagram of the preparation procedure of PDA/TA-ALL@CS coatings.

Characterization of the Prepared PDA/TA-ALL@CS Coatings

The PDA/TA@ALL@CS coatings were fabricated by a layer-by-layer technique as shown in **Figure 5**, and the FTIR spectra of TA, PDA, TA-ALL@CS, and PDA/TA-ALL@CS are demonstrated in **Figure 6**. For the spectrum of TA, the broad peak at 3300 cm^{-1} is composed of the O-H stretching vibration (Dutta et al., 2021). The 1717 cm^{-1} and 1210 cm^{-1} peaks are accounted for the C=O and C-O stretching vibration, respectively (Dutta et al., 2021; Ricci et al., 2015). The peak at 1618 cm^{-1} belongs to the C=C stretching vibration, and the peak at 760 cm^{-1} is attributed to the O-H in a carboxylic group (Dutta et al., 2021; Ricci et al., 2015). In spectrum c, the broad peak at 3500 cm^{-1} to 3300 cm^{-1} belongs to the N-H and O-H stretching vibration of the ALL@CS nanocapsules, and the peaks located at 2947 cm^{-1}which also appears in the spectrum of ALL@CS (**Figure 1** spectrum a) are assigned to the C-H stretching vibration. These results demonstrated that the ALL@CS existed in this system. Moreover, the absorption peaks contributed by C=O and O-H in the carboxylic group of TA also appeared at 1717 cm^{-1} and 760 cm^{-1}, respectively, on spectrum c, indicating that the TA also existed in this system. Hence, the TA-ALL@CS layer was prepared successfully. For the spectrum of PDA, the broad peak at 3300 cm^{-1} is assigned to the N-H stretching vibration, and the peaks at 1618 cm^{-1} and 1518 cm^{-1} belong to the C=C and C=N stretching vibrations of the benzene ring, respectively (Hao et al., 2019). As for spectrum d, the characterization of the curve is similar with spectrum b from 3500 cm^{-1} to 2500 cm^{-1}, which means the stretching vibration of N-H and O-H from PDA is existing in this coating. Furthermore, the 1516 cm^{-1} peak belongs to the C=N stretching vibration from the benzene ring, revealing that the PDA is introduced in this coating further. The peaks at 1717 cm^{-1} (C=O), 1618 cm^{-1} (C=C), and 760 cm^{-1} (O-H) are witnessed in spectrum d demonstrating that the TA/ALL@CS also appears in such coatings. Hence, the PDA/TA-ALL@CS coatings were prepared by the immersion method successfully.

The thickness of the PDA/TA-ALL@CS-n coating was evaluated using SEM, and the results are shown in **Figures 7A-C**. Interestingly, the thickness of the coatings did not increase when the ratio of the ALL@CS nanocapsules increased. The thickness of the PDA/TA-ALL@CS-6, PDA/TA-ALL@CS-7, and PDA/TA-ALL@CS-8 coatings was ~1.9, ~2.0, and ~1.6 μm, respectively. In the top view of these three coatings, the number of introduced nanocapsules was the most for PDA/TA-ALL@CS-7 coatings (**Figure 7E**). Because the amount of the ALL@CS was fewest in the TA-ALL@CS-8 mixture, there were fewer nanocapsules dispersed in the coatings (**Figure 7F**). While for PDA/TA-ALL@CS-6 coating, with the number of nanocapsules increased, precipitation could occur in the mixture due to electrostatic interaction between TA and the ALL@CS nanocapsules, and restrict the deposition process of the TA-ALL@CS layer.

Antibacterial Properties of PDA/TA-ALL@CS-n Coatings

The colony counting method was used to assess the antibacterial properties of the PDA/TA-ALL@CS-6, PDA/TA-ALL@CS-7, and PDA/TA-ALL@CS-8 coatings. **Figure 8** shows that all these three coatings exhibit good antibacterial effects against *E. coli*, *S. aureus*, and *P. aeruginosa*. In **Figure 8A**, the number of the colonies on the surface of the solid medium is lowest after incubation with PDA/TA-ALL@CS-7 coatings in regard to all these three bacteria, which is about 45, 46, and 46 CFU for *E. coli*, *S. aureus*, and *P. aeruginosa*, respectively. Compared with the control group, the bacteriostasis of these three kinds of bacteria is ~89.2, ~89.2, and ~90.7% (**Figure 8B**), respectively. After

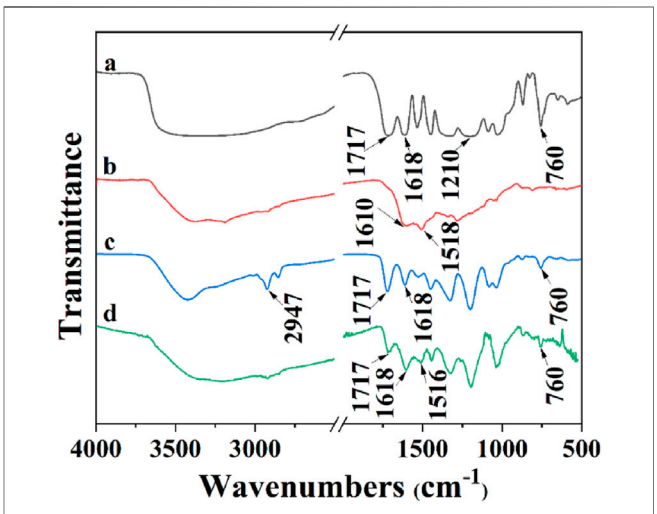

FIGURE 6 | FTIR of TA **(A)**, PDA **(B)**, TA-ALL@CS **(C)**, and PDA/TA-ALL@CS coatings **(D)**.

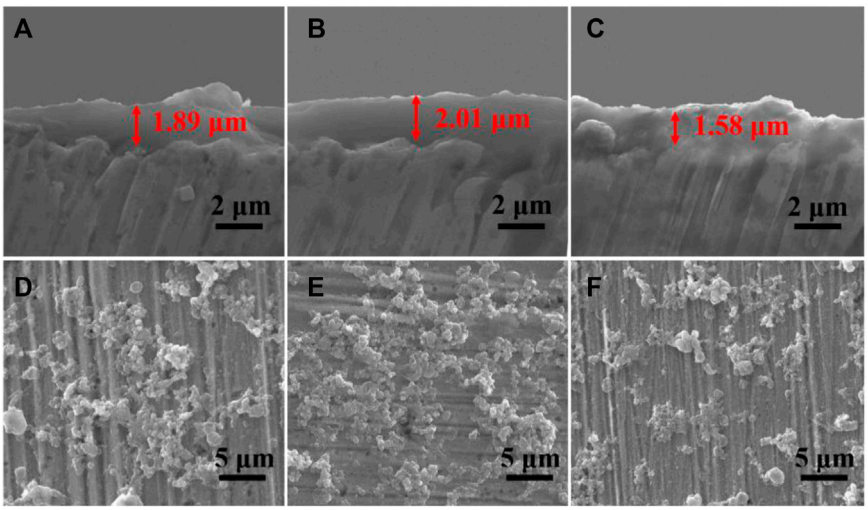

FIGURE 7 | Cross-section and top-view SEM images of PDA/TA-ALL@CS-6 coatings **(A, D)**; PDA/TA-ALL@CS-7 coatings **(B, E)** and PDA/TA-ALL@CS-8 coatings **(C, F)**.

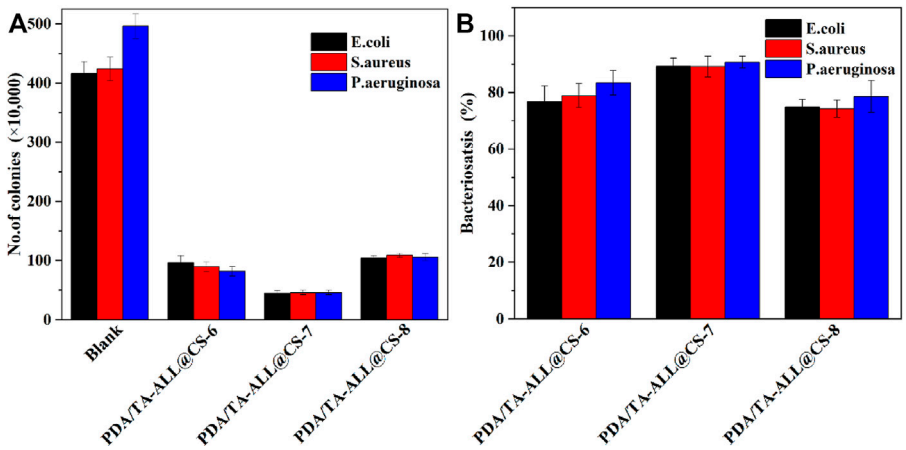

FIGURE 8 | Number of *E. coli*, *S. aureus*, and *P. aeruginosa* bacterial colonies on the solid medium after incubation with the controlled specimen and prepared coatings in Luria-Bertani medium for 18 h **(A)**; the bacteriostasis of *E. coli*, *S. aureus*, and *P. aeruginosa* for the PDA/TA-ALL@CS-n coatings **(B)**. For PDA/TA-ALL@CS-6, PDA/TA-ALL@CS-7, and PDA/TA-ALL@CS-8 coatings, the volume ratios of TA solution to ALL@CS suspension were about 6:4, 7:3, and 8:2, respectively.

incubation with PDA/TA-ALL@CS-8 coated substrates, there are about 104, 109, and 106 CFU on the solid medium, and the antibacterial performance is about 74.9, 74.3, and 78.6% for *E. coli*, *S. aureus*, and *P. aeruginosa*, respectively. According to **Figure 7F**, the number of the introduced ALL@CS nanocapsules is less than that of the other two coatings, which could be the reason why the antibacterial performance is not ideal. Compared with the PDA/TA-ALL@CS-8 group, the antibacterial properties of the PDA/TA-ALL@CS-6 coatings are also lower than the PDA/TA-ALL@CS-7 counterparts, which is decreased by ~12.4, ~10.3, and ~7.3%, respectively.

Generally, the surfaces of the specimens coated with PDA/TA-LL@CS-n have remarkable antibacterial properties. After dying, **Figures 9A–A_2** exhibit almost green spots in view, indicating the bare coupons have little antibacterial properties and nearly all of the bacteria are alive. A few green spots can be witnessed on the PDA/TA-ALL@CS-6 (**Figures 9B–B_2**) and PDA/TA-ALL@CS-8 (**Figures 9D–D_2**), but there are almost all red spots in the view of the PDA/TA-ALL@CS-7 coating surface as seen in a (**Figures 9C–C_2**). This demonstrated that the antibacterial and antifouling effects of the PDA/TA-ALL@CS-7 coating are better than the other coatings. Combined with the results shown in Figures 7D–F, the antibacterial property of the coating was affected by the introduced quantity and dispersion of ALL@CS. Hence, the PDA/TA-ALL@CS-7 coating was selected to evaluate the pH-responsive antibacterial and antifouling bacterial properties.

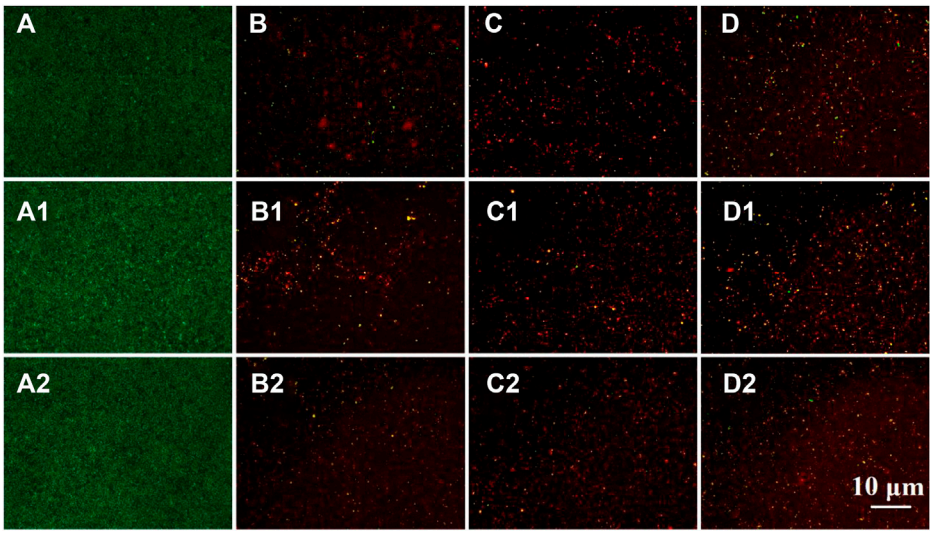

FIGURE 9 | BacLight Live/Dead Kit Assay staining of *E. coli*, *S. aureus*, and *P. aeruginosa* colonized on the bare coupon **(A–A$_2$)**, and the specimens coated with PDA/TA-ALL@CS-6 **(B–B$_2$)**, PDA/TA-ALL@CS-7 **(C–C$_2$)**, PDA/TA-ALL@CS-8 **(D–D$_2$)**, respectively.

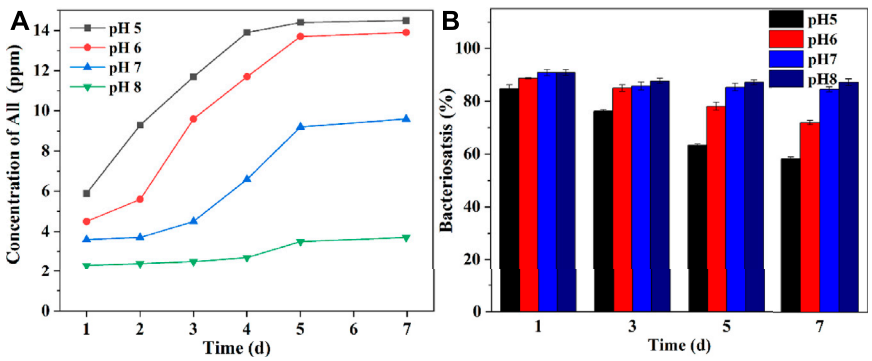

FIGURE 10 | Concentration of ALL released from the PDA/TA-ALL@CS-7 coatings in different pH PBS solutions **(A)**. The bacteriostasis of the PDA/TA-ALL@CS-7 coatings against *P. aeruginosa* after being immersed in different pH PBS solutions for seven days **(B)**.

pH-Responsive Properties of the PDA/TA-ALL@CS Coatings

The releasing behaviors of ALL and the antibacterial properties of the immersed PDA/TA-ALL@CS coatings in different pH PBS (pH 5, 6, 7, and 8) were evaluated using UV-Vis and the colony counting method. In **Figure 10A**, with the increasing pH value of the PBS, the concentration of the released ALL from the coating decreases apparently. After seven days of immersion in pH 5, the amount of released ALL increased gradually from~5.9 ppm to ~14.5 ppm. The concentration of released ALL increased from ~4.5 to ~13.9 ppm after immersion in pH 6 solutions. The release of the ALL was more rapid in the first five days. When the coated coupon was immersed in a neutral solution, the release of the ALL became slower, which was about 3.6, 4.5, 9.2, and 9.6 ppm for released ALL from one, three, five, and seven days, respectively. Because the protonation of the nanocapsules was restricted in an alkaline environment, the amount of the released ALL was maintained at a very low level (3.7 ppm) after immersion in pH 8 PBS solutions for seven days. Hence, the PDA/TA-ALL@CS coatings showed good pH-responsive properties and could restrict the release of antifoulants in the marine environment when bacterial reproduction did not occur.

To further determine the antibacterial effects of PDA/TA-ALL@CS coatings, the bacteriostasis of the PDA/TA-ALL@CS coatings against *P. aeruginosa* after immersion in different pH solutions for seven days is shown in **Figure 10B**. The antibacterial efficiency decreased dramatically after immersion in an acidic environment but was maintained at a high level after immersion in an alkaline environment. The antibacterial properties decreased from ~84.7% after one day to ~58.1% after seven days of immersion in pH 4 PBS solution. As for the pH 5 group, the bacteriostasis rate decreased from ~88.7% after one day to 71.9% after seven days. However, after immersion

in a neutral PBS for seven days, the bacteriostasis only decreased by ~6.4%. When immersed in an environment with a pH value similar to seawater (pH 8), the PDA/TA-ALL@CS coating could maintain an outstanding antibacterial property after seven days, which was ~87.1% (decreased by 3.7%). The above results demonstrated that the PDA/TA-ALL@CS coatings maintained remarkable antibacterial and antifouling properties after immersion for seven days in an alkaline environment, and released ALL to kill bacteria when the pH of the microenvironment was decreased by bacterial reproduction.

CONCLUSION

In this work, the ALL@CS nanocapsules are synthesis by the emulsion method. These nanocapsules exhibit outstanding antibacterial properties against *E. coli*, *S. aureus*, and *P. aeruginosa*. Because of the protonation of CS, the ALL@CS nanocapsules have pH-responsive properties, which can release an amount of ALL in acidic environments and maintain the releasing rate at a low level in alkaline environments. When preparation of the PDA/TA-ALL@CS coatings, the volume ratio of TA and nanocapsules affects the amount of ALL@CS introduced on the coating, and the proper parameters are 7:3 of the volume ratio. The antibacterial and antifouling properties of PDA/TA-ALL@CS-7 coatings are best against *E. coli*, *S. aureus*, and *P. aeruginosa*, and the bacteriostasis is all above 89.2%. Moreover, the PDA/TA-ALL@CS-7 coatings also process pH-responsive properties. The releasing behaviors of ALL differ greatly under seven days of immersion in different pH environments. The ALL release was faster in an acidic environment and slower in an alkaline environment. The ALL contained in the PDA/TA-ALL@CS coating impacts the antibacterial performance directly. After seven days of immersion in pH 8 environment solution, the bacteriostasis of the coatings was still about 87.2%. This work of PDA/TA-ALL@CS coatings supports the idea to design smart antifouling coatings and solve the biofouling problems at the anchoring state.

DATA AVAILABILITY STATEMENT

The original contributions presented in the study are included in the article/Supplementary Material, further inquiries can be directed to the corresponding authors.

AUTHOR CONTRIBUTIONS

XH: investigation, methodology, and writing—original draft. WY: investigation and methodology. ZS: investigation and methodology. JY: investigation. YB: investigation. HQ: investigation. TC: investigation, supervision, and writing-review and editing. DZ: supervision, conceptualization, methodology, writing—original draft, and writing—review and editing. All the authors contributed to the discussion of the work.

FUNDING

The work was supported by the China Postdoctoral Science Foundation (2021M700381) and the Postdoctoral Research Foundation of Shunde Graduate School of University of Science and Technology Beijing (2021BH003).

REFERENCES

Ankri, S., and Mirelman, D. (1999). Antimicrobial Properties of Allicin from Garlic. *Microbes Infect.* 1, 125–129. doi:10.1016/s1286-4579(99)80003-3

Arifin, D. Y., Lee, L. Y., and Wang, C.-H. (2006). Mathematical Modeling and Simulation of Drug Release from Microspheres: Implications to Drug Delivery Systems. *Adv. Drug Deliver. Rev.* 58, 1274–1325. doi:10.1016/j.addr.2006.09.007

Bagley, F., Atlar, M., Charles, A., and Anderson, C. (2015). The Use of Copper-Based Antifoulings on Aluminium Ship Hulls. *Ocean Eng.* 109, 595–602. doi:10.1016/j.oceaneng.2015.09.044

Banerjee, I., Pangule, R. C., and Kane, R. (2011). Antifouling Coatings: Recent Developments in the Design of Surfaces that Prevent Fouling by Proteins, Bacteria, and marine Organisms. *Adv. Mater.* 23, 690–718. doi:10.1002/adma.201001215

Bhatwalkar, S. B., Mondal, R., Krishna, S. B. N., Adam, J. K., Govender, P., and Anupam, R. (2021). Antibacterial Properties of Organosulfur Compounds of Garlic (Allium Sativum). *Front. Microbiol.* 12, 613077. doi:10.3389/fmicb.2021.613077

Bloecher, N., Solvang, T., and Floerl, O. (2021). Efficacy Testing of Novel Antifouling Systems for marine Sensors. *Ocean Eng.* 240, 109983. doi:10.1016/j.oceaneng.2021.109983

Breyer, K. (2013). Evaluating the Efficacy of a Low-Dose Garlic Compound (Allicin) against Infection with Aeromonas Salmonicida in Rainbow trout. *Acta Microbiol. Imm. H.* http://hdl.handle.net/1813/34286.

Cao, H., Zhu, K., Fan, J., and Qiao, L. (2014). Garlic-derived Allyl Sulfides in Cancer Therapy. *Anticancer Agents Med. Chem.* 14, 793–799. doi:10.2174/1871520614666140521120811

Chen, H., Zhi, H., Liang, J., Yu, M., Cui, B., Zhao, X., et al. (2021). Development of Leaf-Adhesive Pesticide Nanocapsules with pH-Responsive Release to Enhance Retention Time on Crop Leaves and Improve Utilization Efficiency. *J. Mater. Chem. B.* 9, 783–792. doi:10.1039/d0tb02430a

Dutta, N., Hazarika, S., and Maji, T. K. (2021). Study on the Role of Tannic Acid–Calcium Oxide Adduct as a green Heat Stabilizer as Well as Reinforcing Filler in the Bio-Based Hybrid Polyvinyl Chloride–Thermoplastic Starch Polymer Composite. *Polym. Eng. Sci.* 61, 2339–2348. doi:10.1002/pen.25761

Greef, D., Barton, E. M., Sandberg, E. N., Croley, C. R., Pumarol, J., Wong, T. L., et al. (2021). Anticancer Potential of Garlic and its Bioactive Constituents: A Systematic and Comprehensive Review. *Semin. Cancer Biol.* 73, 219–264. doi:10.1016/j.semcancer.2020.11.020

Gu, H., Xu, X., Zhang, H., Liang, C., Lou, H., Ma, C., et al. (2018). Chitosan-coated-magnetite with Covalently Grafted Polystyrene Based Carbon Nanocomposites for Hexavalent Chromium Adsorption. *Eng. Sci.* 1, 46–54. doi:10.30919/es.180308

Hao, X., Chen, S., Qin, D., Zhang, M., Li, W., Fan, J., et al. (2020). Antifouling and Antibacterial Behaviors of Capsaicin-Based pH Responsive Smart Coatings in marine Environments. *Mater. Sci. Eng. C Mater. Biol. Appl.* 108, 110361. doi:10.1016/j.msec.2019.110361

Hao, X., Chen, S., Yu, H., Liu, D., and Sun, W. (2016). Metal Ion-Coordinated Carboxymethylated Chitosan Grafted Carbon Nanotubes with Enhanced Antibacterial Properties. *RSC Adv.* 6, 39–43. doi:10.1039/c5ra21003h

Hao, X., Wang, W., Yang, Z., Yue, L., Sun, H., Wang, H., et al. (2019). pH Responsive Antifouling and Antibacterial Multilayer Films with Self-Healing Performance. *Chem. Eng. J.* 356, 130–141. doi:10.1016/j.cej.2018.08.181

Hathout, R. M., Metwally, A. A., El-Ahmady, S. H., Metwally, E. S., Ghonim, N. A., Bayoumy, S. A., et al. (2018). Dual Stimuli-Responsive Polypyrrole

Nanoparticles for Anticancer Therapy. *J. Drug Deliv. Sci. Tec.* 47, 176–180. doi:10.1016/j.jddst.2018.07.002

Hosseini, S. F., Ghaderi, J., and Gómez-Guillén, M. C. (2022). Tailoring Physico-Mechanical and Antimicrobial/antioxidant Properties of Biopolymeric Films by Cinnamaldehyde-Loaded Chitosan Nanoparticles and Their Application in Packaging of Fresh Rainbow trout Fillets. *Food Hydrocolloid.* 124, 107249. doi:10.1016/j.foodhyd.2021.107249

Huang, L., Lou, Y., Zhang, D., Ma, L., and Li, X. (2019). d -Cysteine Functionalised Silver Nanoparticles Surface with a "Disperse-Then-Kill" Antibacterial Synergy. *Chem. Eng. J.* 381, 122662. doi:10.1016/j.cej.2019.122662

Huang, X., Mutlu, H., and Theato, P. (2020). A Bioinspired Hierarchical Underwater Superoleophobic Surface with Reversible pH Response. *Adv. Mater. Inter.* 7, 2000101. doi:10.1002/admi.202000101

Janik-Hazuka, M., Kamiński, K., Kaczor-Kamińska, M., Szafraniec-Szczęsny, J., Kmak, A., Kassassir, H., et al. (2021). Hyaluronic Acid-Based Nanocapsules as Efficient Delivery Systems of Garlic Oil Active Components with Anticancer Activity. *Nanomaterials.* 11, 1354. doi:10.3390/nano11051354

Janská, P., Knejzlík, Z., Perumal, A. S., Jurok, R., Tokárová, V., Nicolau, D. V., et al. (2021). Effect of Physicochemical Parameters on the Stability and Activity of Garlic Alliinase and its Use for *In-Situ* Allicin Synthesis. *Plos One.* 16, e0248878. doi:10.1371/journal.pone.0248878

Jia, Z., Liu, Y., Wang, Y., Gong, Y., Jin, P., Suo, X., et al. (2017). Technology, Flame spray Fabrication of Polyethylene-Cu Composite Coatings with Enwrapped Structures: A New Route for Constructing Antifouling Layers. *Surf. Coat. Tech.* 309, 872–879. doi:10.1016/j.surfcoat.2016.10.071

Kumar, H., Yadav, V., Saha, S. K., and Kang, N. (2021). Adsorption and Inhibition Mechanism of Efficient and Environment Friendly Corrosion Inhibitor for Mild Steel: Experimental and Theoretical Study. *J. Mol. Liq.* 338, 116634. doi:10.1016/j.molliq.2021.116634

Lawrie, G., Keen, I., Drew, B., Chandler-Temple, A., Rintoul, L., Fredericks, P., et al. (2007). Interactions between Alginate and Chitosan Biopolymers Characterized Using FTIR and XPS. *Biomacromolecules.* 8, 2533–2541. doi:10.1021/bm070014y

Lawson, L. D., and Hughes, B. G. (1992). Characterization of the Formation of Allicin and Other Thiosulfinates from Garlic, Planta. *Med.* 58, 345–350. doi:10.1055/s-2006-961482

Lee, K. Y., and Mooney, D. J. (2012). Alginate: Properties and Biomedical Applications. *Prog. Polym. Sci.* 37, 106–126. doi:10.1016/j.progpolymsci.2011.06.003

Lejars, M., Margaillan, A., and Bressy, C. (2012). Fouling Release Coatings: A Nontoxic Alternative to Biocidal Antifouling Coatings. *Chem. Rev.* 112, 4347–4390. doi:10.1021/cr200350v

Lin, C.-C., and Metters, A. T. (2006). Hydrogels in Controlled Release Formulations: Network Design and Mathematical Modeling. *Adv. Drug Deliver. Rev.* 58, 1379–1408. doi:10.1016/j.addr.2006.09.004

Liu, M., Li, S., Wang, H., Jiang, R., and Zhou, X. (2021). Research Progress of Environmentally Friendly marine Antifouling Coatings. *Polym. Chem.* 12, 3702–3720. doi:10.1039/d1py00512j

Qian, H., Yang, J., Lou, Y., and Rahman, O. (2019). Mussel-inspired Superhydrophilic Surface with Enhanced Antimicrobial Properties under Immersed and Atmospheric Conditions. *Appl. Surf. Sci.* 465, 267–278. doi:10.1016/j.apsusc.2018.09.173

Qian, H., Liu, S., Wang, P., Huang, Y., Lou, Y., Huang, L., et al. (2007a). Investigation of Microbiologically Influenced Corrosion of 304 Stainless Steel by Aerobic Thermoacidophilic Archaeon Metallosphaera Cuprina. *Bioelectrochemistry.* 136, 107635.

Qian, P. Y., Lau, S. C. K., Dahms, H. U., Dobretsov, S., and Harder, T. (2007b). Marine Biofilms as Mediators of Colonization by marine Macroorganisms: Implications for Antifouling and Aquaculture. *Mar. Biotechnol.* 9, 399–410. doi:10.1007/s10126-007-9001-9

Ricci, A., Olejar, K. J., Parpinello, G. P., Kilmartin, P. A., and Versari, A. (2015). Application of Fourier Transform Infrared (FTIR) Spectroscopy in the Characterization of Tannins. *Appl. Spectrosc. Rev.* 50, 407–442. doi:10.1080/05704928.2014.1000461

Saadouli, I., Mosbah, A., Ferjani, R., Stathopoulou, P., Galiatsatos, I., Asimakis, E., et al. (2021). The Impact of the Inoculation of Phosphate-Solubilizing Bacteria Pantoea Agglomerans on Phosphorus Availability and Bacterial Community Dynamics of a Semi-arid Soil. *Microoganisms.* 9, 1661. doi:10.3390/microorganisms9081661

Tian, B., Cheng, J., Zhang, T., Liu, Y., and Chen, D. (2022). Multifunctional Chitosan-Based Film Loaded with Hops β-acids: Preparation, Characterization, Controlled Release and Antibacterial Mechanism. *Food Hydrocolloid.* 124, 107337. doi:10.1016/j.foodhyd.2021.107337

Traba, C., and Liang, J. F. (2015). Bacteria Responsive Antibacterial Surfaces for Indwelling Device Infections. *J. Control Release.* 198, 18–25. doi:10.1016/j.jconrel.2014.11.025

Wang, W., Hao, X., Chen, S., Yang, Z., and Guo, Z. (2018). pH-Responsive Capsaicin@chitosan Nanocapsules for Antibiofouling in marine Applications. *Polymer.* 158, 223–230. doi:10.1016/j.polymer.2018.10.067

Wills, E. D. (1956). Enzyme Inhibition by Allicin, the Active Principle of Garlic. *Biochem. J.* 63, 514–520. doi:10.1042/bj0630514

Xu, G., Neoh, K. G., Kang, E.-T., and Teo, S. L.-M. (2020). Switchable Antimicrobial and Antifouling Coatings from Tannic Acid-Scaffolded Binary Polymer Brushes. *ACS Sustain. Chem. Eng.* 8, 2586–2595. doi:10.1021/acssuschemeng.9b07836

Yan, T., He, J., Liu, R., Liu, Z., and Cheng, J. (2020). Chitosan Capped pH-Responsive Hollow Mesoporous Silica Nanoparticles for Targeted Chemo-Photo Combination Therapy. *Carbohyd. Polym.* 231, 115706. doi:10.1016/j.carbpol.2019.115706

Yang, J., Qian, H., Wang, J., Ju, P., Lou, Y., Li, G., et al. (2021). Mechanically Durable Antibacterial Nanocoatings Based on Zwitterionic Copolymers Containing Dopamine Segments. *J. Mater. Sci. Technol.* 89, 233–241. doi:10.1016/j.jmst.2020.11.031

Yebra, D. M., Kiil, S., and Dam-Johansen, K. (2004). Antifouling Technology-Past, Present and Future Steps towards Efficient and Environmentally Friendly Antifouling Coatings. *Prog. Org. Coat.* 50, 75–104. doi:10.1016/j.porgcoat.2003.06.001

Yunessnia lehi, A., Shagholani, H., Ghorbani, M., Nikpay, A., Soleimani lashkenari, M., and Soltani, M. (2019). Chitosan Nanocapsule-Mounted Cellulose Nanofibrils as Nanoships for Smart Drug Delivery Systems and Treatment of Avian Trichomoniasis. *J. Taiwan Inst. Chem. E* 95, 290–299. doi:10.1016/j.jtice.2018.07.014

Zhang, Y., Liu, X., Ruan, J., Zhuang, X., Zhang, X., and Li, Z. (2020). Pharmacotherapy, Phytochemicals of Garlic: Promising Candidates for Cancer Therapy. *Biomed. Pharmacother.* 123, 109730. doi:10.1016/j.biopha.2019.109730

Zhou, Y., Feng, J., Peng, H., Guo, T., Xiao, J., Zhu, W., et al. (2021). Allicin Inclusions with α-cyclodextrin Effectively Masking its Odor: Preparation, Characterization, and Olfactory and Gustatory Evaluation. *J. Food Sci.* 86, 4026–4036. doi:10.1111/1750-3841.15882

Conflict of Interest: The authors declare that the research was conducted in the absence of any commercial or financial relationships that could be construed as a potential conflict of interest.

Publisher's Note: All claims expressed in this article are solely those of the authors and do not necessarily represent those of their affiliated organizations, or those of the publisher, the editors, and the reviewers. Any product that may be evaluated in this article, or claim that may be made by its manufacturer, is not guaranteed or endorsed by the publisher.

frontiers in Materials

ORIGINAL RESEARCH
published: 21 March 2022
doi: 10.3389/fmats.2022.848123

Hydrogen Permeation Behavior of Carbon Steel During Corrosion in Highly Pressed Saturated Bentonite

Qichao Zhang[1,2], Yishan Jiang[2], Xin Zhao[2], Penglei Song[2], Tingting Kuang[1], Juna Chen[2], Zhongtao Sun[2], Yaopeng Zhang[2], Xiayu Ai[2], Dongzhu Lu[1] and Yanliang Huang[1]**

[1]CAS Key Laboratory of Marine Environment of Corrosion and Bio-fouling, Institute of Oceanology, Chinese Academy of Sciences, Qingdao, China, [2]Navy Submarine Academy, Qingdao, China

Deep geological disposal is the most reliable method for high-level nuclear waste, of which metal container as the first barrier for deep geological disposal of high-level nuclear waste is particularly important. Carbon steel is used as a container material because of the low possibility of local corrosion in bentonite. However, after the storage is closed, the decrease of oxygen content will create a near-field environment where the hydrogen embrittlement (HE) in the corrosion process of the container could happen. To evaluate the safety of containers in deep geological disposal of Beshai, the preselected area in China, hydrogen permeation efficiency and HE were estimated in highly pressed saturated bentonite by electrochemical and extrapolation analyses. It is concluded that hydrogen permeation efficiency increases with the disposal year, which proves that the hydrogen evolution reaction dominates the cathode process in the corrosion during long-term disposal. However, slow strain rate tensile shows that Q235 steel has a low HE sensitivity.

Keywords: hydrogen embrittlement, metal corrosion, hydrogen permeation, bentonite, nuclear waste

OPEN ACCESS

Edited by:
Qixin Zhou,
University of Akron, United States

Reviewed by:
Long Hao,
Corrosion and Protection Center of Materials, Institute of Metal Research Chinese Academy of Sciences, Shenyang, China
Ang Liu,
Qingdao University of Technology, China

****Correspondence:***
Dongzhu Lu
421241006@qq.com
Yanliang Huang
263342066@qq.com

Specialty section:
This article was submitted to Environmental Degradation of Materials, a section of the journal Frontiers in Materials

Received: *04 January 2022*
Accepted: *21 January 2022*
Published: *21 March 2022*

Citation:
Zhang Q, Jiang Y, Zhao X, Song P, Kuang T, Chen J, Sun Z, Zhang Y, Ai X, Lu D and Huang Y (2022) Hydrogen Permeation Behavior of Carbon Steel During Corrosion in Highly Pressed Saturated Bentonite. Front. Mater. 9:848123. doi: 10.3389/fmats.2022.848123

INTRODUCTION

As low-carbon energy, nuclear power plays an important role in new energy and is an important basis for realizing the sustainable development of energy in various countries. High-level nuclear waste (HLNW) produced during the use of nuclear energy has the characteristics of strong radioactivity of calorific value, high toxicity, and extremely long decay time (Zhang et al., 2020). According to the nuclear power development plan in China, it is expected that there will be produced 3,200 tons of nuclear waste every year in 2030. Therefore, the safe disposal of nuclear waste is an unavoidable and urgent problem in the development of nuclear energy.

The disposal of nuclear waste is a difficult problem globally (Shoesmith, 2000; Hu and Cheng, 2015). At present, deep geological disposal is the most reliable technology for the disposal of HLNW (Ewing, 2015); that is, nuclear waste solidified in glass is stored in the metal container, surrounded by clay and other buffer materials, then placed in the special disposal repository situated between 500 and 1,000 m underground.

How to deal with nuclear waste efficiently has become a global problem. Various nuclear waste disposal programs have been proposed in the world: space disposal, deep-sea disposal, deep geological disposal, etc. (Arup, 1985; Milnes, 1985; Bradley, 1997). At present, deep geological disposal is generally accepted as the most realistic treatment (Duquette et al., 2009; Guo et al., 2020); that is, nuclear waste will be buried in a disposal repository approximately 500–1,000 m underground, making it completely isolated from the human living environment. Now, China

has selected the Beishan area of Gansu Province as the preselected area of high-level nuclear disposal. The repository contains a "multi-barrier protection system" with engineering barriers including vitrified waste bodies, metal containers, buffer backfill materials, and natural barriers including surrounding rocks, its surrounding geological constructions. Among them, the metal container as the first engineering barrier is particularly important, and its integrity is a necessary factor to ensure that the nuclear waste does not leak. Once the corrosion of the metal container happens during the long disposal process, nuclear waste will migrate with groundwater into the biosphere. It is necessary to study various factors that affect the corrosion behavior of containers in deep geological environments to evaluate the container's safety and reliability.

Container corrosion is related to its surrounding environment. It mainly includes oxygen content (after the repository closed and some oxygen trapped), temperature (nuclear waste decay heat release), and radiation (strong radioactivity of nuclear waste), which are the factors affecting the container corrosion in the deep geological environment. However, the near-field environment of the container will change with the disposal year. For example, the temperature will experience a rise to a drop (up to 360 K), the oxygen content will drop to an anaerobic condition, and the γ radiation intensity will also decrease. Carbon steel is used as a candidate material for the container in countries such as Japan, South Korea, and Canada because of its simple manufacturing process and low cost (King and Padovani, 2011). Liu et al. (2019a, b) studied the corrosion behavior of X65 low-carbon steel during the low-oxygen transition and the anaerobic stage of geological disposal. The results show that the corrosion type is mainly uniform corrosion. The corrosion rate decreases significantly with oxygen reduction, and the corrosion process is controlled by diffusion. The authors' group (Zhang et al., 2019) studied the corrosion behavior of Q235 steel in the highly pressed bentonite environment. It is shown that the maximum corrosion rate appeared in the range of 343–363 K and then decreased when the temperature decreased. Stoulil et al. (2013) studied the effect of temperature on the corrosion rate of low-carbon steel in bentonite environments, and the experiments were carried out at 313 and 363 K. The results show that the higher the temperature, the denser the corrosion product layer, the corrosion rate is slightly slower than that at 313 K, and the color of the corrosion product formed at different temperatures is different. Liu et al. (2018) studied the effect of γ irradiation on the corrosion behavior of X65 low-carbon steel in deep geological groundwater environments. It was found that irradiation increases the empty potential strength of the carbon steel and reduces the open circuit potential, thus accelerating the corrosion rate. Smart et al. (2008) separately studied the effects of different irradiation intensities on the anaerobic corrosion of carbon steel and found that irradiation can increase the corrosion rate. At the higher dose rate, the radiation enhances the corrosion rate most, and some unknown high oxidative corrosion products form.

However, after the repository construction is finished, the oxygen content around the container decreases rapidly and even returns to an anaerobic environment, and hydrogen evolution corrosion may play an important role. The research shows that even under the condition of aerobic corrosion, the reduction of hydrogen ions will also happen, and hydrogen will permeate into carbon steel (Huang and Zhu, 2005; Tsuru et al., 2005). Therefore, hydrogen evolution corrosion will accompany the whole corrosion process of the container. The results reflect that although low-carbon steel shows low sensitivity to stress corrosion and hydrogen embrittlement (HE), its plasticity decreases in slow strain rate tensile (SSRT) under hydrogen charging. The container has circumferential tensile stress under decay thermo-mechanical coupling, up to 57% of the tensile strength (Zhang et al., 2013). During the long disposal process, the container may also be damaged by strong crustal movement such as an earthquake. Therefore, due to the long-term permeation of hydrogen into carbon steel, there may be a risk of HE, which needs to be studied. In this paper, the hydrogen permeation efficiency (HPE) and HE sensitivity of Q235 steel in highly pressed bentonite were studied by accelerated electrochemical test and SSRT. The possibility of HE for Q235 steel as the nuclear waste container on a large time scale was comprehensively analyzed and evaluated.

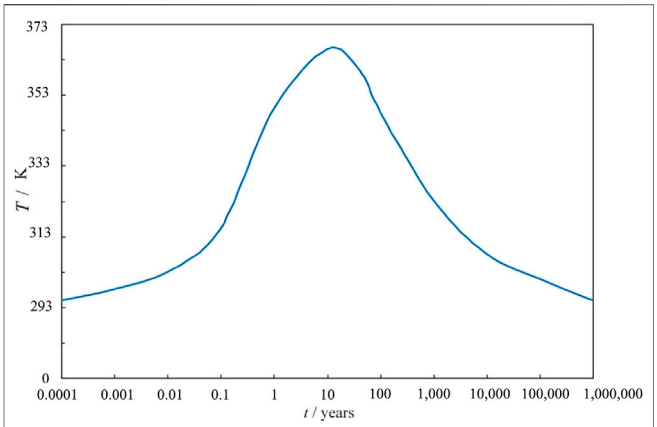

FIGURE 1 | Temperature evolution with time near HLNW container for China.

EXPERIMENTAL

Materials

For the specimens used in the corrosion electrochemical test, the carbon steel materials were cut to dimensions of ϕ10 × 10-mm columnar specimens, which were cleaned with absolute ethanol and dried in the cold air. The copper conductor was attached to one end of the specimen and sealed in a polytetrafluoroethylene tube with epoxy resin, and the other end is the working surface with an area of 0.785cm^2. For the specimens used in the hydrogen permeation electrochemical test, hollow barrel specimens with dimensions of ϕ40 mm × 100 mm were obtained. For the SSRT test, circular carbon steel specimens with a cross-sectional radius of 2 mm and a gauge length of 25mm were used.

TABLE 1 | Predicted temperature corresponding to disposal time.

T/K	363	348	340	323	308	301
t/years	10	100	300	1,000	10,000	100,000

Corrosion Environment Simulation

As we know that the corrosion behavior of metal materials is closely related to their surrounding environment, it is necessary to determine the near-field environment of a nuclear waste container. Nuclear waste containers need to be buried in deep geological disposal for tens of thousands or even hundreds of thousands of years, and the near-field environment will change over time. At present, most studies focus on models to simulate them. The environmental conditions mainly include the following aspects: 1) Temperature. The change of temperature is mainly due to the heat generated by the decay of radionuclides, which is mainly transmitted from the nuclear waste through radiation, convection, and conduction (Seetharam et al., 2006). The evolution law is shown in **Figure 1**. For the deep geological disposal of China's HLNW, the lowest temperature is approximately 295 K, and the temperature reaches the maximum of 363 K after 10 years. This paper mainly evaluates the life of the container on a large time scale, so it focuses on the situation after 10 years. The experiment will use a gradient cooling method by a thermostat or a water bath to simulate the real environmental temperature drop after 10 years. The corresponding age to a specific temperature is shown in **Table 1**. (2) groundwater composition. Zheng et al. (2016) summarized composition of groundwater in Beishan, which is mainly alkaline, including cations such as Na^+ and K^+, while anions including $HCO3^-$, Cl^-, and so on. Components of artificial groundwater simulation solution used in experiment are shown in **Table 2**. (3) Buffer backfill materials. There are two kinds of materials to choose from. Sweden, Finland, and Canada (Rasilainen, 2004; Rosborg and Werme, 2008) used bentonite as a buffer backfill material, whereas Belgium used concrete (Yang et al., 2008). This paper mainly focuses on corrosion behavior of container in bentonite as a buffer backfill material. Components are shown in **Table 3**.

According to **Figure 2**, the groundwater in the buffer backfill material is saturated in approximately 10 years. Therefore, the life prediction of the container on a large time scale is more concerned about the situation after the bentonite reaches saturation.

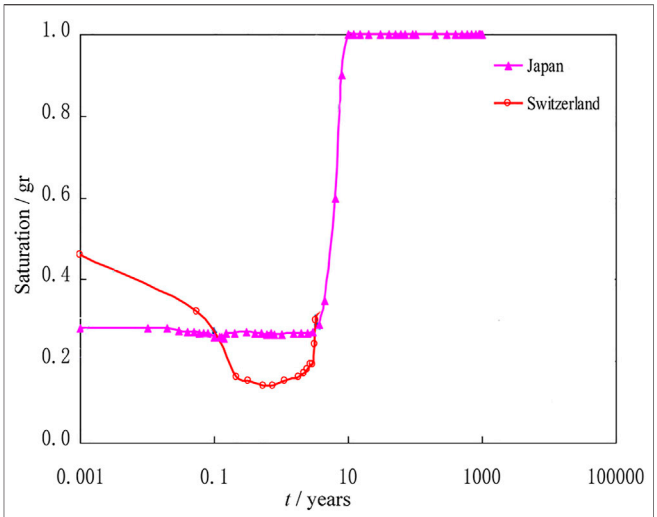

FIGURE 2 | Model of buffer material saturation for HLNW container in short- and long-term.

Experimental Setups and Procedures

As shown in **Figure 3**, it is the device including the hydrogen charging and measurement system for researching the HPE of carbon steel in saturated highly pressed bentonite. The barreled specimen was filled with highly pressed saturated Gaomiaozi-Na-bentonite with simulated groundwater solution as a wetting solution. The measurement was carried out by Model PS-8 Multichannel Potentiostat/Galvanostat. For the hydrogen charging system, a three-electrode system was adopted, the working electrode was the barreled carbon steel specimen, the internal reference was a solid Ag/AgCl electrode, and the counter electrode was the stainless steel shaft (also used as the pressing bentonite device). For the hydrogen measurement system, the three-electrode system was also used, the barreled specimen was still used as the working electrode, the external reference electrode was the HgO/Hg electrode, and the stainless steel barrel wrapped with the carbon steel specimen was the counter electrode. The solution between the specimen and the stainless steel barrel was filled with 0.2 mol L^- NaOH solution. Constant current densities of 0.01–100 A m^{-2} were used for the hydrogen charging system, and a constant potential of 0 V *vs.* (HgO/Hg) was used for the hydrogen measurement system. A thermostated water bath was used to control the temperatures from 298 to 373 K.

As shown in **Figure 4**, the total amount of hydrogen evolution was calculated by subtracting the background current and then integrating the amount of the area under the curve. According to the volume V of the specimen and the formula (1), combined with Faraday's law, the hydrogen concentration in the specimen could finally be calculated.

$$C_H = Q_H/V\,(\mathrm{mg\,m^{-3}}) \quad (1)$$

TABLE 2 | Simulated chemical components of groundwater in Beishan area (mg/L).

Component	$NaNO_3$	KCl	$NaHCO_3$	$MgSO_4{\cdot}7H_2O$	$CaCl_2$	NaCl	Na_2SO_4
Content	37.153	38.205	138.418	571.585	579.193	1,487.465	1,577.697

TABLE 3 | Chemical compositions of Gaomiaozi-Na-bentonite (mass fraction/%).

Component	Al_2O_3	SiO_2	P_2O_5	CaO	K_2O	TiO_2	FeO	TFe_2O_3	MgO	Na_2O	MnO	Loss on ignition
Mass fraction	14.24	68.40	0.05	0.99	0.68	0.14	0.26	2.53	3.31	1.62	0.036	7.67

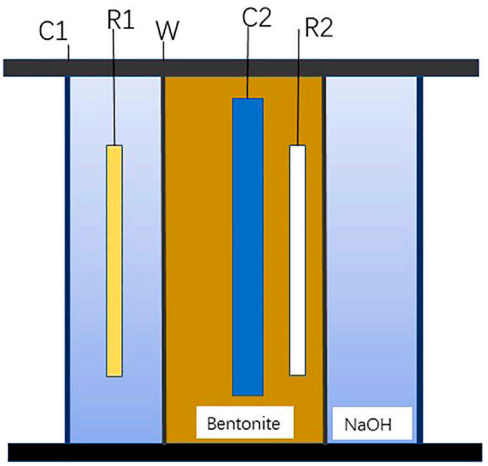

FIGURE 3 | Double electrolytic cell device for hydrogen permeation test of Q235 steel in saturated compacted bentonite.

SSRT mainly judges the HE risk of candidate material for a container. Because hydrogen diffuses extremely quickly in steel, a group control test was carried out: 1) The specimen was not treated in any way and exposed to the air for the tensile test; 2) the specimen was not treated in any way and immersed in 0.2 mol L^{-1} NaOH solution for the tensile test; 3) the specimen was charging in 0.2 mol L^{-1} NaOH solution with a current density of 1 mA cm^{-2} for 15 h and 7 days and then exposed to the air for the tensile test; 4) the tensile test was carried out while the specimen charging in 0.2 mol L^{-1} NaOH solution with current densities of 0.01 and 1 mA cm^{-2}. The morphology of the fracture surface was observed by scanning electron microscope. The experiments discussed earlier were performed at room temperature.

RESULTS AND DISCUSSION

Effect of γ Radiation on Corrosion

The effect of radiation on hydrogen permeation mainly depends on the effect on the steel corrosion behavior. Thus, the effect of γ radiation on steel corrosion was studied. The steel specimens irradiated by γ radiation for 3 months and 1 year were tested in saturated high-pressure bentonite (groundwater content 30%) for potential polarization curve. The fitting results were compared with that of the unirradiated specimens. **Figure 5** shows the corrosion current densities of steel unirradiated and irradiated for 3 months and 1 year in saturated highly compacted bentonite at different temperatures. The results found that the corrosion rate of irradiated steel is significantly higher than that without irradiation at high temperatures, and it increases with the irradiation time.

The maximum corrosion rate of steel irradiated for 3 months and 1 year occurred at the temperature of 348 K, corresponding to the 100 years in deep geological disposal. Because the voids of the compacted bentonite are initially filled with water, the oxygen concentration is low. Oxygen has not yet diffused on the metal surface. The maximum corrosion current density reaches 49.34 μA cm^{-2} after 1 year of irradiation and reaches 17.24 μA cm^{-2} after 3 months of irradiation, which was much higher than 0.77 μA cm^{-2} without irradiation. With the increasing geological disposal year, the film of corrosion product is denser, and the temperature will continue to decrease. The content and diffusion of oxygen determine the cathodic reaction rate, so the corrosion current density of the specimen after radiation gradually decreases as the temperature decreases. However, it is still higher than that of unirradiated in the same period. The main reason is that γ irradiation changes the electrochemical state of metals, which is more obvious at higher temperatures. Liu et al. (2017) studied the corrosion behavior of X65 low-carbon steel unirradiated and irradiated in deep geological environments at

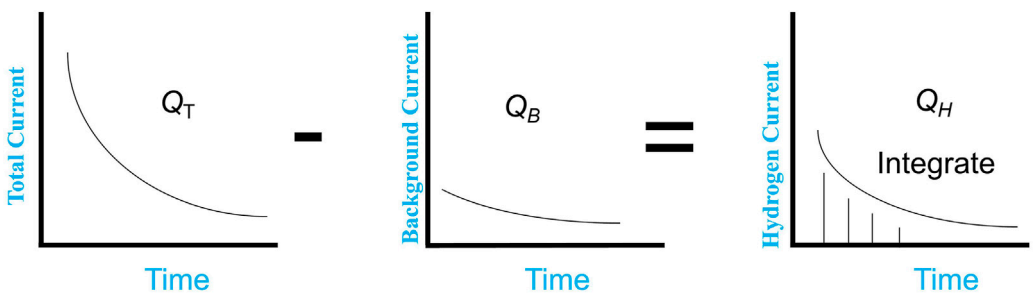

FIGURE 4 | Calculation method of hydrogen concentration.

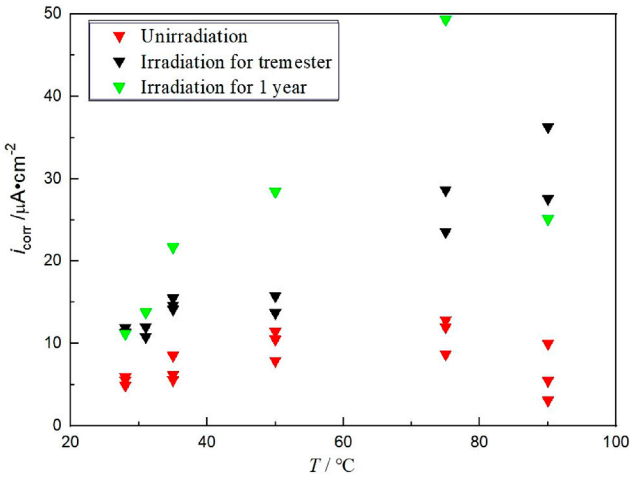

FIGURE 5 | Corrosion current density of Q235 steel unirradiated and irradiated for 3 months and 1 year in saturated highly compacted bentonite at different temperatures.

the temperature of 363 K. It was found that γ irradiation of 2.98 kGy h^{-1} increased the corrosion rate of X65 steel by 33% and that γ irradiation caused two new phases of siderite and magnetite formed. Winsley et al. (2013) studied the effect of irradiation on the corrosion behavior of carbon steel in alkaline simulated pore water (pH = 13.4) at the temperature of 298 and 353 K. The corrosion rate is determined according to the hydrogen production. However, the results found that the hydrogen production rate did not increase significantly under γ radiation of 25 Gy h^{-1}. These results show that the effect of γ irradiation on the corrosion of carbon steel containers is obvious in a higher temperature environment.

The results discussed earlier indicate that γ irradiation could accelerate the corrosion of the steel at high temperatures. However, compared with the whole geological disposal period of nuclear waste containers, the high-temperature stage only exists for a short time. Meanwhile, it is predicted that after the disposal of HLNW, the initial irradiation dose rate on the outer surface of the HLNW container is approximately 0.2–2 Gy h^{-1}, then it will be reduced by one order of magnitude every 100 years according to the difference of vitrified solid waste, container, spatial layout, and thickness (Guo-ding, 2000; Dong et al., 2015). This shows that the radioactivity of nuclear waste will gradually weaken, and the effect of radiation on the container can be basically ignored in the large time-scale prediction. Therefore, the long-term corrosion rate model could refer to the prediction results of a previous study (Zhang et al., 2019).

Hydrogen Permeation Efficiency of Carbon Steel During Corrosion in Highly-Pressed Saturated Bentonite

The results discussed earlier have shown that the effect of irradiation on the corrosion rate of carbon steel containers can be almost ignored on a large time scale. The hydrogen permeation behavior of carbon steel in a deep geological environment is studied based on the long-term corrosion rate model of carbon steel containers obtained in previous research (Zhang et al., 2019). Firstly, the hydrogen permeation law of carbon steel in a deep geological environment was explored. There are two main factors affecting the hydrogen permeation behavior of carbon steel containers in a deep geological environment, temperature and corrosion current density. The research was mainly carried out from these two influencing factors.

Because the buffer backfill material reaches saturation after 10 years, the saturation stage was focused on. The experimental medium is saturated, highly-compacted bentonite. Firstly, the hydrogen permeation law of steel in saturated highly compacted bentonite at different temperatures was studied. As shown in **Figure 6**, it is a variation of hydrogen concentration with time for steel in saturated highly pressed bentonite at different temperatures and different hydrogen charging current densities, in which a is 298 K, b is 313 K, c is 351 K, and d is 363 K (different temperatures correspond to a different year, as shown in **Figure 1**). The calculation method of hydrogen concentration has been introduced in *Experimental Method*. The results show that the hydrogen concentration increases in the steel with increasing hydrogen charging time at the same hydrogen charge current density. At the same hydrogen charging time, the hydrogen concentration in steel increases with the increase of the hydrogen charging current density; however, when the hydrogen charging current density increases to a certain extent, the increase of hydrogen concentration is no longer obvious. Each temperature has a similar pattern. This is because of the hydrogen evolution reaction on carbon steel. The generally accepted reaction scheme for proton reduction can be written as the Volmer reaction (Yan et al., 2007):

$$M + H^+ + e^- \rightarrow MH_{(ads)} \quad (2)$$

$$MH_{(ads)} + MH_{(ads)} \rightarrow 2M + H_2 \quad (3)$$

$$MH_{(ads)} \rightarrow MH_{(abs)} \quad (4)$$

Formula (2) refers to the adsorption of hydrogen, (3) refers to the recombination with hydrogen to form hydrogen molecules, and (4) refers to that some adsorbed H atoms may be absorbed into the lattice. When the hydrogen charging current density increases to a certain extent, reaction (2) is accelerated, resulting in the accumulation of a large amount of $MH_{(ads)}$ on the surface of carbon steel. Therefore, the adsorbed hydrogen binds faster, resulting in the escape of hydrogen. The results show that there is a linear law between the corrosion current density (the corrosion current density in the deep geological environment is much less than the experimental current density) and the hydrogen content in the carbon steel container at the same temperature, that is, the same disposal year.

Figure 7 shows that the hydrogen concentration in steel changes with the charging time at different temperatures under the hydrogen charging current density of 10 A m^{-2}. At the same hydrogen charging current density and time, the hydrogen concentration in the steel increases with the rise in temperature. This shows that the hydrogen diffuses in the steel faster at high temperatures. The diffusion coefficient of hydrogen in steel is a function of temperature. Kiuchi and Mclellan (1986) comprehensively analyzed a large

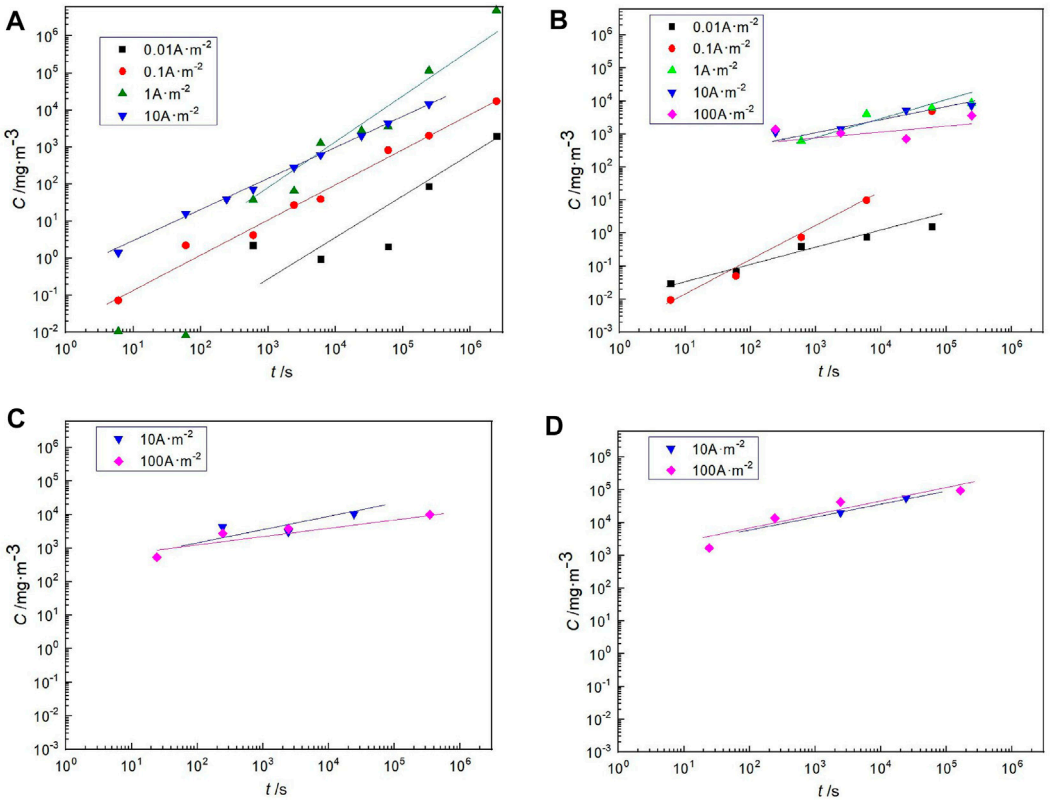

FIGURE 6 | Hydrogen concentration in Q235 steel with different current density of hydrogen charging in saturated highly compacted bentonite at different temperatures; **(A)** 298 K; **(B)** 313 K; **(C)** 351 K; **(D)**, 363 K.

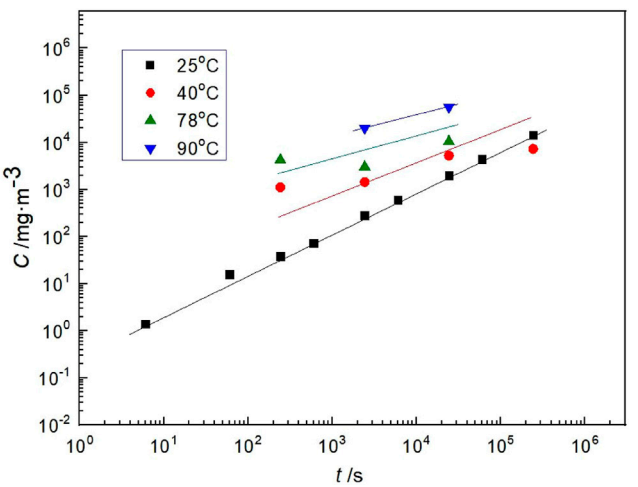

FIGURE 7 | Hydrogen concentration in Q235 steel with temperature at same charging current density of 10 A m^{-2} in saturated highly compacted bentonite.

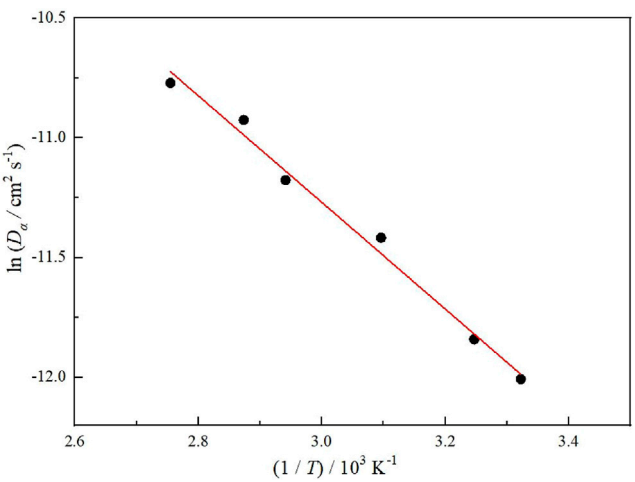

FIGURE 8 | Effect of temperature on hydrogen diffusivity of carbon steel in temperature range from 298 to 373 K

number of hydrogen diffusion data measured by various methods, indicating that the most representative equation of hydrogen diffusion coefficient is as follows:

$$D = 7.23 \times 10^{-8} \exp\left(-5.69\,(kJ/mol)/RT\right) m^2 s^{-1} \quad (5)$$

$$D = (1 \sim 2.52) \times 10^{-7} \exp\left[-(6.70 \sim 7.12)\,(kJ\,mol^{-1})/RT\right] m^2 s^{-1} \quad (6)$$

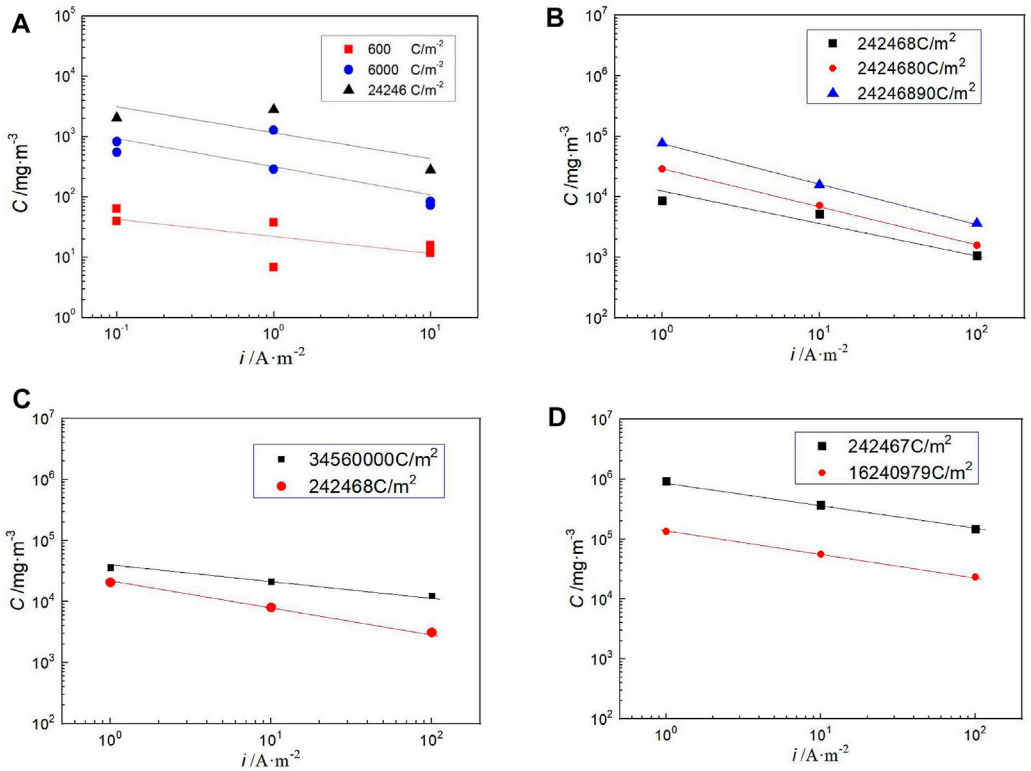

FIGURE 9 | Variation in hydrogen concentration in Q235 steel with charging current density for same fixed total charge at different temperatures in saturated highly compacted bentonite.

The temperature range is 233–353 K for **Equation 5** (323 to 823 K for **Equation 6**).

The diffusion coefficient of hydrogen in highly pressed saturated bentonite was also studied. The diffusivity can be calculated according to the following equation (Tsuru and Latanision, 1982):

$$t_b = 0.5\frac{L^2}{\pi^2 D_\alpha} \tag{7}$$

D at different temperatures was counted by **Equation 7**. **Figure 8** gives the Arrhenius plot of hydrogen diffusivity D against temperature.

$$D = 1.01 \times 10^{-6} \exp(-18.50\,(kJ/mol)/RT)\ m^2 s^{-1} \tag{8}$$

The fitted hydrogen diffusion coefficient equation is close to the research mentioned earlier (Kiuchi and Mclellan, 1986), which also shows that the deep geological environment has no effect on hydrogen diffusion in carbon steel.

The studies discussed earlier have obtained the relationship between temperature, current density, and hydrogen concentration in steel, but the total amount of hydrogen charging is different. **Figure 9** shows the relationship between the hydrogen concentration in steel and the hydrogen charging current density at different temperatures when the total amount of hydrogen charging is the same. The results show that the lower the hydrogen charging current density, the greater the hydrogen concentration in the steel for the same amount of hydrogen charging. This is also related to the hydrogen evolution reaction. Under the smaller hydrogen charging current density, the amount of adsorbed hydrogen produced in reaction (2) is relatively small, which is not enough to combine to generate the escaping hydrogen. So, more adsorbed hydrogen is transformed into absorbed hydrogen and enters the steel.

This study is to estimate the HPE on a large time scale. Obviously, hydrogen charging experiments for thousands of years cannot be completed in the laboratory. However, according to the relationship between hydrogen concentration, hydrogen charging current density, temperature, and the total amount of hydrogen charging in the research discussed earlier, as long as the amount of hydrogen charging in different disposal years could be obtained, the accelerated experiment could be completed in a short time using large hydrogen charging current density and finally predicted by extrapolation method. Previous studies have obtained the model of long-term corrosion rate for carbon steel in a deep geological environment, as shown in **Figure 10** (Zhang et al., 2019). The curve in **Figure 10** could be integrated to get the amount of hydrogen charging under natural corrosion conditions in different disposal years, as shown in **Table 4**.

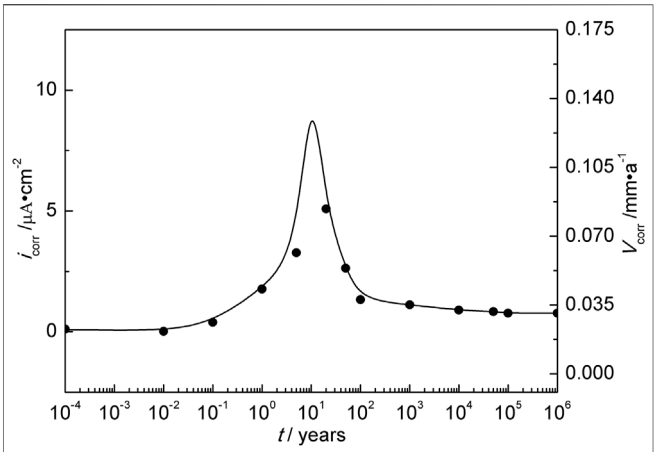

FIGURE 10 | Estimated corrosion rate of Q235 steel in deep geological disposal in Beishan area of China.

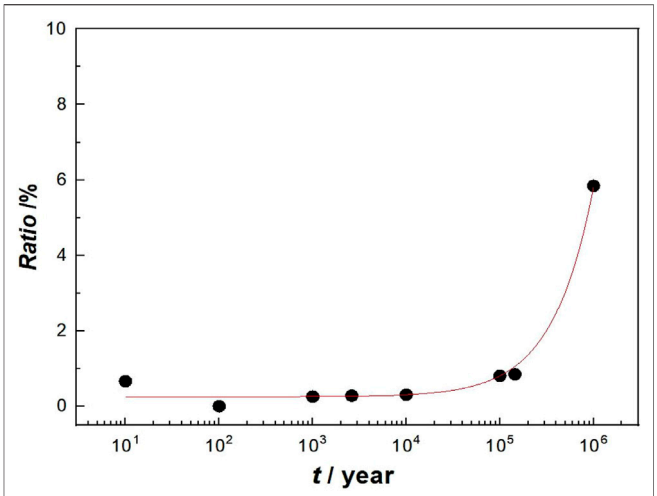

FIGURE 12 | Hydrogen permeation efficiency of Q235 steel in highly compacted bentonite at different disposal time.

TABLE 4 | Total amount of charge for hydrogen charging of carbon steel at different disposal periods under free corrosion conditions.

t/year	10	100	1,000	10,000	100,,000
Q (C m^{-2})	1.6×10^{7}	1.1×10^{8}	4.6×10^{8}	3.0×10^{9}	2.6×10^{10}

Here, HPE is defined as the percentage of the hydrogen content in the steel to the total amount of hydrogen charging into the steel. Based on the linear relationship between hydrogen concentration and hydrogen charging current density (the total amount of hydrogen charging is the same), the HPE under natural corrosion conditions could be obtained by extrapolating the relationship curve between HPE and current density corresponding to hydrogen charging in different geological disposal years to the self-corrosion current density (**Figure 10**). As shown in **Figure 11A** is the result of 10 years, HPE is approximately 0.6%. 2) is the result of 100 years.

By analogy, it was acquired that the HPE of Q235 steel as HLNW container material in different deep geological disposal years, as shown in **Figure 12**. The results show that the HPE increases slowly with the disposal year. This result confirms the previously conjectured situation that the oxygen trapped after the container is buried is consumed through the corrosion reaction, which is related to the change from oxygen reduction to hydrogen reduction in the cathodic process of corrosion. Winsley et al. (2011) believe that when the oxygen content around the container drops to a low value, the hydrogen evolution reaction leads to the cathodic reaction. This result also implies that carbon steel containers are likely to suffer from HE in the medium and long term of deep geological disposal. The HE sensitivity of carbon steel containers in a deep geological environment is further judged by SSRT.

Slow Strain Rate Tensile Test for Q235 Steel

The hydrogen diffusion in carbon steel is relatively fast, so HE sensitivity was studied by a control experiment. **Figure 13** shows the stress–strain curve for Q235 steel specimens; a is stretching in the air without any treatment, b is stretching in

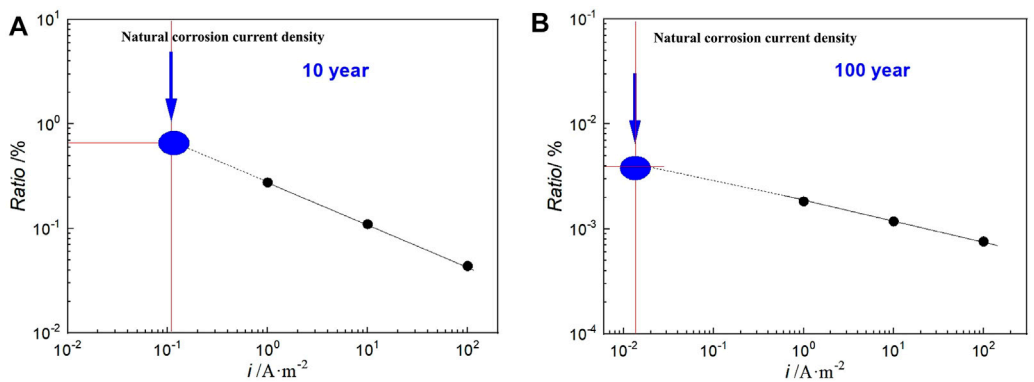

FIGURE 11 | Hydrogen permeation efficiency of Q235 steel in highly compacted bentonite with hydrogen charging density; **(A)** 10 years; **(B)** 100 years.

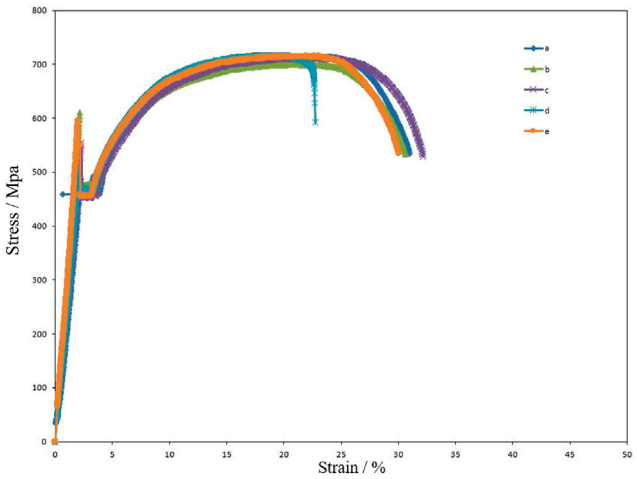

FIGURE 13 | Stress–strain curves for Q235 steel. **(A)** Original specimen; **(B)** specimen without treatment stretched in 0.2 mol L^{-1} NaOH; **(C)** specimen stretched in air after hydrogen charged in 0.2 mol L^{-1} NaOH solution for 7 days with 1 mA cm^{-2}; **(D)** specimen stretched in 0.2 mol L^{-1} NaOH solution with 1 mA cm^{-2} hydrogen charging and stretching at same time; **(E)** stretched in 0.2 mol L^{-1}L NaOH solution with 0.1 mA cm^{-2} hydrogen charging and stretching at same time.

0.2 mol L^{-1} NaOH solution without any treatment, c is stretching in the air after 7 days of hydrogen charging in 0.2 mol L^{-1} NaOH solution, d is hydrogen charging under 1 mA cm^{-2} and stretching in 0.2 mol L^{-1} NaOH solution carried out at the same time, and e is hydrogen charging under 0.1 mA cm^{-2} and stretching in 0.2 mol L^{-1} NaOH solution carried out at the same time. The effect of tensile medium on tensile fracture elongation can be excluded by comparing a and b. **Figure 13C** shows that hydrogen cannot exist in Q235 steel for a long time and will escape quickly, so its fracture elongation is not affected. **Figure 13D** confirms that when hydrogen is always inside the steel, its fracture

TABLE 5 | Elongation of Q235 steel with different treatments and tensile methods (a, b, c, d, and e correspond to **Figure 5**).

Curve	a	b	c	d	e
Elongation/%	30.1	32.1	30.6	22.7	30.0

elongation decreases significantly. However, comparing d and e, it is found that when the hydrogen charging current density is too low, the hydrogen content in the steel is too low to reduce its fracture elongation. In short, Q235 steel is sensitive to HE when hydrogen is always present and when the content is high. **Table 5** summarizes the fracture elongation of specimens after different treatments.

Figure 14 shows the morphology of the fracture surface for SSRT specimens. The original specimens a and b were stretched in air and 0.2 mol L^{-1} NaOH solution, respectively; c is the hydrogen charging and stretching simultaneously in 0.2 mol L^{-1} NaOH solution under 1 mA cm^{-2}. It can be seen obviously that a and b have dimple features, and large dimples are densely surrounded by small dimples, which represent the typical plastic fracture. After hydrogen charging under 1 mA cm^{-2} in 0.2 mol L^{-1} NaOH solution for 7 days, the specimen was stretched in the air. Also, the specimen was charged under 0.1 mA cm^{-2} in 0.2 mol L^{-1} NaOH solution and stretched. The fracture morphology of the two samples is similar to a and b. In **Figure 14C**, an obvious secondary crack can be seen. Furthermore, it is accompanied by a river pattern, which shows a brittle fracture. The result is consistent with **Figure 13**. For Q235 steel, only when its internal hydrogen content reaches a certain level and can exist for a long time will the material be sensitive to HE. Kobayashi et al. (2010) think that the amounts of hydrogen entering the elastic and the plastic deformation regions before the maximum stress had very little effect against the reduction of fracture strain. However, carbon steel container has been buried in a deep

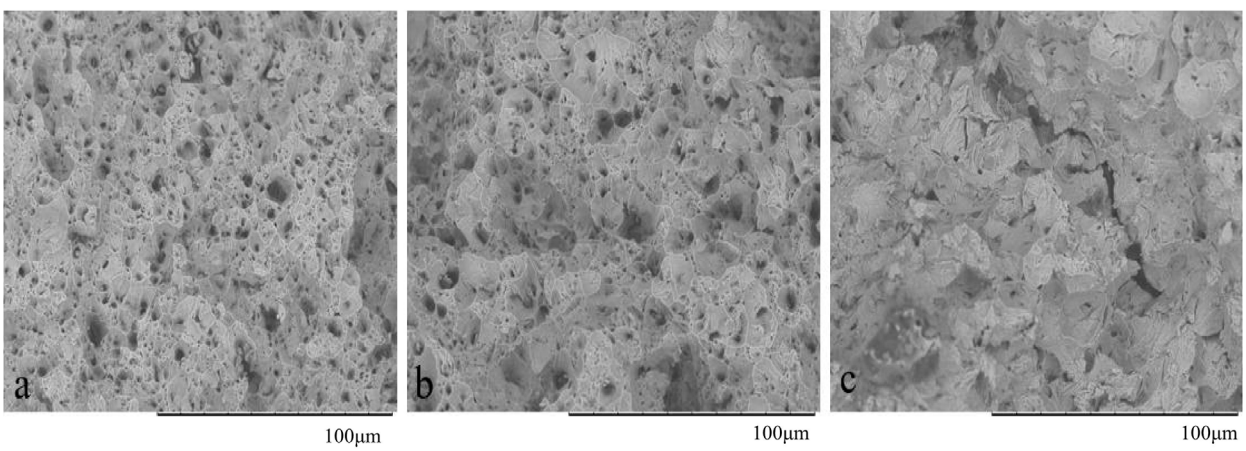

FIGURE 14 | Fracture morphologies of failed Q235 SSRT specimens; a and b are original specimens without treatment stretched in air and 0.2 mol L^{-1} NaOH solution; c is specimen stretched in 0.2 mol L^{-1} NaOH solution with 1 mA cm^{-2} hydrogen charging and stretching at same time.

geological environment for tens of thousands or even hundreds of thousands of years. Due to the rapid diffusion of hydrogen in steel, it will continue to penetrate from the steel surface, and the corrosion current density (maximum corrosion current density is less than 10 μA cm^{-2}) is also far less than the hydrogen charging current density in the experiment. Hydrogen cannot exist in carbon steel for a long time and when the content is low. Although the HPE increases with the disposal year, the HE sensitivity of carbon steel containers is low. Thus, it is likely that the carbon steel container will not be damaged by HE.

CONCLUSION

The HPE of Q235 steel as the nuclear waste container in a deep geological environment was predicted by the electrochemical method, and the possibility of hydrogen embrittlement was evaluated by a slow strain tensile test. The following conclusions are reached:

1) The radiation of nuclear waste will have a certain impact on the corrosion rate of the Q235 steel container, and the higher the temperature, the greater the corrosion rate. However, the high-temperature stage is very short, so it can be ignored that radiation's effect on the corrosion of container on a large time scale.
2) The longer the hydrogen permeation time, the higher the hydrogen concentration in the steel; under the same hydrogen charging time, the greater the hydrogen charging current, the greater the hydrogen concentration in the steel, but the hydrogen concentration does not increase when the current increases to a certain extent; under the same total hydrogen charging, the smaller the hydrogen charging current is, the greater the hydrogen concentration is.
3) The HPE during the corrosion process increases slowly with the increasing geological disposal age, which fully proves that the trapped oxygen is exhausted after the container is buried, and the cathodic process of corrosion changes from oxygen reduction to hydrogen reduction.
4) The Q235 steel will show hydrogen embrittlement sensitivity only when the internal hydrogen content reaches a certain level and can exist for a long time.

According to the conclusions discussed, although the HPE of Q235 steel increases, hydrogen will soon escape from the steel. So, it will show a low hydrogen embrittlement sensitivity from a large time scale for Q235 steel container. Therefore, Q235 steel as the nuclear waste container has a disadvantage of high corrosion rate and an advantage of low possibility of hydrogen embrittlement. Its thickness can be designed to be thicker to overcome the disadvantage.

DATA AVAILABILITY STATEMENT

The original contributions presented in the study are included in the article/Supplementary Material, further inquiries can be directed to the corresponding authors.

AUTHOR CONTRIBUTIONS

QZ has written the draft. YJ analyzed the data. XZ completed the part of the experiments. DL and YH provided guidance and funds. Other authors completed the revised manuscript, part of the experiments, and data.

FUNDING

This work was financially supported by the National Natural Science Foundation of China under grant no. 51471160.

REFERENCES

Arup, O. (1985). *Ocean Disposal of Radioactive Waste by Penetrator Emplacemen*. EUR 10170, London: Graham& Trotmon Let, For the Commission of European Communities.

Bradley, D. J. (1997). *Behind the Nuclear Curtain: Radioactive Waste-Management in the Former Soviet Union*. USA: UN Battelle Memorial Institute.

Dong, L., Zhongtian, Y., Weibing, Y., Qinghong, S., and Wei, L. (2015). Preliminary Study on Gamma Radiation Effects on Modified Sodium Bentonite[J]. *Acta Mineralogica Sinica* 35 (1), 103–106.

Duquette, D. J., Latanision, R. M., Di Bella, C. A. W., and Kirstein, B. E. (2009). Corrosion Issues Related to Disposal of High-Level Nuclear Waste in the Yucca Mountain Repository-Peer Reviewers' Perspective. *Corrosion* 65, 272–280. doi:10.5006/1.3319133

Ewing, R. C. (2015). Long-term Storage of Spent Nuclear Fuel. *Nat. Mater* 14, 252–257. doi:10.1038/nmat4226

Guo, X., Gin, S., Lei, P., Yao, T., Liu, H., Schreiber, D. K., et al. (2020). Self-accelerated Corrosion of Nuclear Waste Forms at Material Interfaces. *Nat. Mater.* 19, 310–316. doi:10.1038/s41563-019-0579-x

Guo-ding, L. I. (2000). Coupled Calculation of Dose Rate and Temperature in the Near Field of a High-Level Radioactive Waste Disposal Repository[J]. *Radiat. Prot.* 20 (3), 153–158. doi:10.1093/rpd/ncx054

Hu, Y., and Cheng, H. (2015). Disposal Capacity for Spent Fuel in China Is Not Ready yet for the Nuclear Power Boom. *Environ. Sci. Technol.* 49, 2596–2597. doi:10.1021/es505855s

Huang, Y., and Zhu, Y. (2005). Hydrogen Ion Reduction in the Process of Iron Rusting. *Corrosion Sci.* 47 (6), 1545–1554. doi:10.1016/j.corsci.2004.07.044

King, F., and Padovani, C. (2011). Review of the Corrosion Performance of Selected Canister Materials for Disposal of UK HLW And/or Spent Fuel. *Corrosion Eng. Sci. Tech.* 46, 82–90. doi:10.1179/1743278211y.0000000005

Kiuchi, K., and Mclellan, R. B. (1986). The Solubility and Diffusivity of Hydrogen in Well-Annealed and Deformed Iron. *Acta Metallurgica* 31, 29–52. doi:10.1016/b978-0-08-034813-1.50009-7

Kobayashi, M., Nishikata, A., and Tsuru, T. (2010). Effect of Stain Rate and Hydrogen Charging Current on Hydrogen Embrittlement of Carbon Steel in High Alkaline Chloride Environment. *Zakaep* 59 (4), 129–135. doi:10.3323/jcorr.59.129

Liu, C., Tian, C., Zhang, Z., Han, E. H., and Wang, J. (2019). Corrosion Behaivour of X65 Low Carbon Steel during Anaerobic Period of High Level Nuclear Waste Disposal. *Corrosion Sci. Prot. Tech.* 31, 371–378. doi:10.11900/0412.1961.2018.00481

Liu, C., Tian, C., Zhang, Z., Han, E. H., and Wang, J. (2019). Corrosion Behaivour of X65 Low Carbon Steel during Redox State Transition Process of High Level Nuclear Waste Disposal. *Acta Metallurgica Sinica* 55, 849–858. doi:10.11900/0412.1961.2018.00481

Liu, C., Wang, J., Zhang, Z., Han, E.-H., Liu, W., Liang, D., et al. (2018). Effect of Cumulative Gamma Irradiation on Microstructure and Corrosion Behaviour of X65 Low Carbon Steel. *J. Mater. Sci. Tech.* 34, 2131–2139. doi:10.1016/j.jmst.2018.03.017

Liu, C., Wang, J., Zhang, Z., and Han, E.-H. (2017). Studies on Corrosion Behaviour of Low Carbon Steel Canister with and without γ-irradiation in China's HLW Disposal Repository. *Corrosion Eng. Sci. Tech.* 52 (Suppl. 1), 136–140. doi:10.1080/1478422x.2017.1348762

Milnes, A. G. (1985). *Geology and Radwaste*. New York: Academic Press.

Rasilainen, K. (2004). *Localisation of the SR 97 Process Report for Posiva's Spent Fuel Repository at Olkiluoto[R]*. Finland: Department of Mathematics and Systems Analysis.

Rosborg, B., and Werme, L. (2008). The Swedish Nuclear Waste Program and the Long-Term Corrosion Behaviour of Copper[J]. *J. Nucl. Mater.* 379 (1-3), 142–153. doi:10.1016/j.jnucmat.2008.06.025

Seetharam, S. C., Cleall, P. J., and Thomas, H. R. (2006). Modelling Some Aspects of Ion Migration in a Compacted Bentonitic Clay[J]. *Eng. Geology.* 85 (1-2), 221–228. doi:10.1016/j.enggeo.2005.09.041

Shoesmith, D. W. (2000). Fuel Corrosion Processes under Waste Disposal Conditions. *J. Nucl. Mater.* 282, 1–31. doi:10.1016/s0022-3115(00)00392-5

Smart, N. R., Rance, A. P., and Werme, L. O. (2008). The Effect of Radiation on the Anaerobic Corrosion of Steel. *J. Nucl. Mater.* 379, 97–104. doi:10.1016/j.jnucmat.2008.06.007

Stoulil, J., Kaňok, J., Kouřil, M., Parschová, H., and Novák, P. (2013). Influence of Temperature on Corrosion Rate and Porosity of Corrosion Products of Carbon Steel in Anoxic Bentonite Environment. *J. Nucl. Mater.* 443, 20–25. doi:10.1016/j.jnucmat.2013.06.031

Tsuru, T., Huang, Y., Ali, M. R., and Nishikata, A. (2005). Hydrogen Entry into Steel during Atmospheric Corrosion Process. *Corrosion Sci.* 47 (10), 2431–2440. doi:10.1016/j.corsci.2004.10.006

Tsuru, T., and Latanision, R. M. (1982). Grain Boundary Transport of Hydrogen in Nickel. *Scripta Metallurgica* 16, 575–578. doi:10.1016/0036-9748(82)90273-3

Winsley, R. J., Smart, N. R., Rance, A. P., Fennell, P. A. H., Reddy, B., and Kursten, B. (2011). Further Studies on the Effect of Irradiation on the Corrosion of Carbon Steel in Alkaline media. *Corrosion Eng. Sci. Tech.* 46 (2), 111–116. doi:10.1179/1743278210y.0000000010

Winsley, R. J., Smart, N. R., Rance, A. P., Fennell, P. A. H., Reddy, B., and Kursten, B. (2013). Further Studies on the Effect of Irradiation on the Corrosion of Carbon Steel in Alkaline media. *Corrosion Eng. Sci. Tech.* 46 (2), 111–116. doi:10.1179/1743278210y.0000000010

Yan, L., Ramamurthy, S., Noel, J. J., and Shoesmith, D. W. (2007). Hydrogen Absorption into Alpha Titanium in Acidic Solutions. *Electrochim. Acta* 52, 1169e1181. 10.1016/j.electacta.2006.07.017.

Yang, C., Samper, J., and Montenegro, L. (2008). A Coupled Non-isothermal Reactive Transport Model for Long-Term Geochemical Evolution of a HLW Repository in clay. *Environ. Geol.* 53 (8), 1627–1638. doi:10.1007/s00254-007-0770-2

Zhang, L., Zhao, W., Li, Y., and Li, S. (2013). Probabilistic Assessment of Failure for Low-Medium Level Nuclear Waste Storage Container. *Chin. J. Appl. Mech.* 30 (2), 287–290. 10.11776/cjam.30.02.D015.

Zhang, Q., Huang, Y., Blackwood, D. J., Zhang, B., Lu, D., Yang, D., et al. (2020). On the Long Term Estimation of Hydrogen Embrittlement Risks of Titanium for the Fabrication of Nuclear Waste Container in Bentonite Buffer of Nuclear Waste Repository. *J. Nucl. Mater.* 533, 152092. doi:10.1016/j.jnucmat.2020.152092

Zhang, Q., Zheng, M., Huang, Y., Kunte, H. J., Wang, X., Liu, Y., et al. (2019). Long Term Corrosion Estimation of Carbon Steel, Titanium and its alloy in Backfill Material of Compacted Bentonite for Nuclear Waste Repository. *Sci. Rep.* 9, 3195. doi:10.1038/s41598-019-39751-9

Zheng, M., Zhang, Q., Huang, Y., Lu, D., Yu, X., Liu, Y., et al. (2016). Determination of Representative Ground-Water for Corrosion Assessment of Candidate Materials Used in Beishan Area Preselected for High-Level Radioactive Waste Disposal Repository[J]. *J. Chin. Soc. Corrosion Prot.* 36 (2), 185–190. doi:10.11902/1005.4537.2015.055

Conflict of Interest: The authors declare that the research was conducted in the absence of any commercial or financial relationships that could be construed as a potential conflict of interest.

Publisher's Note: All claims expressed in this article are solely those of the authors and do not necessarily represent those of their affiliated organizations or those of the publisher, the editors, and the reviewers. Any product that may be evaluated in this article, or claim that may be made by its manufacturer, is not guaranteed or endorsed by the publisher.

frontiers in Materials

ORIGINAL RESEARCH
published: 24 March 2022
doi: 10.3389/fmats.2022.880702

Temperature-Dependence Corrosion Behavior of Ti6Al4V in the Presence of HCl

Fei Yu[1,2]*, *Owen Addison*[3] *and Alison Davenport*[2]

[1]Institute for Translational Medicine, The Affiliated Hospital of Qingdao University, Qingdao University, Qingdao, China, [2]School of Metallurgy and Materials, University of Birmingham, Birmingham, United Kingdom, [3]Faculty of Dentistry, Oral and Craniofacial Sciences, King's College London, London, United Kingdom

Ti alloys have been widely used in biomedical field due to good compatibility and corrosion resistance. However, corrosion-related failures of implanted Ti devices and prostheses have been regularly reported within the medical literature. The corrosion of Ti alloys has attracted much attention *in vivo* and *in vitro*. In the current study, the corrosion behavior of Ti6Al4V alloy was investigated using surface analysis and electrochemical tests. Corrosion of Ti6Al4V in 2 M hydrochloric acid is temperature dependent within the temperature range studied. It has found that the steady state current density at –510 mV vs. SCE (the primary passivation potential at the physiological temperature of 37°C) becomes higher with increasing temperature. The α phase of Ti6Al4V is preferentially dissolved relative to the β phase after potentiostatic measurement at primary passivation potential in 2 M HCl at 37°C. This investigation provides novel and useful information for Ti corrosion-related failures of biomedical implants and prostheses.

Keywords: Ti6Al4V, corrosion, temperature, HCl solution, preferential attack

OPEN ACCESS

Edited by:
Binbin Zhang,
Institute of Oceanology (CAS), China

Reviewed by:
Fahe Cao,
Sun Yat-sen University, China
Xiaohui Chen,
The University of Manchester, United Kingdom

***Correspondence:**
Fei Yu
feiyu@qdu.edu.cn

Specialty section:
This article was submitted to Environmental Degradation of Materials, a section of the journal Frontiers in Materials

Received: *21 February 2022*
Accepted: *10 March 2022*
Published: *24 March 2022*

Citation:
Yu F, Addison O and Davenport A (2022) Temperature-Dependence Corrosion Behavior of Ti6Al4V in the Presence of HCl. Front. Mater. 9:880702. doi: 10.3389/fmats.2022.880702

1 INTRODUCTION

Increasing concern regarding the consequences of metal release from biomedical implants has stimulated efforts to better understand the conditions under which corrosion occurs, and the nature of the corrosion products that are released (Xu et al., 2018; Morrell et al., 2019; Xu et al., 2019). Oxidation-resisting steel, Co-Cr and Ti alloys are the most common biomedical implant metals in use today (Sullivan and Topoleski, 2015; Harun et al., 2017; Xu et al., 2018; Xu et al., 2019). Of these, Ti in its commercially pure and alloyed forms is mostly used for "cementless" implants because of titanium's ability to "osseointegrate" with bone, provide adequate mechanical properties, and exhibit resistance to corrosion under normal physiological conditions (Paka and Pokrowiecki, 2018; Kang and Yang, 2019; Rabadia et al., 2019; Zhang and Chen, 2019; Zhang L.-C. et al., 2020). However, there is increasing evidence to demonstrate that Ti implants do corrode in the body under specific conditions (Addison et al., 2012; Nelson et al., 2020). The combination of multiple crevice environments (metal-metal; metal-bone, metal-soft-tissue) may produce significant changes in the chemistry of the local solution which are not predicted by standard pre-clinical testing regimens (Liu et al., 2021; Smith and Gilbert, 2021). Direct evidence of Ti corrosion *in vivo* has been reported in the orthopaedic literature associated with cemented femoral stems and Morse taper connections (Jacobs et al., 1998a; Jacobs et al., 1998b; Hallam et al., 2004). These geometrical scenarios, specifically provide conditions where aggressive (acidic) chemistries may be maintained, allowing mechanically assisted crevice corrosion (MACC) to occur (Gilbert et al., 1993; Addison et al., 2012; Kubacki and Gilbert, 2021).

Several factors influence the corrosion resistance of Ti including temperature and environmental chemistry. It has been reported that the frequency of thin film breakdown events increases with increasing temperature (Kolman et al., 1998; Yu et al., 2001; Atapour et al., 2012). For biomedical applications experimental measurements are typically conducted 37°C to simulate physiological body temperature (Atapour et al., 2011) although at inflamed sites local tissue temperatures can vary by several degrees. In other applications such as dental implants, temperature fluctuations can be much larger due to ingested hot or cold foods and beverages. Within the relevant literature a range of temperatures from 25 to 50°C have been used to explore mechanistic behaviors (Jackson et al., 2000; Valero Vidal et al., 2010). Alongside temperature, the chemistry of the environment into which the implant is placed is a key factor which can influence the corrosion resistance of Ti and its alloys. In the body, Ti implants encounter a range of liquid environments which can contain components such as reactive oxygen species, or proteins which can modify corrosion resistance (Zhang et al., 2018a). Of particular importance is the presence of Cl^- in tissues fluids (100–110 mM) which reduces the passivation of Ti in acidic conditions (Mi-Kyung et al., 2015). Although an acknowledged extreme, measurement of fluids in contact with Ti alloy orthopaedic implants retrieved during revision surgery has shown that the local acidity may reach levels approaching pH 2.5 (Hallam et al., 2004). Importantly, this is an environment that represents local acidification as a consequence of MACC (Zhang et al., 2018b).

The most common Ti implant substrate in use today is the ASTM Grade V alloy, Ti6Al4V, which exhibits a microstructure containing α and β phases stabilized by Al and V, respectively (Liu et al., 2004; Yu et al., 2015; Zhang et al., 2018a). The manufacturing and processing of Ti6Al4V can be tailored to generate a variety of microstructures with different spatial distributions of the α and β phases (Atapour et al., 2010; Atapour et al., 2012). However it has been observed that these phases can have different corrosion behaviors and should corrosion occur would lead to a differential release of the alloying (Chandrasekaran et al., 2006; Atapour et al., 2011; Zhang H. et al., 2020) elements. Hence, the purpose of this study was to explore the temperature dependent corrosion behavior of Ti6Al4V in the presence of HCl and identify factors which lead to preferential corrosion of the microstructural phases. The corrosion behavior of Ti6Al4V alloy was studied in hydrochloric acid at different temperatures by applying potentiodynamic/potentionstatic polarization scans and surface analysis methods, and novel explanation can be provided regarding failure of biomedical Ti alloys.

2 MATERIALS AND METHODS

2.1 Sample Preparation

Disc-shaped test specimens (14 mm diameter and 1.2 mm thickness) were fabricated from a Ti6Al4V alloy (ASTM Grade V, Titanium Products Ltd., Solihull, United Kingdom) and the surfaces polished to a mirror finish. Polishing involved sequential use of abrasive cloths beginning with MD-Piano (Struers, Rotherham, United Kingdom) and deionized water as a lubricant, followed by MD-Largo with a 9 μm diamond suspension as a lubricant. Finally, a MD-Chem polishing cloth (Struers, Rotherham, United Kingdom) was used with 0.04 μm OP-S Colloidal Silica suspension (Struers, Rotherham, United Kingdom) to produce a mirror finish on both sides of the disc. Following polishing, specimens were thoroughly cleaned sequentially in acetone, ethanol, and deionized water using ultrasonic agitation for 10 min at each stage. Specimens were finally dried in an air stream before further experiments.

2.2 Electrochemical Tests

2.2.1 General Procedures

A standard three-electrode cell with reference electrode (RE), counter electrode (CE) and working electrode (WE) was used. The CE was a Pt mesh (working area ~4 cm^2) and RE was a commercial saturated calomel electrode (SCE). The potential was controlled with a potentiostat (ACM Instruments, United Kingdom). Ti discs were mounted in VARI-SET cold mounting acrylic (MetPrep Ltd., United Kingdom) and used as WE. The electrode was polished to a mirror surface using identical sample preparation methods. To achieve good reproducibility, the time between polishing and electrochemical measurements was controlled using the following approach throughout. After final polishing with an MD-Chem polish cloth, the samples were immediately cleaned with deionized water (Millipore), then dried in an air stream and left in open air for 5 min before immersed in the test solutions. Due to the preparatory procedures of setting up the electrochemical cell, there was a 5 min interval between the initial immersion of the sample and acquisition of the first measurement. The electrochemical cell was immersed in a water bath (Bennett Scientific Limited, Nickel Electro Ltd., England, United Kingdom) with high temperature stability (±0.5°C). The temperature was monitored with a thermocouple connected to a computer.

2.2.2 Potentiodynamic Polarization Curves

Freshly polished Ti6Al4V electrodes were immersed in 2 M HCl at 37°C. The open circuit potential (OCP) was measured for 1 h and then anodic polarization curves were measured by sweeping the potential from −50 mV below the OCP to 0 mV vs. SCE at a rate of 1 mV/s. The anodic polarization curves were measured three times for each condition, using a freshly polished sample and fresh solution in each case.

2.2.3 Potentiostatic Measurements

The corrosion behavior of Ti6Al4V in the presence of 2 M HCl was studied by potentiostatic measurements at various temperatures around the physiological norm (28°C, 31°C, 34°C, 37°C, 40°C, and 43°C). The temperature was controlled by the water bath and was recorded by a thermocouple, which was immersed in the solution. Freshly polished Ti6Al4V was immersed in 2 M HCl. OCP was measured for 30 min and then −510 mV vs. SCE was applied for 3 h. The potentiostatic

measurements were repeated three times for each condition, using a freshly polished sample and fresh solution in each case.

2.3 Surface Characterization

Ti surfaces before and after electrochemical testing were characterized using SEM. Briefly, to locate the same region on the specimen, a hardness indentation was introduced into the center of the mirror polished surface (Vickers hardness test, load: 300 g, MVK-H1 hardness testing machine, Mitutoyo, Japan). After the initial baseline measurement, the carbon layer on the surface resulting from SEM was removed by quickly (~10 s) polishing the sample on an MD-Chem polish cloth with OP-S Colloidal Silica suspension, so that it would not affect the electrochemical experiments. SEM observation was undertaken with JEOL 7000 instrument (Japan Electron Optics Laboratory Co., Ltd. accelerating voltage 20 kV, beam current ~70 μA). Both secondary electron mode (SE) and backscatter electron mode (BSE) imaging were used. Electron back-scattered diffraction (EBSD) analysis was also performed. The elemental composition of the test specimen surfaces was also analyzed by energy dispersive X-ray spectroscopy (EDX detector model: 7558 for JEOL 7000; collecting window: ATW 2; acquisition time: 60 s; quantification method: standard less; Oxford Instrument, United Kingdom).

3 RESULTS

3.1 Characterization of Ti6Al4V

Figure 1 shows the surface morphology and EDX analysis of Ti6Al4V test specimens exhibiting mirror-polished surfaces. When the "as-polished" sample was etched in Kroll's etchant (2% HF and 10% HNO_3 mixed solution) for ~5 s, the β phase was clearly observed (data not shown). Ti6Al4V surfaces show the characteristic two-phase (α and β) microstructure. Increased V and Fe was seen in the β phase and whereas the α phase contained relatively higher Al (**Figure 1C**).

3.2 Effect of HCl on Ti Corrosion

3.2.1 OCP Measurement and Anodic Polarization

Figure 2A shows the OCP as a function of time for mirror-polished Ti6Al4V in naturally-aerated 2 M HCl. The OCP started from ~−350 mV vs. SCE and then abruptly decreased to ~−670 mV vs. SCE for Ti6Al4V, indicating dissolution of the air-formed passive film and surface activation in 2 M HCl. **Figure 2B** shows that Ti6Al4V exhibited obvious active peaks during anodic polarization. The primary passivation potential (E_{pp}) of Ti6Al4V is ~−510 mV vs. SCE.

3.2.2 Temperature Dependence of Corrosion Behavior of Ti6Al4V

Figure 3 shows potentiostatic measurements of the mirror-polished Ti6Al4V in 2 M HCl at different temperatures. It shows that the steady state current density of Ti6Al4V was sensitive to temperature. It can be seen that the corrosion process at 28°C is slightly different from the behaviors above 28°C since the current density of Ti6Al4V was gradually decreased within the measured time until ~4,000 s (before reaching a relative steady state). **Figure 3C** also shows that the steady state current density of Ti6Al4V was increased with increasing temperature at above 28°C, i.e., 31°C, 34°C, 37°C, 40°C and 43°C.

3.2.3 Surface Morphology of Ti6Al4V After Potentiostatic Tests

Figure 4 and **Figure 5** compare the surface morphologies of mirror-polished Ti6Al4V before and after potentiostatic tests at −510 mV vs. SCE in 2 M HCl. It can be seen that Ti6Al4V shows a characteristic α/β two phase microstructure based on the BSE image (**Figure 4B** and **Figure 5B**) and EBSD phase map (**Figure 5A**). There is no sign of corrosion before the test (**Figure 4A**, **Figure 4B** and **Figure 5B**). However, the α phase of Ti6Al4V was found to be attacked more than the β phase after the test (**Figure 4C** and **Figure 4D**). More importantly, **Figure 5C** shows the α phase of Ti6Al4V was preferentially attacked while the β phase of Ti6Al4V stayed the same.

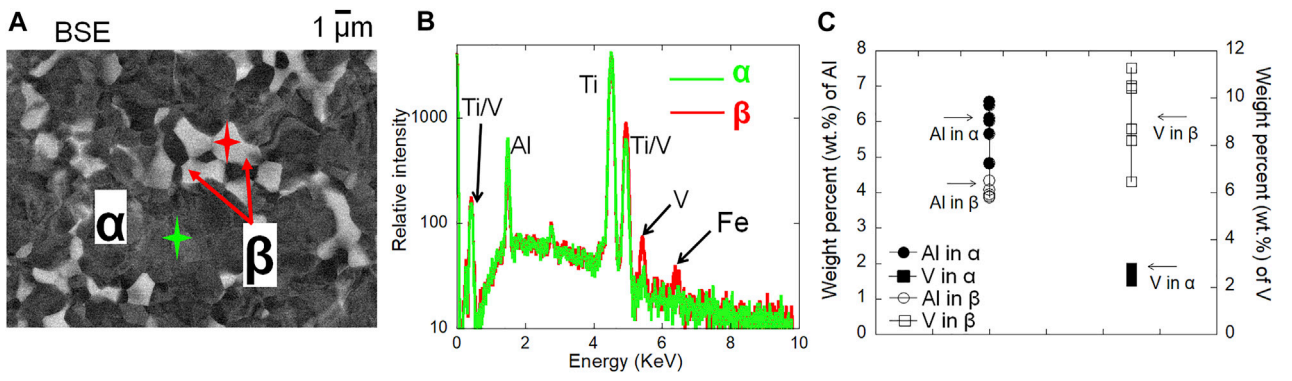

FIGURE 1 | (A) SEM, **(B)** EDX image and **(C)** weight percent (wt.%) of Al and V in α phase and β phase of mirror-polished Ti6Al4V based on the EDX analysis of randomly chosen points on the sample.

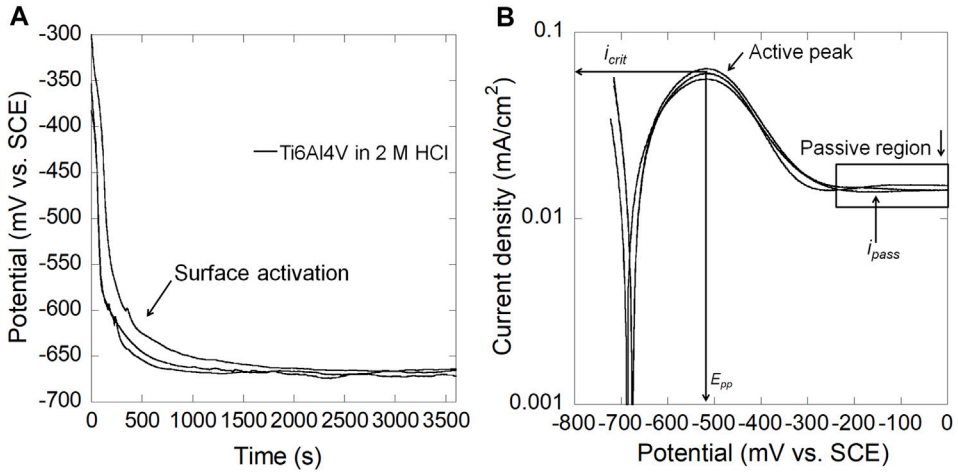

FIGURE 2 | (A) OCP as a function of time and **(B)** anodic polarization curves for mirror-polished Ti6Al4V in 2 M HCl at 37°C (i_{crit}: critical anodic current density; i_{pass}: passive current density; E_{pp}: primary passivation potential).

4 DISCUSSION

4.1 Effect of HCl on Ti6Al4V Corrosion

The current study demonstrated that Ti6Al4V surfaces were activated in naturally-aerated 2 M HCl, which agrees with other studies (Atapour et al., 2010; Atapour et al., 2011). The E-pH diagram (Pourbaix diagram) at 37°C provides preliminary information about the thermodynamically stable state of Ti^{3+} within a wide range of potentials at pH < 1.5 (Yu and Scully, 1997). In the presence of 2 M HCl (pH −0.3), the OCP of Ti6Al4V was −670 mV vs. SCE (**Figure 2**), in which Ti^{3+} is the thermodynamically stable state, and therefore chemical dissolution of the Ti oxide passive film occurred as the first stage before surface activation resulting in an abrupt drop in OCP. The drop in OCP values also agreed with previous studies (Yu et al., 1999; Atapour et al., 2010; Atapour et al., 2011). In addition, a characteristic active-passive transition was observed during anodic polarization in 2 M HCl. Similar E_{pp} and i_{crit} have been reported, i.e., Ti6Al4V in aerated 1.5 M HCl (Atapour et al., 2010) and in deaerated 5% (1.3 M) HCl (Atapour et al., 2012) at 37°C.

4.2 Temperature Dependence of Ti6Al4V in 2 M HCl

The steady state current density of Ti6Al4V at −510 mV vs. SCE has been observed to be increased with increasing temperature above 28°C, i.e., 31°C, 34°C, 37°C, 40 and 43°C (**Figure 3**). Assuming the corrosion process of Ti6Al4V in this study can be analyzed by a simple Arrhenius expression (**Eq. 1**) then the corrosion rate would be represented by current density:

$$\ln i = a - \frac{E_a}{RT} \tag{1}$$

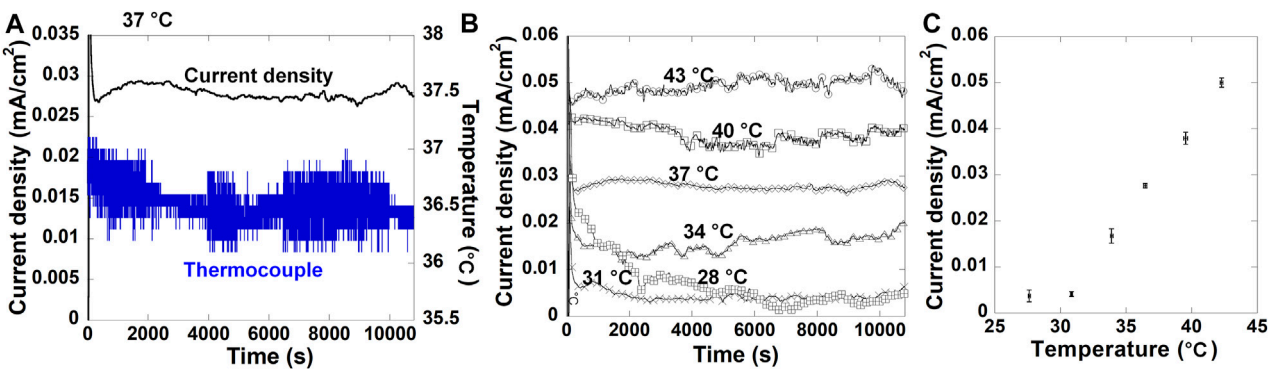

FIGURE 3 | Potentiostatic measurements of mirror-polished Ti6Al4V in 2 M HCl at −510 mV vs. SCE for 3 h **(A)** with thermocouple record at 37°C, **(B)** at different temperatures and **(C)** the relationship between the anodic steady state current density and temperature in the parallel experiments. The values were chosen from 4,000 s to 10,800 s.

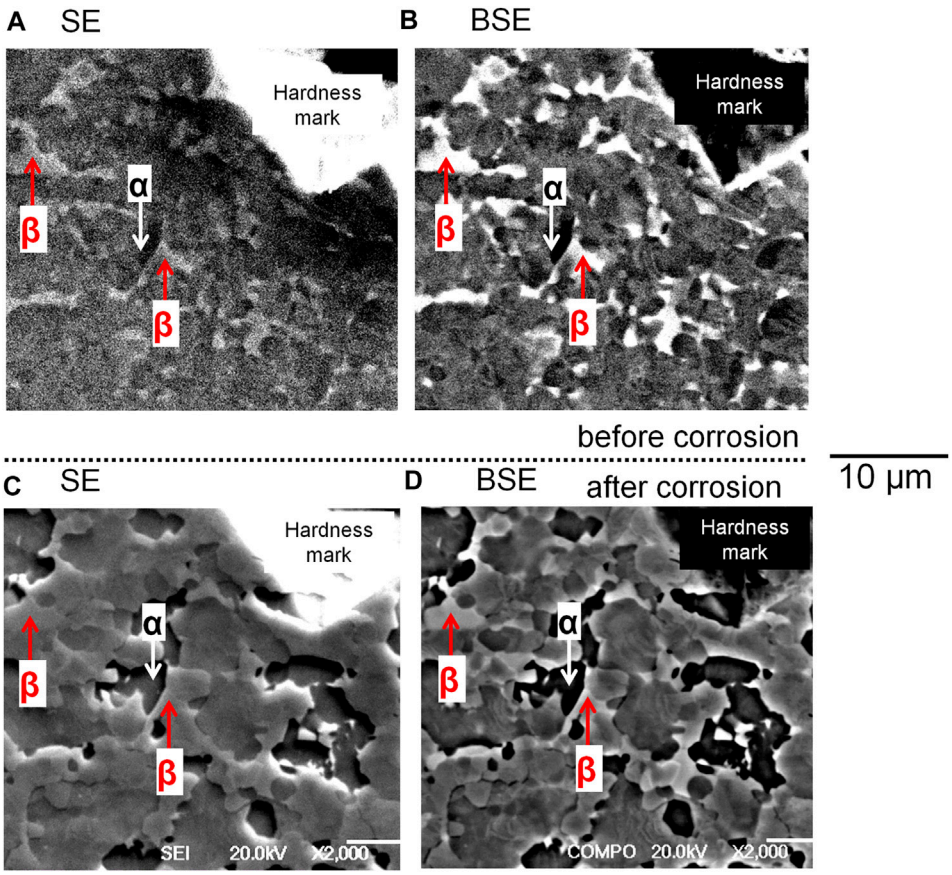

FIGURE 4 | SEM image of mirror-polished Ti6Al4V **(A,B)** before and **(C,D)** after potentiostatic test in 2 M HCl at −510 mV vs. SCE for 30 min at 37°C. SE: secondary electron mode SEM image; BSE: back scattered electron mode SEM image.

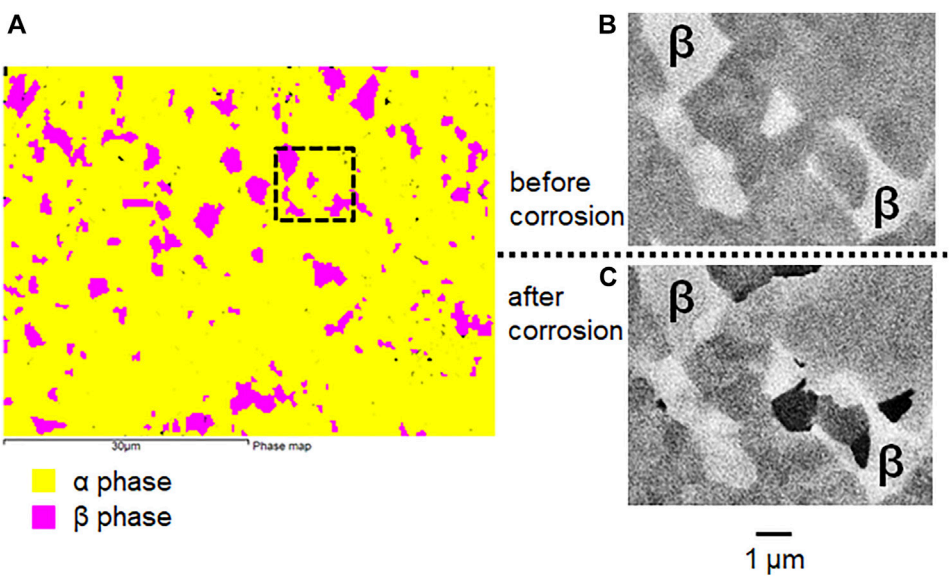

FIGURE 5 | (A) EBSD phase map **(B)** BSE image of mirror-polished Ti6Al4V before and **(C)** BSE image after potentiostatic test in 2 M HCl at −510 mV vs. SCE for 30 min at 37°C.

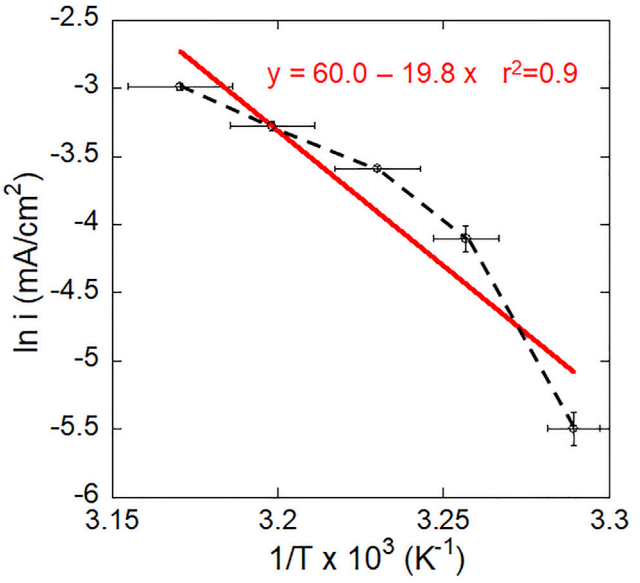

FIGURE 6 | A plot of steady state current at −510 mV vs. SCE vs. temperature for mirror-polished Ti6Al4V in 2 M HCl. The red line shows the fitted linear Arrhenius plot.

where E_a is the activation energy of the corrosion process during potentiostatic polarization, T is the absolute temperature (K) and R is the gas constant (8.3 J/mol·K).

It can be seen from **Figure 6** that the relationship between the natural logarithm of current density and reciprocal temperature is non-linear (black line) and does not obey a linear Arrhenius expression. The corrosion processes of Ti6Al4V in this study cannot therefore be completely described in this way. However, to compare with other works, a fitted Arrhenius plot was conducted (red line) and the calculated activation energy was 164 kJ/mol.

Different activation energies have been previously reported, e.g., 27 kJ/mol by Atapour et al. (Atapour et al., 2012), 57 kJ/mol by Yu et al. (Yu et al., 1999) and 63 kJ/mol by Blackwood et al. (Blackwood et al., 1988), which may be attributed to the different methods used. The activation energy values reported by Yu et al. (Yu et al., 1999) and Blackwood et al. (Blackwood et al., 1988) are related to the dissolution/corrosion of Ti oxide on CP-Ti in deaerated 5 M HCl or 3 M H_2SO_4, respectively, and based on the surface activation time during immersion at OCP. These findings suggest that the corrosion process in this study is complicated and not controlled by a single mechanism. Active dissolution and possible passivation may co-exist since the applied potential is the primary passivation potential (−510 mV vs. SCE). In addition, the applied potential was not far from OCP (−670 mV vs. SCE), where the cathodic reaction may also take place.

4.3 Surface Morphology of Ti6Al4V After Potentiostatic Testing

The effect of microstructure on corrosion is significant, and may induce corrosion defects as a result of preferential dissolution (Zhang H. et al., 2020; Wang et al., 2022; Xu et al., 2022). The corrosion process due to preferential attack has also been documented in the medical literature (Gilbert et al., 2012). The current study demonstrated that the α phase of Ti6Al4V was preferentially attacked relative to the β phase in 2 M HCl at 37°C after potentiostatic measurement at E_{pp} (−510 mV vs. SCE). This observation differs from Atapour's observation (Atapour et al., 2011) that the β phase of Ti6Al4V-ELI (similar to Ti6Al4V but contains lower content of C, N, O and Fe) was preferentially attacked after exposure to 5 M HCl at 37°C for 50 h. However, no over-potential was applied in Atapour's study in contrast to this report. In addition, it has been reported that the preferential dissolution of α phase of Ti-15Mo (with α+β phases microstructure) was observed at potentials in the active region in 40% H_2SO_4 at 80°C (Tomashov et al., 1974). The α phase of Ti-15Mo-3Nb-3Al was also found to be preferentially attacked during anodic polarization in 5 M HCl at 37°C (Yu and Scully, 1997).

For the Ti6Al4V used in this study, there was more Al and less V in the α phase, while there was more V but less Al in the β phase (**Figure 1**). Al has been reported to have a detrimental influence on the passivity and corrosion resistance of the α phase Ti in 5 M HCl (Yu and Scully, 1997), while dissolution of V coupled with conduction channels is also considered to be detrimental for the passive film on Ti in Hank's solution (Metikos-Hukovic et al., 2003). Considering the conditions of this study, both active dissolution and possible passivation of Ti6Al4V would be expected. The detrimental effect of Al may dominate over other factors, resulting in the observed preferential attack of α phase. It is noted that there is also some Fe content (**Figure 1**) in the β phase of Ti6Al4V in this study. Fe-containing β phase has been reported to possibly initiate hydride formation and proton reduction in acidic environment (Yan et al., 2006; Yan et al., 2011). It is likely that the cathodically active hydride sites on β phase co-exist with anodically active of α phase, which may have further resulted in the preferential dissolution of α phase.

5 CONCLUSION

In the current study, the temperature dependent corrosion behavior of Ti6Al4V has been investigated in the presence of HCl. It was found that Ti6Al4V exhibited active-passive behavior in HCl solution after surface activation. Furthermore, the steady state current density at the primary passivation potential becomes higher with increasing temperature. In addition, the factor influencing preferential corrosion of the microstructural phases has been explored. The α phase of Ti6Al4V is preferentially dissolved relative to the β phase after potentiostatic measurement. This study provides convincing evidence on preferential attack of Ti based implants and orthopedic replacements, and also supports corrosion-related failure of biomedical Ti alloys theoretically.

DATA AVAILABILITY STATEMENT

The raw data supporting the conclusion of this article will be made available by the authors, without undue reservation.

AUTHOR CONTRIBUTIONS

FY contributed to methodology, data curation, formal analysis, writing-original draft, OA contributed to writing-review and editing and supervision. AD contributed to methodology and supervision.

FUNDING

FY had been funded in part by the University of Birmingham and the China Scholarship Council. This work was supported by National Natural Science Foundation of China 51701101.

REFERENCES

Addison, O., Davenport, A. J., Newport, R. J., Kalra, S., Monir, M., Mosselmans, J. F. W., et al. (2012). Do 'passive' Medical Titanium Surfaces Deteriorate in Service in the Absence of Wear? *J. R. Soc. Interf.* 9 (76), 3161–3164. doi:10.1098/rsif.2012.0438

Atapour, M., Fathi, M. H., and Shamanian, M. (2012). Corrosion Behavior of Ti-6Al-4V alloy Weldment in Hydrochloric Acid. *Mater. Corrosion* 63 (2), 134–139. doi:10.1002/maco.201005821

Atapour, M., Pilchak, A., Frankel, G. S., Williams, J. C., Fathi, M. H., and Shamanian, M. (2010). Corrosion Behavior of Ti-6Al-4V with Different Thermomechanical Treatments and Microstructures. *Corrosion* 66 (6), 065004. doi:10.5006/1.3452400

Atapour, M., Pilchak, A. L., Frankel, G. S., and Williams, J. C. (2011). Corrosion Behavior of β Titanium Alloys for Biomedical Applications. *Mater. Sci. Eng. C* 31 (5), 885–891. doi:10.1016/j.msec.2011.02.005

Blackwood, D. J., Peter, L. M., and Williams, D. E. (1988). Stability and Open Circuit Breakdown of the Passive Oxide Film on Titanium. *Electrochimica Acta* 33 (8), 1143–1149. doi:10.1016/0013-4686(88)80206-8

Chandrasekaran, N., Bai, Z., and Gilbert, J. L. (2006). *Titanium Electrochemistry in the Presence of the Inflammatory Species H_2O_2.* Translation society for biomaterials annual meeting.

Gilbert, J. L., Buckley, C. A., and Jacobs, J. J. (1993). *In Vivo* corrosion of Modular Hip Prosthesis Components in Mixed and Similar Metal Combinations. The Effect of Crevice, Stress, Motion, and alloy Coupling. *J. Biomed. Mater. Res.* 27 (12), 1533–1544. doi:10.1002/jbm.820271210

Gilbert, J. L., Mali, S., Urban, R. M., Silverton, C. D., and Jacobs, J. J. (2012). *In Vivo* oxide-induced Stress Corrosion Cracking of Ti-6Al-4V in a Neck-Stem Modular Taper: Emergent Behavior in a New Mechanism of *In Vivo* Corrosion. *J. Biomed. Mater. Res.* 100B (2), 584–594. doi:10.1002/jbm.b.31943

Hallam, P., Haddad, F., and Cobb, J. (2004). Pain in the Well-Fixed, Aseptic Titanium Hip Replacement. *The J. Bone Jt. Surg. Br. volume* 86-B (1), 27–30. doi:10.1302/0301-620x.86b1.14326

Han, M.-K., Kim, J.-Y., Hwang, M.-J., Song, H.-J., and Park, Y.-J. (2015). Effect of Nb on the Microstructure, Mechanical Properties, Corrosion Behavior, and Cytotoxicity of Ti-Nb Alloys. *Materials* 8 (9), 5986–6003. doi:10.3390/ma8095287

Harun, W. S. W., Samykano, M., Lah, N. A. C., Ghani, S. A. C., Tarlochan, F., and Raza, M. R. (2017). Corrosion and Surface Modification on Biocompatible Metals: A Review. *Mater. Sci. Eng. C Mater. Biol. Appl.* 77, 1261–1274. doi:10.1016/j.msec.2017.04.102

Jackson, D. R., Omanovic, S., and Roscoe, S. G. (2000). Electrochemical Studies of the Adsorption Behavior of Serum Proteins on Titanium. *Langmuir* 16 (12), 5449–5457. doi:10.1021/la991497x

Jacobs, J. J., Gilbert, J. L., and Urban, R. M. (1998a). Corrosion of Metal Orthopaedic Implants*. *The J. Bone Jt. Surg. (American Volume)* 80 (2), 268–282. doi:10.2106/00004623-199802000-00015

Jacobs, J. J., Skipor, A. K., Patterson, L. M., Hallab, N. J., Paprosky, W. G., Black, J., et al. (1998b). Metal Release in Patients Who Have Had a Primary Total Hip Arthroplasty. A Prospective, Controlled, Longitudinal Study*. *J. Bone Jt. Surg.* 80 (10), 1447–1458. doi:10.2106/00004623-199810000-00006

Kang, L., and Yang, C. (2019). A Review on High-Strength Titanium Alloys: Microstructure, Strengthening, and Properties. *Adv. Eng. Mater.* 21, 1801359. doi:10.1002/adem.201801359

Kolman, D. G., Gaudett, M. A., and Scully, J. R. (1998). Modeling of Anodic Current Transients Resulting from Oxide Rupture of Plastically Strained β + α Titanium. *J. Electrochem. Soc.* 145 (6), 1829–1840. doi:10.1149/1.1838564

Kubacki, G. W., and Gilbert, J. L. (2021). The Effect of Hypochlorous Acid on the Tribocorrosion of CoCrMo/Ti-6Al-4V Bearing Couples. *J. Biomed. Mater. Res.* 109 (12), 2536–2544. doi:10.1002/jbm.a.37248

Liu, X., Chu, P., and Ding, C. (2004). Surface Modification of Titanium, Titanium Alloys, and Related Materials for Biomedical Applications. *Mater. Sci. Eng. R: Rep.* 47 (3-4), 49–121. doi:10.1016/j.mser.2004.11.001

Liu, Y., Zhu, D., and Gilbert, J. L. (2021). Sub-nano to Nanometer Wear and Tribocorrosion of Titanium Oxide-Metal Surfaces by *In Situ* Atomic Force Microscopy. *Acta Biomater.* 126, 477–484. doi:10.1016/j.actbio.2021.03.049

Metikos-Hukovic, M., Kwokal, A., and Piljac, J. (2003). The Influence of Niobium and Vanadium on Passivity of Titanium-Based Implants in Physiological Solution. *Biomaterials* 24 (21), 3765–3775. doi:10.1016/s0142-9612(03)00252-7

Morrell, A. P., Floyd, H., W. Mosselmans, J. F., Grover, L. M., Castillo-Michel, H., Davis, E. T., et al. (2019). Improving Our Understanding of Metal Implant Failures: Multiscale Chemical Imaging of Exogenous Metals in *Ex-Vivo* Biological Tissues. *Acta Biomater.* 98, 284–293. doi:10.1016/j.actbio.2019.05.071

Nelson, K., Hesse, B., Addison, O., Morrell, A. P., Gross, C., Lagrange, A., et al. (2020). Distribution and Chemical Speciation of Exogenous Micro- and Nanoparticles in Inflamed Soft Tissue Adjacent to Titanium and Ceramic Dental Implants. *Anal. Chem.* 92 (21), 14432–14443. doi:10.1021/acs.analchem.0c02416

Pałka, K., and Pokrowiecki, R. (2018). Porous Titanium Implants: A Review. *Adv. Eng. Mater.* 20, 1700648. 1700648. doi:10.1002/adem.201700648

Rabadia, C. D., Liu, Y. J., Chen, L. Y., Jawed, S. F., Wang, L. Q., Sun, H., et al. (2019). Deformation and Strength Characteristics of Laves Phases in Titanium Alloys. *Mater. Des.* 179, 107891. doi:10.1016/j.matdes.2019.107891

Smith, S. M., and Gilbert, J. L. (2021). Interfacial Compliance, Energy Dissipation, Frequency Effects, and Long-term Fretting Corrosion Performance of Ti-6Al-4V/CoCrMo Interfaces. *J. Biomed. Mater. Res* 110, 409–423. doi:10.1002/jbm.a.37299

Sullivan, S. J. L., and Topoleski, L. D. T. (2015). Surface Modifications for Improved Wear Performance in Artificial Joints: A Review. *Jom* 67 (11), 2502–2517. doi:10.1007/s11837-015-1543-0

Tomashov, N. D., Chernova, G. P., Ruscol, Y. S., and Ayuyan, G. A. (1974). The Passivation of Alloys on Titanium Bases. *Electrochimica Acta* 19 (4), 159–172. doi:10.1016/0013-4686(74)85012-7

Valero Vidal, C., Olmo Juan, A., and Igual Muñoz, A. (2010). Adsorption of Bovine Serum Albumin on CoCrMo Surface: Effect of Temperature and Protein Concentration. *Colloids Surf. B: Biointerfaces* 80 (1), 1–11. doi:10.1016/j.colsurfb.2010.05.005

Wang, J., Zhang, B., Xu, W., Zhang, J., Yang, L., Peng, Z., et al. (2022). Microstructure Refinement on Crevice Corrosion of High-Speed Rail Steel U75V Visualized by an *In Situ* Monitoring System. *Front. Mater.* 8. doi:10.3389/fmats.2021.820721

Xu, W., Deng, Y., Zhang, B., Zhang, J., Peng, Z., Hou, B., et al. (2022). Crevice Corrosion of U75V High-Speed Rail Steel with Varying Crevice gap Size by *In-Situ* Monitoring. *J. Mater. Res. Tech.* 16, 1856–1874. doi:10.1016/j.jmrt.2021.12.116

Xu, W., Yu, F., Yang, L., Zhang, B., Hou, B., and Li, Y. (2018). Accelerated Corrosion of 316L Stainless Steel in Simulated Body Fluids in the Presence of H2O2 and Albumin. *Mater. Sci. Eng. C* 92, 11–19. doi:10.1016/j.msec.2018.06.023

Xu, W., Zhang, B., Yang, L., Ni, Q., Li, Y., and Yu, F. (2019). Effect of the Coexistence of Albumin and H2O2on the Corrosion of Biomedical Cobalt Alloys in Physiological saline. *RSC Adv.* 9 (57), 32954–32965. doi:10.1039/c9ra05699h

Yan, L., Noël, J. J., and Shoesmith, D. W. (2011). Hydrogen Absorption into Grade-2 Titanium during Crevice Corrosion. *Electrochimica Acta* 56 (4), 1810–1822. doi:10.1016/j.electacta.2010.11.017

Yan, L., Ramamurthy, S., Noël, J. J., and Shoesmith, D. W. (2006). Hydrogen Absorption into Alpha Titanium in Acidic Solutions. *Electrochimica Acta* 52 (3), 1169–1181. doi:10.1016/j.electacta.2006.07.017

Yu, F., Addison, O., and Davenport, A. J. (2015). A Synergistic Effect of Albumin and H 2 O 2 Accelerates Corrosion of Ti6Al4V. *Acta Biomater.* 26, 355–365. doi:10.1016/j.actbio.2015.07.046

Yu, S. Y., Brodrick, C. W., Ryan, M. P., and Scully, J. R. (1999). Effects of Nb and Zr Alloying Additions on the Activation Behavior of Ti in Hydrochloric Acid. *J. Electrochem. Soc.* 146 (12), 4429–4438. doi:10.1149/1.1392655

Yu, S. Y., and Scully, J. R. (1997). Corrosion and Passivity of Ti-13% Nb-13% Zr in Comparison to Other Biomedical Implant Alloys. *Corrosion* 53 (12), 965–976. doi:10.5006/1.3290281

Yu, S. Y., Scully, J. R., and Vitus, C. M. (2001). Influence of Niobium and Zirconium Alloying Additions on the Anodic Dissolution Behavior of Activated Titanium in HCl Solutions. *J. Electrochem. Soc.* 148 (2), B68–B78. doi:10.1149/1.1337605

Zhang, H., Man, C., Wang, L., Dong, C., Wang, L., Kong, D., et al. (2020a). Different Corrosion Behaviors between α and β Phases of Ti6Al4V in Fluoride-Containing Solutions: Influence of Alloying Element Al. *Corrosion Sci.* 169, 108605. doi:10.1016/j.corsci.2020.108605

Zhang, L.-C., Chen, L.-Y., and Wang, L. (2020b). Surface Modification of Titanium and Titanium Alloys: Technologies, Developments, and Future Interests. *Adv. Eng. Mater.* 22 (5), 1901258. doi:10.1002/adem.201901258

Zhang, L. C., and Chen, L. Y. (2019). A Review on Biomedical Titanium Alloys: Recent Progress and Prospect. *Adv. Eng. Mater.* 21 (4), 1801215. doi:10.1002/adem.201801215

Zhang, Y., Addison, O., Yu, F., Troconis, B. C. R., Scully, J. R., and Davenport, A. J. (2018a). Time-dependent Enhanced Corrosion of Ti6Al4V in the Presence of H2O2 and Albumin. *Sci. Rep.* 8. doi:10.1038/s41598-018-21332-x

Zhang, Y., Davenport, A. J., Burke, B., Vyas, N., and Addison, O. (2018b). Effect of Zr Addition on the Corrosion of Ti in Acidic and Reactive Oxygen Species (ROS)-Containing Environments. *ACS Biomater. Sci. Eng.* 4 (3), 1103–1111. doi:10.1021/acsbiomaterials.7b00882

Conflict of Interest: The authors declare that the research was conducted in the absence of any commercial or financial relationships that could be construed as a potential conflict of interest.

Publisher's Note: All claims expressed in this article are solely those of the authors and do not necessarily represent those of their affiliated organizations, or those of the publisher, the editors and the reviewers. Any product that may be evaluated in this article, or claim that may be made by its manufacturer, is not guaranteed or endorsed by the publisher.

frontiers | Frontiers in Materials

ORIGINAL RESEARCH
published: 19 May 2022
doi: 10.3389/fmats.2022.874899

Corrosion Inhibition and Adsorption Process of 3-Amino-5-Mercapto-1,2,4-Triazole on Aluminium Alloy: Experimental and Theoretical Studies

Xin Guo[1,2,3], *Jinke Wang*[1,2], *Luyao Huang*[4], *Yajie Wang*[1,2], *Li Ma*[3], *Dawei Zhang*[1,2]* and *Lingwei Ma*[1,2,3]*

[1]Beijing Advanced Innovation Center for Materials Genome Engineering, Institute for Advanced Materials and Technology, University of Science and Technology Beijing, Beijing, China, [2]National Materials Corrosion and Protection Data Center, University of Science and Technology Beijing, Beijing, China, [3]State Key Laboratory for Marine Corrosion and Protection, Luoyang Ship Material Research Institute (LSMRI), Qingdao, China, [4]State Key Laboratory of Advanced Power Transmission Technology, Global Energy Interconnection Research Institute Co., Ltd., Beijing, China

The corrosion inhibition effect of 3-amino-5-mercapto-1,2,4-triazole (AMT) on AA2024 aluminium alloy in 3.5 wt.% NaCl solution was investigated, and the corrosion inhibition mechanism was revealed. The influence of AMT concentration on the corrosion inhibition performance was evaluated by potentiodynamic polarization curve and electrochemical impedance spectroscopy (EIS). Surface analysis and surface-enhanced Raman scattering (SERS) spectra were used to study the adsorption process and corrosion inhibition mechanism of AMT on the alloy surface. Polarization curve and EIS results showed that when the AMT concentration was 1.5 g/L, the corrosion current density (i_{corr}) was the lowest and the resistance of adsorption film (R_f) was the largest, illustrating the highest corrosion inhibition efficiency. Moreover, the adsorption kinetics process of AMT was revealed by SERS measurement, and a positive correlation between the SERS intensity and R_f values of AMT after different immersion time was achieved. It indicated that the efficient adsorption of corrosion inhibitors significantly enhanced the corrosion inhibition performance. Density functional theory (DFT) and molecular dynamics simulations were used to give further insight into the adsorption and inhibition mechanism of AMT on the aluminium alloy surface.

Keywords: aluminium alloy, 3-amino-5-mercapto-1,2,4-triazole, corrosion inhibition, surface-enhanced Raman scattering, adsorption process

OPEN ACCESS

Edited by:
Roger Charles Newman,
University of Toronto, Canada

Reviewed by:
Saviour A. Umoren,
King Fahd University of Petroleum and Minerals, Saudi Arabia
Renhui Zhang,
East China Jiaotong University, China

***Correspondence:**
Dawei Zhang
dzhang@ustb.edu.cn
Lingwei Ma
mlw1215@ustb.edu.cn

Specialty section:
This article was submitted to Environmental Degradation of Materials, a section of the journal Frontiers in Materials

Received: *13 February 2022*
Accepted: *31 March 2022*
Published: *19 May 2022*

Citation:
Guo X, Wang J, Huang L, Wang Y, Ma L, Zhang D and Ma L (2022) Corrosion Inhibition and Adsorption Process of 3-Amino-5-Mercapto-1,2,4-Triazole on Aluminium Alloy: Experimental and Theoretical Studies. Front. Mater. 9:874899. doi: 10.3389/fmats.2022.874899

INTRODUCTION

Because of the high strength, low density (about 2.7 g/cm^3), good electrical and thermal conductivity, as well as easy mechanical processing, aluminium alloys have great application prospects and irreplaceable importance in the fields of automotive manufacturing, light construction materials, aerospace, shipping, and military hardware. One of the most widely used aluminium alloys is AA2024 aluminium alloy, which has high specific strength and high fatigue strength (Marcelin and Pébère, 2015; Wang et al., 2017). Although the presence of alloying elements such as copper and magnesium enhances the mechanical properties of the aluminium matrix, it also reduces the corrosion resistance due to the presence of intermetallic particles (IMPs) with segregation at grain

boundaries (Recloux et al., 2018). The presence of IMPs results in the high corrosion sensitivity of the alloy due to the potential difference between the IMPs and the alloy matrix (Parvizi et al., 2018). In particular, the Al_2CuMg particles (also called S-phase) with more negative potential and higher electrochemical activity will be the initial sites of localized corrosion on the aluminium alloy (Hashimoto et al., 2016).

The utilization of organic/inorganic inhibitors is considered as one of the most useful means to prevent metals against corrosion degradation (Wang et al., 2018; Al Zoubi and Ko, 2019). The corrosion efficiency of these inhibitors depends on their adsorption ability on the metal surface *via* active sites, such as π-bonds, heteroatoms (N, S, and O), and polar functional groups (Qiang et al., 2016). Thus, the adsorption films can be formed on metals through covalent bonding (chemisorption) and/or electrostatic interaction (physical adsorption), which can protect metals from corrosive attack (Dutta et al., 2017; Hao et al., 2017). Recently, novel corrosion inhibitors with low toxicity, promising inhibitory efficacy and cost effectiveness have been the subject of current and long-term research focus. Among many nitrogenous compounds used as inhibitors, triazoles, tetrazoles, imidazoles, thiadiazoles and their derivatives are considered as environmental friendly chemicals that are harmless to the human health and the environment (Abdallah, 2004; El-Naggar, 2007; Obot et al., 2009).

3-amino-5-mercapto-1,2,4-triazole (AMT), a 5-membered heterocyclic compound containing a thiol group and an amino group, has been recognized as a good corrosion inhibitor for copper and copper alloys because of its strong adsorption ability on metal surfaces (Balbo et al., 2012). Yu et al. (2010) investigated the corrosion inhibition effect of AMT against copper corrosion in 3.5 wt.% NaCl solution. The inhibition efficiency (IE) increased with the AMT concentration, and the IE% maintained about 94% with an AMT concentration of 5×10^{-3} mol/L. The adsorption of AMT obeyed the Langmuir adsorption isotherm on copper surface, and the adsorption type was chemical adsorption. Sherif and Park (2006) studied the corrosion behavior of unalloyed copper in 0.5 M HCl with and without AMT inhibitors. The weight loss and corrosion rate of copper decreased with the increase of AMT concentration. The strong adsorption of AMT on the copper surface was confirmed by Raman spectra, hence preventing the formation of cuprous chloride and oxychloride complex. However, to the best of our knowledge, the corrosion inhibition effect of AMT on aluminium alloy has not been investigated yet. The fundamental mechanism of the proposed inhibiting interactions and the formation of corrosion protective layer for aluminium alloy are not well-understood, which are pivotal in evaluating the inhibitory performance of AMT molecules.

In this study, the adsorption performance and corrosion inhibition mechanism of AMT on AA2024 aluminium alloy in 3.5 wt.% NaCl solution are presented. The corrosion inhibition effect of AMT was evaluated by potentiodynamic polarization curve, electrochemical impedance spectroscopy (EIS) and surface observation techniques. Surface-enhanced Raman scattering (SERS) technique was applied to obtain the enhanced Raman spectra of corrosion inhibitors adsorbed on the surface of aluminium alloy after different immersion time. Furthermore, the corresponding adsorption and inhibition mechanism at the molecular level are proposed by density functional theory (DFT) and molecular dynamics simulations. This work provides new insights into the inhibition mechanism of organic inhibitors and offers practical guidance for the application of AMT as an effective inhibitor in industrial applications.

MATERIAL AND METHODS

Materials

AA20204 alloy ($4.0 \times 3.0 \times 0.1\ cm^3$) consists the following compositions: Cu 3.94 wt.%, Mg 1.46 wt.%, Mn 0.85 wt.%, Fe 0.45 wt.%, Zn 0.10 wt.%, Cr 0.05 wt.%, Si 0.05 wt.% and Al balance. The AA2024 alloy was successively polished by 400, 800, 1,500 and 2,000 grit sandpapers, and was washed thoroughly by ethanol before use. AMT and NaCl were purchased from Aladdin and used as received.

Electrochemical Tests

EIS and potentiodynamic polarization curves were performed by CHI 660E workstation based on a three-electrode system at room temperature. AA2024 aluminium alloy, platinum foil, and saturated calomel electrode were employed as the working electrode (WE), the counter electrode, and the reference electrode (RE), respectively. Before each measurement, the AA2024 alloy was dipped into 3.5 wt.% NaCl solution at an open circuit potential (OCP) for half an hour. Thereafter, EIS tests were recorded in the frequency range from 0.01 Hz to 100 kHz with a sinusoidal perturbation of 10 mV potential amplitude. Potentiodynamic polarization curves were obtained by scanning within ±250 mV potential range at 0.1666 mV s^{-1} versus OCP. Three parallel tests were performed under the same condition. To calculate the inhibition efficiency from polarization measurements, **Equation 1** was used:

$$IE(\%) = \frac{i_{corr,0} - i_{corr,i}}{i_{corr,0}} \times 100 \quad (1)$$

where $i_{corr,0}$ and $i_{corr,i}$ are the corrosion current densities in the absence and presence of corrosion inhibitors, respectively.

Surface Analysis

The corrosion morphology and chemical composition of the alloy surfaces after immersion in 3.5 wt.% NaCl solution for 72 h without and with AMT inhibitor were characterized by scanning electron microscopy (SEM, Merlin, Zeiss) and energy dispersive X-ray spectroscopy (EDX). The surface roughness of AA2024 surfaces was tested by confocal laser scanning microscopy (CLSM, VK-X, Keyence). Water contact angle (WCA) was calculated by a contact angle meter (Dataphysics OCA25) with a DI water drop volume of 5 μL at room temperature. A high-resolution camera was used to capture the static water images, and WCAs were calculated using the image processing software. The chemical

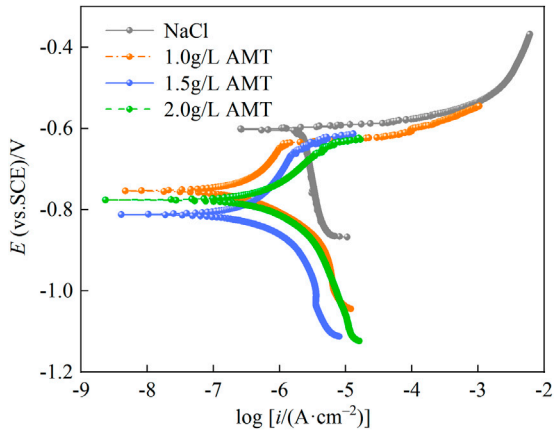

FIGURE 1 | Polarization curves of aluminium alloy after 6 h of immersion in 3.5 wt.% NaCl solution without and with various concentrations of AMT (1.0, 1.5, 2.0 g/L).

compositions of the uninhibited and inhibitor adsorbed alloy surfaces were analyzed by X-ray photoelectron spectroscopy (XPS, K-Alpha, Thermo Scientific).

Surface-Enhanced Raman Scattering Detection

To characterize the adsorption of AMT on the AA2024 alloy surface, SERS spectra were measured by a Raman spectrometer (i-Raman Plus, B&W TEK Inc.) equipped with a 785 nm laser and at a laser power of 150 mW (Wang et al., 2021). A SERS active tape was pasted onto the alloy surface before SERS detection. The diameter of the laser spot was ~80 μm, and the acquisition time was set to be 10 s for each detection spot. Five spectra were recorded on each substrate to ensure reproducibility.

Density Functional Theory Study

To investigate the electronic structure of AMT inhibitor, the quantum calculation method was adopted by DFT at the level B3LYP/6-311G++ base set (d) using the Gaussian 09 and GaussView 5.0.8 software (Zhang et al., 2020). Besides, the Fukui indices can be used to reflect the local reactivity of molecules. They determine the electron density in response to electrophilic or nucleophilic attack. The Fukui indices calculated from Mulliken's population value are as follows (El-Hajjaji et al., 2020), where $P_k(N+1)$, $P_k(N)$ and $P_k(N-1)$ are the charge values of k atoms to cations, neutral and anions, respectively.

For nuclearophilic attack

$$fk^{+} = P_k(N+1) - P_k(N) \tag{2}$$

For electrophilic attack

$$fk^{-} = P_k(N) - P_k(N-1) \tag{3}$$

Moreover, it is necessary to study the adsorption mode and binding strength of inhibitor on metal surface. The interaction nature between the inhibitor molecule and aluminium was performed using molecular mechanics method as implemented in Forcite module of Material studio 8.0 software. A simulation box of 34.18 × 34.18 × 68.86 $Å^3$ dimension containing six layers of Al (111), one inhibitor molecule, 500 H_2O molecules, 5 Cl^-, 5 Na^+ and 40 Å vacuum layer was established. The periodic boundary condition and COMPASS force field were used in this system. A fine quality simulation was accomplished with 500 ps simulation time and 1 fs time step using NVT canonical ensemble.

RESULTS AND DISCUSSION

Potentiodynamic Polarization

The corrosion inhibition effect of AMT on AA2024 substrate was first assessed by potentiodynamic polarization. **Figure 1** shows the polarization curves of aluminium alloy after 6 h of immersion in 3.5 wt.% NaCl solution without and with various concentrations of AMT (1.0, 1.5, 2.0 g/L). It can be seen that the application of inhibitors made the corrosion potential (E_{corr}) shift towards the negative potential and significantly decreased the corrosion current density (i_{corr}). The cathodic current density decreased evidently, indicating that AMT mainly acted as a cathode-type inhibitor to restrict the oxygen diffusion process (Shen et al., 2013). In the anodic branch, the polarization curve of the sample immersed in blank NaCl solution showed immediate pitting and the E_{corr} was around −0.60 V. With the addition of AMT, a passivation behavior of the alloy was observed, which was associated with the formation of a protective film via the adsorption of inhibitors. The fitted E_{corr} and i_{corr} parameters along with the inhibition efficiency are listed in **Table 1**. As can be seen, the i_{corr} values decreased apparently with the addition of inhibitors. The lowest i_{corr} value was observed for aluminium alloy in the presence of 1.5 g/L AMT (0.239 μA/cm^2), which was reduced by one order of magnitude compared with that of the blank alloy sample (2.397 μA/cm^2). The inhibition efficiencies were calculated to be 87.6% for 1.0 g/L AMT, 90.0% for 1.5 g/L AMT, and 82.6% for 2.0 g/L AMT, respectively, demonstrating superior suppression of the corrosion process in saline solutions.

Electrochemical Impedance Spectroscopy

The corrosion inhibition effect of AMT was further examined by EIS measurement. **Figure 2** shows the Nyquist diagrams and Bode plots of AA2024 aluminium alloy in 3.5 wt.% NaCl solution containing different concentrations of AMT inhibitors. The measured impedance implies the capacitive and resistive properties of the inhibitor film and is related to the corrosion kinetic of the metal in aggressive media. In the Nyquist diagrams, the capacitive loops of the blank alloy sample were relatively small, which decreased gradually with the increase of immersion time. After the addition of AMT, the diameter of capacitive loops increased significantly, and enlarged with the prolonging of immersion time. When the AMT concentration was 1.5 g/L, the capacitive loops reached the maximum. The impedance modulus plots illustrated similar trend, i.e., the impedance magnitude of aluminium alloy increased considerably after the addition of AMT, and reached the highest values when the AMT concentration was 1.5 g/L. In general, the low frequency

TABLE 1 | Polarization curve fitting data of AA2024 aluminium alloy in 3.5 wt.% NaCl solution containing different concentrations of AMT.

AMT concentration	E_{corr} (V)	i_{corr} (×10^{-6}A/cm^2)	-β_c (mV dec^{-1})	β_a (mV dec^{-1})	*IE* (%)
0	–0.601	2.397	1,092.8	15.5	–
1.0 g/L	–0.753	0.298	96.6	171.5	87.6%
1.5 g/L	–0.812	0.239	98.2	176.8	90.0%
2.0 g/L	–0.776	0.418	97.8	110.1	82.6%

impedance modulus $|Z|_{0.01Hz}$ is used as a semi-quantitative measure of the corrosion resistance property. After 72 h, the exposure to AMT solution led to the increase of $|Z|_{0.01Hz}$ value by more than 50 times compared to that of the blank alloy. Regarding to the phase angle plots, the blank AA2024 alloy possessed two time constants, the one in the low frequency (10^{-2}–10^{0} Hz) represented the charge transfer process, and the one in the mid frequency (10^{0}–10^{3} Hz) was assigned to the formation of metal oxide layer on the substrate (Liu et al., 2016; Ma et al., 2021). In contrast, with the addition of AMT inhibitors, the corrosion electrochemical process in the low-frequency region was greatly suppressed (Liao et al., 2017), and the broader time constant in the middle-to-high frequency indicated that the corrosion inhibitor was effectively adsorbed on the surface of aluminium alloy to form a robust protection layer (Zeng et al., 2021).

To verify the EIS interpretation, the electric equivalent circuits (EECs) in **Figure 3** are selected to fit the data in **Figure 2**, (Coelho et al., 2018). The EEC without inductance includes a solution resistance (R_s) in series with a constant phase element (CPE_f) in parallel with a film resistance (R_f) in series with another constant phase element (CPE_{dl}) in parallel with a charge transfer resistance (R_{ct}). The inductive loop (L) occurred due to the alloy dissolution during the adsorption process or due to the presence of the by-products on the electrode surface. Without AMT, R_f and CPE_f represent the resistance and the constant phase element of the native oxide layer (Fekry et al., 2014). For the inhibited substrates, R_f and CPE_f are assigned to the resistance and constant phase element of the inhibitor film (Yan et al., 2020; Zhu et al., 2021; Cao et al., 2022). CPE_{dl} corresponds to the double layer capacitance. The fitted EIS parameters are presented in **Table 2** and **Figure 4**. It is shown that the addition of AMT increased the $\underline{R}_{ct}$ and R_f values and the inhibition performance was promoted with increasing the AMT concentration. At the same time, the values of CPE_f and CPE_{dl} tended to decrease as the increase of AMT concentration due to the increase of AMT layer thickness and/or the local dielectric constant. It can be concluded that the addition of AMT formed an adsorption film on the alloy surface, thus slowing down the corrosion process of aluminium alloy in NaCl solution.

Surface Characterization

To assess the surface morphology of AA2024 aluminium alloy exposed to the aggressive media, 3D profilometry and SEM images were performed on the alloy after immersion in 3.5 wt.% NaCl solution for 72 h without and with 1.5 g/L AMT inhibitor. It is clearly seen in **Figure 5** that the unprotected alloy surface was remarkably corroded with the appearance of many pits and corrosion products, and the surface roughness was as high as ~0.389 μm. On the contrary, the AMT protected aluminium surface was relative smooth and uniform, with a lower surface roughness value of 0.225 μm. It is known that the AA2024 alloy is highly susceptible to corrosion in NaCl solution due to the existence of IMPs, which have been demonstrated to be the active sites for localized corrosion (Zheludkevich et al., 2005). The EDX analysis from the red spot in **Figure 5A** revealed the presence of Al, Cu, Mg, Mn, C and O elements on the alloy surface, and the very high oxygen content verified the presence of corrosion products such as $Al(OH)_3$ and Al_2O_3 on the alloy matrix (Visser et al., 2019). For the AMT protected AA2024 surface, no corrosion pit was visible. The EDX results from the blue spot and the green spot in **Figure 5B** showed much lower oxygen content and higher Al content, demonstrating a low level of corrosion products on the alloy surface. Hence, the surface analysis data are in good agreement with the electrochemical data, indicating that AMT can considerably improve the corrosion resistance property of the aluminium alloy.

To investigate the hydrophilic and hydrophobic nature of different surfaces, the WCAs were tested on the AA2024 aluminium alloy after immersion in 3.5 wt.% NaCl solution for 72 h without and with 1.5 g/L AMT inhibitor. As shown in **Figure 6**, the blank alloy exhibited a WCA of 65.3°, and the inhibitor adsorbed alloy displayed a higher WCA of 76.8°. These results indicate that the corrosive media can reach the uninhibited alloy surface more easily, whereas there is a competitive adsorption between inhibitors and water molecules in solution on the AMT adsorbed surface. The increase of the adsorption ability of corrosion inhibitors strengthens the hydrophobicity of the metal surface, hence decreasing the corrosion tendency (Zhang et al., 2021).

Surface-Enhanced Raman Scattering Detection of Inhibitors

SERS technology is one of the most important surface analytical methods because of its rapid detection, high sensitivity, high selectivity, and *in-situ* characterization of the surface composition (Yue et al., 2022). The adsorption kinetics of AMT molecules on AA2024 alloy surfaces after different exposure time to NaCl solution was characterized by

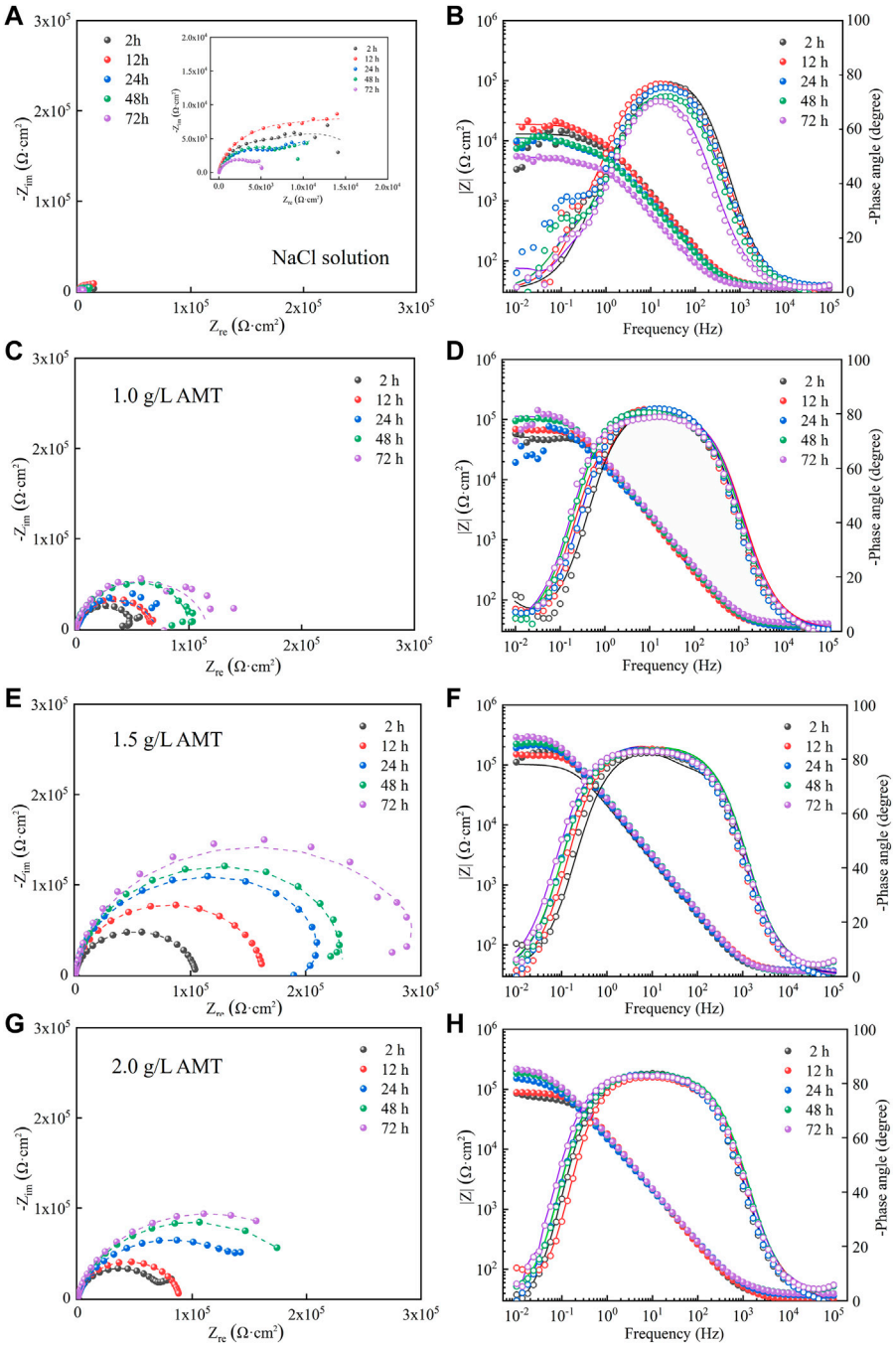

FIGURE 2 | (A,C,E,G) Nyquist diagrams and **(B,D,F,H)** Bode plots of AA2024 aluminium alloy in 3.5 wt.% NaCl solution containing different concentrations of AMT inhibitors.

SERS measurement, using silver nanorods decorated SERS active tape as the Raman signal amplifier (Wang et al., 2021; Ma et al., 2020). **Figure 7A** shows the SERS spectra of AMT molecules adsorbed on the surface of AA2024 aluminium alloy after immersing in 3.5 wt.% NaCl solution with 1.5 g/L AMT for different times. The SERS spectra clearly revealed the characteristic Raman bands of AMT molecules, including 702, 856, 929, 1,130, 1,405, and 1,606 cm^{-1}. The peaks at 702 and 929 cm^{-1} are attributed to triazole ring torsion. The peak at 856 cm^{-1} corresponds to the triazole ring breathing pattern. The peak value at 1,130 cm^{-1} is attributed to the N-N bending vibration. The peak at 1,405 cm^{-1} is assigned to the tensile vibration of the triazole ring. The peak at 1,606 cm^{-1} belongs to the bending vibration

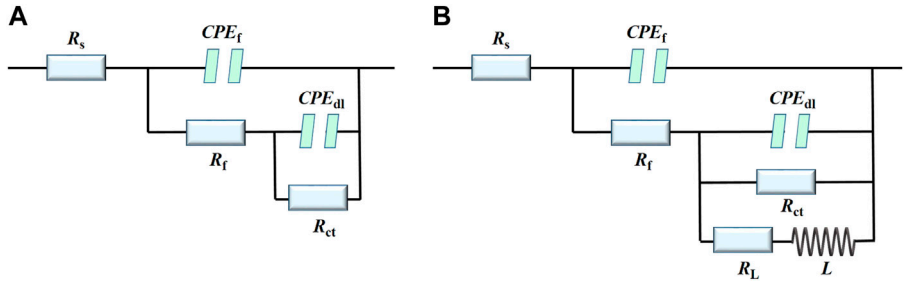

FIGURE 3 | EECs of AA2024 aluminium alloy in 3.5wt.% NaCl solution containing AMT.

TABLE 2 | EIS fitting data of AA2024 alloy in 3.5 wt.% NaCl solution containing different concentrations of AMT.

C_{AMT} (g/L)	Time (h)	Q_f ($\Omega^{-1}\cdot cm^{-2}\ S^n$)	n_f	R_f ($\Omega\cdot cm^2$)	Q_{dl} ($\Omega^{-1}\cdot cm^{-2}\cdot S^n$)	n_{dl}	R_{ct} ($\Omega\cdot cm^2$)	L (H cm^{-2})	R_L ($\Omega\cdot cm^2$)	χ^2 ($\times 10^{-3}$)
0	2	1.03×10^{-5}	0.93	9.37×10^{3}	7.70×10^{-5}	1.00	3.82×10^{3}	—	—	4.8
	12	1.27×10^{-5}	0.92	1.46×10^{4}	9.61×10^{-5}	1.00	4.62×10^{3}	—	—	2.0
	24	1.76×10^{-5}	0.89	7.40×10^{3}	2.77×10^{-4}	0.94	3.92×10^{3}	—	—	1.1
	48	1.52×10^{-5}	0.88	8.34×10^{3}	3.92×10^{-4}	1.00	3.16×10^{3}	—	—	1.1
	72	1.09×10^{-5}	0.90	6.97×10^{3}	4.32×10^{-4}	0.97	2.26×10^{3}	—	—	1.9
1.0	2	8.06×10^{-6}	0.94	5.14×10^{4}	3.87×10^{-5}	1.00	4.43×10^{4}	—	—	5.1
	12	8.29×10^{-6}	0.94	5.96×10^{4}	2.84×10^{-5}	1.00	5.03×10^{4}	—	—	1.5
	24	7.65×10^{-6}	0.90	6.94×10^{4}	6.40×10^{-6}	0.94	6.42×10^{4}	—	—	1.9
	48	7.21×10^{-6}	0.91	7.63×10^{4}	7.23×10^{-7}	1.00	7.83×10^{4}	1.83×10^{3}	3.03×10^{4}	1.6
	72	5.93×10^{-6}	0.92	8.71×10^{4}	7.72×10^{-7}	1.00	1.06×10^{5}	—	—	4.0
1.5	2	6.94×10^{-6}	0.94	7.34×10^{4}	8.22×10^{-7}	1.00	1.55×10^{5}	—	—	4.3
	12	6.21×10^{-6}	0.95	1.35×10^{5}	5.82×10^{-7}	1.00	2.11×10^{5}	—	—	1.7
	24	6.08×10^{-6}	0.94	1.95×10^{5}	5.42×10^{-7}	1.00	2.68×10^{5}	1.23×10^{4}	5.82×10^{4}	0.6
	48	4.26×10^{-6}	0.94	2.43×10^{5}	3.99×10^{-7}	0.98	3.07×10^{5}	3.10×10^{4}	8.24×10^{4}	0.6
	72	3.03×10^{-6}	0.94	2.62×10^{5}	1.30×10^{-7}	0.96	6.91×10^{5}	1.11×10^{5}	1.03×10^{5}	0.9
2.0	2	6.16×10^{-6}	0.93	4.49×10^{4}	9.66×10^{-7}	1.00	6.64×10^{4}	—	—	0.8
	12	6.21×10^{-6}	0.94	5.61×10^{4}	9.64×10^{-7}	0.88	8.88×10^{4}	—	—	5.1
	24	5.96×10^{-6}	0.87	7.97×10^{4}	6.84×10^{-7}	1.00	9.32×10^{4}	—	—	1.3
	48	5.12×10^{-6}	0.98	8.62×10^{4}	8.65×10^{-7}	1.00	2.06×10^{5}	—	—	3.2
	72	5.66×10^{-6}	0.88	1.25×10^{5}	7.97×10^{-7}	1.00	6.21×10^{5}	—	—	1.1

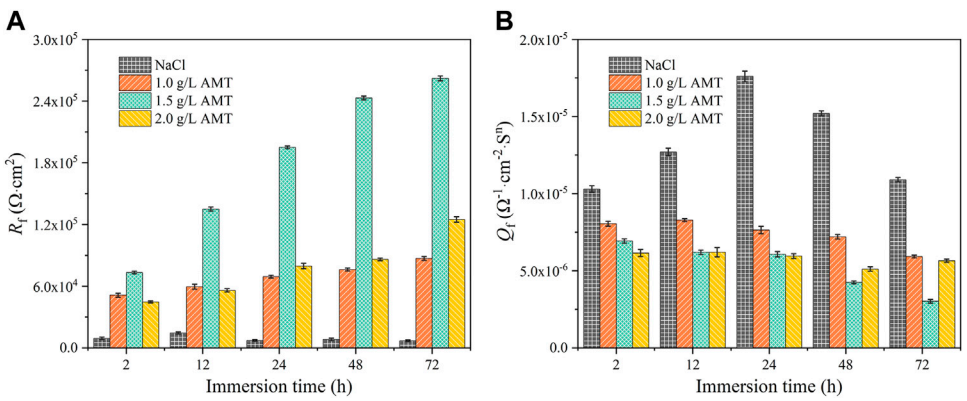

FIGURE 4 | Evaluation of **(A)** R_f and **(B)** Q_f parameters of AA2024 aluminium alloy in 3.5wt.% NaCl solution containing AMT.

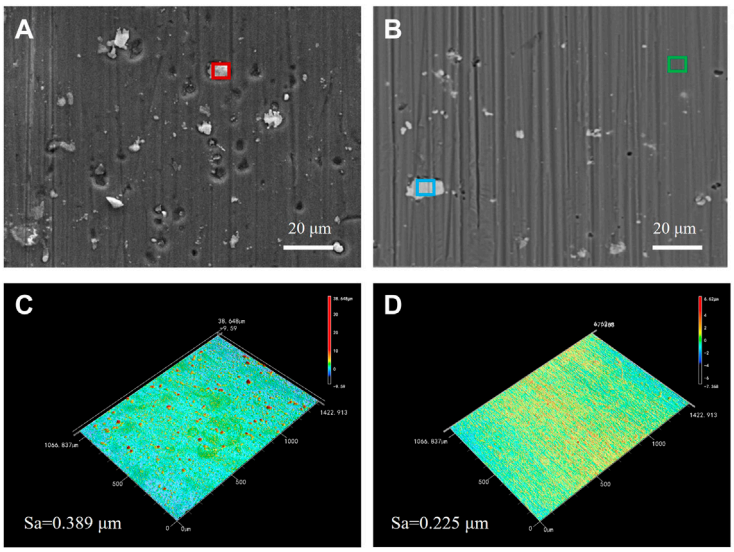

E

Element	Atomic percent (%)
C	17.66
O	14.89
Cu	8.10
Mg	1.48
Mn	0.46
Al	57.41

Element	Atomic percent (%)
C	15.22
O	6.22
Cu	17.31
Mg	1.00
Mn	0.10
Al	60.16

Element	Atomic percent (%)
C	10.62
O	3.82
Cu	1.33
Mg	2.52
Mn	0.31
Al	81.40

FIGURE 5 | SEM images after immersing the AA2024 aluminium alloy in 3.5 wt.% NaCl solution for 72 h **(A)** without and **(B)** with 1.5 g/L AMT inhibitors; CLSM images after immersing the AA2024 alloy in 3.5 wt.% NaCl solution for 72 h **(C)** without and **(D)** with 1.5 g/L AMT inhibitors; **(E)** EDX calculation results from the red, blue and green areas.

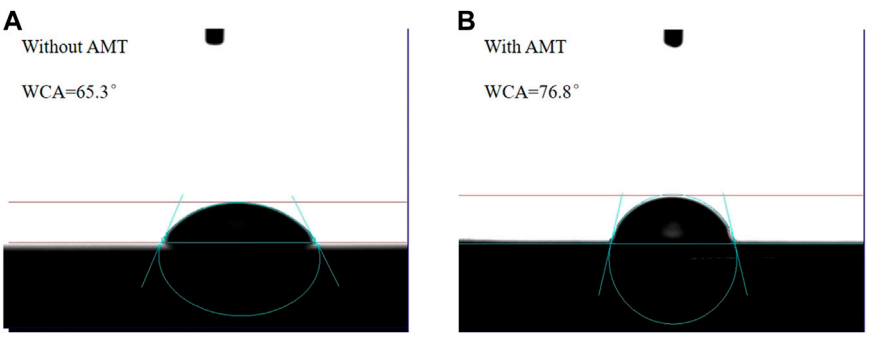

FIGURE 6 | The WCA of the AA2024 aluminium alloy after immersion in 3.5 wt.% NaCl solution for 72 h **(A)** without and **(B)** with 1.5 g/L AMT inhibitor.

of NH_2 (Sherif et al., 2010; Wang et al., 2011; Xavier and Gobinath, 2012). The appearance of these characteristic Raman peaks indicates that AMT molecules have been effectively adsorbed on the surface of AA2024 alloy. More importantly, the variation of Raman intensity can reflect the adsorption kinetics process of analytes. It is noted that with the increase of immersion time, the SERS signals on the aluminium alloy surface increased gradually. From 2 to 48 h, the SERS signals of corrosion inhibitors increased significantly, indicating that the adsorption rate was relatively high. Subsequently, the SERS intensity and corresponding adsorption amount reached saturation from 48 to 72 h. To correlate the AMT adsorption behavior with the corrosion inhibition property on the AA2024 alloy surface, **Figure 7B** plots the R_f values of the substrate immersed in 3.5 wt.% NaCl solution containing 1.5 g/L AMT versus the corresponding SERS peak intensities at 1,606 cm^{-1}. A positive correlation was clearly shown between the SERS signals and R_f values. Since the R_f parameter can reflect the surface coverage of inhibitor film, the dramatic increase of R_f value indicates the gradual coverage of metal surface via inhibitor adsorption, which is confirmed by the continuous increase and saturation of SERS signals during immersion.

XPS Characterization

To further identify the adsorption of corrosion inhibitors on the alloy surface, the chemical compositions of surface films were studied by XPS. **Figure 8** shows the XPS survey spectra and high resolution spectra of AA2024 aluminium alloy surface after immersion for 72 h in 3.5 wt.% NaCl solution without or with 1.5 g/L AMT inhibitors. It is seen that the peaks of Al, C and O elements were detected on the alloy

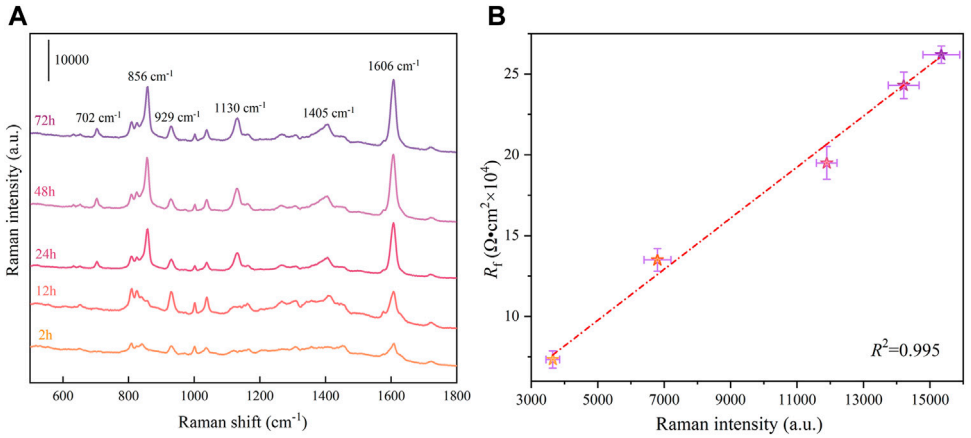

FIGURE 7 | (A) SERS spectra of AMT molecules adsorbed on the surface of AA2024 aluminium alloy after immersing in 3.5 wt.% NaCl solution with 1.5 g/L AMT for different times; **(B)** the R_f values of the substrate immersed in 3.5 wt.% NaCl solution containing 1.5 g/L AMT versus the corresponding SERS peak intensities at 1,606 cm^{-1}.

surface in blank solution. After adding inhibitors, new elemental peaks of S and N were shown, which were assigned to the AMT molecules. **Figure 8B** shows the high resolution peaks of Al 2p in the blank and inhibitor adsorbed alloy surfaces. The Al 2p spectrum consisted of three components at binding energies of 74.9, 74.3, and 73.1 eV, corresponding to $Al(OH)_3$, Al_2O_3 and AlO_x, respectively (Kozlica et al., 2021). **Figure 8C** illustrates the high resolution peaks of S 2p. The S element signal was not observed on the surface of blank AA2024 alloy. In the presence of AMT, the S 2p spectrum with two peaks was clearly seen. The peaks at 161.8 and 164.0 eV can be ascribed to

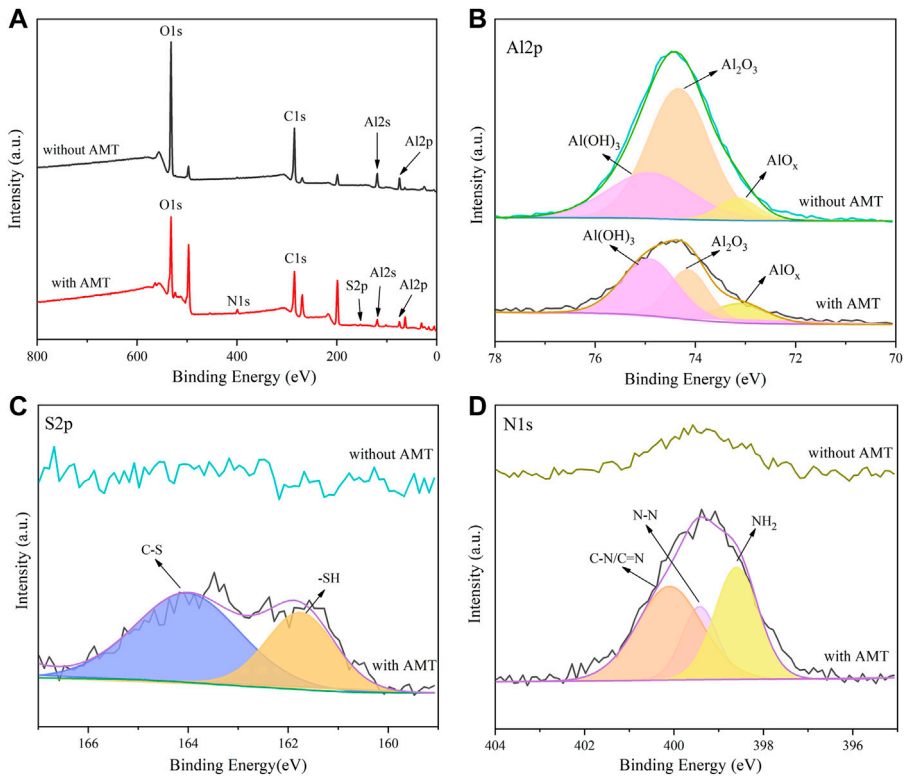

FIGURE 8 | The XPS survey spectra and high resolution spectra of AA2024 aluminium alloy surface after immersion for 72 h in 3.5 wt.% NaCl solution without or with 1.5 g/L AMT inhibitors.

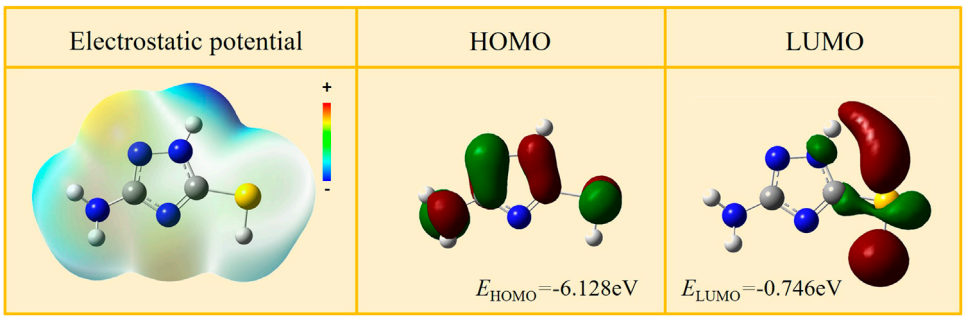

FIGURE 9 | Frontier molecular density distribution of the AMT molecule.

TABLE 3 | Fukui indices of AMT.

Atoms	f_-	f_+	f_0
C1	0.06	0.06	0.06
N2	0.05	0.05	0.05
N4	0.17	0.07	0.12
N5	0.08	0.04	0.07
C6	0.07	0.03	0.06
N7	0.16	0.03	0.10
S10	0.21	0.40	0.31

the sulfhydryl group and C-S bond between heterocycle and sulfhydryl group. As for the N 1s spectrum (**Figure 8D**), in the presence of AMT, it can be fitted into three peaks of 400.0, 399.4 and 398.6 eV, which were ascribed to the C-N/C=N, N-N and NH_2 bonds of AMT molecules (Huang and Bu, 2020). Therefore, the AMT inhibitors are successfully adsorbed on the alloy surface, which is in agreement with the results from EDS and Raman measurements.

Molecular Modeling

Quantum chemistry calculation of AMT molecules was carried out to further investigate the corrosion protection mechanism of AMT. **Figure 9** shows the highest occupied molecular orbital (HOMO) and the lowest unoccupied molecular orbital (LUMO) as well as the electrostatic potential (ESP) of AMT molecules. According to the Frontier molecular orbital theory, the transition of the electrons is mainly related to the HOMO and LUMO of a molecule (Pareek et al., 2019; Wang et al., 2022). As for AMT, the HOMO is distributed uniformly over the entire surface of the molecule, and the LUMO is localized around the S atom, which exhibits an extremely strong electron gaining ability as can be seen from the huge red region in the molecular orbital diagram.

We used condensed Fukui functions to analyze the local reactivity of molecules and quantitatively describe the possibility of each atom as an adsorption site. The sites with larger f values exhibit increased activity and are potential candidates to be adsorbed on metal surfaces (El-Hajjaji et al., 2020). **Table 3** shows the condensed Fukui functions and f values for the C, N, and S atoms of AMT molecules. **Figure 10** shows the corresponding graphs. As can be seen, N4 and N7 have large f_- values, which indicate that these atoms are preferred sites for electrons transfer from AMT molecules to metals during electrophilic attacks. S atom exhibits great electron-giving and electron-accepting ability owing to the much larger f_+ and f_- values, which is consistent

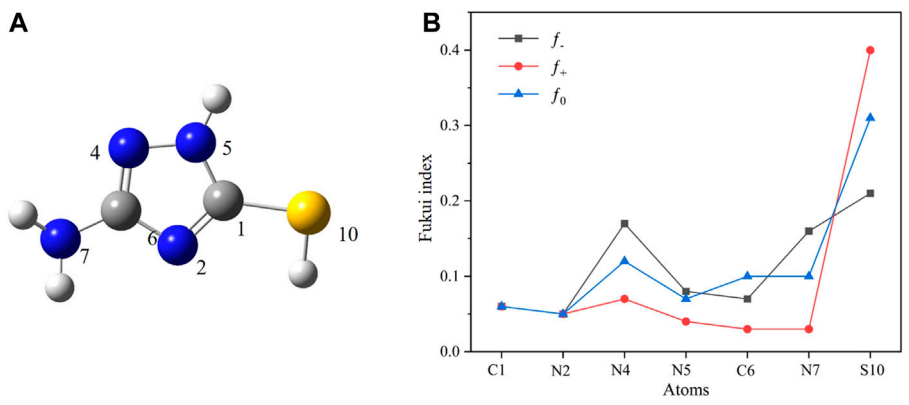

FIGURE 10 | (A) The optimized structure of AMT molecular; **(B)** Fukui indices and components of molecular orbitals of AMT.

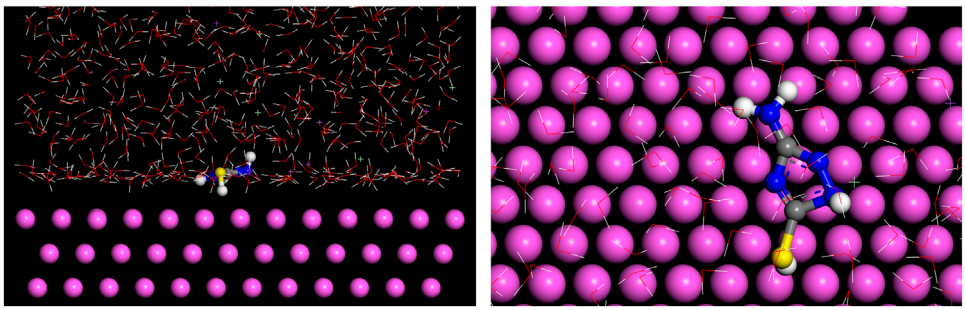

FIGURE 11 | Adsorption equilibrium configuration of AMT molecules on Al (111) surface.

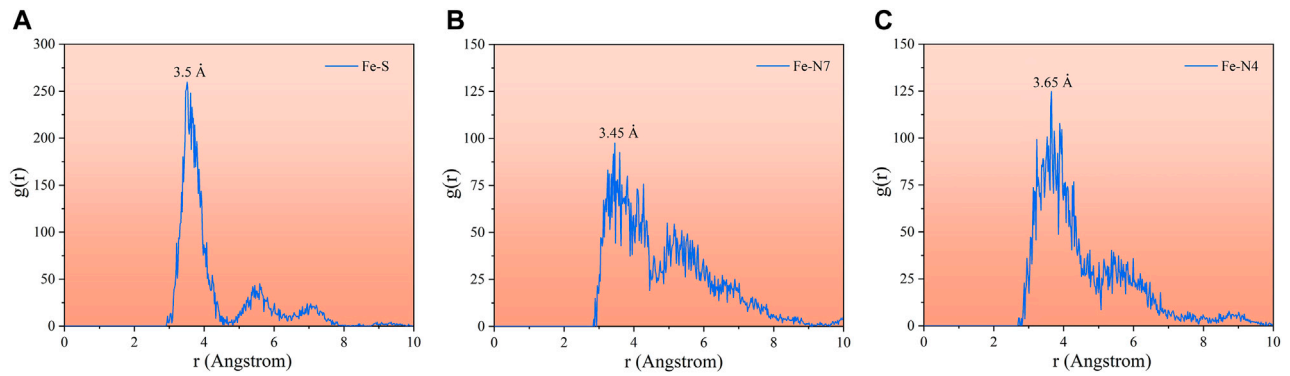

FIGURE 12 | The relevant RDF analysis of AMT molecule **(A)** Fe-S, **(B)** Fe-N7 and **(C)** Fe-N4.

with the conclusion of molecular orbital analysis. Therefore, special attention should be paid to these highly active sites when calculating the adsorption model of AMT molecule on metal surface.

Molecular dynamics simulation can provide novel insights into the interfacial interactions between organic molecules and metal substrates (Kovačević and Kokalj, 2011). **Figure 11** shows the side and the top views of the equilibrium adsorption configuration of AMT molecule on Al (111) surface. AMT adsorbs on the Al surface in a nearby flat manner, which is beneficial for improving the surface coverage of AMT on the metal surface (Bouoidina et al., 2021). The electron-giving and electron-receiving processes of AMT adsorption are promoted by S and N atoms (Luo et al., 2021). These interactions lead to the formation of coordination bonds between AMT and Al surface, and can form a compact film that prevents the aggressive media to reach the metal surface (Ammouchi et al., 2020; Li et al., 2022).

The radial distribution function (RDF) g (r) derived from MD orbital data is a good method to estimate the bond information. Generally, peak bond lengths from 1 to 3.5 Å are associated with the chemisorption, while those beyond 3.5 Å are assigned to the physical interactions (Lgaz et al., 2017; Singh et al., 2018). **Figure 12** shows the RDF analysis of the major heteroatoms of the AMT molecule on the Al (111) surface. As can be seen from the figure, the bond lengths of Fe-N7 (3.45 Å) and Fe-S (3.5 Å) are no more than 3.5 Å, which means that the N7 and S atoms are attached to the metal substrate via chemisorption; on the other hand, N4 (3.65 Å) is adsorbed on the metal substrate as physical adsorption. These findings confirm that these active centers have great ability for donating and accepting electrons to/from Al that lead to good inhibition performance of the studied AMT molecules.

CONCLUSION

In this work, the excellent corrosion inhibition effect of AMT on AA2024 aluminium alloy in 3.5 wt.% NaCl solution was demonstrated by electrochemical test and surface analysis, and the corrosion inhibition mechanism was explained by DFT and molecular dynamics simulation. AMT mainly acted as a cathode-type corrosion inhibitor, and the highest corrosion inhibition efficiency was achieved when the concentration of AMT was

1.5 g/L. SERS spectra characterized the adsorption kinetics process of AMT on the alloy surface, and a positive correlation between the SERS signals and R_f values was clearly shown, which indicated that the continuous adsorption of AMT strengthened the corrosion inhibition efficiency. The heterogeneous donor atoms (N and S) of AMT molecule can act as the active sites to contribute to the bonding of the metal surface. The adsorbed AMT molecules tended to adsorb on the Al (111) surface in the parallel orientation to obtain the maximum coverage.

DATA AVAILABILITY STATEMENT

The raw data supporting the conclusion of this article will be made available by the authors, without undue reservation.

AUTHOR CONTRIBUTIONS

XG: Conceptualization, methodology, software. JW: Data curation, writing—original draft preparation. LH: Visualization. YW: Investigation. LM: Supervision. DZ: Supervision, validation. LWM: Writing—reviewing and editing.

FUNDING

This work was supported by the National Natural Science Foundation of China (No. 51901015); Young Elite Scientists Sponsorship Program by China Association for Science and Technology (YESS, 2020QNRC001); and the Research Fund of State Key Laboratory for Marine Corrosion and Protection, Luoyang Ship Material Research Institute (LSMRI) under the contract No. KFJS1902.

REFERENCES

Abdallah, M. (2004). Antibacterial Drugs as Corrosion Inhibitors for Corrosion of Aluminium in Hydrochloric Solution. *Corrosion Sci.* 46, 1981–1996. doi:10.1016/j.corsci.2003.09.031

Al Zoubi, W., and Ko, Y. G. (2019). Self-assembly of Hierarchical N-Heterocycles-Inorganic Materials into Three-Dimensional Structure for superior Corrosion protection. *Chem. Eng. J.* 356, 850–856. doi:10.1016/j.cej.2018.09.089

Ammouchi, N., Allal, H., Belhocine, Y., Bettaz, S., and Zouaoui, E. (2020). DFT Computations and Molecular Dynamics Investigations on Conformers of Some Pyrazinamide Derivatives as Corrosion Inhibitors for Aluminum. *J. Mol. Liquids* 300, 112309. doi:10.1016/j.molliq.2019.112309

Balbo, A., Chiavari, C., Martini, C., and Monticelli, C. (2012). Effectiveness of Corrosion Inhibitor Films for the Conservation of Bronzes and Gilded Bronzes. *Corrosion Sci.* 59, 204–212. doi:10.1016/j.corsci.2012.03.003

Bouoidina, A., Ech-chihbi, E., El-Hajjaji, F., El Ibrahimi, B., Kaya, S., and Taleb, M. (2021). Anisole Derivatives as Sustainable-green Inhibitors for Mild Steel Corrosion in 1 M HCl: DFT and Molecular Dynamic Simulations Approach. *J. Mol. Liquids* 324, 115088. doi:10.1016/j.molliq.2018.08.05310.1016/j.molliq.2020.115088

Cao, K., Huang, W., Huang, X., and Pan, J. (2022). Imidazo [1,2-a] Pyrimidine Derivatives as Effective Inhibitor of Mild Steel Corrosion in HCl Solution: Experimental and Theoretical Studies. *Front. Mater.* 9, 843522. doi:10.3389/fmats.2022.843522

Coelho, L. B., Cossement, D., and Olivier, M.-G. (2018). Benzotriazole and Cerium Chloride as Corrosion Inhibitors for AA2024-T3: An EIS Investigation Supported by SVET and ToF-SIMS Analysis. *Corrosion Sci.* 130, 177–189. doi:10.1016/j.corsci.2017.11.004

Dutta, A., Saha, S. K., Adhikari, U., Banerjee, P., and Sukul, D. (2017). Effect of Substitution on Corrosion Inhibition Properties of 2-(substituted Phenyl) Benzimidazole Derivatives on Mild Steel in 1 M HCl Solution: a Combined Experimental and Theoretical Approach. *Corrosion Sci.* 123, 256–266. doi:10.1016/j.corsci.2017.04.017

El-Hajjaji, F., Ech-Chihbi, E., Rezki, N., Benhiba, F., Taleb, M., Chauhan, D. S., et al. (2020). Electrochemical and Theoretical Insights on the Adsorption and Corrosion Inhibition of Novel Pyridinium-Derived Ionic Liquids for Mild Steel in 1 M HCl. *J. Mol. Liquids* 314, 113737. doi:10.1016/j.molliq.2020.113737

El-Naggar, M. M. (2007). Corrosion Inhibition of Mild Steel in Acidic Medium by Some Sulfa Drugs Compounds. *Corrosion Sci.* 49, 2226–2236. doi:10.1016/j.corsci.2006.10.039

Fekry, A. M., Ghoneim, A. A., and Ameer, M. A. (2014). Electrochemical Impedance Spectroscopy of Chitosan Coated Magnesium Alloys in a Synthetic Sweat Medium. *Surf. Coat. Tech.* 238, 126–132. doi:10.1016/j.surfcoat.2013.10.058

Hao, Y., Sani, L. A., Ge, T., and Fang, Q. (2017). The Synergistic Inhibition Behaviour of Tannic Acid and Iodide Ions on Mild Steel in H 2 SO 4 Solutions. *Corrosion Sci.* 123, 158–169. doi:10.1016/j.corsci.2017.05.001

Hashimoto, T., Zhang, X., Zhou, X., Skeldon, P., Haigh, S. J., and Thompson, G. E. (2016). Investigation of Dealloying of S Phase (Al 2 CuMg) in AA 2024-T3 Aluminium alloy Using High Resolution 2D and 3D Electron Imaging. *Corrosion Sci.* 103, 157–164. doi:10.1016/j.corsci.2015.11.013

Huang, H., and Bu, F. (2020). Correlations between the Inhibition Performances and the Inhibitor Structures of Some Azoles on the Galvanic Corrosion of Copper Coupled with Silver in Artificial Seawater. *Corrosion Sci.* 165, 108413. doi:10.1016/j.corsci.2019.108413

Kovačević, N., and Kokalj, A. (2011). Analysis of Molecular Electronic Structure of Imidazole- and Benzimidazole-Based Inhibitors: A Simple Recipe for Qualitative Estimation of Chemical Hardness. *Corrosion Sci.* 53, 909–921. doi:10.1016/j.corsci.2010.11.016

Kozlica, D. K., Kokalj, A., and Milošev, I. (2021). Synergistic Effect of 2-mercaptobenzimidazole and Octylphosphonic Acid as Corrosion Inhibitors for Copper and Aluminium - an Electrochemical, XPS, FTIR and DFT Study. *Corrosion Sci.* 182, 109082. doi:10.1016/j.corsci.2020.109082

Lgaz, H., Salghi, R., Subrahmanya Bhat, K., Chaouiki, A., Shubhalaxmiand Jodeh, S. (2017). Correlated Experimental and Theoretical Study on Inhibition Behavior of Novel Quinoline Derivatives for the Corrosion of Mild Steel in Hydrochloric Acid Solution. *J. Mol. Liquids* 244, 154–168. doi:10.1016/j.molliq.2017.08.121

Li, Q., Xia, X., Pei, Z., Cheng, X., Zhang, D., Xiao, K., et al. (2022). Long-term Corrosion Monitoring of Carbon Steels and Environmental Correlation Analysis via the Random forest Method. *Npj Mater. Degrad.* 6, 1. doi:10.1038/s41529-021-00211-3

Liao, L. L., Mo, S., Luo, H. Q., and Li, N. B. (2017). Longan Seed and Peel as Environmentally Friendly Corrosion Inhibitor for Mild Steel in Acid Solution: Experimental and Theoretical Studies. *J. Colloid Interf. Sci.* 499, 110–119. doi:10.1016/j.jcis.2017.03.091

Liu, J., Wang, D., Gao, L., and Zhang, D. (2016). Synergism between Cerium Nitrate and Sodium Dodecylbenzenesulfonate on Corrosion of AA5052 Aluminium alloy in 3 wt.% NaCl Solution. *Appl. Surf. Sci.* 389, 369–377. doi:10.1016/j.apsusc.2016.07.107

Luo, X., Dong, C., Xi, Y., Ren, C., Wu, J., Zhang, D., et al. (2021). Computational Simulation and Efficient Evaluation on Corrosion Inhibitors for Electrochemical Etching on Aluminum Foil. *Corrosion Sci.* 187, 109492. doi:10.1016/j.corsci.2021.109492

Ma, L., Wang, J., Ren, C., Ju, P., Huang, Y., Zhang, F., et al. (2020). Detection of Corrosion Inhibitor Adsorption via a Surface-Enhanced Raman Spectroscopy (SERS) Silver Nanorods Tape Sensor. *Sensors Actuators B: Chem.* 321, 128617. doi:10.1016/j.snb.2020.128617

Ma, L., Wang, J., Zhang, D., Huang, Y., Huang, L., Wang, P., et al. (2021). Dual-action Self-Healing Protective Coatings with Photothermal Responsive Corrosion Inhibitor Nanocontainers. *Chem. Eng. J.* 404, 127118. doi:10.1016/j.cej.2020.127118

Marcelin, S., and Pébère, N. (2015). Synergistic Effect between 8-hydroxyquinoline and Benzotriazole for the Corrosion protection of 2024 Aluminium alloy: a

Local Electrochemical Impedance Approach. *Corrosion Sci.* 101, 66–74. doi:10.1016/j.corsci.2015.09.002

Obot, I. B., Obi-Egbedi, N. O., and Umoren, S. A. (2009). Antifungal Drugs as Corrosion Inhibitors for Aluminium in 0.1M HCl. *Corrosion Sci.* 51, 1868–1875. doi:10.1016/j.corsci.2009.05.017

Pareek, H., Jain, D., Hussain, S., Biswas, A., Shrivastava, R., Parida, S. K., et al. (2019). A New Insight into Corrosion Inhibition Mechanism of Copper in Aerated 3.5 wt.% NaCl Solution by Eco-Friendly Imidazopyrimidine Dye: Experimental and Theoretical Approach. *Chem. Eng. J.* 358, 725–742. doi:10.1016/j.cej.2018.08.079

Parvizi, R., Hughes, A. E., Glenn, A. M., Cizek, P., Tan, M. Y., and Forsyth, M. (2018). Role of Microstructure in Corrosion Initiation of a Highly-Deformed AA2024 Wire. *Corrosion Sci.* 144, 184–197. doi:10.1016/j.corsci.2018.08.052

Qiang, Y., Zhang, S., Xu, S., and Li, W. (2016). Experimental and Theoretical Studies on the Corrosion Inhibition of Copper by Two Indazole Derivatives in 3.0% NaCl Solution. *J. Colloid Interf. Sci.* 472, 52–59. doi:10.1016/j.jcis.2016.03.023

Recloux, I., Andreatta, F., Druart, M.-E., Coelho, L. B., Cepek, C., Cossement, D., et al. (2018). Stability of Benzotriazole-Based Films against AA2024 Aluminium alloy Corrosion Process in Neutral Chloride Electrolyte. *J. Alloys Comp.* 735, 2512–2522. doi:10.1016/j.jallcom.2017.11.346

Shen, S., Guo, X.-y., Song, P., Pan, Y.-C., Wang, H.-q., Wen, Y., et al. (2013). Phytic Acid Adsorption on the Copper Surface: Observation of Electrochemistry and Raman Spectroscopy. *Appl. Surf. Sci.* 276, 167–173. doi:10.1016/j.apsusc.2013.03.061

Sherif, E.-S. M., Erasmus, R. M., and Comins, J. D. (2010). *In Situ* Raman Spectroscopy and Electrochemical Techniques for Studying Corrosion and Corrosion Inhibition of Iron in Sodium Chloride Solutions. *Electrochimica Acta* 55, 3657–3663. doi:10.1016/j.electacta.2010.01.117

Sherif, E. M., and Park, S. M. (2006). 2-Amino-5-ethyl-1, 3, 4-thiadiazole as a Corrosion Inhibitor for Copper in 3.0% NaCl Solutions. *Corros. Sci.* 48, 4065–4079. doi:10.1016/j.corsci.2006.03.011

Singh, A., Ansari, K. R., Haque, J., Dohare, P., Lgaz, H., Salghi, R., et al. (2018). Effect of Electron Donating Functional Groups on Corrosion Inhibition of Mild Steel in Hydrochloric Acid: Experimental and Quantum Chemical Study. *J. Taiwan Inst. Chem. Eng.* 82, 233–251. doi:10.1016/j.jtice.2017.09.021

Visser, P., Marcoen, K., Trindade, G. F., Abel, M.-L., Watts, J. F., Hauffman, T., et al. (2019). The Chemical Throwing Power of Lithium-Based Inhibitors from Organic Coatings on AA2024-T3. *Corrosion Sci.* 150, 194–206. doi:10.1016/j.corsci.2019.02.009

Wang, J., Ma, L., Guo, X., Wu, S., Liu, T., Yang, J., et al. (2022). Two Birds with One Stone: Nanocontainers with Synergetic Inhibition and Corrosion Sensing Abilities towards Intelligent Self-Healing and Self-Reporting Coating. *Chem. Eng. J.* 433, 134515. doi:10.1016/j.cej.2022.134515

Wang, X., Liu, X., and Wang, X. (2011). Self-assembled Synthesis of Ag Nanodendrites and Their Applications to SERS. *J. Mol. Struct.* 997, 64–69. doi:10.1016/j.molstruc.2011.04.041

Wang, Y., Wang, J., Ma, L., Ren, C., Zhang, D., Ma, L., et al. (2021). Qualitative and Quantitative Detection of Corrosion Inhibitors Using Surface-Enhanced Raman Scattering Coupled with Multivariate Analysis. *Appl. Surf. Sci.* 568, 150967. doi:10.1016/j.apsusc.2021.150967

Wang, Z., Chen, P., Li, H., Fang, B., Song, R., and Zheng, Z. (2017). The Intergranular Corrosion Susceptibility of 2024 Al alloy during Re-ageing after Solution Treating and Cold-Rolling. *Corrosion Sci.* 114, 156–168. doi:10.1016/j.corsci.2016.11.013

Wang, Z., Gong, Y., Zhang, L., Jing, C., Gao, F., Zhang, S., et al. (2018). Self-assembly of New Dendrimers Basing on strong π-π Intermolecular Interaction for Application to Protect Copper. *Chem. Eng. J.* 342, 238–250. doi:10.1016/j.cej.2018.02.080

Xavier, R. J., and Gobinath, E. (2012). FT-IR, FT-Raman, Ab Initio and DFT Studies, HOMO-LUMO and NBO Analysis of 3-Amino-5-Mercapto-1,2,4-Triazole. *Spectrochimica Acta A: Mol. Biomol. Spectrosc.* 86, 242–251. doi:10.1016/j.saa.2011.10.031

Yan, T., Zhang, S., Feng, L., Qiang, Y., Lu, L., Fu, D., et al. (2020). Investigation of Imidazole Derivatives as Corrosion Inhibitors of Copper in Sulfuric Acid: Combination of Experimental and Theoretical Researches. *J. Taiwan Inst. Chem. Eng.* 106, 118–129. doi:10.1016/j.jtice.2019.10.014

Yu, J., Li, J., and Gan, F. (2010). Inhibition of Copper Corrosion in Deionized Water by 3-Amino-5-Mercapto-1, 2, 4-triazole. *J. Chin. Soc. Corrosion Prot.* 30, 21–24.

Yue, S., Fang, J., and Xu, Z. (2022). Advances in Droplet Microfluidics for SERS and Raman Analysis. *Biosens. Bioelectron.* 198, 113822. doi:10.1016/j.bios.2021.113822

Zeng, Y., Kang, L., Wu, Y., Wan, S., Liao, B., Li, N., et al. (2021). Melamine Modified Carbon Dots as High Effective Corrosion Inhibitor for Q235 Carbon Steel in Neutral 3.5 Wt% NaCl Solution. *J. Mol. Liq.* 349, 118108. doi:10.1016/j.molliq.2021.118108

Zhang, R., Xiong, L., He, Z., Pu, J., and Guo, L. (2021). Synthesis and Structure of Water-Soluble Sb Quantum Dots and Enhanced Corrosion Inhibition Performance and Mechanisms. *Inorg. Chem.* 60, 16346–16356. doi:10.1021/acs.inorgchem.1c02172

Zhang, X., Pan, G., Hu, L., and Wang, H. C. (2020). Effects of Nitrilotriacetic Acid and Corrosion Inhibitor on Cobalt Barrier Chemical-Mechanical Polishing: Experimental and Density Functional Theory Analysis. *Colloids Surf. A: Physicochemical Eng. Aspects* 605, 125392. doi:10.1016/j.colsurfa.2020.125392

Zheludkevich, M. L., Yasakau, K. A., Poznyak, S. K., and Ferreira, M. G. S. (2005). Triazole and Thiazole Derivatives as Corrosion Inhibitors for AA2024 Aluminium alloy. *Corrosion Sci.* 47, 3368–3383. doi:10.1016/j.corsci.2005.05.040

Zhu, M., He, Z., Guo, L., Zhang, R., Anadebe, V. C., Obot, I. B., et al. (2021). Corrosion Inhibition of Eco-Friendly Nitrogen-Doped Carbon Dots for Carbon Steel in Acidic media: Performance and Mechanism Investigation. *J. Mol. Liquids* 342, 117583. doi:10.1016/j.molliq.2021.117583

Conflict of Interest: All authors declare that the research was conducted in the absence of any commercial or financial relationships that could be construed as a potential conflict of interest.

Publisher's Note: All claims expressed in this article are solely those of the authors and do not necessarily represent those of their affiliated organizations, or those of the publisher, the editors and the reviewers. Any product that may be evaluated in this article, or claim that may be made by its manufacturer, is not guaranteed or endorsed by the publisher.

frontiers | Frontiers in Materials

ORIGINAL RESEARCH
published: 14 July 2022
doi: 10.3389/fmats.2022.910152

Graphene Oxide-Hybridized Waterborne Epoxy Coating for Simultaneous Anticorrosive and Antibiofilm Functions

Ying Zhou[1,2], *Haoran Wang*[3], *Cheng Zhang*[3], *Qixin Zhou*[3]* *and Debora F. Rodrigues*[2,4]*

[1]Department of Materials Chemistry, Huzhou University, Huzhou, China, [2]Department of Civil and Environmental Engineering, University of Houston, Houston, TX, United States, [3]Department of Chemical, Biomolecular and Corrosion Engineering, The University of Akron, Akron, OH, United States, [4]Department of Material Science and Engineering, University of Houston, Houston, TX, United States

Multifunctional coatings with simultaneous antibacterial and anticorrosive properties are essential for marine environments, oil and gas industry, medical settings, and domestic/public appliances to preserve integrity and functionality of pipes, instruments, and surfaces. In this work, we developed a simple and effective method to prepare graphene oxide (GO)-hybridized waterborne epoxy (GOWE) coating to simultaneously improve anticorrosive and antibacterial properties. The effects of different GO filler ratios (0.05, 0.1, and 0.5, 1 wt%) on the electrochemical and antibacterial behaviors of the waterborne epoxy coating were investigated over short- and long-term periods. The electrochemical behavior was analyzed with salt solution for 64 days. The antibacterial effect of GOWE coating was evaluated with *Shewanella oneidensis* (MR-1), which is a microorganism that can be involved in corrosion. Our results revealed that concentrations as low as 0.1 wt% of the GO was effective performance than the waterborne epoxy coating without graphene oxide. This result is due to the high hydrophilicity of the graphene oxide fillers, which allowed great dispersion in the waterborne epoxy coating matrix. Furthermore, this study used a corrosion relevant bacterium as a model organism, that is, *Shewanella oneidensis* (MR-1), which is more relevant for real-word applications. This as-prepared GO-hybridized waterborne polymeric hybrid film provides new insight into the application of 2D nanomaterial polymer composites for simultaneous anticorrosive and antibacterial applications.

Keywords: anticorrosive, antibacterial, graphene oxide, waterborne epoxy coating, antibiofilm

OPEN ACCESS

Edited by:
Cem Örnek,
Istanbul Technical University, Turkey

Reviewed by:
Joseph Raj Xavier,
Saveetha University, India
Dmitry S Kharitonov,
Polish Academy of Sciences, Poland

***Correspondence:**
Qixin Zhou
qzhou@uakron.edu
Debora F. Rodrigues
dfrigirodrigues@uh.edu

Specialty section:
This article was submitted to Environmental Degradation of Materials, a section of the journal Frontiers in Materials

Received: *31 March 2022*
Accepted: *07 June 2022*
Published: *14 July 2022*

Citation:
Zhou Y, Wang H, Zhang C, Zhou Q and Rodrigues DF (2022) Graphene Oxide-Hybridized Waterborne Epoxy Coating for Simultaneous Anticorrosive and Antibiofilm Functions. Front. Mater. 9:910152. doi: 10.3389/fmats.2022.910152

INTRODUCTION

Metals or alloys are widely used materials in industry and in our daily life; however, they are prone to electrochemical corrosion and biofilm formation, which can impact their performance (Fichman et al., 2014; Van Haute et al., 2018). The global economic loss of biofilm and corrosion is enormous, which is estimated to be 2.5 trillion (3.4% of the global GDP) (Lim, 2012; Koch et al., 2016; Nguyen et al., 2017a). Additionally, there is urgent health concerns involving increased chances of infection caused by various bacterial biofilms, especially in medical facilities (Mallakpour et al., 2021). To prevent such issues, special surface modifications involving antibacterial and anticorrosion

properties are required for long-term applications of these metallic materials in industrial facilities (e.g., oil and gas equipment (Al Abbas et al., 2013) and marine industry (Lekbach et al., 2019)), biomedical implants (e.g., bone/tissue implants (Chopra et al., 2021; Zhang et al., 2021)), and domestic appliances (Nie et al., 2020). Hence, both anticorrosive and antibacterial coatings must be developed for these metallic surfaces.

Epoxy is an efficient coating material and is commonly used to enhance the interfacial surface property due to its strong adhesion, excellent corrosion resistance, low curing shrinkage, good reservoir for additive corrosion inhibitors, and outstanding chemical properties (Li et al., 2018; Atta et al., 2020; Meng et al., 2020). However, the main drawback of epoxy coatings is their tendency to suffer from surface abrasion resulting in localized defects and corrosion, and the potential polymer degradation under UV radiation (Christopher et al., 2015). Therefore, recent studies have been conducted to incorporate inorganic fillers in the epoxy matrix to stimulate a synergic effect and overcome these challenges. For instance, inorganic particles, like montmorillonite, were shown to provide good barrier effect and enhance the bonding strength at the surface interface. However, there are still some issues with the incorporation of these inorganic fillers, such as complex manufacturing, high dosage, or easy cracking (Nematollahi et al., 2010; Meng et al., 2015).

More recently, nano-sized fillers (like SiO_2, TiO_2, and ZnO) have been studied to alleviate microscopic defects and enhance the cross-linking density of the coating due to their high specific surface area (Yadav et al., 2019). Among the nanofillers, graphene oxide (GO), as a relatively new class of materials for corrosion control (Georgakilas et al., 2015), has been considered as an ideal candidate for real potential large-scale applications due to its outstanding properties, including mechanical, electrical, low cost, aqueous/thermal stability, barrier effect, high specific surface area (~2630 m^2/g), and inherent antibacterial property (Geim and Novoselov, 2010; Compton et al., 2011; Georgakilas et al., 2015). Researchers have shown great interest in graphene oxide or graphene oxide-derivative composites for anticorrosive protection (Yu et al., 2014; Ding et al., 2019).

Furthermore, researchers have also found that graphene oxide composite polymeric coatings are promising antibacterial materials due to their ability to induce oxidative stress by reactive oxygen species (ROS) (Nguyen et al., 2017a). For instance, Liu et al. (2018) have reported that a solvent-borne epoxy with GO exhibited high antibacterial capability against *E.coli*. Graphene oxide has also shown to improve the antibacterial property of other polymers (e.g., poly DMA, poly (DMA-co-MEA)) in our previous studies (Fan et al., 2017; Peña-Bahamonde et al., 2018). Additionally, graphene oxide/GO and their derivatives have even exhibited a potential effect against COVID-19 (Hu et al., 2010).

Recently, modification of waterborne polymeric coatings with graphene oxide and its derivatives was exploited for specific functions and barrier performance enhancement, including antibacterial and anticorrosive properties (Mirmohseni et al., 2019; Ning et al., 2021). This interest arises from the increasing pressure for low carbon emission requirements, where waterborne polymers have been considered as a promising coating material with negligible VOC emission (Zhang et al., 2018; Chen et al., 2020). More recently, graphene oxide or its derivatives have been incorporated into waterborne polymeric matrix coatings, such as waterborne epoxy (WEP) and waterborne polyurethane (WPU) for simultaneous anticorrosive and antibacterial properties (Wang et al., 2018). However, most of the studies used *Escherichia coli* (*E. coli*) as their model organism, which is not involved in corrosive activity. Herein, in our study, to simulate the actual steel corrosion environment, an Fe (III) reduction bacterium (IRB) model, *Shewanella oneidensis* MR-1, which can contribute to steel corrosion (Glasauer et al., 2002), was applied to systematically investigate the antibacterial function for potential real applications.

Specifically, the objectives of this study are to systematically investigate the doping concentration of graphene oxide on the corrosion resistance of GOWE coating through a long-term electrochemical testing and to determine the antibacterial property of GOWE toward *Shewanella oneidensis* biofilm formation for both short-term and extended periods using confocal laser scanning microscopy (CLSM) analysis. The materials produced were fully characterized to determine the dispersion of graphene oxide nanofillers in the WEP matrix as well as the successful formation of GOWE films through optic spectra, Raman, and field emission scanning electron microscopy (FESEM) analysis. Our research presents an effective strategy to produce a GOWE coating with simultaneous anticorrosive property and antibacterial function, with the potential for further applications in industrial, medical, and domestic fields.

EXPERIMENTAL

Materials

Waterborne epoxy resin (BECKOPOX EP 385W) and polyamine curing agent (BECKOPOX EH 613W) were obtained from Allnex Company (Langley, SC, United States). Luria–Bertani (LB) broth medium was purchased from Fisher-Scientific (Massachusetts, United States). Graphite (<20 μm), sulfuric acid (H_2SO_4, 98 wt%), sodium nitrate, potassium permanganate, and hydrogen peroxide (30 wt%) were purchased from Sigma Aldrich (Austin, TX, United States). Propidium iodide (PI) and SYTO9 dyes were obtained from Invitrogen Corporation (CA, United States). All reagents and solvents were used without further purification. All the chemicals were ACS grade.

Preparation of Graphene Oxide Nanoplates

Graphene oxide nanofiller was synthesized from natural graphite flakes using the modified Hummers' method, which was reported in our previous study (Nguyen et al., 2017b). In brief, 2.5 g of graphite, 25 ml of concentrated H_2SO_4, and 2.0 g of $KMnO_4$ were mixed in an ice bath and followed by stirring at 35°C for 10 h. Then the mixture was further heated at 90 ± 1°C for 1.5 h with a dropwise dosing of H_2O_2 solution. Finally, the graphene oxide suspension was centrifuged at 8000 rpm and washed four to five

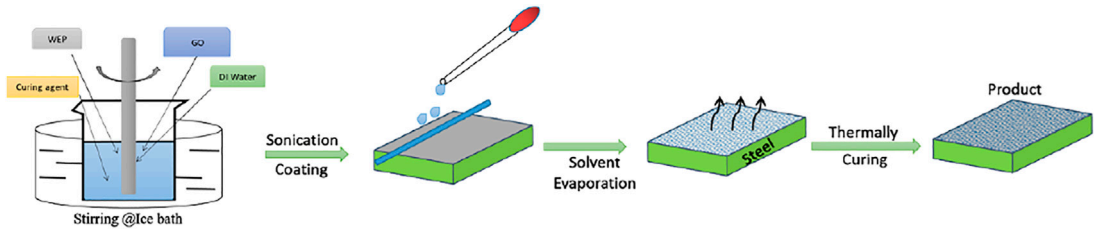

FIGURE 1 | Schematic illustration of the GOWE coating preparation.

TABLE 1 | Formulation of graphene oxide-hybridized waterborne epoxy coating.

	GO (mg)	Waterborne epoxy resin (solid content: 56 wt%) (g)	Curing agent (solid content: 80 wt%) (g)	Dry thickness (μm)
GOWE-0	0	5	0.79	60 ± 3
GOWE-0.05	1.72	5	0.79	63 ± 2
GOWE-0.1	3.43	5	0.79	62 ± 4
GOWE-0.5	17.16	5	0.79	64 ± 5
GOWE-1	34.32	5	0.79	61 ± 3

times with distilled water. The washed samples were further freeze-dried to achieve the final product.

Graphene Oxide–Waterborne Epoxy Composite (GOWE) Coating Fabrication

Concentrations (wt%) of 0.05, 0.1, 0.5, and 1 graphene oxide were first dispersed in the waterborne epoxy resin by ultrasonic treatment for 1 h in an ice bath. Subsequently, a stoichiometric amount of the polyamine curing agent was added to the dispersion. The aforementioned mixture was magnetically stirred for 20 min, followed by sonication for 15 min to remove air bubbles. Then the coating mixture was applied onto a steel substrate (QD36, Q-Lab Corporation, Ohio, United States) to prepare GOWE coatings. The prepared coatings were left at room temperature for 24 h, followed by thermally curing at 120°C for 1 h. The film preparation procedure is shown in **Figure 1**. The dry film thickness of the control (without adding graphene oxide) and GOWE coatings were around 60 μm measured by a thickness gauge (byko-test 8500, BYK). The formulation of the waterborne epoxy coating with graphene oxide nanofillers is shown in **Table 1**.

Corrosive Resistance Measurement

The corrosion resistance of coated samples was measured through electrochemical impedance spectroscopy (EIS) measurements by using the Reference 600+ Potentiostat (Gamry Instrument). The testing coatings were immersed in 3.5 wt% NaCl solution with an exposure area of 7.07 cm^2. The steel panel, saturated calomel electrode (SCE), and platinum mesh with 6.25 cm^2 surface area were used as working, reference, and counter electrodes, respectively. All EIS tests were run in a Faraday cage at room temperature using 10 mV AC perturbation with a frequency range of 10^5–10^{-2} Hz.

For the biofilm testing, the coating samples were cut into 2 × 2 cm small coupons. The backside and the edges of the coating coupons were applied with epoxy coating to avoid water penetration. The coating coupons after the biofilm testing were immersed in 3.5 wt% NaCl solution for corrosion resistance assay.

Antibacterial Performance Testing

Antibacterial experiments were performed using a model metal reduction bacterium (*S. oneidensis* MR-1, Gram-negative). *S. oneidensis* MR-1 was cultured overnight in a freshly prepared Luria–Bertani broth medium (LB, 1.0 wt% tryptone, 0.5 wt% yeast extract, 1.0 wt% NaCl, and 1.5 wt% agar powder) with constant shaking (150 rpm, 30°C) by using a shaker (Thermo Fisher, United States). The pH of the medium was adjusted to 7.0. The initial concentration of bacteria in the LB media was in the range of ~3.0 × 10^7 CFU/ml (OD_{600} = 0.60). The details of the microbial biofilm growth were described in our previous study (Nguyen et al., 2017a; Ansari et al., 2021). In brief, bacterial growth was batch cultivated in a sterile six-well plate (BioLite, United States) at 28°C in the LB medium. Before transferring to the plates, each coated steel plate was sterilized with UV light for 15 min in the biosafety hood. After that, 100 μl of the *S. oneidensis* culture was dosed to 10 ml of the LB growth media. Then 100 μl of the above diluted culture mixture plus 6 ml of the LB medium were transferred to six sterilized steel plates. The plates were further incubated at 30°C for short term (72 h) and long term (10 days) under static conditions. For the long-term test, the *S. oneidensis* culture medium was replaced with 2 ml fresh media each day. After the testing, the specimens were gently rinsed three times with phosphate-buffered saline (PBS) to remove nonadherent bacteria for further characterization (Nguyen et al., 2017a).

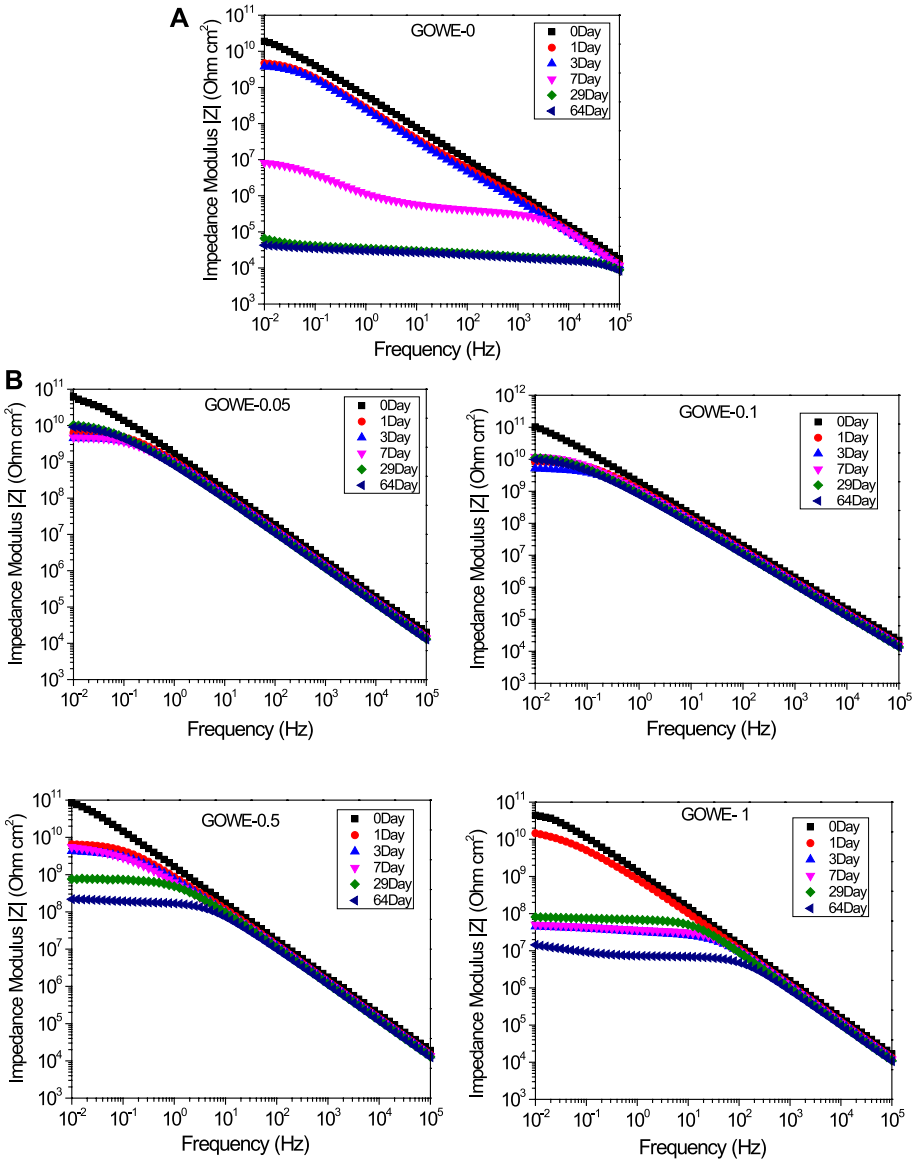

FIGURE 2 | (A) Bode plots of neat waterborne epoxy coating GOWE-0 (without graphene oxide) in the immersion of 3.5 wt% NaCl solution; and **(B)** Bode plots of GOWE coatings (GOWE-0.05, GOWE-0.1, GOWE-0.5, and GOWE-1) in the immersion of 3.5 wt% NaCl solution. The formulation of GOWE coatings is listed in **Table 1**.

All the testing were performed in triplicate and repeated at least three times for analysis.

Characterization and Analysis

All coupons coated with GOWE for corrosion and biofilm growth were characterized using Fourier transformed infrared spectroscopy, Raman spectroscopy, scanning electron microscopy (SEM), and confocal microscopy. The spectra were obtained with the Nicolet iS10 FT-IR spectrometer (resolution: 4 cm^{-1}; scan number: 32) equipped with Nicolet smart attenuated total reflectance. The range of scanning wavenumber was from 4000 to 400 cm^{-1}. The Raman measurements were conducted to analyze the elemental composition using a Czerny–Turner Raman microspectroscopy (IHR320, HORIBA Scientific). The analysis was done with an excitation wavelength of 532 nm. The field emission SEM (Tescan Lyra3) was used for capturing the structural morphology of the coated samples.

A confocal laser scanning microscope (CLSM, Leica Lasertechnik, Heidelberg, Germany) was used to investigate the distribution of living and dead cells on the coating interface. For the confocal imaging, the coating samples were removed from the liquid culture under a biosafety hood. The biofilms were stained with a live/dead backlight bacterial viability kit (Invitrogen) (Meng et al., 2020). This kit contains two nucleic acid dyes: SYTO 9 and propidium iodide (PI) (Fan et al., 2017). The detailed procedure of the biofilm formation quantification is described in our previous study (Nguyen et al., 2017a). All analyses were done in triplicate.

RESULTS AND DISCUSSION

Anticorrosive Property of GOWE Coating

Before electrochemical impedance measurements, the open circuit potential (OCP) was measured to achieve a steady potential. In this study, the OCP value of graphene oxide hybrid coating (GOWE-0.1) was higher than that of the pure epoxy coating sample (data not shown), which indicated the barrier role of graphene oxide nanofiller in the epoxy matrix.

EIS measurements were performed to semi-quantitatively evaluate the overall anticorrosive properties of the developed GO-hybridized composite coatings with a different nano doping ratio at various immersion periods (0 to 64 days in 3.5 wt% NaCl solution). The Bode plots of log |Z| vs. log f for the prepared coatings are shown in **Figure 2**. The initial measurements showed that the impedance modulus at 0.01 Hz of all the coatings was larger than 10^{10} $\Omega{\cdot}cm^2$, which indicated an excellent corrosion protection (Wang and Zhou, 2018). All the GOWE coatings maintained a much higher initial impedance modulus at 0.01 Hz (~10^{11} $\Omega{\cdot}cm^2$) (**Figure 2B**) than the pure epoxy coating (~10^{10} $\Omega{\cdot}cm^2$), which revealed that generally the graphene oxide nanofiller could significantly improve the inherent corrosion resistance of waterborne epoxy coatings. On the other hand, during the long-term immersion time in the saline solution, due to the diffusion of water and corrosion ions into the coating substrates (Zhou and Wang, 2013), both the GOWE and pure epoxy coatings showed a decreasing trend of impedance modulus at 0.01 Hz. This phenomenon was more evident for the pure waterborne epoxy coatings since the impedance modulus of GOWE-0 at a low frequency region reduced sharply with longer immersion time. The result shows a steep degradation of impedance modulus, which dropped about six orders of magnitude (1.90×10^{10} $\Omega{\cdot}cm^2$ to 6.5×10^4 $\Omega{\cdot}cm^2$) in 29 days of immersion and then remained stable for 64 days (**Figure 2A**).

In contrast, for GOWE-0.05 and GOWE-0.1 coatings, the impedance modulus at 0.01 Hz showed a much slower degradation trend than the other coatings, and maintained a value of up to 9.0×10^9 $\Omega{\cdot}cm^2$ and 9.7×10^9 $\Omega{\cdot}cm^2$ after 64 days of immersion, which corresponded to two and one orders of magnitude decline for GOWE-0.05 and GOWE-0.1, respectively. The results suggested that the graphene oxide nanofiller could effectively prevent corrosion. However, interestingly, with the increasing of the GO doping ratio, GOWE-0.5 and GOWE-1 coatings exhibited a higher initial low-frequency impedance modulus but they dropped three and four orders of magnitude, respectively, after 64 days of immersion. This drop could be the result of the aggregation of 2D graphene oxide nanosheets in the coating, and thus, some local "defects" were generated during the coating curing process, which deteriorated the barrier capability of the coatings (Pourhashem et al., 2020). This phenomenon was further confirmed *via* SEM imaging (**Figure 2B**). As a result, the concentrations of 0.1 wt% graphene oxide presented the best corrosion resistance than the other graphene oxide concentrations. These results illustrated that well-dispersed graphene oxide can effectively enhance the barrier properties of anticorrosion coatings.

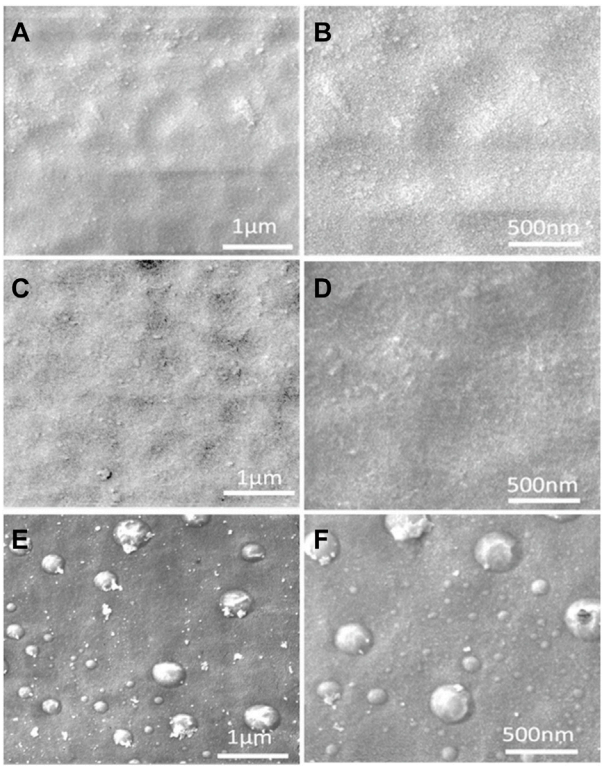

FIGURE 3 | SEM images of the coatings: **(A)** WEP (control, without graphene oxide) with scale 1 μm, **(B)** WEP (control, without graphene oxide) with scale 500 nm, **(C)** GOWE-0.1 (0.1 wt% graphene oxide) with scale 1 μm, **(D)**, GOWE-0.1 (0.1 wt% graphene oxide) with scale 500 nm, **(E)** GOWE-0.5 (0.5 wt% graphene oxide) with scale 1 μm, and **(F)** GOWE-0.5 (0.5 wt% graphene oxide) with scale 500 nm.

Furthermore, from the SEM characterization of the coatings, the GOWE-0.1 coating film exhibited the best graphene oxide dispersion within the epoxy matrix, presenting a more homogeneous and smooth coating surface without significant defects or clusters (**Figure 3B**). The GOWE-0.5 (0.5 wt% GO) (**Figure 3C**), on the other hand, showed obvious defects on the coated surface, which came from the heterogenous dispersion of graphene oxide in the epoxy matrix when the graphene oxide content was high.

Antibacterial Property of GOWE Coatings

Effects of Graphene Oxide Concentration on Biofilm Formation

The growth of *S. oneidensis* on the coated surface was monitored to determine the antibacterial performance of the GOWE coatings. *S. oneidensis* growth mainly includes the process of initial attachment, cells' rapid division on the surface, and isolated microcolonies formation. Eventually, biofilms will develop into an extensive three-dimensional structure with strong interactions with the

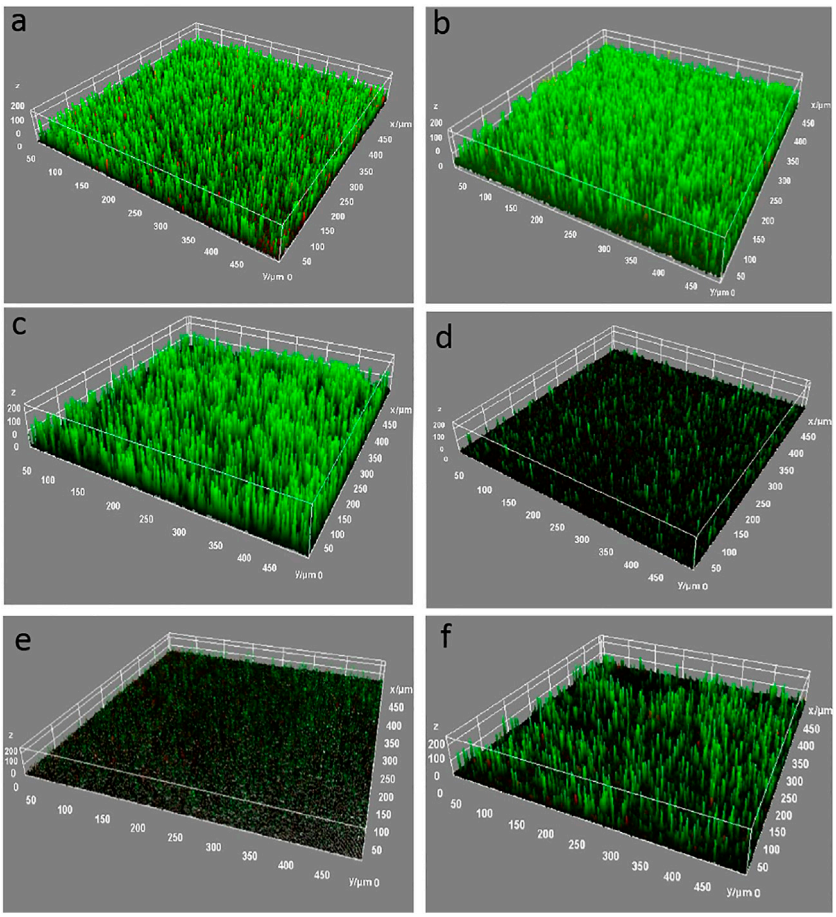

FIGURE 4 | CLSM images of biofilm growth for 72 h on different coating surfaces. **(A)** bare steel; **(B)** WEP coating (control); **(C)** GOWE-0.05 (0.05 wt% GO); **(D)** GOWE-0.1 (0.1 wt% GO); **(E)** GOWE-0.5 (0.5 wt% GO); **(F)** GOWE-1(1 wt% GO). The green color corresponds to living bacterial cells growing on the surface. Experiments were run at 25°C under static batch condition. The units are in micron.

surface due to electrostatic, Van der Waals, and hydrophobic forces (Thormann et al., 2004; Makabenta et al., 2021).

The analysis of the biofilm formed on the GOWE coatings was done *via* the live–dead staining and observation through confocal microscopy. In this work, the waterborne epoxy films (control) and GOWE films with different graphene oxide concentrations (0.05 wt%, 0.1 wt%, 0.5 wt%, and 1 wt%) were exposed to the culture of *S. oneidensis MR-1* in the LB growth medium (containing 1 wt% NaCl) overnight to simulate a real environmental condition. As illustrated in **Figure 4**, the CLSM images for the surfaces of the control coating (without GO) and the bare steel coupon were almost completely green and had a thick biofilm after 72 h exposure, which demonstrated that a healthy biofilm was formed on these surfaces. In contrast, an overwhelming fraction of dead cells were observed on the surface of GOWE coating films, which demonstrated that graphene oxide had a high ability to inhibit bacterial growth (see **Supporting Information**). When the graphene oxide content increased from 0.05 wt% (**Figure 4C**) to 0.5 wt% (**Figure 4E**), less biofilm was observed on the coated surface. However, as the GO concentration increased to 1 wt% (**Figure 4F**), the antibacterial capacity reduced as seen from the increasing numbers of live cells (green) on the coated surface. The less uniform biofilm growth 1 wt% graphene oxide loading could be due to graphene oxide aggregation and subsequent random distribution in the coating. Considering the results of the salt corrosion above and the antimicrobial experiments, the 0.1 wt% graphene oxide concentration was considered the optimal dosage for the coating for simultaneous antibacterial and anticorrosion properties.

Long-Term Antibacterial Performance

In this investigation, the above optimized GOWE-0.1 coating was selected for the long-term exposure investigation of *S. oneidensis* MR-1 in the LB growth medium to evaluate the coating antibacterial performance. As shown in **Figure 5A**, most of the *S. oneidensis* cells were alive (green) with almost no dead (red) cells visible on the surface of the pure epoxy coating (control) after 24 h exposure. In contrast, a relatively higher fraction of dead cells was observed on the surface of the GOWE-0.1 specimen (**Figure 5D**). As the exposure continued to 96 h, the living cells with green fluorescence still dominated on

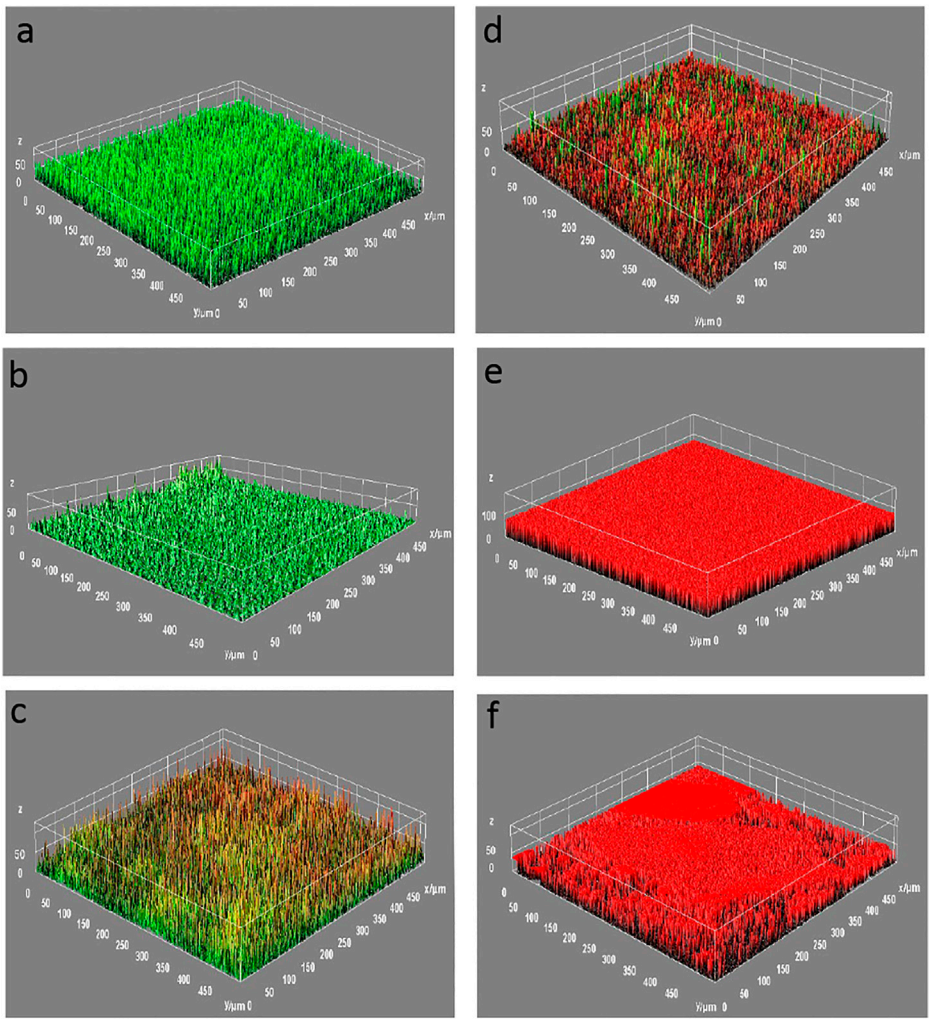

FIGURE 5 | CLSM images of biofilms grown for **(A)** 24 h, **(B)** 96 h, and **(C)** 10 days for the WEP coating (control) and **(D)** 24 h, **(E)** 96 h, and **(F)** 10 days for GOWE-0.1 coating. The coating was stained with SYTO9 and PI prior to microscopic observation. The red color corresponds to dead bacterial cells and the green color corresponds to living bacterial cells. The scale is in microns.

the surface of the pure epoxy coating (**Figure 5B**), while dead (red) cells accounted for a large proportion on the surface of GOWE-0.1 coatings (**Figure 5E**). Furthermore, it is noteworthy that healthy biofilms were formed on the surface of the pure epoxy coating. In comparison, biofilms on the surface of GOWE-0.1 coating were built up by loosely attached cells, which could be easily peeled off from the surface due to large number of dead cells and, therefore, less production of EPS (extracellular polymeric substance) secretion that can make the biofilm sticky (Flemming et al., 2016). This result showed the beneficial addition of graphene oxide to the epoxy to alleviate the biofilm growth. As the exposure time continued to 10 days, almost all living (green) cells were still on the surface of the control coating (**Figure 5C**), whereas almost all cells were dead (red) on the surface of the GOWE-0.1 coating (**Figure 5F**), which clearly demonstrated the sustainable ability of this coating to prevent biofilm formation.

After the antibacterial performance test, the coating samples were cleaned by sonication and DI water to be further analyzed to investigate the surface morphology through SEM. From the SEM images in **Figure 6**, there were no significant surface damages and accumulated corrosion products on the surface of the GOWE-0.1 coating during the 10 days testing, while rough surface and unremoved accumulated products were easily observed on the surface of the pure epoxy coating.

Effects of Biofilm Formation on Anticorrosive Performance of the GOWE Coating

In this study, *Shewanella oneidensis* MR-1, a facultative metallic-reducing bacterium with metabolic versatility including aerobic respiration and dissimilatory Fe (III) reduction, was employed as an Fe (III) reduction bacterium (IRB) model since it can be found

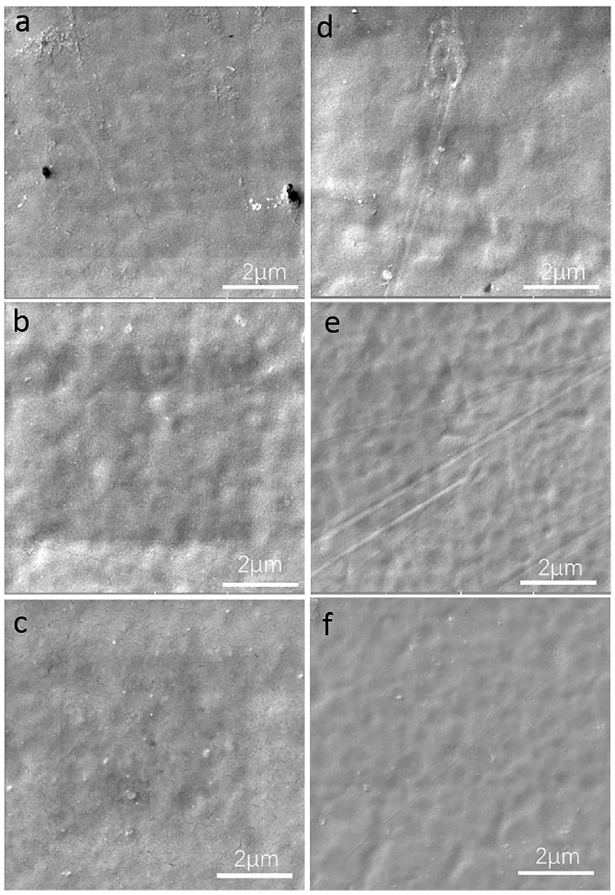

FIGURE 6 | Surface morphology of the WEP coating (control) and GOWE-0.1 coating (0.1 wt% GO) after the exposure in *S. oneidensis* culture for **(A)** 24 h, control **(B)** 96 h, control, and **(C)** 10 days, control; **(D)** 24 h, GOWE-0.1 coating; **(E)** 96 h, GOWE-0.1 coating, and **(F)** 10 days, GOWE-0.1 coating.

under steel corrosion conditions (Wurzler et al., 2020). The influence of Fe reduction bacteria on the corrosion performance remains controversial. Recent literature reviews have demonstrated that the effects of *Shewanella sp.* biofilm on the corrosion behavior of a material can be negative or positive, and highly dependent on the specific environmental factors, such as aerobic or anoxic (anaerobic) conditions, the presence of different electron acceptors, associated metabolic activities, and metabolic versatility (Miller et al., 2016; Bertling et al., 2020; Jiang et al., 2020; Li et al., 2021). For example, Faisal et al. discovered that *Shewanella oneidensis sp.* could inhibit corrosion of X52 carbon steel through iron respiration (Al Abbas et al., 2013). Contrarily, more recently, Li et al. reported *Shewanella sp.* could accelerate uniform or pitting corrosions *via* bioanodic (biocathodic) EET (extracellular electron transfer) (Jiang et al., 2020; Li et al., 2021). Similarly, Miller et al. reported *S. oneidensis* MR-1 promoted corrosion under nitrate reducing conditions (Miller et al., 2016).

Therefore, understanding how *Shewanella sp.* contributes to the material corrosion is important since multiple environmental factors could synergistically promote or inhibit corrosion. Another aspect to be considered is the fact that most approaches for the protection of electrochemical corrosion and biofilm mediated corrosion have been developed by using nano patterning and surface treatment, which can resist bacterial attachment (Singhal et al., 2021), thus efficiently impeding short-range electron transfers between bacteria and substrates. However, from this angle, the actual effects of *Shewanella oneidensis* MR-1 on the composite polymeric coating, such as the epoxy coating, are still rarely reported. Hence, in this context, the real effects of *Shewanella oneidensis* MR-1 on corrosion were also investigated in this experiment.

Specifically, to study the influence of biofilm formation on the anticorrosive performance of GOWE coatings, GOWE-0.1 coating samples with and without biofilm were evaluated by the EIS measurement for 14 days. **Figure 7** shows the impedance modulus at 0.01 Hz as a function of the immersion time for the control and GOWE-01 coating samples. Results show that the coating without bacteria exhibited better corrosion protection than the coating with bacteria. This fact clearly demonstrated that the biofilm formed on the coating surface would accelerate the corrosion. These results also supported the previous study that *S. oneidensis* could accelerate the corrosion progress of graphene oxide composite films under relative anaerobic conditions (Lou et al., 2021). Although our experiments were not done in strictly anaerobic conditions, the fact that we did not mix constantly the media with the cells to well aerate the growth media could have generated a microaerophilic and anoxic condition on the surface of the coupons that were at the bottom of the wells. This could have explained the corrosive effects with the *S. oneidensis* in the presence of salt in the growth medium.

Characterization of the Best GOWE Coating

Two-Dimensional (2D) Graphene Oxide Nanolayer Characterization

The morphological image of the as-prepared graphene oxide with the modified Hummers' method is shown in **Figure 8A**. A sheet-

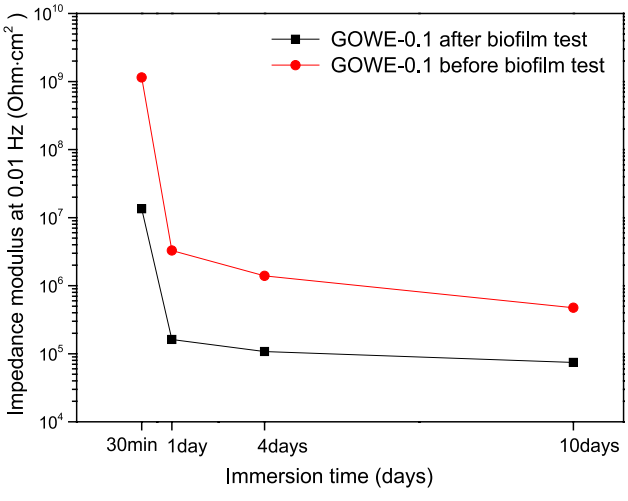

FIGURE 7 | Impedance modulus at 0.01 Hz as a function of the immersion time for GOWE-0.1 coatings with and without biofilm testing.

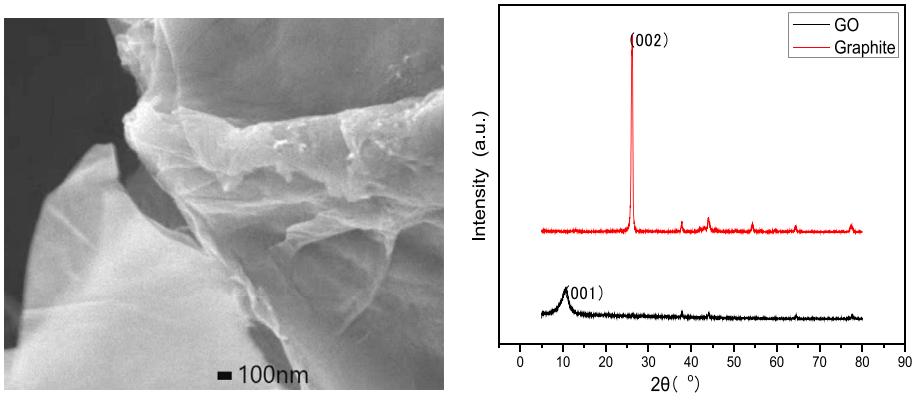

FIGURE 8 | SEM image and XRD patterns of graphene oxide.

like two-dimensional nanolayer structure was observed. The sharp edges and small few layers can be seen clearly. **Figure 8B** indicated the XRD patterns of the raw material graphite and the synthesized graphene oxide. A sharp diffraction peak of pure graphite was present at $2\theta = 26^{\circ}$ (002 plane), which corresponds to the graphite characteristic 002 plane (PDF No: 41-1487) and is consistent with the previous research (Li et al., 2014). For graphene oxide, the broader peak at $2\theta = 10.7^{\circ}$ was observed, which was assigned to (001) diffraction peak due to the chemical oxidation action. This result was very close to the reported value in the literature, and this suggested the successful synthesis of graphene oxide. Meanwhile, the disappearance of graphite (002) plane further proved that the complete oxidation of graphene oxide occurred after the chemical exfoliation (Paulchamy et al., 2015).

Optimal GOWE Coating Characterization

The coatings prior to the analyses were characterized. Here, we report the characterization results of the optimum graphene oxide concentration in the waterborne epoxy coating, which was determined to be 0.1 wt% from the abovementioned anticorrosive and antibacterial study. Therefore, the GOWE-0.1 coating film was characterized by Fourier transform infrared (FTIR) and Raman spectroscopy. The FTIR spectra of WEP (waterborne epoxy), GO (graphene oxide), and GOWE-0.1 (0.1 wt% GO) coatings are shown in **Figure 9**. The typical characteristic peaks of GO (blue curve in **Figure 9**) were observed at 1735 cm^{-1} (C = O stretching vibration of – COOH groups), 3600 cm^{-1} (O – H stretching vibrations), 1095 cm^{-1} (C – O – C stretching vibration), 1260 cm^{-1} (– COH stretching), 1408 cm^{-1} (tertiary C – OH stretching vibration), 1018 and 1636 cm^{-1} (C = C stretching), and 2968 cm^{-1} (– CH stretching), which are in good agreement with the previously reported graphene oxide spectrum (Paredes et al., 2008; Dreyer et al., 2010; Shen et al., 2010; Ma et al., 2016; Ensafi et al., 2017; Harfouche et al., 2017). Furthermore, the spectrum of waterborne epoxy (red curve in **Figure 9**) showed the typical characteristic IR band at 944 cm^{-1} (epoxide ring vibrations). Other representative groups of the epoxy resin include 1037, 1240, and 1110 cm^{-1} (symmetrical aromatic and aliphatic C – O stretch); 1183, 1296,

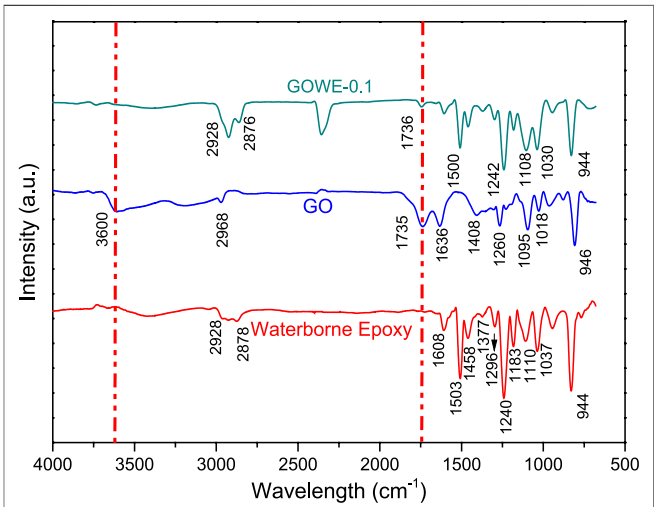

FIGURE 9 | Fourier transform infrared spectra of GO, waterborne epoxy (control), and GOWE-0.1.

and 1377 cm^{-1} (tertiary C – OH stretching vibration); 1458 cm^{-1} (deformation of C – H of CH_2/CH_3); 1503 and 1608 cm^{-1} (C = C of aromatic rings/C – C skeletal stretching); and 2878 and 2928 cm^{-1} (stretching C – H of CH_2 and C – H aromatic and aliphatic), which confirm the characteristic bands of key functional groups in the epoxy matrix (Yu et al., 2016). For GOWE-0.1 coating (green curve in **Figure 9**), similar absorption bands were observed as the waterborne epoxy, especially in the region between 900 and 1600 cm^{-1} due to the relatively low content of graphene oxide in the epoxy matrix. A distinct new band was found in the GOWE-0.1 coating, which was not observed in the pure epoxy and assigned to the characteristic absorption peaks of graphene oxide at 1735 cm^{-1}, which clearly showed a C = O bond for the carboxyl group due to the existence of graphene oxide. However, it is obvious that the intensity of the carboxyl groups (1735 cm^{-1}) became weaker and hydroxyl groups (– OH, 3600 cm^{-1}) disappeared when combining graphene oxide with the epoxy matrix. This indicates that

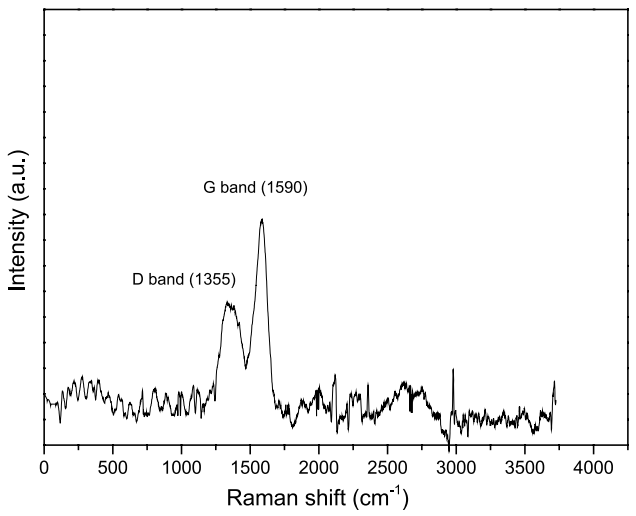

FIGURE 10 | Raman spectra of the GOWE-0.1 coating.

some reactions might have occurred between the carboxyl and hydroxyl groups of graphene oxide with the curing agent during the curing process (Chauhana et al., 2018; Vryonis et al., 2019; Ding et al., 2021). As a result, a three-dimensional graphene oxide network structure was formed in the waterborne epoxy matrix (Her and Zhang, 2021).

The Raman spectrum of the GOWE-0.1 (0.1 wt% graphene oxide) film is shown in **Figure 10**. The peak of GO at 1590 cm^{-1} displayed the G-band, which corresponds to E2g phonon of sp2 carbon–carbon bond and isolated double bonds on graphene oxide sheets (Pan et al., 2017). D-band appeared at 1355 cm^{-1}, which is the characteristic of the graphene tangential vibrational mode (the breathing modes of six-membered rings activated by defects) (Kudin et al., 2008). These Raman peaks for graphene oxide agree well with those reported previously by others (Díaz et al., 2017; Pan et al., 2017; Azizighannad and Mitra, 2018). The ratio of the intensity of the D and G bands (ID/IG) of the GOWE-0.1 coating was approximately 0.89 by integrating the areas of D and G peaks. This was aligned with the typical graphene oxide value obtained through oxidization and exfoliation of graphite as described in previous reports (Kudin et al., 2008; Jhajharia and Selvaraj, 2015), which demonstrated a good dispersion of the graphene oxide nanofillers in the waterborne epoxy matrix. Other Raman peaks located at 1012, 1156, 1709, 2639, and 2759 cm^{-1} are assigned to the vibrations of the epoxy (Kudin et al., 2008).

Corrosion Protection Mechanism of the Prepared Coating

The anticorrosive enhancement of graphene oxide-hybridized coating can be schematically illustrated in **Figure 11**. To understand the anticorrosive mechanism by graphene oxide nanofillers, the coating surface was cut 2 cm in length by a blade for both the WEP coating and GOWE-0.1 coating to simulate the accelerated local corrosion defects. The coated samples were first immersed in the salt solution (8 wt% NaCl) for 120 h. The images of the surfaces for waterborne epoxy coating with and without graphene oxide after immersion are shown in **Figure 11**. After 120 h testing, the WEP control (**Figure 11A**) clearly showed serious local corrosion that demonstrated the corrosion agents (e.g., Cl^-, O_2, and H_2O) had penetrated through the interface of the epoxy/metal and hydrolytically destroyed the coating, which caused the pit corrosion (Chang et al., 2014). Furthermore, these pits near the crack regions on the coating could connect to each other first followed by the occurrence of spalling (**Figure 11A**).

On the other hand, there was no obvious corrosion defects on the surface of the GOWE-0.1 coating. In fact, the optimal GO content (0.1 wt%) was assumed to form a homogeneous three-dimensional network structure, according to the abovementioned analysis (**sections 3.3**, **3.4**), which could prevent local corrosion and significantly retard the propagation of the defects within the network structure. Additionally, the better coating adhesion achieved by

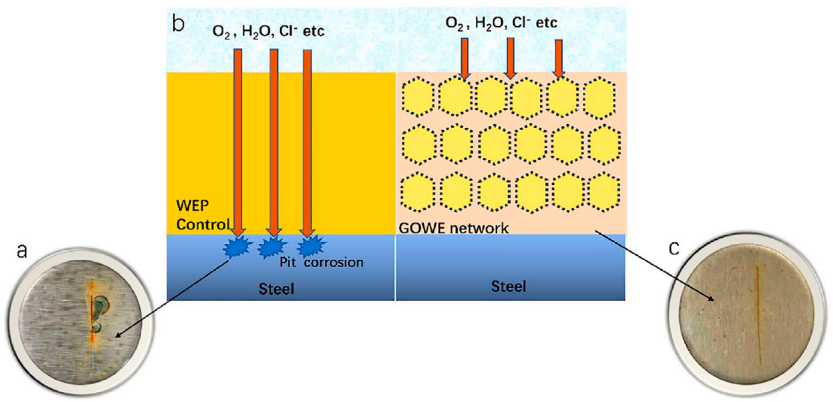

FIGURE 11 | Surface morphology of the WEP coating (control, without GO) and GOWE-0.1 (0.1 wt% GO) before and after the exposure in 8 wt% NaCl solution. **(A)** WEP coating 120 h; **(C)** GOWE-0.1 coating, 120 h; **(B)** schematic diagrams of the anticorrosive mechanism of the WEP coating and the GOWE coating.

incorporating well-dispersed graphene oxide nanoplates in the epoxy allowed improved corrosive protection by the coating (Pourhashem et al., 2017). In addition, electrons from iron oxidation in the micro-anode region can migrate through conductive nanoparticles, such as graphene oxide, which can alleviate the oxidation–reduction reaction of corroded areas (Yu et al., 2017). As a result, the prepared composite coating exhibited better corrosion protection than the waterborne epoxy control (**Figure 11**), which was mainly attributed to the built three-dimensional network structure with well dispersed graphene oxide.

CONCLUSION

In this study, an effective graphene oxide-hybridized waterborne epoxy coating was successfully developed as a coating material. The best concentration of graphene oxide as a nanofiller was identified to be 0.1 wt% for simultaneous anticorrosive and antibacterial protection of steel. The protection of steel was observed for more than 60 days for both 3.5% NaCl and against *S. oniedensis* MR-1. The protection against *S. oniedensis* MR-1 against corrosion was probably due to the biofilm inhibition observed in the coated material, since the non-coated material and the materials lacking graphene oxide presented the establishment of a biofilm and corrosion. Therefore, the newly developed graphene oxide-hybridized waterborne epoxy coating can be potentially employed for applications that require simultaneous enhancement of anticorrosive and antibacterial functions.

DATA AVAILABILITY STATEMENT

Any data presented in this study is available upon request. Please contact the corresponding authors for any inquiries.

AUTHOR CONTRIBUTIONS

YZ was responsible for preparing the materials, characterizing and performing the antimicrobial investigation, and writing that aspect of the work. HW and CZ performed the corrosion investigation in the manuscript. DR and QZ were responsible for the conceptualization of the work, editing, and assisting with the data analysis.

FUNDING

The authors would like to acknowledge the following funding sources: Qatar National Research Foundation, award number: NPRP 9-318-1-064; the Robert A. Welch Foundation, award number: E-2011-20190330; and the National Science Foundation under Grant No. CHE-1904472.

SUPPLEMENTARY MATERIAL

The Supplementary Material for this article can be found online at: https://www.frontiersin.org/articles/10.3389/fmats.2022.910152/full#supplementary-material

REFERENCES

Al Abbas, F. M., Bhola, S. M., Spear, J. R., Olson, D. L., and Mishra, B. (2013). The Shielding Effect of Wild Type Iron Reducing Bacterial Flora on the Corrosion of Linepipe Steel. *Eng. Fail. Anal.* 33, 222–235. doi:10.1016/j.engfailanal.2013.05.020

Ansari, A., Peña-Bahamonde, J., Wang, M., Shaffer, D. L., Hu, Y., and Rodrigues, D. F. (2021). Polyacrylic Acid-Brushes Tethered to Graphene Oxide Membrane Coating for Scaling and Biofouling Mitigation on Reverse Osmosis Membranes. *J. Membr. Sci.* 630, 119308. doi:10.1016/j.memsci.2021.119308

Atta, A. M., Ezzat, A. O., El-Saeed, A. M., Tawfeek, A. M., and Sabeela, N. I. (2020). Self-healing of Chemically Bonded Hybrid Silica/epoxy for Steel Coating. *Prog. Org. Coatings* 141, 105549. doi:10.1016/j.porgcoat.2020.105549

Azizighannad, S., and Mitra, S. (2018). Stepwise Reduction of Graphene Oxide (GO) and its Effects on Chemical and Colloidal Properties. *Sci. Rep.* 8, 10083. doi:10.1038/s41598-018-28353-6

Bertling, K., Banerjee, A., and Saffarini, D. (2020). Aerobic Respiration and its Regulation in the Metal Reducer Shewanella Oneidensis. *Front. Microbiol.* 12, 723835. doi:10.3389/fmicb.2021.723835

Chang, K., Hsu, M.-H., Lu, H.-I., Lai, M.-C., Liu, P.-J., Hsu, C., et al. (2014). Room-temperature Cured Hydrophobic Epoxy/graphene Composites as Corrosion Inhibitor for Cold-Rolled Steel. *Carbon* 66, 144–153. doi:10.1016/j.carbon.2013.08.052

Chauhana, D. S., Quraishia, M. A., Ansaria, K. R., and Salehb, T. A. (2018). One-step Surface Modification of Graphene Oxide and Influence of its Particle Size on the Properties of Graphene Oxide/epoxy Resin Nanocomposites. *Eur. Polym. J.* 101, 211–217. doi:10.1016/j.eurpolymj.2018.02.036

Chen, C., Xiao, G., He, Y., Zhong, F., Li, H., Wu, Y., et al. (2020). Bio-inspired Superior Barrier Self-Healing Coating: Self-Assemble of Graphene Oxide and Polydopamine-Coated Halloysite Nanotubes for Enhancing Corrosion Resistance of Waterborne Epoxy Coating. *Prog. Org. Coatings* 139, 13. doi:10.1016/j.porgcoat.2019.105402

Chopra, D., Gulati, K., and Ivanovski, S. (2021). Understanding and Optimizing the Antibacterial Functions of Anodized Nano-Engineered Titanium Implants. *Acta Biomater.* 127, 80–101. doi:10.1016/j.actbio.2021.03.027

Christopher, G., Anbu Kulandainathan, M., and Harichandran, G. (2015). Comparative Study of Effect of Corrosion on Mild Steel with Waterborne Polyurethane Dispersion Containing Graphene Oxide versus Carbon Black Nanocomposites. *Prog. Org. Coatings* 89, 199–211. doi:10.1016/j.porgcoat.2015.09.022

Compton, O. C., Jain, B., Dikin, D. A., Abouimrane, A., Amine, K., and Nguyen, S. T. (2011). Chemically Active Reduced Graphene Oxide with Tunable C/O Ratios. *ACS Nano* 5, 4380–4391. doi:10.1021/nn1030725

Díaz, D. L., Holgado, M. L., Fierro, J. L. G., and Velázquez, M. M. (2017). Evolution of the Raman Spectrum with the Chemical Composition of Graphene Oxide. *J. Phys. Chem. C* 121, 20489–20497. doi:10.1021/acs.jpcc.7b06236

Ding, J., Zhao, H., Zhou, M., Liu, P., and Yu, H. (2021). Super-anticorrosive Inverse Nacre-like Graphene-Epoxy Composite Coating. *Carbon* 181, 204–211. doi:10.1016/j.carbon.2021.05.017

Ding, R., Chen, S., Lv, J., Zhang, W., Zhao, X.-d., Liu, J., et al. (2019). Study on Graphene Modified Organic Anti-corrosion Coatings: A Comprehensive Review. *J. Alloys Compd.* 806, 611–635. doi:10.1016/j.jallcom.2019.07.256

Dreyer, D. R., Park, S., Bielawski, C. W., and Ruoff, R. S. (2010). The Chemistry of Graphene Oxide. *Chem. Soc. Rev.* 39, 228–240. doi:10.1039/b917103g

Ensafi, A. A., Noroozi, R., Zandi--Atashbar, N., and Rezaei, B. (2017). Cerium(IV) Oxide Decorated on Reduced Graphene Oxide, a Selective and Sensitive Electrochemical Sensor for Fenitrothion Determination. *Sensors Actuators B Chem.* 245, 980–987. doi:10.1016/j.snb.2017.01.186

Fan, J., Grande, C. D., and Rodrigues, D. F. (2017). Biodegradation of Graphene Oxide-Polymer Nanocomposite Films in Wastewater. *Environ. Sci. Nano.* 4. doi:10.1039/c7en00396j

Fichman, G., Adler-Abramovich, L., Manohar, S., Mironi-Harpaz, I., Guterman, T., Seliktar, D., et al. (2014). Seamless Metallic Coating and Surface Adhesion of Self-Assembled Bioinspired Nanostructures Based on Di-(3,4-dihydroxy-l-phenylalanine) Peptide Motif. *ACS Nano* 8, 7220–7228. doi:10.1021/nn502240r

Flemming, H.-C., Wingender, J., Szewzyk, U., Steinberg, P., Rice, S. A., and Kjelleberg, S. (2016). Biofilms: an Emergent Form of Bacterial Life. *Nat. Rev. Microbiol.* 14, 563–575. doi:10.1038/nrmicro.2016.94

Geim, A. K., and Novoselov, K. S. (2010). The Rise of Graphene. *Nat Mater.* 6 (3), 183–191. doi:10.1038/nmat1849

Georgakilas, V., Perman, J. A., Tucek, J., and Zboril, R. (2015). Broad Family of Carbon Nanoallotropes: Classification, Chemistry, and Applications of Fullerenes, Carbon Dots, Nanotubes, Graphene, Nanodiamonds, and Combined Superstructures. *Chem. Rev.* 115, 4744–4822. doi:10.1021/cr500304f

Glasauer, S., Langley, S., and Beveridge, T. J. (2002). Intracellular Iron Minerals in a Dissimilatory Iron-Reducing Bacterium. *Science* 295, 117–119. doi:10.1126/science.1066577

Harfouche, N., Gospodinova, N., Nessark, B., and Perrin, F. X. (2017). Electrodeposition of Composite Films of Reduced Graphene Oxide/polyaniline in Neutral Aqueous Solution on Inert and Oxidizable Metal. *J. Electroanal. Chem.* 786, 135–144. doi:10.1016/j.jelechem.2017.01.030

Her, S.-C., and Zhang, K.-C. (2021). Mode I Fracture Toughness of Graphene Reinforced Nanocomposite Film on Al Substrate. *Nanomaterials* 11, 1743. doi:10.3390/nano11071743

Hu, W., Peng, C., Luo, W., Lv, M., Li, X., Li, D., et al. (2010). Graphene-based Antibacterial Paper. *ACS Nano* 4, 4317–4323. doi:10.1021/nn101097v

Jhajharia, S. K., and Selvaraj, K. (2015). Non-templated Ambient Nanoperforation of Graphene: A Novel Scalable Process and its Exploitation for Energy and Environmental Applications. *Nanoscale* 7, 19705–19713. doi:10.1039/c5nr05715a

Jiang, Z., Shi, M., and Shi, L. (2020). Degradation of Organic Contaminants and Steel Corrosion by the Dissimilatory Metal-Reducing Microorganisms Shewanella and Geobacter Spp. *Int. Biodeterior. Biodegrad.* 147, 104842. doi:10.1016/j.ibiod.2019.104842

Koch, G. H., Varney, J. N., Thompson, O., Moghissi, M. G., and Payer, J. (2016). *International Measures of Prevention, Application, and Economics of Corrosion Technologies Study*. Houston, HO, USA: NACE International.

Kudin, K. N., Ozbas, B., Schniepp, H. C., Prud'homme, R. K., Aksay, I. A., and Car, R. (2008). Raman Spectra of Graphite Oxide and Functionalized Graphene Sheets. *Nano Lett.* 8, 36–41. doi:10.1021/nl071822y

Lekbach, Y., Dong, Y., Li, Z., Xu, D., El Abed, S., Yi, Y., et al. (2019). Catechin Hydrate as an Eco-Friendly Biocorrosion Inhibitor for 304L Stainless Steel with Dual-Action Antibacterial Properties against *Pseudomonas aeruginosa* Biofilm. *Corros. Sci.* 157, 98–108. doi:10.1016/j.corsci.2019.05.021

Li, J., Ge, S., Wang, J., Du, H., Song, K., Fei, Z., et al. (2018). Water-based Rust Converter and its Polymer Composites for Surface Anticorrosion. *Colloids Surfaces A Physicochem. Eng. Aspects* 537, 334–342. doi:10.1016/j.colsurfa.2017.10.041

Li, J., Zeng, X., Ren, T., and Van der Heide, E. (2014). The Preparation of Graphene Oxide and its Derivatives and Their Application in Bio-Tribological Systems. *Lubricants* 2, 137–161. doi:10.3390/lubricants2030137

Li, Z., Chang, W., Cui, T., and Xu, D. (2021). MR-1 Bacteria Could Corrode Steels via Bioanodic or Biocathodic EET in Adaptation to the Passive or Active State of the Steel Surface. *Commun. Mater.* 2. doi:10.1038/s43246-021-00173-8

Lim, H. L. (2012). Assessing Level and Effectiveness of Corrosion Education in the UAE. *Int. J. Corros.* 2012, 785701. doi:10.1155/2012/785701

Liu, Y., Wen, J., Gao, Y., Li, T., Wang, H., Yan, H., et al. (2018). Antibacterial Graphene Oxide Coatings on Polymer Substrate. *Appl. Surf. Sci.* 436, 624–630. doi:10.1016/j.apsusc.2017.12.006

Lou, Y., Chang, W., Cui, T., Wang, J., Qian, H., Ma, L., et al. (2021). Microbiologically Influenced Corrosion Inhibition Mechanisms in Corrosion Protection: A Review. *Bioelectrochemistry* 141, 107883. doi:10.1016/j.bioelechem.2021.107883

Ma, Y., Di, H., Yu, Z., Liang, L., Lv, L., Pan, Y., et al. (2016). Fabrication of Silica-Decorated Graphene Oxide Nanohybrids and the Properties of Composite Epoxy Coatings Research. *Appl. Surf. Sci.* 360, 936–945. doi:10.1016/j.apsusc.2015.11.088

Makabenta, J. M. V., Nabawy, A., Li, C.-H., Schmidt-Malan, S., Patel, R., and Rotello, V. M. (2021). Nanomaterial-based Therapeutics for Antibiotic-Resistant Bacterial Infections. *Nat. Rev. Microbiol.* 19, 23–36. doi:10.1038/s41579-020-0420-1

Mallakpour, S., Azadi, E., and Hussain, C. M. (2021). Recent Breakthroughs of Antibacterial and Antiviral Protective Polymeric Materials during COVID-19 Pandemic and after Pandemic: Coating, Packaging, and Textile Applications. *Curr. Opin. Colloid & Interface Sci.* 55. doi:10.1016/j.cocis.2021.101480

Meng, F., Liu, L., Tian, W., Wu, H., Li, Y., Zhang, T., et al. (2015). The Influence of the Chemically Bonded Interface between Fillers and Binder on the Failure Behaviour of an Epoxy Coating under Marine Alternating Hydrostatic Pressure. *Corros. Sci.* 101, 139–154. doi:10.1016/j.corsci.2015.09.011

Meng, J., Liu, X., Niu, C., Pang, Q., Li, J., Liu, F., et al. (2020). Advances in Metal-Organic Framework Coatings: Versatile Synthesis and Broad Applications. *Chem. Soc. Rev.* 49, 3142–3186. doi:10.1039/c9cs00806c

Miller, R. B., Sadek, A., Rodriguez, A., Iannuzzi, M., Giai, C., Senko, J. M., et al. (2016). Use of an Electrochemical Split Cell Technique to Evaluate the Influence of Shewanella Oneidensis Activities on Corrosion of Carbon Steel. *PLoS One* 11, e0147899. doi:10.1371/journal.pone.0147899

Mirmohseni, A., Azizi, M., and Seyed Dorraji, M. S. (2019). Facile Synthesis of Copper/ Reduced Single Layer Graphene Oxide as a Multifunctional Nanohybrid for Simultaneous Enhancement of Antibacterial and Antistatic Properties of Waterborne Polyurethane Coating. *Prog. Org. Coatings* 131, 322–332. doi:10.1016/j.porgcoat.2019.02.031

Nematollahi, M., Heidarian, M., Peikari, M., Kassiriha, S. M., Arianpouya, N., and Esmaeilpour, M. (2010). Comparison between the Effect of Nanoglass Flake and Montmorillonite Organoclay on Corrosion Performance of Epoxy Coating. *Corros. Sci.* 52, 1809–1817. doi:10.1016/j.corsci.2010.01.024

Nguyen, H. N., Nadres, E. T., Alamani, B. G., and Rodrigues, D. F. (2017). Designing Polymeric Adhesives for Antimicrobial Materials: Poly(ethylene Imine) Polymer, Graphene, Graphene Oxide and Molybdenum Trioxide-A Biomimetic Approach. *J. Mat. Chem. B* 28, 6616–6628. doi:10.1039/C6EN00442C

Nguyen, H. N., Nadres, E. T., Alamani, B. G., and Rodrigues, D. F. (2017). Designing Polymeric Adhesives for Antimicrobial Materials: Poly(ethylene Imine) Polymer, Graphene, Graphene Oxide and Molybdenum Trioxide - A Biomimetic Approach. *J. Mater Chem. B* 5, 6616–6628. doi:10.1039/c7tb00722a

Nie, Y., Huang, J., Ma, S., Li, Z., Shi, Y., Yang, X., et al. (2020). MXene-Hybridized Silane Films for Metal Anticorrosion and Antibacterial Applications. *Appl. Surf. Sci.* 527, 146915. doi:10.1016/j.apsusc.2020.146915

Ning, Y.-J., Zhu, Z.-R., Cao, W.-W., Wu, L., Jing, L.-C., Wang, T., et al. (2021). Anti-corrosion Reinforcement of Waterborne Polyurethane Coating with Polymerized Graphene Oxide by the One-Pot Method. *J. Mater Sci.* 56, 337–350. doi:10.1007/s10853-020-05243-9

Pan, Y.-T., Wan, J., Zhao, x., Li, c., and Wang, D.-Y. (2017). Interfacial Growth of MOF-Derived Layered Double Hydroxide Nanosheets on Graphene Slab towards Fabrication of Multifunctional Epoxy Nanocomposites. *Chem. Eng. J.* 330, 1222–1231. doi:10.1016/j.cej.2017.08.059

Paredes, J. I., Villar-Rodil, S., Martínez-Alonso, A., and Tascón, J. M. D. (2008). Graphene Oxide Dispersions in Organic Solvents. *Langmuir* 24, 10560–10564. doi:10.1021/la801744a

Paulchamy, B., Arthi, G., and Lignesh, B. D. (2015). A Simple Approach to Stepwise Synthesis of Graphene Oxide Nanomaterial. *J. Nanomed. Nanotechnol.* 6, 2–5. doi:10.4172/2157-7439.1000253

Peña-Bahamonde, J., San-Miguel, V., Cabanelas, J. C., and Rodrigues, D. F. (2018). Biological Degradation and Biostability of Nanocomposites Based on Polysulfone with Different Concentrations of Reduced Graphene Oxide. *Macromol. Mat. Eng.* 303, 1700359.

Pourhashem, S., Saba, F., Duan, J., Rashidi, A., Guan, F., Nezhad, E. G., et al. (2020). Polymer/Inorganic Nanocomposite Coatings with Superior Corrosion Protection Performance: A Review. *J. Industrial Eng. Chem.* 88, 29–57. doi:10.1016/j.jiec.2020.04.029

Pourhashem, S., Vaezi, M. R., Rashidi, A., and Bagherzadeh, M. R. (2017). Exploring Corrosion Protection Properties of Solvent Based Epoxy-Graphene Oxide Nanocomposite Coatings on Mild Steel. *Corros. Sci.* 115, 78–92. doi:10.1016/j.corsci.2016.11.008

Shen, J., Hu, Y., Shi, M., Li, N., Ma, H., and Ye, M. (2010). One Step Synthesis of Graphene Oxide-Magnetic Nanoparticle Composite. *J. Phys. Chem. C* 114 (3), 1498–1503. doi:10.1021/jp909756r

Singhal, A. V., Malwal, D., Thiyagarajan, S., and Lahiri, I. (2021). Antimicrobial and Antibiofilm Activity of GNP-Tannic Acid-Ag Nanocomposite and Their

Epoxy-Based Coatings. *Prog. Org. Coatings* 159, 106421. doi:10.1016/j.porgcoat.2021.106421

Thormann, K. M., Saville, R. M., Shukla, S., Pelletier, D. A., and Spormann, A. M. (2004). Initial Phases of Biofilm Formation in Shewanella Oneidensis MR-1. *J. Bacteriol.* 186, 8096–8104. doi:10.1128/jb.186.23.8096-8104.2004

Van Haute, D., Liu, A. T., and Berlin, J. M. (2018). Coating Metal Nanoparticle Surfaces with Small Organic Molecules Can Reduce Nonspecific Cell Uptake. *ACS Nano* 12, 117–127. doi:10.1021/acsnano.7b03025

Vryonis, O., Virtanen, S. T. H., Andritsch, T., Vaughan, A. S., and Lewin, P. L. (2019). Understanding the Cross-Linking Reactions in Highly Oxidized Graphene/epoxy Nanocomposite Systems. *J. Mater Sci.* 54, 3035–3051. doi:10.1007/s10853-018-3076-8

Wang, H., and Zhou, Q. (2018). Evaluation and Failure Analysis of Linseed Oil Encapsulated Self-Healing Anticorrosive Coating. *Prog. Org. Coatings* 118, 108–115. doi:10.1016/j.porgcoat.2018.01.024

Wang, N., Gao, H., Zhang, J., and Kang, P. (2018). Effect of Graphene Oxide/ZSM-5 Hybrid on Corrosion Resistance of Waterborne Epoxy Coating. *Coatings* 8, 179. doi:10.3390/coatings8050179

Wurzler, N., Schutter, J. D., Wagner, R., Dimper, M., Lützenkirchen-Hecht, D., and Ozcan, O. (2020). Abundance of Fe(III) during Cultivation Affects the Microbiologically Influenced Corrosion (MIC) Behaviour of Iron Reducing Bacteria Shewanella Putrefaciens. *Corros. Sci.* 174, 108855. doi:10.1016/j.corsci.2020.108855

Yadav, P. S., Purohit, R., and Kothari, A. (2019). Study of Friction and Wear Behaviour of Epoxy/Nano SiO2 Based Polymer Matrix Composites- A Review. *Mater. Today Proc.* 18, 5530–5539. doi:10.1016/j.matpr.2019.07.666

Yu, D., Wen, S., Yang, J., Wang, J., and Wu, Y. (2017). RGO Modified ZnAl-LDH as Epoxy Nanostructure Filler: a Novel Synthetic Approach to Anticorrosive Waterborne Coating. *Surf. Coat. Technol.* 326. doi:10.1016/j.surfcoat.2017.07.053

Yu, H., Zhang, B., Bulin, C., Li, R., and Xing, R. (2016). High-efficient Synthesis of Graphene Oxide Based on Improved Hummers Method. *Sci. Rep.* 6, 36143. doi:10.1038/srep36143

Yu, Y.-H., Lin, Y.-Y., Lin, C.-H., Chan, C.-C., and Huang, Y.-C. (2014). High-performance Polystyrene/graphene-Based Nanocomposites with Excellent Anti-corrosion Properties. *Polym. Chem.* 5, 535–550. doi:10.1039/c3py00825h

Zhang, J., Lin, W., Zhu, C., Lv, J., Zhang, W., and Feng, J. (2018). Dark, Infrared Reflective, and Superhydrophobic Coatings by Waterborne Resins. *Langmuir* 34, 5600–5605. doi:10.1021/acs.langmuir.8b00929

Zhang, S., Liang, X., Gadd, G. M., and Zhao, Q. (2021). A Sol-Gel Based Silver Nanoparticle/polytetrafluorethylene (AgNP/PTFE) Coating with Enhanced Antibacterial and Anti-corrosive Properties. *Appl. Surf. Sci.* 535, 147675. doi:10.1016/j.apsusc.2020.147675

Zhou, Q., and Wang, Y. (2013). Comparisons of Clear Coating Degradation in NaCl Solution and Pure Water. *Prog. Org. Coatings* 76, 1674–1682. doi:10.1016/j.porgcoat.2013.07.018

Conflict of Interest: The authors declare that the research was conducted in the absence of any commercial or financial relationships that could be construed as a potential conflict of interest.

Publisher's Note: All claims expressed in this article are solely those of the authors and do not necessarily represent those of their affiliated organizations, or those of the publisher, the editors, and the reviewers. Any product that may be evaluated in this article, or claim that may be made by its manufacturer, is not guaranteed or endorsed by the publisher.

Advantages of publishing in Frontiers

OPEN ACCESS
Articles are free to read for greatest visibility and readership

FAST PUBLICATION
Around 90 days from submission to decision

HIGH QUALITY PEER-REVIEW
Rigorous, collaborative, and constructive peer-review

TRANSPARENT PEER-REVIEW
Editors and reviewers acknowledged by name on published articles

Frontiers
Avenue du Tribunal-Fédéral 34
1005 Lausanne | Switzerland

Visit us: www.frontiersin.org
Contact us: frontiersin.org/about/contact

REPRODUCIBILITY OF RESEARCH
Support open data and methods to enhance research reproducibility

DIGITAL PUBLISHING
Articles designed for optimal readership across devices

FOLLOW US
@frontiersin

IMPACT METRICS
Advanced article metrics track visibility across digital media

EXTENSIVE PROMOTION
Marketing and promotion of impactful research

LOOP RESEARCH NETWORK
Our network increases your article's readership